Effective Kugel-Khomskii type models for d⁴ and d⁵ materials

Von der Fakultät Mathematik und Physik der Universität Stuttgart
zur Erlangung der Würde eines Doktors der Naturwissenschaften
(Dr. rer. nat.) genehmigte Abhandlung

Vorgelegt von

Pascal Strobel

aus Stuttgart

Hauptberichterin:	Prof. Dr. Maria Daghofer
Mitberichter:	Prof. Dr. Mathias Scheurer
Tag der mündlichen Prüfung:	09.11.2023

Institut für Funktionelle Materie und Quantentechnologien

der Universität Stuttgart

2023

Contents

Acronyms

3U1D "3-up-1-down"

AFM antiferromagnet

AP arbitrary polarization

CF crystal field

CP circular polarization

DFT density functional theory

DOSF dynamic orbital structure factor

DSSF dynamic spin structure factor

ED exact diagonalization

FM ferromagnet

FOPT feedback optimized parallel tempering

INS inelastic neutron scattering

KHI Kitaev-Heisenberg interactions

KSL Kitaev spin liquid

LI light induced interactions

LP linear polarization

MC Monte Carlo

NN nearest neighbor

NNN next nearest neighbor

ORA off resonance approximation

PM paramagnet

PTMC parallel tempering Monte-Carlo

RPA retractable path approximation

SOC spin-orbit coupling

SSF spin structure factor

TNN third nearest neighbor

VCA variational cluster approach

Inhaltsangabe

$4d$ und $5d$ Übergangsmetall basierte Mott-Isolatoren mit beträchtlicher Spin-Bahn Kopplung waren im Fokus wissenschaftlicher Forschung der letzten Jahre. Dies ist der Fall, da sie Kandidaten für interessante Grundzustandseigenschaften, wie z.B. exzitonischer Magnetismus, Quantenspinflüssigkeiten sind. Der Grund dafür, dass diese Materialien solche ungewöhnlichen Grundzustände beherbergen, ist die komplexe Wechselwirkung zwischen starken Korrelationen, Spin-Bahn Kopplung und anderen Effekten wie z.B. der Kristallfeldaufspaltung. Um diese Materialien von einem theoretischen Standpunkt aus untersuchen zu können, ist es oft notwendig den Hamiltonian mit einem effektiven Modell zu approximieren, da eine exakte Beschreibung oft nicht möglich ist. Ziel dieser effektiven Modelle ist es, wichtige physikalische Eigenschaften zu erfassen und akkurate Vorhersagen für Experimente zu treffen. Eines der bedeutendsten Modelle im Kontext von stark korrelierten Mott-Isolatoren ist das Kugel-Khomskii Modell, welches Spin- und Orbitalinteraktionen lokalisierter Elektronen störungstheoretisch beschreibt. Allerdings beschreibt dieses Modell nicht den Einfluss der Spin-Bahn-Kopplung, welche Spin- und Orbitalfreiheitsgrade verknüpft. Diese ist ein entscheidender Faktor für die Entstehung von spezifischen Interaktionen, die z.B. notwendig zur Realisierung einer Quantenspinflüssigkeit sind. Die allgemeine Herangehensweise für die in dieser Thesis diskutierten Materialien ist daher zuerst ein effektives Kugel-Khomskii Modell herzuleiten und daraufhin die Spin-Bahn Kopplung zu berücksichtigen.

Im Kontext der d^5 Materialien, die in dieser Thesis untersucht werden, wurden bereits sowohl das effektive Spin-Bahn-Modell als auch der Einfluss der Spin-Bahn Kopplung exzessiv untersucht. Dies führte u.a. zum bekannten Kitaev-Heisenberg Modell, welches Interaktionen beherbergt, die eine Quantenspinflüssigkeit realisieren können. Der Vorschlag von Khaliullin und Jackeli [1], dass dieses Modell in Festkörpern realisierbar sein könnte, führte zu einer Welle an theoretischen und experimentellen Studien [2, 3], mit dem Ziel ein Material zu finden, was ebenjene Quantenspinflüssigkeit als Grundzustand realisiert. Bisher zeigten allerdings nur wenige Materialien Signaturen einer Quantenspinflüssigkeit [2, 4] und alle in dieser Thesis untersuchten Materialien zeigen magnetische Ordnung bei niedrigen Temperaturen. Ein Fokus aktueller Forschung liegt daher darauf, Materialien, die Kandidaten für ein Kitaev-Modell sind,

so zu manipulieren, dass sie eine Quantenspinflüssigkeit realisieren. In dieser Thesis wollen wir die Möglichkeit diskutieren Materialien, im speziellen α-RuCl$_3$, mit einem zeitperiodischen Lichtfeld so zu manipulieren, dass die Kitaev Interaktionen signifikant verstärkt werden. Der Einfluss solcher Lichtfelder kann mithilfe des Floquet Formalismus beschrieben werden, welcher einen zeitunabhängigen Hamiltonian liefert, der den Einfluss des Lichts auf die Interaktionen beschreibt. Mit diesem Ansatz ist es uns möglich ein Kitaev-Heisenberg-Modell herzuleiten, in dem die Interaktionen von der Polarisation, Stärke, und Frequenz des externen Lichtfelds abhängen. Nach unserem Wissen ist unser Modell das erste, welches sowohl den Einfluss beliebiger Polarisationen als auch alle essenziellen Störterme im Kugel-Khomskii-Modell berücksichtigt. In unserer Studie finden wir neuartige Interaktionen, die polarisationsabhängig sind, sowie die Möglichkeit Kitaev Interaktionen signifikant zu verstärken.

Im Gegensatz zur d^5 Familie ist die Wechselwirkung von Spin-Bahn Kopplung, Kugel-Khomskii Interaktionen, und Kristallfeld in der Familie der d^4 Quadratgittermaterialien, die wir in dieser Thesis untersuchen, noch nicht vollständig geklärt. Im Speziellen das Material Ca$_2$RuO$_4$ war Gegenstand von Diskussionen aufgrund des ungeklärten Ursprungs seines magnetischen Grundzustands. Für signifikante Spin-Bahn Kopplung wäre die intuitive Vermutung, dass der Grundzustand nicht magnetisch ist, da Spin- $S = 1$ und Orbitalfreiheitsgrade $L = 1$ zu einem Gesamtdrehimpuls $J = 0$ koppeln sollten. In Ca$_2$RuO$_4$ wurde jedoch, für niedrige Temperaturen, eine antiferromagnetische Ordnung, die in der Ebene orientiert ist, gemessen. Da der Ursprung ebenjener magnetischen Ordnung nicht vollständig geklärt ist, leiten wir ein effektives Kugel-Khomskii-Modell her, welches bestimmte t_{2g}^4 Quadratgitter Mott-Isolatoren, wie z.B. Ca$_2$RuO$_4$, beschreibt. Mit diesem Modell ist es uns möglich ein Phasendiagramm in Abhängigkeit von der Spin-Bahn Kopplung und Kristallfeldaufspaltung zu skizzieren, und in diesem Ca$_2$RuO$_4$ zu lokalisieren. Des Weiteren untersuchen wir den Einfluss von Kristallfeldaufspaltung und Spin-Bahn Kopplung auf die Spin-Dynamiken des Systems, um die Natur des Grundzustands zu klären. Die Resultate unserer Studie zeigen eine exzellente Übereinstimmung mit inelastischen Neutronenstreuungs-Experimenten [5]. Um unser Modell weiter zu validieren, untersuchen wir zudem die Néel Temperatur von Ca$_2$RuO$_4$, um diese mit experimentellen Daten zu vergleichen. Zudem untersuchen wir den Einfluss der Kristallfeldaufspaltung und Spin-Bahn-Kopplung auf die Néel Temperatur. Erneut finden wir eine qualitativ gute Übereinstimmung mit experimentellen Ergebnissen, was unser effektives Kugel-Khomskii-Modell zu einem vielversprechenden Startpunkt für Materialien mit ähnlichen Eigenschaften wie Ca$_2$RuO$_4$ machen könnte.

Abstract

$4d$ and $5d$ transition-metal-based Mott insulators with sizable spin-orbit coupling have been focal points of scientific research over the last decade because they might host interesting ground state properties such as excitonic magnetism and quantum spin liquids. The reason for unique phases arising in these materials is the intricate interplay between strong correlations, spin-orbit coupling, and other effects, such as crystal field. To make these materials accessible from a theoretical point of view it can be advisable to derive effective models simplifying the Hamiltonian because an exact description is often impossible. These effective models should capture relevant physical properties well and give accurate predictions concerning experiments. A hallmark effective model in the context of strongly correlated Mott insulators is the Kugel-Khomskii model, which describes spin and orbital interactions of the located electrons via perturbation theory. However, this model does not capture the effect of spin-orbit coupling, which intertwines spin and orbital degrees of freedom and is an essential factor for unique interactions realizing, e.g., quantum spin liquids. The general approach in describing the materials discussed in this thesis thus is to derive an effective Kugel-Khomskii model and then consider the spin-orbit coupling.

In the context of d^5 honeycomb materials studied in this thesis, the effective spin-orbit model and the influence of spin-orbit coupling yield the famous Kitaev-Heisenberg model. This model includes Kitaev interactions, which, on its own, would lead to an exactly solvable quantum spin liquid ground state. The proposal of Khaliullin and Jackeli [1] that this model could find realization in condensed matter caused a surge of theoretical and experimental work [2,3] to find a material realizing this quantum spin liquid ground state. However, until today only a few of the materials show signatures of a quantum spin liquid [2,4], while the materials considered in this thesis all order magnetically at low temperatures. Hence, focus turned to manipulating promising candidate materials so they realize a quantum spin liquid. In this thesis, we want to discuss the possibility of tuning candidate materials via a time-periodic light field to significantly enhance Kitaev interactions. We capture the influence of time-periodic light fields via the Floquet formalism, which yields a time-independent Hamiltonian describing the influence of the light on the interactions. With this approach, we can derive a Kitaev-Heisenberg model

dependent on polarization, strength, and frequency of the external light field. To our knowledge, this is the first model that captures the influence of all possible Lissajous polarizations and includes all essential interactions in the Kugel-Khomskii model. In our study, we find new polarization-dependent interactions arising and the possibility of significantly enhancing Kitaev interactions.

In contrast to the d^5 family, for the family of d^4 materials considered in this thesis, especially Ca_2RuO_4, the interplay of spin-orbit coupling, Kugel-Khomskii type interactions, and crystal field is not completely clarified yet. The d^4 square lattice compound Ca_2RuO_4 has been the center of discussion due to the origin of its magnetic ground state. For sizable spin-orbit coupling one would assume a nonmagnetic ground state, because, in principle, the spin $S = 1$ and orbital $L = 1$ degrees of freedom should couple to a total angular momentum of $J = 0$. However, Ca_2RuO_4 orders antiferromagnetically in-plane at low temperatures. Since the origin of this order is yet not completely solved, we derive an effective Kugel-Khomskii model for t_{2g}^4 square lattice Mott insulators, like Ca_2RuO_4. We can derive a phase diagram in dependence of crystal field and spin-orbit coupling, in which we locate Ca_2RuO_4. In addition, we investigate the influence of spin-orbit coupling and crystal field on the dynamics to clarify the nature of the ground state. Our results of the dynamics show excellent agreement with inelastic neutron scattering measurements. To further validate our model we compare finite temperature properties, especially the Néel temperature, of Ca_2RuO_4 with experimental data. Additionally, we elaborate on the influence of crystal field and spin-orbit coupling on the Néel temperature. Again, we find a qualitative good agreement with theory and experiment, which makes the Kugel-Khomskii model a promising starting point for materials with similar properties as Ca_2RuO_4.

1 Introduction

The family of strongly correlated transition metal compounds, especially Mott insulators, have shown to host a variety of intriguing properties, ranging from spin liquids and excitonic magnetism to superconductivity. Since an exact theoretical description of these models is almost always impossible, one often has to work with effective models, which simplify the theoretical description but yield reliable predictions comparable with experimental data. A hallmark model in the context of Mott insulators is the Kugel-Khomskii model, treating the electron hopping as a perturbation, which yields an effective interaction between located electrons and reduces the respective Hilbert space. This concept is the foundation of this thesis, as we investigate Mott insulating transition metal compounds argued to realize excitonic magnetism or quantum spin liquids. We want to derive models for these materials, which give realistic predictions of ground state properties and excitations.

1.1 Floquet engineering in candidate d^5 Kitaev-Heisenberg materials

The Kitaev model [6] has been a focal point of solid-state physics research in the past decade due to its capability to realize an exactly solvable quantum spin liquid ground state. Ever since Jackeli and Khaliullin proposed that such a model could be realized in Mott insulators with five electrons in the d-shell and strong spin-orbit coupling (SOC) [1], attention has been drawn to models with such properties. Interest was first mainly in iridates like Na_2IrO_3 [7] and α-LiIrO$_3$ [8], but after experiments suggested that these systems realize a zig-zag [9–11] and incommensurate [12] ordered ground state respectively, focus has turned to ruthenates like α-RuCl$_3$ [13]. While α-RuCl$_3$ also does not show a Kitaev spin liquid (KSL) ground state, in the presence of a magnetic field, there are arguably indicators for a quantum spin liquid [14,15]. That leads to the conclusion that α-RuCl$_3$ might be close to the KSL, making it one of the more promising materials in this context. Since, to our knowledge, in none of the materials considered in this thesis, the

KSL arises naturally, there have been multiple attempts to drive the considered materials into the much desired quantum spin liquid state. The most promising pathway up to date, as mentioned, is applying an external magnetic field [16–20], but there have been also studies about applying pressure [21–23] and doping [24–26].

One yet relatively undiscovered pathway is the possibility of tuning these strongly correlated materials with light periodic in time. In a time-periodic system, the Floquet theorem applies and one can describe the system via a time-independent effective Floquet Hamiltonian. This Hamiltonian is valid for a short but experimental accessible time span [27–29], after which heating becomes a decisive factor. Tuning with light gives a variety of possibilities to alter system properties, e.g., via light frequency, amplitude, and polarization.

In this thesis, we investigate the most promising ways to tune Kitaev candidate materials via light. First, we derive an effective Floquet Hamiltonian for the well-known Kitaev-Heisenberg model and show that the Kitaev, Heisenberg, and Γ interactions depend on the light angle, amplitude, and frequency. This procedure is supported by the results of multiple publications [30–32]. We start our analysis by considering linear polarization (LP). Here, we only consider perturbation theory up to the second order as suggested by [30].

After choosing appropriate frequencies we show that we can alter the sign and magnitude of the interactions via the light amplitude in all considered materials. We observe that the Heisenberg interaction here takes a unique role because amplitude and frequency dependency are fundamentally different from the other interactions. Additionally, we show that system intrinsic anisotropies can be enhanced or suppressed via the angle of the LP. Turning to circular polarization (CP), we show that it is possible to suppress the third nearest neighbor Heisenberg interactions, which arguably are a factor in favor of the measured zig-zag phase [33].

Recent studies [31, 32] have shown that for CP novel effects like the inverse Faraday effect arise, if one calculates third-order terms in perturbation theory explicitly instead of implicitly including them in second-order like previously done. To build upon these reports we derive an effective Kugel-Khomskii model in fourth-order perturbation theory for arbitrary polarization (AP). The inclusion of terms up to the fourth order is mandatory to capture all interactions present in the simplified second-order model [34], which implicitly includes third and fourth-order terms. With a Hamiltonian for AP, we are capable of connecting the limiting cases CP and LP, evaluating crucial differences between the limiting cases. We derive such an effective model by replacing the CP/LP ansatz with a Lissajous figure ansatz, which has already been done for different systems [35–38]. With this novel effective model we can showcase the importance of fourth order terms for CP, yielding far better agreement with numerical results than previous third-order

results. Additionally, we can also study the limiting case of LP. The comparison of fourth-order results with the second-order results showed us that including higher-order terms also has a tremendous effect on LP, as it introduces two completely novel interactions inducing spatial anisotropies. From there, we can, in principle, cover the whole phase space of polarization possibilities. We show exemplary results for elliptical as well as more complicated Lissajous figures.

1.2 Effective model and parameter studies of the d^4 compound Ca_2RuO_4

The second main building block of this thesis is the study of ground state properties of t_{2g}^4 Mott insulating square lattice transition metal compounds with sizable SOC, especially Ca_2RuO_4. Ca_2RuO_4 will be the focal point of our studies because of the controversies surrounding its magnetic ground state.

While for sizable SOC one would expect a non-magnetic ground state due to SOC combining spin $S = 1$ and orbital degrees of freedom $L = 1$ to a total angular momentum of $J = 0$, the superexchange mechanism present in these materials drives a transition between the non-magnetic $J = 0$ and the magnetic states $J = 1$. This mechanism, known as excitonic magnetism [39], leads to a magnetic ground state. However, there has also been another explanation for the ground state properties [40, 41], claiming that SOC is not large enough to justify an effective J model. In this case, a $S = 1$ model would describe the system, intuitively leading to a magnetic ground state, with SOC just correcting excitation properties.

To shine a light on this discussion, we derive a general Kugel-Khomskii model for t_{2g}^4 Mott insulators with square lattice geometry. Our model is distinct from previously derived similar models [39], taking into account anisotropic hoppings and Hund's coupling J_{H}. Since experimental data suggest that anisotropic hoppings and sizable Hund's coupling are present in Ca_2RuO_4, we expect our model to be more accurate than previous ones. To interpret the nature of the magnetism of Ca_2RuO_4, we obtain a phase diagram in dependency of crystal field and SOC, in which we can locate Ca_2RuO_4. With that, we can qualitatively determine the stability of magnetism in Ca_2RuO_4 and explore phases in proximity to Ca_2RuO_4. Furthermore, we investigate dynamics and compare these with experimental neutron scattering results [5]. Last but not least, we measure the distribution of the two holes in the three d orbitals, indicating whether SOC justifies an effective J model. Our results lead us to believe that the magnetic ground state is excitonic.

Ca_2RuO_4 has a phase transition from an in-plane antiferromagnet to a paramagnetic ground state at $T_{\mathrm{N}} \approx 113\,\mathrm{K}$ [42, 43]. We can capture this phase transition, with a semi-classical Monte Carlo analysis. Our results show a qualitatively good agreement of the

Néel temperature. Furthermore, we investigate the influence of SOC and crystal field (CF) on the Néel temperature.

1.3 Outline

In Chap. 2 we discuss the underlying models and methods essential for this thesis. Here we introduce the Kugel-Khomskii model, the Kitaev-Heisenberg model, and the Floquet formalism. Additionally, we discuss the, for this thesis relevant, physical background like transition metals, excitonic magnetism, and spin liquids. Last but not least we introduce the numerical methods used in this thesis.

We divide the remainder of the thesis into the two main topics, I discussing possibilities of Floquet engineering in Kitaev candidate materials (Chap. 3-5) and II Investigating the possible phases arising in materials like Ca_2RuO_4 and their origin (Chap. 6-8).

We start part I in Chap. 3 by obtaining the second-order effective model for Kitaev-Heisenberg models under the influence of LP periodic in time. In Chap. 4, we analyze the model obtained in Chap. 3. Here, we discuss the influence of light angle, frequency, and amplitude and consider LP and CP. Chap. 5 extends the model introduced in Chap. 3 to an effective model up to fourth order in perturbation theory. Additionally, we introduce AP in the form of Lissajous figures, to capture the effects more complex polarizations have on the system's intrinsic interactions and bridge the gap between CP and LP.

In Chap. 6, we start our analysis of the d^4 square lattice, by deriving an effective Kugel-Khomskii model via second-order perturbation theory, including Hund's coupling and anisotropic hoppings. We proceed by calculating ground state properties of the in Chap. 6 introduced model, for varied SOC and crystal field, via exact diagonalization (ED). This leads to a phase diagram including Ca_2RuO_4 presented in Chap. 7. To confirm the phase diagram, we analyze the same model via semi-classical Monte Carlo and an effective triplon model via ED. With the help of these methods, we complete our findings and derive a more sufficient phase diagram. Additionally, we also study dynamics for several parameter settings and compare them with experimental results from [5].

Extending our studies of the model with Monte-Carlo to finite temperatures in Chap. 8 gives us a pathway to study the effect of SOC and crystal field on the Néel temperature. We compare the Néel temperature of our effective model for Ca_2RuO_4 with experimental results.

In Chap. 9, we conclude this thesis and give an outlook on interesting future studies.

2

Basics

In this chapter, we want to discuss the basics that lay the foundation of this thesis. We introduce the physical motivation behind this thesis and the tools required to obtain realistic results. As for tools, we mainly focus on mathematical approaches to describe effective models. Additionally, we introduce numerical methods to solve these. These two, together with the physical motivation, are the three pillars of this thesis, and likewise for most theoretical studies.

2.1 Transition metal compounds

In this thesis, we focus on transition metal compounds with non-filled valence bands and strong Coulomb repulsion. The latter can lead to a localization of itinerant electrons, causing an insulating behavior. This "unexpected" insulator arising due to strong electron-electron correlations, originally found by Mott [44, 45], is called a Mott insulator. In the family of Mott insulators, we are interested in materials with a d-valence band occupied by four and five electrons respectively. Here, we mainly focus on layered systems with weak interlayer interaction thus realizing a quasi 2D system.

2.1.1 d^5 materials

In this section, we are mainly focusing on transition metal compounds with five electrons residing in the valence d-shell (d^5 configuration), e.g., oxides like $NaIrO_3$ or chlorides like α-$RuCl_3$, which form a hexagonal lattice. These materials have been extensively investigated due to the possibility of realizing a KSL ground state [2, 3]. In the mentioned materials, the ligand atoms form an octahedron around the transition metal (Fig. 2.1). These octahedra arrange edge-sharing, resulting in a hexagonal arrangement of the transition metals.
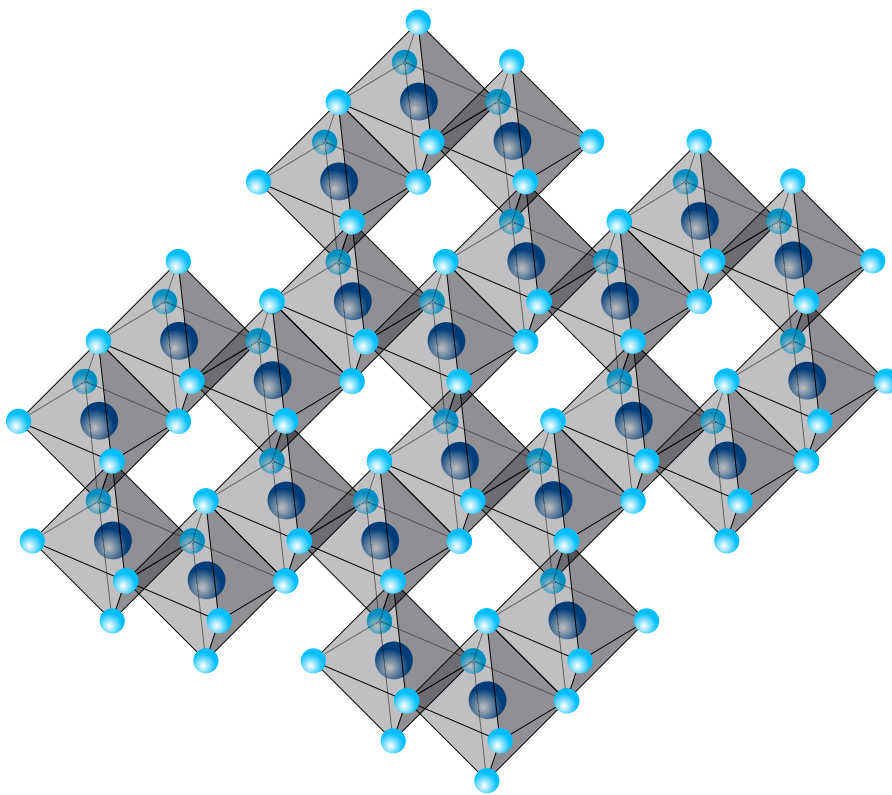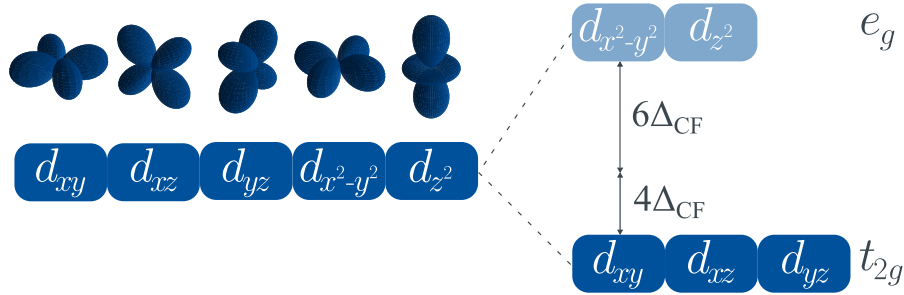
Figure 2.1: Sketch of transition metals with edge-sharing octahedra building a honeycomb lattice. Dark blue spheres depict the transition metals forming the hexagonal lattice. Light blue spheres depict the ligands forming octahedra around the transition metals. Materials with this geometry are, e.g., Na_2IrO_3, α-Li_2IrO_3, and α-$RuCl_3$.

Figure 2.2: Octahedral CF splitting of the d orbitals. The fivefold degeneracy of the d orbitals, from the considered transition metal, gets lifted due to the CF of the ligands forming an octahedra around it. This splitting gives rise to a two-fold degenerated e_g level consisting of the $d_{x^2-y^2}$ and d_{z^2} orbital and a three-fold degenerated t_{2g} level consisting of the d_{xy}, d_{yz}, and d_{xz} orbital.

The ligand atoms cause an octahedral CF, which lifts the five-fold degenerated d-shell of the transition metal compound. d_{xy}, d_{yz}, and d_{zx} orbitals get energetically lowered and build the new threefold degenerated t_{2g} manifold, while d_{z^2} and $d_{x^2-y^2}$ levels get energetically raised and form the e_g manifold. Since we consider materials, where the octahedral CF is significantly larger than the Hund's coupling J_{H}, the five electrons all reside in the energetically favored t_{2g} manifold, Fig. 2.2. Instead of considering five electrons in the t_{2g} shell, we can also consider the remaining hole in this manifold. Therefore, we can reduce our five-particle system to a one-hole system via particle-hole transformation. From now we only consider the hole in the t_{2g} manifold, i.e., the operators introduced are hole operators instead of electron operators.

Since the d^5 materials considered in this thesis have a relatively high atomic number, SOC couples spin and orbital degrees of freedom to a total angular momentum $J = 1/2$ (see Sec. 2.2.3 for more details).

2.1.2 d^4 materials

As the name suggests, d^4 materials have four electrons which reside in the t_{2g} manifold introduced in Sec. 2.1.1. The focal point in this thesis will be the material Ca_2RuO_4, which has gathered significant interest because of its yet not entirely resolved ground state properties.

In Ca_2RuO_4 the ligand oxygen atoms form an octahedra around the transition metal compound Ru, comparable to the considered d^5 materials discussed in Sec. 2.1.1. However, contrary to the d^5 materials that we consider in this thesis, Ca_2RuO_4 does not arrange in a honeycomb structure but forms a square lattice structure (see Fig. 2.3). This square lattice consists of ruthenium-oxygen octahedra that arrange in a corner-sharing manner (Fig. 2.3), while in the materials discussed in Sec. 2.1.1, octahedra arrange edge-sharing (Fig. 2.1). As previously discussed, the ligand atoms cause a splitting
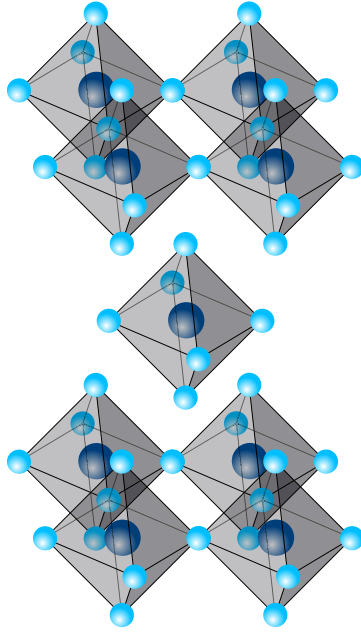
Figure 2.3: Crystal structure of Ca_2RuO_4. Oxygen ligand atoms (light blue) form an octahedron (grey-shaded) around the Ru transition metal (dark blue). The octahedra arrange in a corner-sharing manner in the x-y-plane, which leads to a square lattice formed by the Ru atoms. The x-y layers stack with an offset displayed in the figure.

of the five-fold degenerated d orbitals into a three-fold degenerated t_{2g} and a two-fold degenerated e_g manifold, see Sec. 2.1.1. In Ca_2RuO_4, four electrons reside within the t_{2g} manifold. Like in Sec. 2.1.1, we change to the hole picture yielding two holes in the t_{2g} orbitals. This makes Ca_2RuO_4 an effective $S = 1$, $L = 1$ system, where the three t_{2g} orbitals yield the $L = 1$ nature, as explained in [1], and the two holes with $S = 1/2$ give rise to total spin of $S = 1$. Here, we are working under the assumption that the octahedral field splitting is large enough to localize the holes in the t_{2g} manifold. Besides the square lattice structure, this is the second distinction from the considered d^5 materials.

The effect of SOC in Ca_2RuO_4 is yet not fully resolved. As a starting point, one can recapture the scenario of Kitaev materials, i.e., sizable SOC, where $S = 1/2$ and $L = 1$ coupled to a total angular momentum $J = 1/2$, one would naively expect that an effective $J = 0$ model captures Ca_2RuO_4. This would mean the ground state of Ca_2RuO_4 is non-magnetic. However, experimental measurements [40, 46–48] have revealed that the ground state of Ca_2RuO_4 is an in-plane antiferromagnet (AFM). This means the assumption of a $J = 0$ ground state does not hold. The explanation for the magnetic ground state in Ca_2RuO_4 has been the subject of controversies lately.

Some believe [40, 41] the root of magnetism is mainly attributed to the presence of a strong CF splitting, arising from a quenching of the octahedra in z direction (see Sec. 2.2.4 for further details). This CF lifts the degeneracy of the t_{2g} manifold, increasing the energy of the d_{xz} and d_{yz} orbital. This would lead to an orbitally ordered ground

state with holes that reside in the d_{xy} orbitals. The effect of spin-orbit coupling here would have a minor influence that alters only excitations [40, 41]. Therefore, the $J = 0$ picture would not be feasible. Others [5, 47] state that SOC is dominant and that the total angular moment J picture is valid. The explanation for the observed magnetism is the fact that the superexchange on the square lattice can mix $J = 0$ and $J = 1$, leading to an effective magnetization, also known as excitonic magnetism [39]. The current assumption is that the truth probably lies somewhere in between, which makes the two scenarios "two sides of the same coin" [49], with both CF and spin-orbit coupling having a sizable effect.

Above the Néel temperature of $T_{\mathrm{N}} = 110\,\mathrm{K}$ Ca_2RuO_4 loses the magnetic order [50]. However, orbital order can still prevail above T_{N} as has been shown by [51]. Additionally, Ca_2RuO_4 has a metal-insulator transition at $T_{\mathrm{MIT}} \approx 360\,\mathrm{K}$ [43], up to which the material is in a Mott insulating state. A description within an effective Kugel-Khomskii model [52] (see Sec. 2.3.1) appears to be feasible at low temperatures up to the Néel temperature.

2.2 Interactions

After discussing the lattice structure and electron configuration of t_{2g}^5 and t_{2g}^4 materials investigated in this thesis, we introduce the interactions present in these materials. A few of them were already discussed qualitatively in Sec. 2.1, like CF and SOC, and we will discuss them in more detail in this section. We divide the relevant interactions in these systems into on-site and inter-site interactions.

2.2.1 Inter-site interactions

The inter-site interactions, i.e., hopping from a hole between sites, can be expressed via the Hubbard model

$$H_{\mathrm{kin}} = \sum_{i,j} \sum_{\sigma} \sum_{\alpha,\beta} \left(t_{\alpha,\beta} c_{i,\alpha,\sigma}^{\dagger} c_{j,\beta,\sigma} + h.c. \right), \tag{2.1}$$

with hole creation (annihilation) operators $c^{\dagger}$ (c), spin σ, hopping strength $t_{\alpha,\beta}$, orbitals α and β, and lattice sites i and j. The general form of the Hubbard model holds for both t_{2g}^4 and t_{2g}^5 materials. However, due to the distinct lattice geometry, the hopping strength between the orbitals α and β varies drastically.

We first consider t_{2g}^5 materials with edge-sharing octahedra. Looking at the bond geometry (Fig. 2.4) between two transition metal atoms and their possible orbital configurations, one can identify four different possible types of hopping. First, there is hopping between orbitals lying in bond directions, mediated through an "overlap" of the orbitals, and from here on referred to as a direct exchange, t_3 in Fig. 2.4(iv). Additionally, hop-

(i) t_2 (ii) t_1 (iii) t_4 (iv) t_3
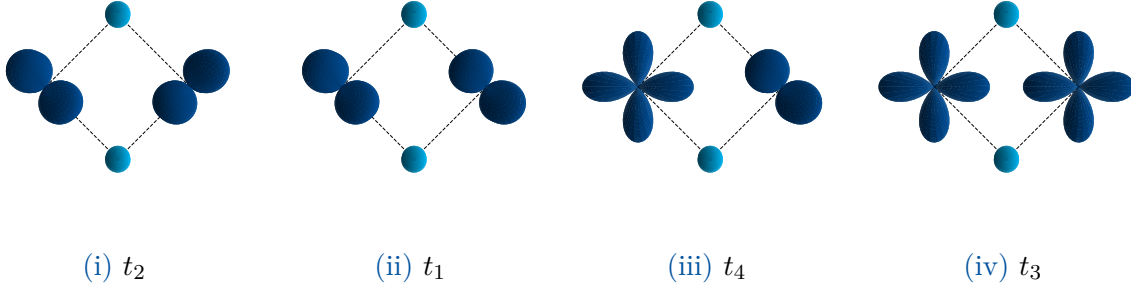
Figure 2.4: Possible hoppings present in edge-shared octahedra. Transition metal d orbitals are dark blue, and ligand atom p orbitals are light blue. (i) Superexchange $t_2 = t_{pd\pi}^2/\Delta_{pd} + (t_{dd\pi} - t_{dd\delta})/2$ mediated through mainly ligand atoms between d_{xz} and d_{yz} orbitals. (ii) Orbital preserving hopping $t_1 = (t_{dd\pi} + t_{dd\delta})/2$ between d_{xz} or d_{yz} orbitals. (iii) Hopping $t_4 = t_{dd\delta}$ between d_{xy} and either d_{xz} or d_{yz}. (iv) Direct exchange $t_3 = (3t_{dd\sigma} + t_{dd\delta})/4$ between d_{xy} and d_{xy} orbitals. $t_{pd\pi}$, $t_{dd\delta}$, $t_{dd\sigma}$, and $t_{dd\pi}$ are Slater-Koster parameters from [53] and Δ_{pd} is the charge transfer gap between d and p orbitals.

(i) t_{xz}/t_{yz} (ii) t_{xy} (iii) $t_{xy,3}$
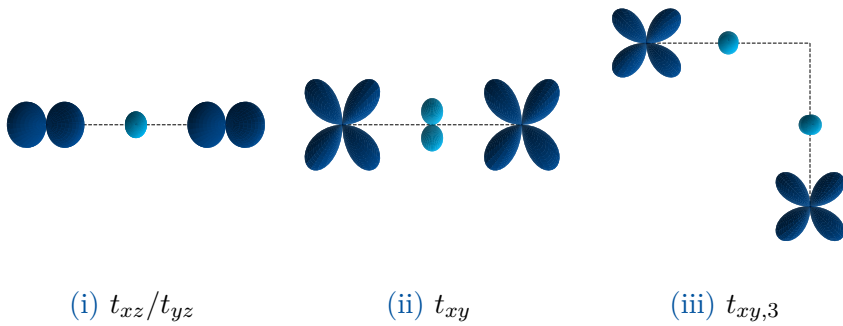
Figure 2.5: Possible hoppings present in a corner shared octahedra. Transition metal d orbitals are dark blue, and ligand atom p orbitals are light blue. The active orbitals on a given nearest neighbor (NN) bond lie in the bond direction. These are either, depending on the bond direction, d_{xz} or d_{yz} orbitals on both sites (i) and the d_{xy} orbital (ii). For second nearest neighbor (NN)'s, there is a significant contribution arising from the d_{xy} overlap (iii) comparable to the direct exchange in Fig. 2.4(iv).

ping can be mediated through the p-ligand atoms between orbitals pointing towards the same ligand atom, t_2 in Fig. 2.4(i). Furthermore, non-vanishing hopping strengths occur between orbitals in bond direction and orbitals lying in ligand direction, t_1 in Fig. 2.4(ii), as well as orbitals not pointing in bond direction and towards different ligand atoms, t_4 in Fig. 2.4(iii). While for an ideal geometry, these hoppings would be zero, lattice distortions arising in realistic materials can lead to non-vanishing contributions of these hoppings.

For the t_{2g}^4 compounds, we consider the hoppings displayed in Fig. 2.5. Here, the p orbital lies between the transition metal compounds due to the corner-sharing arrangement. In a square lattice, only two different nearest neighbor (NN) bond types in x and y directions exist. Both bonds have a sizable hopping strengths t_{xy} arising from an overlap of the d_{xy} orbitals on adjacent sites with the p_y/p_x oxygen atom in-between, Fig. 2.5(ii). The other t_{2g} orbitals, d_{yz} and d_{zx}, only have significant contributions for y and x bonds respectively. For an x bond, Fig. 2.5(i), d_{zx} orbitals point in the bond direction and have a significant overlap mediated by the p_z oxygen ligand atom. These are typically all considered NN interactions [1,54]. However, we do consider one next nearest neighbor (NNN) interaction displayed in Fig. 2.5(iii), arising from the direct overlap of d_{xy} orbitals similar to the case in Fig. 2.4(iv), with the difference that the spatial distance is decisively larger and $t_{xy,3}$ much weaker because of that.

2.2.2 Kanamori interaction

In addition to kinetic interactions, introduced in Sec. 2.2.1, the considered transition metals typically have strong on-site interactions. In this thesis, we focus on three types of on-site interactions. Kanamori interactions and spin-orbit coupling are present in both t_{2g}^4 and t_{2g}^5 as well as CF splitting, only discussed for t_{2g}^4 materials. As described in Sec. 2.1, the reason for the insulating behavior of the considered transition metals is the strong Coulomb repulsion in these materials. The Kanamori-Hamiltonian [55]

$$
\begin{aligned}
H_{\text{int}} =& U \sum_{i,\alpha} n_{i\alpha\uparrow} n_{i\alpha\downarrow} + U' \sum_{i,\sigma} \sum_{\alpha<\beta} n_{i\alpha\sigma} n_{i\beta\,-\sigma} \\
&+ (U' - J_{\text{H}}) \sum_{i,\sigma} \sum_{\alpha<\beta} n_{i\alpha\sigma} n_{i\beta\sigma} \\
&- J_{\text{H}} \sum_{i,\alpha\neq\beta} (c_{i\alpha\uparrow}^\dagger c_{i\alpha\downarrow} c_{i\beta\downarrow}^\dagger c_{i\beta\uparrow} - c_{i\alpha\uparrow}^\dagger c_{i\alpha\downarrow}^\dagger c_{i\beta\downarrow} c_{i\beta\uparrow}),
\end{aligned}
\tag{2.2}
$$

with intraorbital Hubbard interaction U, interorbital $U' = U - 2J_{\text{H}}$ and Hund's coupling J_{H} describes the Coulomb repulsion. Here we set $U' = U - 2J_{\text{H}}$, because we consider the holes to only reside in the t_{2g} orbitals [56]. Hund's coupling favors a parallel spin alignment with electrons residing in different orbitals according to Hund's rules, while

f	$\mathcal{E}_{2,f}$		$|\Psi_{2,f}\rangle$
1	$U - 3J_{\mathrm{H}}$	$\mathcal{E}_P$	$|\sigma, \sigma, 0\rangle$
2	$U - 3J_{\mathrm{H}}$		$1/\sqrt{2}\,(|\uparrow, \downarrow, 0\rangle + |\downarrow, \uparrow, 0\rangle)$
3	$U - J_{\mathrm{H}}$	$\mathcal{E}_D$	$1/\sqrt{2}\,(|\uparrow, \downarrow, 0\rangle - |\downarrow, \uparrow, 0\rangle)$
4	$U - J_{\mathrm{H}}$		$1/\sqrt{2}\,(|\uparrow\downarrow, 0, 0\rangle - |0, \uparrow\downarrow, 0\rangle)$
5	$U + 2J_{\mathrm{H}}$	$\mathcal{E}_S$	$1/\sqrt{3}\,(|\uparrow\downarrow, 0, 0\rangle + |0, \uparrow\downarrow, 0\rangle + |0, 0, \uparrow\downarrow\rangle)$

Table 2.1: Eigenstates and eigenergies of the Kanamori-Hamiltonian for two holes on one site, with σ the spin of the hole and $\alpha, \beta, \gamma \in [d_{xz}, d_{xy}, d_{yz}]$ the orbital flavor of the corresponding hole.

f	$\mathcal{E}_{3,f}$	$|\Psi_{3,f}\rangle$
1	$3U - 4J_{\mathrm{H}}$	$1/\sqrt{2}\,(|\uparrow\downarrow, \uparrow, 0\rangle + |0, \uparrow, \uparrow\downarrow\rangle)$
2	$3U - 6J_{\mathrm{H}}$	$1/\sqrt{2}\,(|\uparrow\downarrow, \uparrow, 0\rangle - |0, \uparrow, \uparrow\downarrow\rangle)$
3	$3U - 9J_{\mathrm{H}}$	$1/\sqrt{3}\,(|\uparrow, \downarrow, \uparrow\rangle + |\downarrow, \uparrow, \uparrow\rangle + |\uparrow, \uparrow, \downarrow\rangle)$
4	$3U - 6J_{\mathrm{H}}$	$1/\sqrt{2}\,(-|\uparrow, \uparrow, \downarrow\rangle + |\downarrow, \uparrow, \uparrow\rangle)$
5	$3U - 6J_{\mathrm{H}}$	$1/\sqrt{6}\,(|\uparrow, \uparrow, \downarrow\rangle + |\downarrow, \uparrow, \uparrow\rangle - 2\,|\uparrow, \downarrow, \uparrow\rangle)$
6	$3U - 9J_{\mathrm{H}}$	$|\sigma, \sigma, \sigma\rangle$

Table 2.2: Eigenstates and eigenergies of the Kanamori-Hamiltonian for three holes on one site, with σ the spin of the hole and $\alpha, \beta, \gamma \in [d_{xz}, d_{xy}, d_{yz}]$ the orbital flavor of the corresponding hole.

Coulomb repulsion taxes the placement of two electrons on one site with the energy U.

In the case of t_{2g}^5 materials, we are mainly interested in the interaction energy for two holes on one site, because we want to calculate the energy cost of an electron temporarily occupying an adjacent site. The eigenstates and eigenergies of the Kanamori-Hamiltonian for this subspace are given in Tab. 2.1 [57]. For one hole on one site, one intuitively obtains $\mathcal{E}_1 = 0$.

For the t_{2g}^4 compounds, we are interested in the eigenstates of three holes residing on one site in addition to the scenarios discussed for t_{2g}^5. This is the case because moving an electron to an adjacent site in these compounds results in a d^3d^1 configuration. App. C derives these energies in detail. Tab. 2.2 shows the results for three electrons.

2.2.3 Spin-orbit coupling

Spin-orbit coupling is a relativistic effect that couples the spin and orbital degrees of freedom of an electron (hole). The coupling strength increases with the atomic number $\propto Z^2$ [58, 59]. Since the materials considered in this thesis have, in general, relatively high atomic numbers (e.g., Ru $Z = 44$) and nonvanishing orbital and spin moments, we have to consider this effect. In this work we only consider the case $J_{\mathrm{H}} \gg \lambda$, where the

Russell-Saunders coupling

$$H_{\text{SOC}} = \lambda \sum_j \mathbf{S}_j \mathbf{L}_j, \tag{2.3}$$

with lattice sites j, is a valid description. Here, we work under the assumption that spin and orbital momenta s_i and l_i of the single electrons (holes) i couple to a total spin and orbital momentum $S = \sum_i s_i$ and $L = \sum_i l_i$, which then couple to a total angular momentum $J = S + L$ via (2.3). In the considered systems, SOC tends to be strong and we can express the Hamiltonian in the basis of eigenstates of the SOC Hamiltonian. For the transition metals in question, we have three t_{2g} orbitals, i.e., we can write them in an effective $L_{\text{eff}} = 1$ basis, which only differs from the conventional angular momentum by negative sign [2, 60], i.e., $\left[L_{\text{eff}}^{\alpha}, L_{\text{eff}}^{\beta}\right] = -i\epsilon_{\alpha,\beta,\gamma} L_{\text{eff}}^{\gamma}$ with $\alpha, \beta, \gamma \in [x, y, z]$ and L_{eff}^{α} given in (2.7). From now we will refer to this effective angular momentum as L for simplicity reasons. The effective angular momentum expressed in the orbital basis then reads

$$|L = 1, m_L = \pm 1\rangle = -\frac{1}{\sqrt{2}} (i \, |d_{xz}\rangle \pm |d_{yz}\rangle)$$
$$|L = 1, m_L = 0\rangle = |d_{xy}\rangle. \tag{2.4}$$

SOC couples this effective angular momentum $L = 1$ with the spin $S = 1/2$. Therefore, the eigenstates of H_{SOC} become

$$|J = 1/2, m_J = \pm 1/2\rangle = \frac{1}{\sqrt{3}} |L = 1, m_L = 0, S = 1/2, m_S = \pm 1/2\rangle$$
$$- \sqrt{\frac{2}{3}} |L = 1, m_L = \pm 1, S = 1/2, m_S = \mp 1/2\rangle$$
$$|J = 3/2, m_J = \pm 1/2\rangle = \sqrt{\frac{2}{3}} |L = 1, m_L = 0, S = 1/2, m_S = \pm 1/2\rangle$$
$$+ \frac{1}{\sqrt{3}} |L = 1, m_L = \pm 1, S = 1/2, m_S = \mp 1/2\rangle$$
$$|J = 3/2, m_J = \pm 3/2\rangle = |L = 1, m_L = \pm 1, S = 1/2, m_S = \pm 1/2\rangle. \tag{2.5}$$

The eigenvalues of the two distinct J values are $\mathcal{E}_{J=3/2} = -\lambda/2$ and $\mathcal{E}_{J=1/2} = \lambda$, meaning SOC lifts the degeneracy of the three-fold degenerated t_{2g} level into a $J = 1/2$ and two $J = 3/2$ levels. Since there are five electrons residing in the t_{2g} manifold, there is a fully occupied $J = 3/2$ with one electron and one hole remaining in the $J = 1/2$ manifold (see Fig. 2.6). Thus, we can describe the hole in the $J = 1/2$ via an effective spin-1/2 model.

For the t_{2g}^4 compounds, the influence of SOC becomes a little bit more intricate than for the case of t_{2g}^5 configurations. Since we are only considering SOC decisively
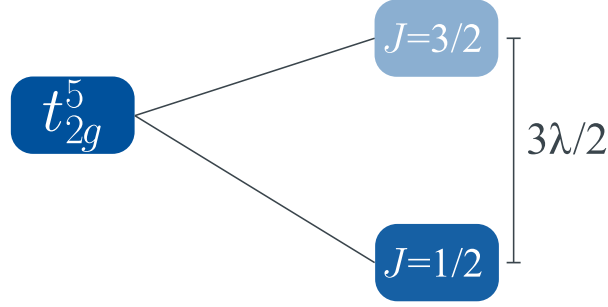
Figure 2.6: Splitting of the t_{2g} level due to SOC. The threefold degeneracy gets lifted into a twofold degenerated $J = 3/2$ level at $-\lambda/2$ and a $J = 1/2$ level at λ. In the considered systems five electrons reside in the t_{2g} manifold thus, there is a fully occupied $J = 3/2$ level with one electron remaining in the $J = 1/2$ level. Since we perform a particle-hole transformation, i.e., considering the physics of the one hole in the system instead of the five electrons, the level structure gets inverted and we obtain a pseudospin $1/2$ system for the hole.

smaller than Hund's coupling J_{H} and U, we first have to consider the splitting of the t_{2g}^4 according to the Kanamori Hamiltonian. We did not discuss this for the t_{2g}^5 because one hole per site does not experience an energy correction from H_{int}. The eigenvalues and eigenstates for two holes on one site, see Tab. 2.1. We observe a splitting of the t_{2g}^4 into three distinct levels with $L = 1, S = 1$ ($\mathcal{E}_P = U - 3J_{\mathrm{H}}$), $L = 2, S = 0$ ($\mathcal{E}_D = U - J_{\mathrm{H}}$), and $L = 0, S = 0$ ($\mathcal{E}_S = U + 2J_{\mathrm{H}}$) see Fig. 2.7. Since we consider materials with sizable Hund's coupling it is feasible to assume that the ground state is firmly in the $L = 1, S = 1$ manifold. This manifold consists of nine distinct states (Tab. 2.1). A finite spin orbit coupling $0 < \lambda \ll J_{\mathrm{H}}$ splits this manifold into the $J = 0$, $J = 1$, and $J = 2$ level with an energy splitting of $\lambda/2$ and λ see Fig. 2.7. The lowest energy level considering Kanamori interactions and SOC would be the $J = 0$ state. However, as we will see, this changes with inclusion of kinetic terms and the on-site CF.

2.2.4 Crystal field

At the metal-insulator transition, Ca_2RuO_4 also undergoes a structural transition [61,62] leading to octahedra with compressed z axis, see Fig. 2.6. This leads to an effective tetragonal CF acting on the t_{2g} orbitals of the transition metal compound [48,63]

$$H_{\mathrm{CF}} = \Delta \sum_i L_i^{z\,2} = \Delta \sum_i (|zx\rangle_i \langle zx|_i + |yz\rangle_i \langle yz|_i). \tag{2.6}$$
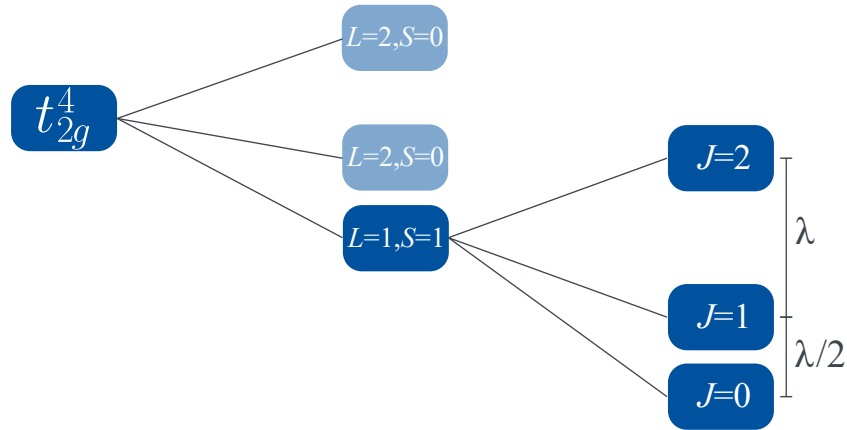
Figure 2.7: Splitting of the t_{2g}^4 level due to SOC. Sizable Hund's coupling lifts the degeneracy of the t_{2g}^4 level into the $|L = 1, S = 1\rangle$, $|L = 2, S = 0\rangle$, and $|L = 0, S = 0\rangle$. SOC then splits the $|L = 1, S = 1\rangle$ manifold in to the $|J = 0\rangle$, $|J = 1\rangle$, and the $|J = 2\rangle$ level.
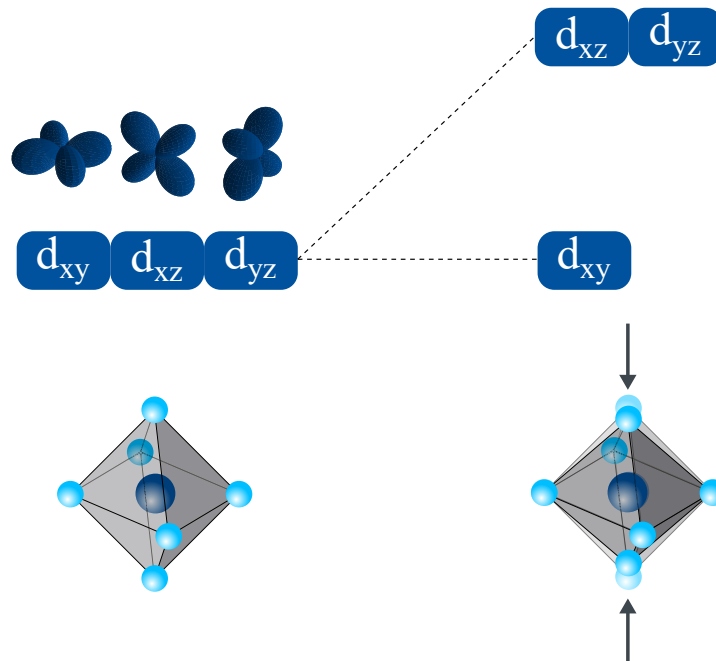
Figure 2.8: CF splitting of the t_{2g} manifold in Ca_2RuO_4. The octahedra of Ca_2RuO_4 are quenched in z direction, leading to a splitting that favors the d_{xy} orbital over the d_{xz} and d_{yz} orbital.

(i) $\mathcal{E}_{\mathrm{d},1}$ (ii) $\mathcal{E}_{\mathrm{d},2}, \mathcal{E}_{\mathrm{d},3}$ (iii) $\mathcal{E}_{\mathrm{d},4}, \mathcal{E}_{\mathrm{d},5}$

Figure 2.9: Possible energies of the doublon excitations. There are three different kinds of double occupations. Same spin different orbitals which only has an overlap with the Kanamori eigenstate [55] with $\mathcal{E}_m = U - 3J_{\mathrm{H}}$ (i), different spins different orbitals with possible energies $\mathcal{E}_m = U - 3J_{\mathrm{H}}$ or $\mathcal{E}_m = U - J_{\mathrm{H}}$ (ii), same orbital different spins with $\mathcal{E}_m = U + 2J_{\mathrm{H}}$ or $\mathcal{E}_m = U - J_{\mathrm{H}}$ (iii).

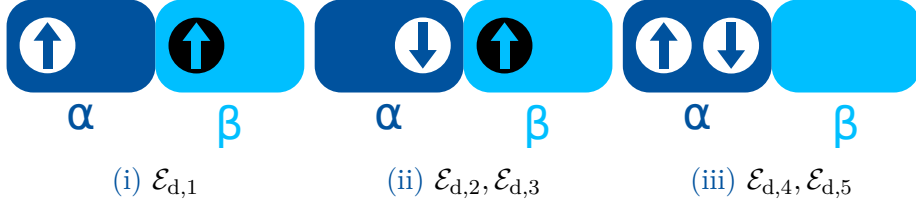Here, we used the definition of the effective angular momentum operators [39, 64]

$$
\begin{aligned}
L^x &= i(|xy\rangle \langle zx| - |zx\rangle \langle xy|) \\
L^y &= i(|yz\rangle \langle xy| - |xy\rangle \langle yz|) \\
L^z &= i(|zx\rangle \langle yz| - |yz\rangle \langle zx|).
\end{aligned}
\tag{2.7}
$$

H_{CF} lifts the degeneracy of the t_{2g} manifold, where d_{yz} and d_{zx} orbital get energetically lifted by the strength of the tetragonal CF Δ compared to the d_{xy} orbital, see Fig. 2.8. We notice that tetragonal CF Δ and spin-orbit coupling λ are competing entities. While CF favors an orbital polarization so that just the d_{xy} orbital has a double occupancy, spin-orbit coupling favors the $J = 0$ state, which has an equal occupation of d_{xy}, d_{yz}, and d_{zx} orbital. This makes the hole density in the d_{xy} orbital a quantity, which can determine whether one is in the d_{xy} polarized or the $J = 0$ limit.

2.3 Models

2.3.1 Kugel-Khomskii model

In Mott insulators strong, Coulomb repulsion suppresses the hopping of holes. This means that $t \ll U$ and we can treat the kinetic part of the Hamiltonian via second-order perturbation theory

$$
\mathcal{H}_{\mathrm{eff}}^{i,j} = \sum_{l,n \neq m} \frac{|\Psi_{\mathrm{g},l}\rangle \langle \Psi_{\mathrm{g},l}| H_{\mathrm{kin}} |\Psi_m\rangle \langle \Psi_m| \mathcal{H}_{\mathrm{kin}}^{i,j} |\Psi_{\mathrm{g},n}\rangle \langle \Psi_{\mathrm{g},n}|}{\mathcal{E}_{\mathrm{g}} - \mathcal{E}_m},
\tag{2.8}
$$

where $|\Psi_{\mathrm{g}}\rangle$ describes the ground state manifold of the Kanamori Hamiltonian $\mathcal{H}_{\mathrm{K}}$ with ground state energy $\mathcal{E}_{\mathrm{g}}$. As we see in Sec. 2.2.2, the ground state manifold differs for the t_{2g}^4 and t_{2g}^5 materials. $|\Psi_m\rangle$ is the eigenstate manifold of H_K with energy $\mathcal{E}_m$ accessible through application of $\mathcal{H}_{\mathrm{kin}}^{i,j}$, i.e., the movement of a hole from site i to site j. This treatment of the kinetic Hamiltonian in degenerate second-order perturbation theory

leads to an effective Hamiltonian, also known as the Kugel-Khomskii type Hamiltonian. In the following, we discuss the derivation of the Kugel-Khomskii type Hamiltonian for both t_{2g}^4 and t_{2g}^5 materials.

For t_{2g}^5 materials, the hopping from a hole to an adjacent state via H_{kin} gives rise to a d^2d^0 configuration. We can distinguish between three different kinds of double occupations: Distinct orbital same spin, distinct orbital distinct spin, and same orbital distinct spin. The first scenario only has an overlap with states $|\psi_{2,1}\rangle$ (Tab. 2.1) thus it yields an excitation energy of $U - 3J_{\text{H}}$. For the second case the resulting state $H_{\text{kin}}|\Psi_1\rangle$ has overlap with both $|\psi_{2,2}\rangle$ and $|\Psi_{2,3}\rangle$, leading to interaction terms $\propto -1/(U - 3J_{\text{H}})$ and $\propto -1/(U - J_{\text{H}})$. Lastly for the double occupation of one orbital we get a nonzero overlap with $|\Psi_{\text{d},4}\rangle$ and $|\Psi_{\text{d},5}\rangle$, yielding intermediate energies of $U - J_{\text{H}}$ and $U + 2J_{\text{H}}$. We summarize the possible configurations with their possible excitation energies in Fig. 2.7. Considering the four distinct hoppings of H_{kin}, introduced in Sec. 2.2.1, we can distinguish three fundamental virtual hopping processes. First, there is the direct exchange where both hopping processes are orbital preserving, i.e., of kind t_1 and t_3 see Fig. 2.10. Second, there is the virtual hopping where both processes are of orbital changing nature, i.e., t_2 and t_4. Here, virtual interactions that preserve the initial orbital occupation and interactions that change the orbital flavor exist. Lastly, we have a mixed exchange, where one hopping process is orbital preserving, and the other changes the orbital flavor. In this case, the virtual hopping process changes the orbital flavor.

Summarizing all these interactions leads to a Kugel-Khomskii-type Hamiltonian, which we write in the basis of creation/annihilation operators introduced in (2.1). Since the ground state manifold for d^5 materials consists of $S = 1/2$, $L = 1$ states, we can project the Hamiltonian into the spin-orbit basis

$$H_{\text{KK}}^{\text{SL}} = \sum_{m_l, m_l'} \sum_{m_s, m_s'} |m_s, m_l\rangle \langle m_s, m_l| H_{\text{KK}} |m_s', m_l'\rangle \langle m_s', m_l'|, \qquad (2.9)$$

with $m_s = \pm 1/2$ and $m_l = -1, 0, 1$ as introduced in (2.4). This procedure has proven itself to be useful in multi-orbital models with a sizable Coulomb repulsion compared to the hopping strength, especially Mott insulators [65–67].

Like for the t_{2g}^5 materials, one can derive an effective Kugel-Khomskii Hamiltonian for t_{2g}^4 materials treating the kinetic Hamiltonian as a perturbation, with the unperturbed Hamiltonian being the Kanamori Hamiltonian of [55]. However, there are some intricate but decisive differences in the derivation of the effective Hamiltonian for, e.g., Ca_2RuO_4. First, the lattice geometry gives rise to different hopping processes than the honeycomb lattice (Fig. 2.5). Second, due to the d^4 occupation of each site, on-site energies $\mathcal{E}_g$ change as well as the excitation energies $\mathcal{E}_m$ arising from a d^1d^3 configuration. Here the d^3 eigenstates of the Kanamori Hamiltonian were introduced in Tab. 2.2. Last but
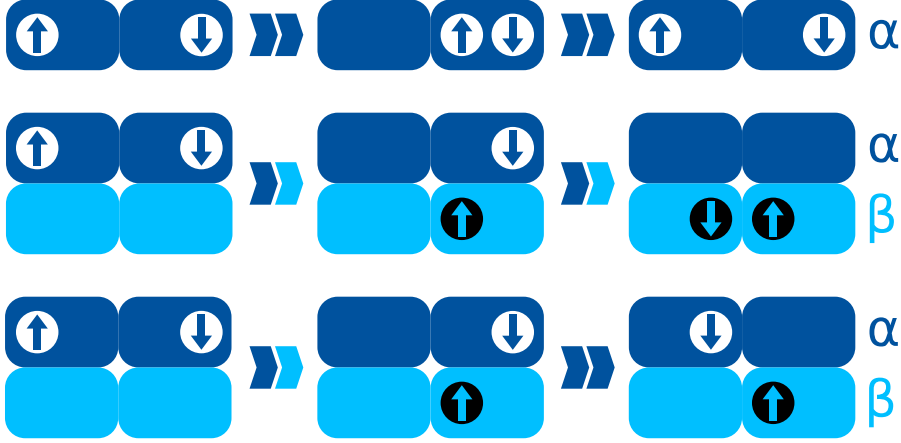
Figure 2.10: Possible virtual hopping processes for d^5 materials. Light and dark blue display the different orbitals α and β. The top sketch shows orbital preserving hopping processes possible for two holes with opposite spins. The middle sketch displays a hopping where both holes change the orbital flavor, mediated via hoppings t_2 and t_4, which are orbital flipping (see Sec. 2.2.1). Lastly, we have hopping processes where one hopping process flips the orbital flavor while the other preserves the orbital flavor, resulting in a virtual process where only one site changes the orbital flavor.

not least, because Hund's coupling is sizable, the spin-orbital model only considers the $S = 1, L = 1$ subspace depicted in Fig. 2.7 (see App.C). We give the detailed derivation of the effective Hamiltonian in Chap. 6 and App.C.

2.3.2 Kitaev-Heisenberg model

As discussed in Sec. 2.2.2, SOC in t_{2g}^5 compounds leads to a splitting of the Kanamori ground state manifold into a $J = 1/2$ and $J = 3/2$ level, with the hole residing in the $J = 1/2$. Therefore, it is feasible to project the Kugel-Khomskii Hamiltonian into the basis of the SOC ground state manifold, i.e., into the $|J = 1/2, m_J = 1/2\rangle$ and $|J = 1/2, m_J = -1/2\rangle$ basis. This reduces the degrees of freedom per site from six, three orbital and two spin, to two degrees of freedom. Since this makes the system an effective spin-1/2 model, we will from now refer to $J = 1/2$ operators as spin operators. This model is intuitively easier to solve numerically than the complete Kugel-Khomskii model. In the new basis, the effective model then becomes

$$\bar{H}_{\text{eff}} = \sum_{\langle ij \rangle \in \alpha\beta(\gamma)} \Big[J^\gamma \mathbf{S}_i \mathbf{S}_j + K^\gamma S_i^\gamma S_j^\gamma + \Gamma^\gamma (S_i^\alpha S_j^\beta + S_i^\beta S_j^\alpha)$$
$$+ \Gamma'^\gamma (S_i^\alpha S_j^\gamma + S_i^\gamma S_j^\alpha + S_i^\beta S_j^\gamma + S_i^\gamma S_j^\beta) \Big], \tag{2.10}$$

with $\alpha, \beta, \gamma \in [x, y, z]$ the three distinct bond directions in a honeycomb lattice, pseudospin operators S_i^α, and the interaction strengths J, K, Γ and Γ'. We divide the four interactions into two subgroups, the bond-independent Heisenberg interaction J and the

bond-dependent Kitaev, Γ, and Γ' interaction. The striking feature is the presence of Kitaev interactions on a honeycomb lattice, which, if all other interactions are absent, leads to an exactly solvable Kitaev spin liquid ground state [6]. The parameters J, K, Γ, and Γ' arise from the virtual hopping processes calculated via second-order perturbation theory (Sec. 2.3.1). As shown in [34] we can write these interactions in terms of hopping $t_{\alpha,\beta}$, Coulomb interaction U, and Hund's coupling J_{H}

$$J^\gamma = \frac{4}{27}\left\{ \left[-9t_4^{\gamma\,2} + 2(t_1^\gamma - t_3^\gamma)^2\right]\left(\frac{1}{U-3J_{\mathrm{H}}} - \frac{1}{U-J_{\mathrm{H}}}\right) \right.$$
$$\left. + (2t_1^\gamma + t_3^\gamma)^2\left(\frac{1}{U+2J_{\mathrm{H}}} + \frac{2}{U-3J_{\mathrm{H}}}\right) \right\}, \tag{2.11}$$

$$K^\gamma = \frac{4}{9}\left[(t_1^\gamma - t_3^\gamma)^2 - 3(t_2^{\gamma\,2} - t_4^{\gamma\,2})\right]\left(\frac{1}{U-3J_{\mathrm{H}}} - \frac{1}{U-J_{\mathrm{H}}}\right), \tag{2.12}$$

$$\Gamma^\gamma = \frac{4}{9}\left[3t_4^{\gamma\,2} + 2t_2^\gamma(t_1^\gamma - t_3^\gamma)\right]\left(\frac{1}{U-3J_{\mathrm{H}}} - \frac{1}{U-J_{\mathrm{H}}}\right), \tag{2.13}$$

$$\Gamma'^\gamma = -\frac{4}{9}t_4^\gamma\left(t_1^\gamma - t_3^\gamma - 3t_2^\gamma\right)\left(\frac{1}{U-3J_{\mathrm{H}}} - \frac{1}{U-J_{\mathrm{H}}}\right), \tag{2.14}$$

meaning the strength of the different hopping processes introduced in Sec. 2.2.1 has a significant influence on the relative strength of the interactions.

One of the first proposed materials to potentially realize such a KSL was the iridate Na_2IrO_3 [9, 10, 68], which has dominant t_2 interactions. However, experiments showed that Na_2IrO_3 has a zig-zag ground state. Other iridate compounds like Li_2IrO_3 also showed a non-Kitaev ground state. Up to date one material that is arguably close to the KSL ground state is the ruthenate α-$RuCl_3$ [69, 70]. However, the ground state in α-$RuCl_3$ is still a magnetic ordered zig-zag state. One pathway beyond others (e.g., applying a magnetic field, substituting interlayer atoms, etc.) for Kitaev-Heisenberg materials is to manipulate the interaction strength so that the considered material realizes a KSL.

2.3.3 Triplon model

Like for t_{2g}^5, we can project the spin-orbital model for t_{2g}^4 materials into the basis of the SOC Hamiltonian. In the t_{2g}^4 materials we consider in this thesis, SOC is not strong enough to allow for a projection in just the $J = 0$ level (Fig. 2.7). To derive an effective model, it has been shown [39] that it is possible to describe Ca_2RuO_4 via a projection into the $J = 0$ and $J = 1$ manifold. This projection still reduces the degrees of freedom

per site from nine to four. Only considering the $J = 0$ and $J = 1$ states

$$|J = 0, m_J = 0\rangle = \frac{1}{\sqrt{3}} (|m_S = 1, m_L = -1\rangle + |-1, 1\rangle - |0, 0\rangle)$$

$$|J = 1, m_J = 1\rangle = \frac{1}{\sqrt{2}} (|1, 0\rangle - |0, 1\rangle) = |\mathcal{T}_1\rangle$$

$$|J = 1, m_J = 0\rangle = \frac{1}{\sqrt{2}} (|1, -1\rangle - |-1, 1\rangle) = |\mathcal{T}_0\rangle$$

$$|J = 1, m_J = -1\rangle = \frac{1}{\sqrt{2}} (|-1, 0\rangle - |0, -1\rangle) = |\mathcal{T}_{-1}\rangle\,, \tag{2.15}$$

and neglecting $J = 2$ states, one obtains an effective Hamiltonian in the J basis. Instead of introducing pseudospin 1/2 operators like for the Kitaev-Heisenberg model, one introduces triplon operators $\mathcal{T}^{\dagger}_{-1/0/1}$ ($\mathcal{T}_{-1/0/1}$) which create (annihilate) the respective $J = 1$ triplet and annihilate (create) the $J = 0$ state. From there, one can define [39]

$$\mathcal{T}_x = -\frac{i}{\sqrt{2}} (\mathcal{T}_1 - \mathcal{T}_{-1})$$

$$\mathcal{T}_y = \frac{1}{\sqrt{2}} (\mathcal{T}_1 + \mathcal{T}_{-1})$$

$$\mathcal{T}_z = i\mathcal{T}_0, \tag{2.16}$$

and with that $\mathbf{T} = (\mathcal{T}_x, \mathcal{T}_y, \mathcal{T}_z)$, analogue to spin and orbital vectors. We can project the spin-orbit Hamiltonian into the triplon basis (2.15) and rewrite it in form of the operators $\mathbf{T} = (\mathcal{T}_x, \mathcal{T}_y, \mathcal{T}_z)$, i.e., $H(\mathbf{S}, \mathbf{L}) \to H(\mathcal{T})$. Our model reduces to an effective singlet-triplet model because we only consider $J = 0$ and $J = 1$. The detailed derivation of this Hamiltonian can be found for isotropic hopping and $J_{\mathrm{H}} = 0$ in [39]. It has been shown that in this Hamiltonian terms, which create (annihilate) triplons occur [39, 71]. These terms couple the $J = 0$ and $J = 1$ states, so the ground state becomes a superposition of $J = 1$ and $J = 0$ states, which leads to a nonzero magnetization. Khalliulin first discovered this effect in [39], also known as excitonic magnetism.

2.3.4 Floquet formalism

For a Hamiltonian periodic in time

$$H(\tau) = H(\tau + T), \tag{2.17}$$

it has been shown [27] that physics for short times can be accessed via a time-independent effective Hamiltonian. This assumption is also known as Floquet's theorem. The reasoning is similar to Bloch's theorem, which is valid for periodic lattices. Like in the case of Bloch's theorem, we first can assume that the eigenstates of $H(\tau)$ also obey a time

periodicity, and therefore Floquet's theorem states that one can write eigenstates of the system as

$$\Psi_n(\tau) = u_n(\tau)e^{-i\epsilon_n\tau}, \tag{2.18}$$

where $\Psi_n(\tau)$ is the eigenstate of $H(\tau)$, $u_n(\tau)$ is a function periodic in time, i.e., $u_n(\tau) = u_n(\tau + T)$, ϵ_n are the so called Floquet quasi-energies, and $\hbar = 1$. Since $\Psi_n(\tau)$ also has to be periodic in time, for the Floquet energies

$$\epsilon_n = n\frac{2\pi}{T} = n\omega \quad n \in \mathbb{N} \tag{2.19}$$

has to hold. In this thesis, we investigate the interaction with a periodic light field. Therefore, we can interpret (2.19) as the energy provided by the absorption (emission) of n photons in the system. We see that without loss of generality, we can insert an additional $1 = e^{im\omega\tau}e^{-im\omega\tau}$ with $m \in \mathbb{N}$,

$$\Psi_n(\tau) = u_n(\tau)e^{im\omega\tau}e^{-im\omega\tau}e^{-i\epsilon_n\tau} = u_{nm}(t)e^{-i(\epsilon_n+m\omega)\tau}. \tag{2.20}$$

Plugging this ansatz into the time-dependent Schrödinger equation yields

$$\begin{aligned} H(\tau)\Psi_n(\tau) &= i\partial_\tau\Psi_n(\tau) \\ &= i\left[(\partial_\tau u_{nm}(\tau))e^{-i(\epsilon_n+m\omega)\tau} - i\left(\epsilon_n + m\omega\right)u_{nm}(\tau)e^{-i(\epsilon_n+m\omega)\tau}\right]. \end{aligned} \tag{2.21}$$

We can rewrite this expression in the form of a time-independent Schrödinger equation

$$\underbrace{H(\tau) - i\partial_\tau}_{\bar{H}(\tau)} u_{nm}(\tau) = (\epsilon_n + m\omega)u_{nm}(\tau), \tag{2.22}$$

with the difference being that $\bar{H}(\tau)$ is defined in the extended Hilbert space $\mathcal{F} = \mathcal{H} \otimes \mathcal{L}_T$ [72,73], with $\mathcal{H}$ being the Hilbert space of $H(t)$ and $\mathcal{L}_T$ the space of square-integrable time periodic functions. States in $\mathcal{F}$ can be expressed as $|\alpha(\mathbf{r})\rangle \otimes |\beta(\tau)\rangle$ with the scalar product defined as in [73]

$$\langle\alpha(\mathbf{r})|\alpha(\mathbf{r})\rangle \otimes \langle\beta(\tau)|\beta(\tau)\rangle = \langle\alpha(\mathbf{r})|\alpha(\mathbf{r})\rangle \otimes \frac{1}{T}\int_0^T \beta^*(\tau)\beta(\tau)\mathrm{d}\tau. \tag{2.23}$$

A complete orthonormal basis of $\mathcal{L}_T$ is given by $\beta(\tau) = e^{im\omega\tau}$ with $m \in \mathbb{N}$ the photon number in the system. Therefore, we will refer to the basis states of $\mathcal{L}_T$ as $|m\rangle$ and the basis states of $\mathcal{F}$ as $|\alpha, m\rangle = |\alpha(\mathbf{r})\rangle \otimes |m\rangle$. With this, we can write the Hamiltonian

$\bar{H}(\tau)$ in the basis of the extended Hilbert space $\mathcal{F}$. This yields

$$
\begin{aligned}
\langle \alpha', m' | \bar{H}(\tau) | \alpha, m \rangle &= \langle \alpha' | \frac{1}{T} \int_0^T e^{-im'\omega\tau} \left(H(\tau) - i\hbar\partial_\tau \right) e^{im\omega\tau} \mathrm{d}\tau | \alpha \rangle \\
&= \frac{1}{T} \langle \alpha' | \int_0^T (H(\tau) + \hbar m\omega) e^{i(m-m')\omega\tau} \mathrm{d}\tau | \alpha \rangle \\
&= \langle \alpha' | \frac{1}{T} \int_0^T H(\tau) e^{i(m-m')\omega\tau} \mathrm{d}\tau | \alpha \rangle + \delta_{\alpha,\alpha'} \delta_{m,m'} \hbar m\omega.
\end{aligned}
\tag{2.24}
$$

The first part of the expectation value describes the emission/absorption of Δm photons

$$
H_{\Delta m} = \frac{1}{T} \int_0^T H(t) e^{i\Delta m\omega\tau} \mathrm{d}\tau,
\tag{2.25}
$$

with $\Delta m = m - m'$. This part yields both diagonal and off-diagonal elements. The second part only has diagonal contributions due to the Kronecker-δ's. In total, the Hamiltonian in the $\alpha \otimes \beta$ basis can be written as

$$
\bar{H} = \begin{pmatrix}
\ddots & \vdots & \vdots & \vdots & \vdots & \cdots \\
\cdots & H_0^{\alpha\alpha} + 2\omega & H_1^{\alpha\alpha} & H_2^{\alpha\alpha} & H_3^{\alpha\alpha} & \cdots \\
\cdots & H_{-1}^{\alpha\alpha} & H_0^{\alpha\alpha} + \omega & H_1^{\alpha\alpha} & H_2^{\alpha\alpha} & \cdots \\
\cdots & H_{-2}^{\alpha\alpha} & H_{-1}^{\alpha\alpha} & H_0^{\alpha\alpha} & H_1^{\alpha\alpha} & \cdots \\
\cdots & H_{-3}^{\alpha\alpha} & H_{-2}^{\alpha\alpha} & H_{-1}^{\alpha\alpha} & H_0^{\alpha\alpha} - \omega & \cdots \\
\iddots & \vdots & \vdots & \vdots & \vdots & \ddots
\end{pmatrix},
\tag{2.26}
$$

where the displayed block is for elements $|\alpha\rangle = |\alpha'\rangle$. We can dissect $\bar{H}$ into a diagonal part $\bar{H}_D$ describing the energy of the system with m photons in the system and a non-diagonal part describing the absorption/emission of m photons.

In our case, the Hamiltonian with a periodic time dependence is $H_{\mathrm{kin}} \to H_{\mathrm{kin}}(\tau)$, as introduced in Sec. 2.2. With this the time dependence total Hamiltonian becomes $H(t) = H_{\mathrm{K}} + H_{\mathrm{kin}}(\tau)$. Choosing $|\alpha\rangle$ to be the eigenstates of H_{K}, we see that the diagonal elements $H_0^{\alpha\alpha}$ yield the eigenenergies of the Kanamori Hamiltonian E_K^α. The off-diagonal elements have only nonzero contributions from the kinetic Hamiltonian $H_{\mathrm{kin},m}^{\alpha'\alpha} = H_m^{\alpha'\alpha}$. Therefore, we can rewrite (2.26) to

$$
\bar{H} = \begin{pmatrix}
\ddots & \vdots & \vdots & \vdots & \vdots & \cdots \\
\cdots & E_K^{\alpha'} + 2\omega & 0 & H_2^{\alpha'\alpha} & 0 & \cdots \\
\cdots & 0 & E_K^{\alpha'} + \omega & H_1^{\alpha'\alpha} & 0 & \cdots \\
\cdots & H_{-2}^{\alpha\alpha'} & H_{-1}^{\alpha\alpha'} & E_K^\alpha & H_1^{\alpha'\alpha} & \cdots \\
\cdots & 0 & 0 & H_{-1}^{\alpha\alpha'} & E_K^{\alpha'} - \omega & \cdots \\
\iddots & \vdots & \vdots & \vdots & \vdots & \ddots
\end{pmatrix}.
\tag{2.27}
$$

Like in the time-independent case, if the energy splitting between the ground state manifold $|\alpha, 0\rangle$ and the excited states $|\alpha', m\rangle$ is significantly larger than the energy scale of H_m, in our case hopping strength t, we can treat H_m in a perturbative manner. This yields an effective Floquet-Hamiltonian of Kugel-Khomskii type in second-order perturbation theory

$$\bar{H}_{\text{eff}} = \sum_{\alpha'', \alpha} \sum_{\alpha' \neq \alpha'', \alpha} \sum_m |\alpha'', 0\rangle \frac{H_{-m}^{\alpha'' \alpha'} H_m^{\alpha' \alpha}}{E_K^\alpha - (E_K^{\alpha'} + m\omega)} \langle \alpha, 0| , \tag{2.28}$$

with $|\alpha\rangle$ and $|\alpha''\rangle$ states from the ground state manifold of H_K, and $|\alpha'\rangle$ element of the excited state manifold of H_K. The derivation of this effective Floquet Hamiltonian is a high-frequency expansion like discussed in [72], with the distinction that $H_m^{\alpha' \alpha}$ does not just change the number of photons in the system but also causes an excitation in the form of hopping from an electron to an adjacent site $|\alpha\rangle \rightarrow |\alpha'\rangle$. Therefore we demand $E_K^\alpha - (E_K^{\alpha'} + m\omega) \gg t$ instead of $\omega \gg t$, which is assumed in the high frequency expansion.

To derive the effective Floquet-Hamiltonian, one could also perform a time-dependent perturbation theory for the Hamiltonian to arrive at a time-dependent effective Hamiltonian. Since this Hamiltonian is still periodic in time, one can then apply Floquet's theorem to derive the desired result. While this approach is convenient for low orders, it becomes cumbersome for orders $\propto t^{\gamma 3}$ thus we believe that the approach introduced in this section is, in general, favorable. We showcase the derivation of the effective Floquet-Hamiltonian via time-dependent perturbation theory in Sec. 3.3. It is important to note that the order in which one applies perturbation theory and Floquet's theorem is arbitrary and the effective Hamiltonian derived is equivalent.

2.4 Numerics

Deriving effective models describing complex materials (Sec. 2.3) and capturing ground state properties is one side of the coin. However, there are rarely analytical solutions for these models. Therefore, a numerical approach is often mandatory to make meaningful predictions for analytically derived models. In this thesis, we use two of the most used numerical methods of solving these problems, ED and Monte Carlo (MC), which we will briefly discuss in the following sections.

2.4.1 Exact diagonalization

Most experimental samples of transition metal compounds are macroscopic. Therefore, theoretical models should ideally work in the thermodynamic limit to be comparable to experimental measurements. However, this means one has to describe a model with

$N \to \infty$ particles causing an infinite dimensional Hilbert space, which is not solvable numerically. The basic concept behind ED is that a suitable finite system [74] can mimic the physical properties of the thermodynamic limit. In the case of transition metal compounds, Sec. 2.1, this finite system manifests itself as a cluster of transition metal atoms. The determination of a suitable cluster is the cornerstone of every ED approach. To find the ideal cluster, one has to find the largest common denominator between physical value and hardware limitations. On one hand, the cluster should capture the lattice geometry and the most prominent magnetic and orbital orderings. On the other hand, the computational cost of determining physical properties should come at an acceptable price. Since the Hilbert space increases exponentially with the cluster size N, the number of realizable clusters that have physical value is sparse.

As an example, we want to consider the d^4 compound Ca_2RuO_4, introduced in Sec. 2.1. The degrees of freedom per site is $f = \binom{6}{2} = 15$, resulting in a Hilbert space dimension of 15^N. However, because neither H_{kin} (2.1) nor H_{int} (2.2) change the total spin, we can dissect our Hilbert space into three independent subspaces with $S_{tot} = 1, 0, -1$, which one can solve separately. The sector with the largest Hilbert space is then the $S_{tot} = 0$ sector with $\dim(\mathcal{H}) = 9^N$.

For our calculations we use an eight site cluster with $\sqrt{8} \times \sqrt{8}$ geometry and periodic boundary conditions (Fig. 7.1). The Kitaev-Heisenberg model describing α-$RuCl_3$ has only $f = 2$ per site, which means larger clusters up to at least $N = 24$ are possible. The first step of ED is to find a finite system compatible with the computational capabilities describing magnetic order and excitations in the thermodynamic limit reasonably well.

After defining the finite system, we can use the fact that, in second quantization, the Schrödinger equation becomes an algebraic eigenvalue problem. The Lanczos method is a fast and efficient method to determine the lowest eigenvalues and the corresponding states. In the following, we give a short overview of the Lanczos algorithm. A detailed explanation can, e.g., be found in [74]. The base premise of the Lanczos method is to tridiagonalize the Hamiltonian via a basis transformation to speed up the diagonalization process. The Krylov space, where the Hamiltonian takes a tridiagonal form, is an orthonormal basis spanned by

$$|v_0\rangle, H|v_0\rangle, H^2|v_0\rangle, ..., H^L|v_0\rangle, \tag{2.29}$$

with an arbitrary starting vector $|v_0\rangle$ [74]. One constructs the orthonormal basis vectors iteratively. Starting with applying H once on $|v_0\rangle$ we obtain

$$|v_1\rangle \underbrace{\langle v_1| H |v_0\rangle}_{b_1} = |\tilde{v}_1\rangle = H|v_0\rangle - |v_0\rangle \underbrace{\langle v_0| H |v_0\rangle}_{a_0}, \tag{2.30}$$

where $b_1 = \langle v_1 | H | v_0 \rangle$ normalizes $|\tilde{v}_1\rangle$ and a_0 ensures that $|v_1\rangle$ is orthogonal to $|v_0\rangle$. With $|v_1\rangle$ we can construct the next basis vector $|v_2\rangle$ via

$$b_2 |v_2\rangle = |\tilde{v}_2\rangle = H |v_1\rangle - \sum_{i=0}^{1} |v_i\rangle \langle v_i | H |v_1\rangle = H |v_1\rangle - a_1 |v_1\rangle - b_1 |v_0\rangle, \qquad (2.31)$$

where $a_1 = \langle v_1 | H | v_1 \rangle$. Like in (2.30), the sum guarantees the orthogonality and b_2 the normalization. In general to determine $|v_{n+1}\rangle$ we have to calculate

$$b_{n+1} |v_{n+1}\rangle = H |v_n\rangle - \sum_{i=0}^{n} |v_i\rangle \langle v_i | H |v_n\rangle. \qquad (2.32)$$

At first glance, it is not obvious that H expressed in this basis becomes tridiagonal. However, looking at $n + 1 = 3$ we obtain

$$b_3 |v_3\rangle = H |v_2\rangle - a_2 |v_2\rangle - b_2 |v_1\rangle - |v_0\rangle \underbrace{\langle v_0 | H |v_2\rangle}_{=0}, \qquad (2.33)$$

where the last matrix element vanishes due to (2.31). Therefore, (2.32) can be simplified to

$$H |v_n\rangle = a_n |v_n\rangle + b_{n+1} |v_{n+1}\rangle + b_n |v_{n-1}\rangle, \qquad (2.34)$$

with $b_n = \langle v_n | H |v_{n-1}\rangle$ and $a_n = \langle v_n | H |v_n\rangle$. This has a tridiagonal form

$$\begin{pmatrix}
a_0 & b_1 & 0 & 0 & & 0 & 0 \\
b_1 & a_1 & b_2 & 0 & \dots & 0 & 0 \\
0 & b_2 & a_2 & b_3 & & 0 & 0 \\
0 & 0 & b_3 & a_3 & & 0 & 0 \\
& \vdots & & & \ddots & \vdots & \\
0 & 0 & 0 & 0 & \dots & a_n - 1 & b_n \\
0 & 0 & 0 & 0 & & b_n & a_n
\end{pmatrix}. \qquad (2.35)$$

It has been shown [74] that determining the lowest eigenvalue of this matrix is a good approximation of the ground state energy E_0 of H. Since, in this thesis, we are mainly interested in ground state properties and low excitation energies, the Lanczos method [75] is suitable for the considered models.

2.4.2 Semi-classical MC

The second numerical method used in this thesis is the semi-classical MC approach. In the classical approach, one treats spins (and orbital momentum if present) as classical

vectors with a fixed length, e.g., $S = 1$ for the spin vector in Ca_2RuO_4. The ground state is then found by minimizing the energy functional

$$E\left(|\psi\rangle\right) = \langle\psi|\,\hat{H}\,|\psi\rangle. \tag{2.36}$$

One achieves the minimization via the Markov Chain, where one starts at a random initial state Ψ_{in} with $E_{\mathrm{in}} = E\left(|\Psi_{\mathrm{in}}\rangle\right)$. From there one constructs a new state Ψ_{new} with $E_{\mathrm{new}} = E\left(|\psi_{\mathrm{new}}\rangle\right)$. We determine this new state by rotating the spin of a random site i by a random angle Φ. Acceptance of this state as the new initial state has the probability

$$P = \begin{cases} 1 & E_{\mathrm{in}} > E_{\mathrm{new}} \\ \mathrm{e}^{-\beta(E_{\mathrm{new}}-E_{\mathrm{in}})} & E_{\mathrm{new}} \geq E_{\mathrm{in}} \end{cases}, \tag{2.37}$$

where $\beta = 1/k_B T$. Repeating this process, one reaches the global minimum of the energy functional E_{min}. This method is very efficient in determining ground state properties for system sizes decisively larger than the typical system sizes of the ED method.

However, this method has two issues considering Ca_2RuO_4. First, for Ca_2RuO_4, we are interested in the ground state properties for $T \to 0$. This causes an exceedingly large β and a low probability of accepting a new state with higher energy. Therefore, the energy functional is more likely to get stuck in local minima. Hence, MC can have problems finding the ground state. A solution to this problem is the parallel tempering MC method proposed by [76]. Sec. 8.3 discusses parallel tempering Monte-Carlo (PTMC) in more detail.

The second issue of the classical MC approach is the approximation of the quantum mechanical spin as a classical object. To calculate the accurate ground state of Ca_2RuO_4, this is not sufficient because the real scalar nature of the vector components of $\mathbf{S}$ can't capture the behavior of an operator $\hat{S}_i$ with $i \in [x, y, z]$. To address this issue, we use the semi-classical MC approach [77], which is comparable to the approach of [78]. Here we define the trial wavefunctions $|\Psi_{\mathrm{T}}\rangle$ in direct product form

$$|\Psi_{\mathrm{T}}\rangle = \bigotimes_i \left(|S_i\rangle \otimes |L_i\rangle\right) \tag{2.38}$$

and are thus entanglement-free. Here, i indicates the lattice site and we define spin (angular) momentum operators as a linear superposition of the S_i^z (L_i^z) eigenvalues. In the case of Ca_2RuO_4 where $L_i = 1$ and $S_i = 1$ this yields

$$|S_i\rangle = \mu_{i,1}\,|m_{S_i} = 1\rangle + \mu_{i,0}\,|m_{S_i} = 0\rangle + \mu_{i,-1}\,|m_{S_i} = -1\rangle, \tag{2.39}$$

where $\mu = (\mu_{i,1}, \mu_{i,0}, \mu_{i,-1})$ is an arbitrary complex three dimensional vector. Therefore,

for each spin/orbital momentum, we have five degrees of freedom, contrary to the two degrees of freedom for the classical approach. With these classical complex vectors, we then can calculate the energy functional (2.36) and minimize it via the Markov chain approach of the classical Metropolis algorithm.

This method has proven successful for $S = 1$ problems where the classical approach has failed [78, 79]. Therefore, we believe this method is superior to the classical MC approach for our $S = 1$, $L = 1$ problem. Like classical MC, the computational cost of the semi-classical MC is minute compared to the ED approach and therefore provides the opportunity to investigate larger cluster sizes.

Last but not least, MC gives rise to the ground state properties for arbitrary temperatures and, for this reason, access to finite temperature properties like the specific heat C_T and susceptibility χ. Both of these quantities can be directly compared to experimental results and can yield qualitative information on the dependence of the Néel temperature on properties such as CF and SOC.

2.5 Summary

In Fig. 2.10, we summarize the introduced models (light blue), numerical methods (grey), and the physical concepts (dark blue) lying below these. This mind map is supposed to give a review of this thesis. All materials considered in this thesis are transition metal compounds (Sec. 2.1) and fall under the category of Mott insulators. A powerful method to describe Mott insulators are Kugel-Khomskii type models (Sec. 2.3.1), which all Hamiltonians considered in this thesis are. In particular we focus on Mott insulators with a d^5 (Sec. 2.1.1) [80] and a d^4 configuration (Sec. 2.1.2) [63, 77].

For d^5 materials (I), we are interested in Kitaev-Heisenberg models (Sec. 2.3.2) arising for materials with strong spin-orbit coupling. Here, our focal point is tuning candidate Kitaev materials into the Kitaev spin liquid via time-periodic driving with a light beam. We can obtain the effective model, which describes the influence of light, via the Floquet formalism Sec. 2.3.4.

In II, we investigate d^4 materials similar to Ca_2RuO_4. Here, we study the phase diagram for the ground state at $T = 0$ for varied CF and SOC (Sec. 2.2.2) via exact diagonalization (Sec. 2.4.1) and, supporting ED, semi-classical MC (Sec. 2.4.2). We also investigate the behavior of d^4 compounds for strong SOC, where we can simplify the Kugel-Khomskii model to an effective triplon model (Sec. 2.3.3). Last but not least, we explore finite temperature properties, like susceptibility and specific heat, via semi-classical MC.
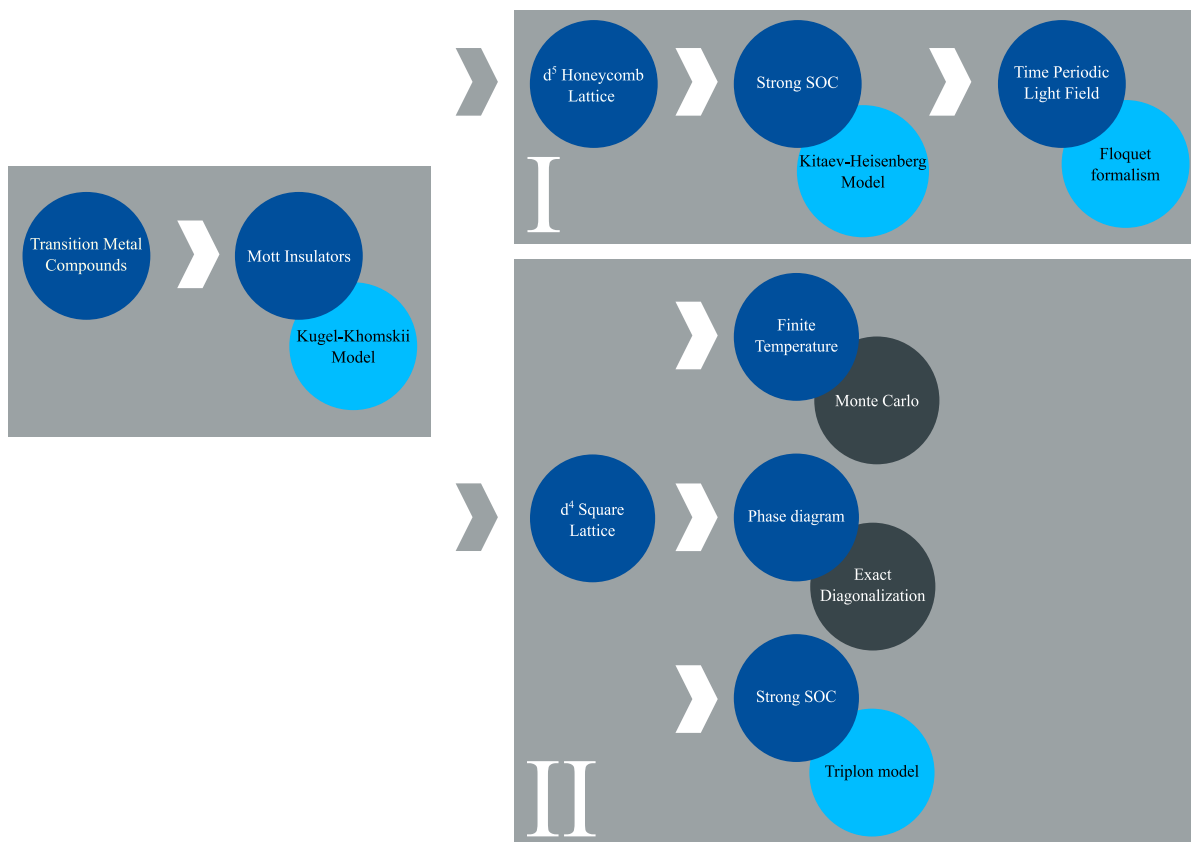
Figure 2.11: Overview of the structure of this thesis. Light blue depicts the models introduced in Sec. 2.3, dark blue the physical concepts, and dark grey the numerical methods. The number in the box denotes the part of this thesis where we discuss these topics.

I

Floquet engineering in Kitaev-Heisenberg models

3

Second order Floquet Hamiltonian

In this chapter we derive the effective Floquet Kitaev-Heisenberg Hamiltonian for d^5 honeycomb materials such as iridates and ruthenates [68, 69, 81], which is capable of describing light-matter interaction for a light field periodic in time. We consider second-order perturbation theory as a starting point for light-matter interactions in Kitaev-Heisenberg materials. Within this framework, we discuss different polarizations and the influence of heating effects.

3.1 Candidate Materials

Most of the more promising candidates to realize the KSL appear to have a magnetically ordered ground state. From applying a magnetic field [16–20], chemical doping [24–26], graphene substrates [82], and applying pressure [21–23] there have been multiple approaches to drive these materials from the magnetically ordered into the Kitaev spin liquid ground state.

A yet relatively unexploited method is to drive candidate materials via light-matter interactions periodic in time [83–85]. As we have shown in Sec. 2.3.4, one then can describe the system via a time-independent effective Floquet Hamiltonian [86–89], which should be valid at short but accessible time scales [27]. One can estimate a lower limit for these timescales via formula (15) of [27]. In our case, the shortest timescales are in the range of a few fs, which could be experimentally realizable [90]. In this chapter, we will focus on the derivation of such an effective Floquet Hamiltonian for d^5 transition metals with honeycomb lattices.

	LP	CP	AP
$A_x(\tau)$	$E_x/\omega \sin(\omega\tau)$	$E_x/\omega \sin(\omega\tau)$	$E_x/\omega \sin(\omega\tau)$
$A_y(\tau)$	$E_y/\omega \sin(\omega\tau)$	$E_y/\omega \cos(\omega\tau)$	$E_y/\omega \sin(N\omega\tau + \epsilon)$

Table 3.1: Vector potential $\mathbf{A}(\tau)$ for LP, CP, and AP with the driving frequency ω, electric field $\mathbf{E}$, time τ, frequency ratio N, and phase shift ϵ.

3.2 Peierl's substitution

One can capture the effect of a time-periodic light field on the kinetic Hamilton via the Peierls substitution [91, 92], where the hopping amplitude becomes time dependent such that H_{kin} reads

$$
\begin{aligned}
H_{\mathrm{kin}}(\tau) &= -\sum_{\alpha,\beta} \sum_{\substack{\gamma,\sigma \\ \langle ij \rangle_\gamma}} e^{i(\mathbf{r}_j - \mathbf{r}_i)\mathbf{A}(\tau)} t^\gamma_{\alpha,\beta} c^\dagger_{i,\alpha,\sigma} c_{j,\beta,\sigma} \\
&= -\sum_{\substack{\gamma,\sigma \\ \langle ij \rangle_\gamma}} \underbrace{e^{i(\mathbf{r}_j - \mathbf{r}_i)\mathbf{A}(\tau)}}_{\Omega(t)} \underbrace{\mathbf{c}^\dagger_{i,\sigma} \mathbf{T}^\gamma \mathbf{c}_{i,\sigma}}_{\hat{v}_{ij}},
\end{aligned}
\tag{3.1}
$$

with the bond direction γ, the orbital flavor $\alpha, \beta \in [xy, yz, zx]$, and the vector of annihilation operators $\mathbf{c}_i = (c_{i,xy,\sigma}, c_{i,yz,\sigma}, c_{i,zx,\sigma})$ (2.1).

Since in the honeycomb lattice each of the three orbitals is pointing in one of the bond directions of the lattice Fig. 3.2(ii), we label the orbital flavor according to the corresponding bond direction ($yz \to x$ etc.) as introduced in [34]. The bond-dependent hopping matrices $\mathbf{T}^\gamma$ are

$$
\mathbf{T}^z = \begin{pmatrix} t^z_1 & t^z_2 & t^z_4 \\ t^z_2 & t^z_1 & t^z_4 \\ t^z_4 & t^z_4 & t^z_3 \end{pmatrix}, \quad
\mathbf{T}^x = \begin{pmatrix} t^x_3 & t^x_4 & t^x_4 \\ t^x_4 & t^x_1 & t^x_2 \\ t^x_4 & t^x_2 & t^x_1 \end{pmatrix}, \quad
\mathbf{T}^y = \begin{pmatrix} t^y_1 & t^y_4 & t^y_2 \\ t^y_4 & t^y_3 & t^y_4 \\ t^y_2 & t^y_4 & t^y_1 \end{pmatrix},
\tag{3.2}
$$

with the four distinct hopping procceses introduced in Sec. 2.2.1 labeled according to [33].

$\mathbf{A}(\tau)$ describes the vector-potential of the light field. The expressions for $\mathbf{A}(\tau)$ are listed in Tab. 3.1 for LP, CP and AP. For AP N describes the frequency ratio and ϵ the phase difference between x and y polarized light. CP and LP therefore are the limiting cases $N = 1, \epsilon = \pi/2$ and $n = 1, \epsilon = 0$ of AP. We display the lowest orders of the Lissajous figures in Fig. 3.1 to give a rough impression of how Lissajous figures can look. $\mathbf{r}_{i,j} = \mathbf{r}_j - \mathbf{r}_i$ denotes the vector between sites i and j, which in polar coordinates becomes $\mathbf{r}_{i,j} = r_{i,j} [\cos(\phi), \sin(\phi)]$.
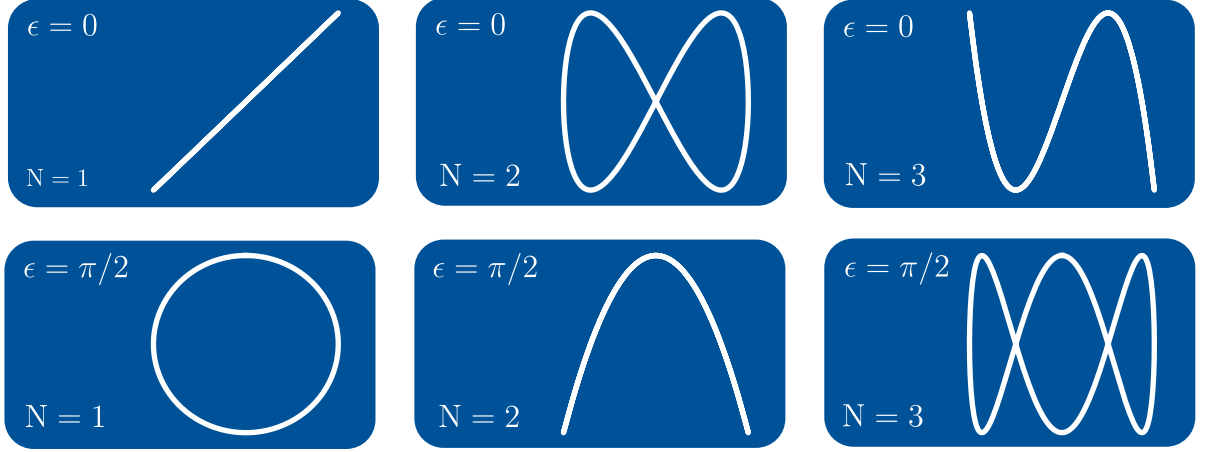
Figure 3.1: The lowest three orders of Lissajous figures are displayed for a phase shift of $\epsilon = 0$ and $\epsilon = \pi/2$. For the lowest order $N = 1$, the Lissajous figures for $\epsilon = 0$ and $\epsilon = \pi/2$ become LP and CP respectively. With the definition of Tab. 3.1, it is, in principle, possible to describe arbitrary polarization.

For CP we set $E_x = E_y = E_0$ and the hopping term becomes

$$t(\tau)_{\alpha\beta} = t_{\alpha\beta} e^{i(\mathbf{r}_j - \mathbf{r}_i)\mathbf{A}(t)} = t_{\alpha\beta} e^{i\frac{E_0}{\omega} r_{i,j}[\cos(\phi)\sin(\omega\tau) + \sin(\phi)\cos(\omega\tau)]} = t_{\alpha\beta} e^{i\frac{E_0}{\omega} r_{i,j} \sin(\phi + \omega\tau)}. \quad (3.3)$$

As we will see in Sec. 3.3.2 this results in an ϕ independent effective Hamiltonian. Hence, light influences each bond direction in the same manner. We can rewrite the expression in (3.3) with the help of the Jacobi-Anger expansion to

$$t_{\alpha,\beta}(\tau) = t_{\alpha,\beta} \sum_{l=-\infty}^{\infty} \mathcal{J}_{-l}(u_{ij}^C) e^{-i\,l(\omega\tau + \phi)}, \quad (3.4)$$

where $u_{ij}^C(r_{ij}, E_0, \omega) = E_0/\omega r_{i,j}$ and $\mathcal{J}_n(u_{ij}^C)$ the $n-$th Bessel function of the first kind. The u_{ij} term here carries the information of the light frequency ω and amplitude E_0. Additionally, this expression for CP depends on the distance to the nearest neighbor (or further nearest neighbor) and not the direction of the respective neighbor.

For LP, such a simplification is impossible and the light has a distinct influence on different bond directions. If we use the Jacobi-anger expansion for the time-dependent hopping parameters $t(\tau)$, we obtain, for LP with $E_x = E_0\cos(\varphi)$ and $E_y = E_0\sin(\varphi)$

$$e^{iu_{ij}^L sin(\omega\tau)} = \sum_{l=-\infty}^{\infty} \mathcal{J}_{-l}(u_{ij}^L) e^{-i\,l\omega\tau}, \quad (3.5)$$
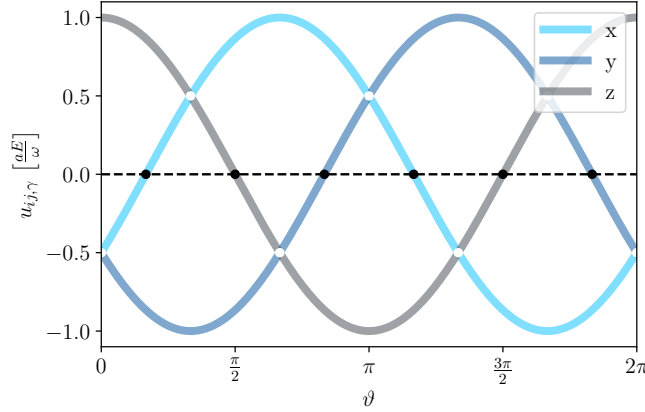
(i) $u_{ij,\gamma}$ as a function of the light angle
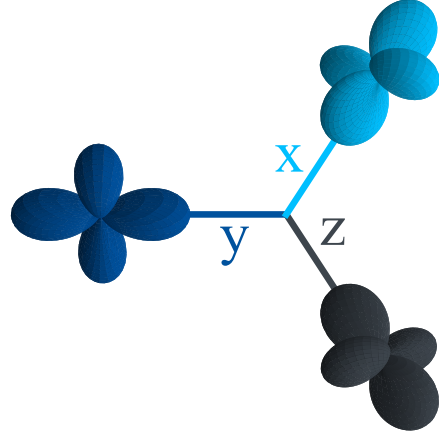
(ii) x, y, and z bond in the honeycomb lattice

Figure 3.2: (i) The frequency dependence of the hopping for linear polarized light $u_{ij,\gamma}$ is plotted in dependence of the light angle φ for the three distinct bond directions. The white dots denote the scenarios where two bond directions have the same ω dependence. The black dots denote light angles where one bond direction decouples from the light field and, because of that, does not depend on the frequency and amplitude of the light. (ii) Displayed are the three different bond directions present in the honeycomb lattice x (light blue), y (blue), and z (anthracite) in the honeycomb lattice. d_{xy} (anthracite), d_{yz} (light blue), and d_{zx} orbital (blue) are colored according to the corresponding bond direction.

with

$$u_{ij}^L(\mathbf{r}_{ij}^\gamma, \varphi, E_0, \omega) = \frac{E_0}{\omega}\, \mathbf{r}_{ij}^\gamma \begin{pmatrix} \cos(\varphi) \\ \sin(\varphi) \end{pmatrix}. \tag{3.6}$$

We observe that, contrary to u_{ij}^C, u_{ij}^L depends on the light angle φ as well as on the direction of $\mathbf{r}_{ij}^\gamma$. For the Honeycomb lattice we therefore obtain distinct u_{ij}^L for the three different bond directions present (see Fig. 3.2)

$$u_{ij,x} = a\frac{E_0}{\omega}\left[-\frac{1}{2}\cos(\varphi) + \frac{\sqrt{3}}{2}\sin(\varphi)\right] \tag{3.7}$$

$$u_{ij,y} = a\frac{E_0}{\omega}\left[-\frac{1}{2}\cos(\varphi) - \frac{\sqrt{3}}{2}\sin(\varphi)\right] \tag{3.8}$$

$$u_{ij,z} = a\frac{E_0}{\omega}\cos(\varphi), \tag{3.9}$$

with $a = |\mathbf{r}_{ij}|$ the distance between site i and j. As we can see in Fig. 3.2, we can tune (3.7)-(3.9) in such a manner that two bond interactions have the same E_0 and ω dependency (white dots) or one bond direction completely decouples from E_0 and ω, i.e., $u_{ij,\gamma}^L = 0$ (black dots).

3.3 Time dependent second order perturbation theory

Experiments have shown that all materials considered in this thesis, i.e., Na_2IrO_3, α-Li_2IrO_3, and α-$RuCl_3$, are in a Mott insulating phase at low temperatures [7, 8, 13]. Therefore, the electron number per site is fixed and one can treat the kinetic part of the Hamiltonian via perturbation theory, see Sec. 2.3.1. As a starting point, we consider just second-order perturbation theory, which has proven successful for the time-independent case. Through the course of this thesis, we will build up on the findings of this section and expand the model to higher orders.

The periodic time dependence in the kinetic Hamiltonian enters through the Peierls substitution introduced in (3.1). We could proceed like in Sec. 2.3.4, but in this section, we want to highlight a different approach to deriving the effective Floquet Hamiltonian. Instead of time averaging over $H_{kin}(\tau)$ before performing perturbation theory, we consider time-dependent perturbation theory to obtain the effective time-dependent Hamiltonian, averaging over time yields the effective Floquet Hamiltonian. In our opinion, this procedure showcases the origin of the propagation operator, which propagates the doublon-holon excitation $(d^2 d^0)$ through the lattice conveniently. As we will see in Sec. 3.5, the propagator of a relevant quantity near resonances, i.e., the denominator in (2.28) does not fulfill the condition $\mathcal{E}_K^\alpha - (\mathcal{E}_K^{\alpha'} + m\omega) \gg t$ anymore. We again want to emphasize that both approaches lead to the same effective Hamiltonian.

The time-dependent perturbation theory approach has been already used for $LaTiO_3$ and $YTiO_3$ [86, 93]. As in [93], we start by considering the time-dependent Schrödinger equations

$$i\delta_\tau \left|\Phi_1(\tau)\right\rangle = \hat{H}_{int} \left|\Phi_1(\tau)\right\rangle + \sum_f \hat{P}_1 \hat{H}_{kin}(\tau) \left|\Phi_f(\tau)\right\rangle \tag{3.10}$$

$$i\delta_\tau \left|\Phi_f(\tau)\right\rangle = \hat{P}_f \hat{H}_{kin}(\tau) \left|\Phi_1(\tau)\right\rangle + \hat{P}_f \left(\hat{H}_{kin}(\tau) + \hat{H}_{int}\right) \left|\Phi_f(\tau)\right\rangle, \tag{3.11}$$

where we only considered the subspace with zero excited holes and the subspace where one hole has moved to another site. That means, in the latter case, we have one doublon-holon pair in the system. $\left|\Phi_1\right\rangle$ is defined in the Hilbert space $\mathcal{H}_1$ spanned by the states with exactly one hole per site. The energy for these states is $\mathcal{E}_1 = 0$.

Analogously $\left|\Phi_f\right\rangle$ is defined in the Hilbert space $\mathcal{H}_f$ spanned by the states with one doublon-holon pair with flavor f at adjacent sites i and j in the lattice. The flavor f (see Tab. 2.1) denotes the possible eigenstates $\left|\Psi_{2,f}\right\rangle$ with two holes. For the remainder of this chapter we define $\left|d_f\right\rangle_i = \left|\Psi_{2,f}\right\rangle_i$ as the doublon state with flavor f.

The operators $\hat{P}_f$ and $\hat{P}_1$ projects on the states spanning $\mathcal{H}_f$ and $\mathcal{H}_1$ respectively. $\hat{K}_f(\tau) = \hat{P}_f \hat{H}_{kin}(\tau) \hat{P}_f$ describes the propagation of the doublon-holon pair within the subspace with energy $\mathcal{E}_f$. $\hat{H}_{kin}(\tau)$ and H_{int} are the Hamiltonians defined in Sec. 2.2.1 and

Sec. 2.2.2. It is of note that in this thesis we only consider propagations that preserve the "flavor" f of the doublon $|d_f\rangle_j$, i.e., we neglect propagations of the type $|d_f\rangle_j \to |d_{f'}\rangle_{j-1}$.

It has been shown [93] that the propagation operator within the $|\Phi_f\rangle$ subspace can be described approximately by its time average $\hat{K}_f = 1/T \int_0^T \hat{K}_f(\tau)$. Therefore, we can rewrite the Schrödinger equation of the one doublon-holon space to

$$(i\delta_\tau - \hat{K}_f - \hat{H}_{\text{int}})\,|\Phi_f(\tau)\rangle = \hat{P}_f \hat{H}_{\text{kin}}(\tau)\,|\Phi_1(\tau)\rangle$$
$$e^{-i(\hat{K}_f + \hat{H}_{\text{int}})t} i\delta_\tau e^{i(\hat{K}_f + \hat{H}_{\text{int}})\tau}\,|\Phi_f(\tau)\rangle = \hat{P}_f \hat{H}_{\text{kin}}(\tau)\,|\Phi_1(\tau)\rangle$$
$$i\delta_\tau e^{i(\hat{K}_f + \hat{H}_{\text{int}})\tau}\,|\Phi_f(\tau)\rangle = e^{i(\hat{K}_f + \hat{H}_{\text{int}})\tau}\hat{P}_f \hat{H}_{\text{kin}}(\tau)\,|\Phi_1(\tau)\rangle. \tag{3.12}$$

Integrating (3.12) over time then yields an expression for $|\Phi_f(\tau)\rangle$

$$|\Phi_f(\tau)\rangle = -ie^{-i(\hat{K}_f + \hat{H}_{\text{int}})\tau} \int d\tau' e^{i(\hat{K}_f + \hat{H}_{\text{int}})\tau'}\hat{P}_f \hat{H}_{\text{kin}}(\tau')\,|\Phi_1(\tau')\rangle. \tag{3.13}$$

The expression (3.13) can then be plugged into (3.10) to obtain an effective Hamiltonian for $\mathcal{H}_1$ of the form

$$i\delta_\tau\,|\Phi_1(\tau)\rangle = H_{\text{eff}}(\tau)\,|\Phi_1(\tau)\rangle. \tag{3.14}$$

In the following section, we will discuss the derivation of $H_{\text{eff}}(\tau)$ for different polarizations.

3.3.1 Linear polarized light

We start our derivation of the time-independent effective Floquet Hamiltonian for LP and discuss the differences to arbitrary and circular polarization introduced in Sec. 3.2. Plugging the definition of the time-dependent kinetic Hamiltonian for linear polarized light from (3.5) into (3.13), we obtain

$$|\Phi_f(\tau)\rangle = -\sum_{l=-\infty}^{\infty} i e^{-i(\hat{K}_f + \mathcal{E}_f)\tau} \mathcal{J}_{-l}(u_{ij}^L) \int_\tau e^{i(\hat{K}_f + \mathcal{E}_f - l\omega)\tau'} \hat{v}_{ij}^{f,1}\,|\Phi_1(\tau')\rangle\, d\tau', \tag{3.15}$$

with $\hat{v}_{ij}^{f,1} = \hat{P}_f \hat{v}_{ij} \hat{P}_1$. Integrating this expression by parts then yields

$$|\Psi_f(\tau)\rangle = -\sum_{l=-\infty}^{\infty} \mathcal{J}_{-l}(u_{ij}^c) \frac{1}{\hat{K}_f + \mathcal{E}_f - l\omega} \hat{v}_{ij}^{f,1} e^{-il\omega\tau}\,|\Phi_1(\tau)\rangle + \mathcal{O}(t/U^2), \tag{3.16}$$

where terms of order $\mathcal{O}(t/U^2)$ are negligible due to the condition $t \ll U$ for Mott insulators. We can plug the expression for $|\Phi_f(\tau)\rangle$ into (3.10) to obtain

$$
\begin{aligned}
i\delta_\tau |\Phi_1(\tau)\rangle &= -\sum_f \sum_{l=-\infty}^{\infty} \hat{P}_1 \hat{H}_{\text{int}} \hat{P}_f \frac{1}{\hat{K}_f + \mathcal{E}_f - l\omega} e^{-il\omega\tau} \mathcal{J}_{-l}(u_{ij}^L) \hat{v}_{ij}^{f,1} |\Psi_1(\tau)\rangle \\
&= \underbrace{-\sum_f \sum_{l,k=-\infty}^{\infty} e^{i(k-l)\omega\tau} \mathcal{J}_k(u_{ji}^L) \mathcal{J}_{-l}(u_{ij}^L) \hat{v}_{ji}^{1,f} \frac{1}{\hat{K}_f + \mathcal{E}_f - l\omega} \hat{v}_{ij}^{f,1}}_{H_{\text{eff}}(\tau)} |\Phi_1(\tau)\rangle \quad (3.17)
\end{aligned}
$$

Since $H_{\text{eff}}(\tau)$ is periodic in time with $T = 2\pi/\omega$ we can apply Floquet's theorem introduced in Sec. 2.3.4. If we average over time, we obtain

$$
\begin{aligned}
H_{\text{eff}}^F &= \frac{1}{T} \int_0^T H_{\text{eff}}(\tau) \mathrm{d}\tau \\
&= -\sum_f \hat{v}_{ji}^{1,f} \frac{1}{\hat{K}_f + \mathcal{E}_f - l\omega} \hat{v}_{ij}^{f,1} \sum_{l,k=-\infty}^{\infty} \mathcal{J}_k(u_{ji}^L) \mathcal{J}_{-l}(u_{ij}^L) \delta_{k,l} \\
&= -\sum_f \hat{v}_{ji}^{1,f} \frac{1}{\hat{K}_f + \mathcal{E}_f - l\omega} \hat{v}_{ij}^{f,1} \sum_{l=-\infty}^{\infty} \mathcal{J}_l(u_{ji}^L)^2. \quad (3.18)
\end{aligned}
$$

Here we used the hermiticity condition $u_{ij} = -u_{ji}$ as well as the condition $\mathcal{J}_{-l}(x) = \mathcal{J}_l(-x)$ for Bessel functions. This is the time-independent effective Floquet Hamiltonian, describing the system at short time scales. H_{eff}^F is very similar to the time-independent case, with the difference that hopping parameters depend on the frequency and amplitude of the light. This yields the opportunity to modify hopping parameters via the light field.

3.3.2 Circular polarized light

In case we use CP instead of LP the kinetic Hamiltonian becomes (see [31])

$$
H_{\text{kin}}(\tau) = \sum_{l=-\infty}^{\infty} \mathcal{J}(u_{ij}^C) e^{-il(\omega\tau+\phi)} \hat{v}_{ij}. \quad (3.19)
$$

With this, we can derive the effective Floquet Hamiltonian for CP in the same manner as LP. We end up with the effective time-dependent Floquet Hamiltonian

$$
H_{\text{eff}}(\tau) = -\sum_f \sum_{l,k=-\infty}^{\infty} e^{i(k-l)(\omega\tau+\phi)} \mathcal{J}_k(u_{ji}^C) v_{ji}^{1,f} \frac{1}{\hat{K}_f + \mathcal{E}_f - l\omega} \mathcal{J}_{-l}(u_{ij}^C) v_{ij}^{f,1}. \quad (3.20)
$$

Averaging over time then yields

$$
\begin{aligned}
H_{\mathrm{eff}}^F &= -\sum_f \frac{1}{T} \int_0^T \sum_{l,k=-\infty}^{\infty} e^{i(k-l)(\omega\tau+\phi)} \mathcal{J}_k(u_{ji}^C) v_{ji}^{1,f} \frac{1}{\hat{K}_f + \mathcal{E}_f - l\omega} \mathcal{J}_{-l}(u_{ij}^C) v_{ij}^{f,1} \\
&= -\sum_f \sum_{l,k} v_{ji}^{1,f} \frac{1}{\hat{K}_f + \mathcal{E}_f - l\omega} v_{ij}^{f,1} \delta_{k,l} \mathcal{J}_k(u_{ji}^C) \mathcal{J}_{-l}(u_{ji}^C) e^{i(k-l)\phi} \\
&= -\sum_f \sum_{l=-\infty}^{\infty} v_{ji}^{1,f} \frac{1}{\hat{K}_f + \mathcal{E}_f - l\omega} v_{ij}^{f,1} \mathcal{J}_l(u_{ji}^C)^2.
\end{aligned}
\tag{3.21}
$$

At first glance, this seems equivalent to the LP case. However, it is important to highlight that u_{ij}^C does not depend on the bond direction, while u_{ij}^L does. The only ϕ dependence in the circularly polarized light Hamiltonian vanishes due to averaging over time. Therefore, all bond directions have the same E_0 and ω dependence.

3.3.3 Lissajous figures

Lissajous figures are a convenient way to describe arbitrary polarizations via the, in Tab. 3.1 introduced, parameters N and ϵ. One main aspect is that in the Lissajous formalism it is possible to continuously connect LP and CP by just varying ϵ, which are commonly discussed unique cases in Floquet engineering [30–32, 80, 89, 94]. For arbitrary polarization, the derivation via time-dependent perturbation theory, as introduced in [86], is quite cumbersome. Therefore, we derive the effective Hamiltonian like in Sec. 2.3.4 [89, 95]. We neglected the propagator $\hat{K}_m$ intentionally because in the frequency regimes we study for AP, the propagator is negligible, see Sec. 3.5.1. This procedure reverses the order of applying Floquet's theorem and perturbation theory, which is valid because both H_{kin} and the effective time-dependent Hamiltonian derived in [80] are periodic in time. As discussed in Sec. 2.3.4, this approach yields the same results as Sec. 3.3. For arbitrary polarization (2.25) becomes

$$
\begin{aligned}
H_l^F &= \frac{1}{T} \int_0^T \hat{v}_{ij}^{f,1} e^{iE_0(\cos(\varphi)\sin(\omega\tau)+\sin(\varphi)\sin(N\omega\tau+\epsilon))} e^{il\omega\tau} d\tau \\
&= \frac{1}{T} \int_0^T \hat{v}_{ij}^{f,1} \sum_{l_1,l_2=-\infty}^{\infty} \mathcal{J}_{l_1}(E_0\cos(\varphi)) \mathcal{J}_{l_2}(E_0\sin(\varphi)) e^{il_1\omega\tau} e^{il_2(N\omega+\epsilon)\tau} e^{il\omega\tau} d\tau \\
&= \hat{v}_{ij}^{f,1} \sum_{l_1,l_2=-\infty}^{\infty} \mathcal{J}_{l_1}(E_0\cos(\varphi)) \mathcal{J}_{l_2}(E_0\sin(\varphi)) e^{il_2\epsilon} \delta_{l_1+Nl_2,-l} \\
&= \hat{v}_{ij}^{f,1} \underbrace{\sum_{l_2=-\infty}^{\infty} \mathcal{J}_{-l-Nl_2}(E_0\cos(\varphi)) \mathcal{J}_{l_2}(E_0\sin(\varphi)) (\cos(l_2\epsilon) + i\sin(l_2\epsilon))}_{\mathcal{B}_l(E_0,\omega,N,\epsilon,\varphi)},
\end{aligned}
\tag{3.22}
$$

where l_1, l_2 sums over all n Bessel functions, like l in (3.4). Plugging this into the second-order perturbation theory we obtain

$$
\begin{aligned}
H_{\text{eff}}^F &= -\sum_f \sum_{l=-\infty}^{\infty} \frac{v_{ji}^{1,f} v_{ij}^{f,1}}{\mathcal{E}_f - l\omega} B_{-l} B_l \\
&= -\sum_f \sum_{l=-\infty}^{\infty} \frac{v_{ji}^{1,f} v_{ij}^{f,1}}{\mathcal{E}_f - l\omega} \left\{ \left[\sum_{l_2} \mathcal{J}_{-l-Nl_2}(E_0 \cos(\theta)) \mathcal{J}_{l_2}(E_0 \sin(\theta)) \cos(l_2 \epsilon) \right]^2 \right. \\
&\quad \left. + \left[\sum_{l_2} \mathcal{J}_{-l-Nl_2}(E_0 \cos(\theta)) \mathcal{J}_{l_2}(E_0 \sin(\theta)) \sin(l_2 \epsilon) \right]^2 \right\},
\end{aligned}
\tag{3.23}
$$

here we used that $B_{-l} = B_l^*$. The effective Hamiltonian has the same form as in [31] with the distinction that the Bessel functions get replaced by the B_l functions. With this effective Floquet Hamiltonian, we can capture the influence of arbitrary light and bridge the gap between the limiting cases CP and LP.

3.4 Projection in the $j = 1/2$ picture

In the $4d$ and $5d$ materials we are investigating, namely iridates and ruthenates, SOC λ is expected to be dominant due to a high atomic number Z and $\lambda \propto Z^2$ [96]. As we showed in Sec. 2.3.2, the materials can be projected into the effective $j = 1/2$ picture in the non-driven case, giving rise to an effective Kitaev-Heisenberg model. One can do the same for the effective Floquet Hamiltonian. If we consider that the influence of the light field only enters as a prefactor in H_{eff}^F, the derivation of the spin-orbit model is completely analog to the non-driven scenario in the second order. The only difference from the non-driven model is a dressing of the already defined interactions. If we perform the calculation and projection into the $j = 1/2$, we end up with a Kitaev-Heisenberg model of the form

$$
\begin{aligned}
H_{\text{eff}}^F &= \sum_{\langle ij \rangle \in \alpha\beta(\gamma)} \left[J^\gamma(\omega, E_0, \epsilon, N) \mathbf{S}_i \mathbf{S}_j + K^\gamma(\omega, E_0, \epsilon, N) S_i^\gamma S_j^\gamma + \Gamma^\gamma(\omega, E_0, \epsilon, N) \right. \\
&\quad \left. \times (S_i^\alpha S_j^\beta + S_i^\beta S_j^\alpha) + \Gamma'^\gamma(\omega, E_0, \epsilon, N)(S_i^\alpha S_j^\gamma + S_i^\gamma S_j^\alpha + S_i^\beta S_j^\gamma + S_i^\gamma S_j^\beta) \right].
\end{aligned}
\tag{3.24}
$$

Here, the frequency and amplitude of the light as well as the Lissajous parameters N and ϵ alter the magnitude of the Heisenberg J, Kitaev K, Γ, and Γ' interaction. Except for CP, interactions additionally depend on the bond direction γ. While the Kitaev-Heisenberg model arguably has bond-independent interaction strengths under ideal circumstances (e.g., $K_x = K_y = K_z$), we can induce a bond anisotropy via light. This anisotropy is independent of external effects arising in experiments (like distortions,

impurities, etc.). If we write down the single interaction terms, we obtain

$$J^\gamma = \sum_{l=-\infty}^{\infty} \mathcal{J}_l^2(u_{ij}^\gamma) \frac{4}{27} \bigg\{ \left[-9t_4^{\gamma\,2} + 2(t_1^\gamma - t_3^\gamma)^2 \right]$$
$$\times \mathcal{A}_l(\omega, U, J_H) + (2t_1^\gamma + t_3^\gamma)^2 \mathcal{B}_l(\omega, U, J_H) \bigg\}, \tag{3.25}$$

$$K^\gamma = \sum_{l=-\infty}^{\infty} \mathcal{J}_l^2(u_{ij}^\gamma) \frac{4}{9} \left[(t_1^\gamma - t_3^\gamma)^2 - 3(t_2^{\gamma\,2} - t_4^{\gamma\,2}) \right] \mathcal{A}_l(\omega, U, J_H), \tag{3.26}$$

$$\Gamma^\gamma = \sum_{l=-\infty}^{\infty} \mathcal{J}_l^2(u_{ij}^\gamma) \frac{4}{9} \left[3t_4^{\gamma\,2} + 2t_2^\gamma(t_1^\gamma - t_3^\gamma) \right] \mathcal{A}_l(\omega, U, J_H), \tag{3.27}$$

$$\Gamma'^\gamma = -\sum_{n=-\infty}^{\infty} \mathcal{J}_n^2(u_{ij}^\gamma) \frac{4}{9} t_4^\gamma \left(t_1^\gamma - t_3^\gamma - 3t_2^\gamma \right) \mathcal{A}_l(\omega, U, J_H), \tag{3.28}$$

where γ denotes the bond directions and

$$\mathcal{A}_l(\omega, U, J_H) = g_{\mathrm{dh}}(U - 3J_H - l\omega) - g_{\mathrm{dh}}(U - J_H - l\omega) \tag{3.29}$$

$$\mathcal{B}_l(\omega, U, J_H) = g_{\mathrm{dh}}(U + 2J_H - l\omega) + 2g_{\mathrm{dh}}(U - 3J_H - l\omega). \tag{3.30}$$

Here we introduce the doublon-holon Green's functions for flavor f as

$$g_{\mathrm{dh},f} = \left\langle \Phi_f \left| \frac{1}{\mathcal{E}_f - l\omega + \hat{K}_f} \right| \Phi_f \right\rangle, \tag{3.31}$$

which can be directly inferred from (3.21) and (3.18). In (3.30)-(3.25), we assumed that the Green's functions for all states with the same energy $\mathcal{E}_f$ are identical, i.e. $g_{\mathrm{dh},f} = g_{\mathrm{dh},f'} = g_{\mathrm{dh}}(\mathcal{E}_f - l\omega)$ if $\mathcal{E}_f = \mathcal{E}_{f'}$. This allows for an expression of (3.30)-(3.25) with just three distinct Green's functions for $\mathcal{E}_S$, $\mathcal{E}_P$, and $\mathcal{E}_D$. We are aware that this is a simplification, but we believe that we can still describe the behavior close to resonances qualitatively well within this approximation, which is the goal of this thesis.

We note that the anisotropy of the interactions (3.30)-(3.25) can enter either via the Bessel functions via $u_{ij}(\omega, E_0, \varphi_\gamma) \to u_{ij}^\gamma$ or through the hopping parameters t^γ. The influence of the light field causes the former, while the latter is a product of external effects, e.g., lattice distortions.

Heisenberg interactions experience a unique influence of the light field as it is the only interaction depending on (3.30). Therefore, tuning of Heisenberg interactions respective to the remaining interactions is feasible. This is a promising sign because Heisenberg interactions prevent a KSL ground state [97].

It becomes evident that g_{dh} replaces the $1/\Delta\mathcal{E}$-terms of the non-driven Kitaev-Heisenberg model [34]. We can attribute this change to the introduction of the doublon-holon propagator $\hat{K}_m$ in Sec. 3.3. It is crucial to find a reasonable approximation of g_{dh}

Figure 3.3: Virtual hopping process of holes, depicted in white, under the influence of a light field. Like for time-independent perturbation theory, the kinetic Hamiltonian drives the excitation from a $d^5 d^5$ into a $d^4 d^6$ excitation on sites i and j. However, because the energy gap between those states is significantly larger than the hopping amplitude t^γ the hole immediately hops back to its initial site, which results in a virtual $d^5 d^5 \to d^4 d^6 \to d^5 d^5$ excitation. The influence of a light field periodic in time alters the hopping amplitude t^γ and the energy gap. Since the energy gap is now dependent on the driving frequency, the condition $t^\gamma \ll \mathcal{E}_f - l\omega$ does not hold for arbitrary ω, see [86].

to understand the Floquet-Kitaev-Heisenberg model and its limitations.

3.5 Approximations of the doublon-holon Green's function

An exact evaluation of the propagator $\hat{K}_f$ in the denominator of g_{dh} is impossible. In this section, we want to look at two approximations for $\hat{K}_f$, making g_{dh} analyzable.

3.5.1 Off resonance approximation

Considering only the fraction of g_{dh}, for $\mathcal{E}_f \approx l\omega$, the propagator becomes the dominant part of the denominator. In this regime, the light field causes a resonant excitation of doublon-holon pairs. *Vice versa* for a off-resonant light field $|\mathcal{E}_f - l\omega| \gg 0$, the propagator becomes negligible and we obtain

$$g_{\mathrm{dh}} = \left\langle \Phi_f \left| \frac{1}{\mathcal{E}_f - l\omega} \right| \Psi_f \right\rangle \approx \frac{1}{\mathcal{E}_f - l\omega} = \frac{1}{\epsilon}, \tag{3.32}$$

where we introduce $\epsilon = \epsilon_{f,l}(\omega) = \Delta\mathcal{E}_f - l\omega$ in order to simplify further calculations. In this approximation, g_{dh} becomes equivalent to the time-independent perturbation theory result (2.8). The distinct feature here is the ω dependency, describing the absorption/emission of l photons with energy ω (with $\hbar = 1$). Evidently (3.31), an external light field modifies the energy gap from the ground to the first excited state. However, as long as ω is off-resonant, the energy gap is still large enough to justify a perturbative treatment of H_{kin} without considering doublon-holon propagation. From now we refer to this approach as off resonance approximation (ORA). We display the light-mediated virtual hopping process for the ORA in Fig. 3.3. The strength of this virtual hopping process is affected by both frequency ω and amplitude E_0, while the denominator is just modified by ω.
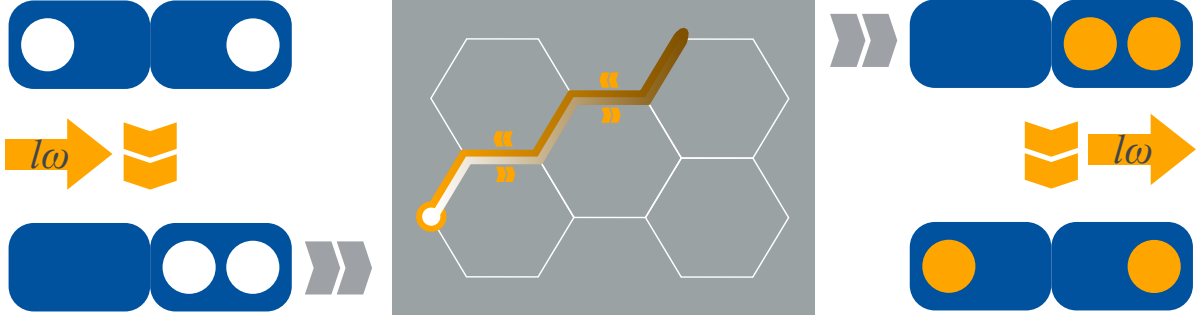
Figure 3.4: Displayed is the virtual hopping, with the consideration of retractable doublon-holon propagation within the excited subspace. The left-hand side displays the excitation of a doublon-holon pair mediated through the kinetic Hamiltonian in combination with the influence of the light. In the middle (gray shaded area), contrary to Fig. 3.3, we now consider possible propagations of the doublon/holon through the lattice. Here, we restrict ourselves to paths with the same starting and end point that do not form a closed loop. The restriction to these retractable paths has first been suggested by [98]. On the right-hand side, we depict the de-excitation of the doublon-holon pair back into the ground state mediated through the kinetic Hamiltonian and the light field.

3.5.2 Retractable path approximation

The $|\epsilon| \gg 0$ limitation of the ORA raises the questions "What happens at resonance?" and "What is off-resonance?". To tackle these problems, we consider the retractable path approximation (RPA) able to capture the interaction at/near resonance. With this approximation, we can also quantify the term "off-resonance". This approximation was first introduced by Brinkmann [98] in the context of NiO, dioxides, and sesquioxides. The RPA has already found application for $LaTiO_3$ and $YTiO_3$ [99]. In this thesis, we consider the RPA for d^5 transition materials. In the RPA, we can describe the parameter regime $|\epsilon| \approx 0$. In this case, the propagator is not negligible anymore, and we have to consider doublon-holon propagation within the excited subspace.

The base premise of the RPA is that the most dominant contribution to the propagation arises from paths of the doublon/holon ending up in the same state as the initial excited state with the same way away then back, see Fig. 3.4. If we assume an uncorrelated movement of doublons and holons, we can separate g_{dh} into a holon g_h and a doublon g_d function [93]. One can connect these two functions via the convolution integral

$$g_{dh}(\epsilon) = -i \int \frac{d\Omega}{2\pi} \underbrace{\langle h|_j \frac{1}{\Omega + \hat{K}_f} |h\rangle_j}_{g_h(\Omega)} \underbrace{\langle d_f|_i \frac{1}{\epsilon - \Omega + \hat{K}_f} |d_f\rangle_i}_{g_d(\epsilon - \Omega)}. \qquad (3.33)$$

The problem then reduces to a separate solution for the Green's functions for the holon

and the doublon. Henceforth, we only consider the holon Green's function. The solution
of the doublon Green's function can be derived completely analogue. As a first step we
expand $g_h(\Omega)$ in powers of $\hat{K}_f$, which gives rise to

$$g_\text{h}(\Omega) = \frac{1}{\Omega} \langle \Psi_0 | c_{j\beta\sigma}^\dagger \left[1 + \left(-\frac{\hat{K}_f}{\Omega} \right) + \left(-\frac{\hat{K}_f}{\Omega} \right)^2 + \left(-\frac{\hat{K}_f}{\Omega} \right)^3 + ... \right] c_{j\beta\sigma} | \Psi_0 \rangle . \qquad (3.34)$$

Since we only consider retractable paths, all odd-order terms in (3.34) can be neglected.
This yields

$$g_\text{h}(\Omega) = \frac{1}{\Omega} \langle h |_j \left[1 + \left(-\frac{\hat{K}_f}{\Omega} \right)^2 + ... \right] | h \rangle_j . \qquad (3.35)$$

As mentioned in [93, 98], one can solve this series via an ansatz of the form

$$g_\text{h}(\Omega) = \frac{1}{\Omega(1 - \Sigma(\Omega))}, \qquad (3.36)$$

where $\Sigma(\Omega)$ represents the self-energy. The derivation of the self-energy is then com-
pletely analogue to [98]. We start with the just considering paths going to the nearest
neighbors and back, for this $\Sigma(\Omega)$ trivially becomes $\Sigma^{(1)}(\Omega) = (zt_h^2)/(\Omega)$. Here, z is the
coordination number of the lattice, which counts the number of nearest neighbors, and
t_h describes the hopping strength of the holon. In our case, we have $z = 3$ because
we consider a hexagonal lattice. Here we make yet another simplification, namely that
we assume the same hopping strength t_h for the propagation of holons and all different
doublon flavors. This might be a significant restriction at first glance, but if we set
t_h to the maximum value of all propagations, we simply overestimate heating effects.
This is not dramatic because we want to identify frequencies where heating is, without a
doubt, absent and the ORA is valid. To estimate the maximal t_h, for which heating-free
driving is possible, we will keep t_h as a free parameter in our later calculations. For the
self-energy describing all paths, which include the next nearest neighbors, we have to
modify the denominator of $\Sigma^{(1)}(\Omega)$ (see [98]). We then obtain the self-energy

$$\Sigma^{(2)}(\Omega) = \frac{zt_h^2}{\Omega^2 \left(1 - \frac{(z-1)t_h^2}{\Omega^2} \right)}, \qquad (3.37)$$

where the factor $(z - 1)$ arises because we only consider paths going away from the
starting point. Therefore, the self energy formula, obtained in [98], for the nth nearest

neighbor becomes

$$\Sigma^{(n)} = \frac{z}{(z-1)} \underbrace{\frac{(z-1)t_h^2}{\Omega^2\left(1 - \dfrac{(z-1)t_h^2}{\Omega^2\left(1 - \dfrac{(z-1)t_h^2}{\Omega^2\left(1 - \dfrac{(z-1)t_h^2}{\Omega^2}\cdots\right)}\right)}\right)}}_{\Sigma_A(\Omega)}, \tag{3.38}$$

where we can define $\Sigma_A(\Omega)$ in a self-consistent manner

$$\Sigma^A(\Omega) = \frac{(z-1)t_h^2}{\Omega^2(1 - \Sigma^A(\Omega))}. \tag{3.39}$$

Solving (3.39) yields an exact expression for the self-energy

$$\Sigma^A(\Omega) = \frac{1}{2}\left[1 \pm \sqrt{1 - 4(z-1)\frac{t_h^2}{\Omega^2}}\,\right], \tag{3.40}$$

which we can plug into the holon Green's function,

$$g_{\mathrm{h}}(\Omega) = \frac{1}{\Omega\left(1 - \frac{z}{z-1}\frac{1}{2}\left[1 \pm \sqrt{1 - 4(z-1)\frac{t_h^2}{\Omega^2}}\right]\right)}. \tag{3.41}$$

As we have sown in Sec. 3.5.1, for large values of Ω the function should become $g_{\mathrm{h}}(\Omega) = 1/\Omega$. With this at hand, the relevant solution of (3.41) has to be the one with the negative sign. If we assume that the doublon-holon Green's function can derived in the same manner, we can write the convolution integral as

$$g_{\mathrm{dh}}(\epsilon) = -i\int \frac{\mathrm{d}\Omega}{2\pi} \frac{16}{\left(\Omega + 3\sqrt{\Omega^2 - 8t_h^2}\right)} \frac{1}{\left((\epsilon - \Omega) + 3\sqrt{(\epsilon - \Omega)^2 - 8t_h^2}\right)}. \tag{3.42}$$

Due to the square roots in the denominator of the second term, we have two branch cuts in the complex Ω-plane, as shown in Fig. 3.5. If we use Cauchy's theorem, we can deform the contour $(-\infty, \infty)$ into a contour around the $-\eta < \Omega < \eta$ branch cut, with $\eta = \sqrt{8}t_h$.

We have to distinguish the calculation of the integral around the branch cut for four different scenarios. In the first scenario, all values of the branch cut centered around ϵ (branch cut II) are strictly smaller than the ones of the branch cut centered around 0 (branch cut I) [Fig. 3.5(i)]. For the second case, displayed in Fig. 3.5 (ii), all values of branch cut II are strictly larger than the ones of branch cut I. In the other two cases, branch cut II overlaps with branch cut I. Here, we distinguish the cases displayed

(i) $\epsilon < -2\eta$ (ii) $\epsilon > 2\eta$

(iii) $-2\eta < \epsilon < 0$ (iv) $0 < \epsilon < 2\eta$
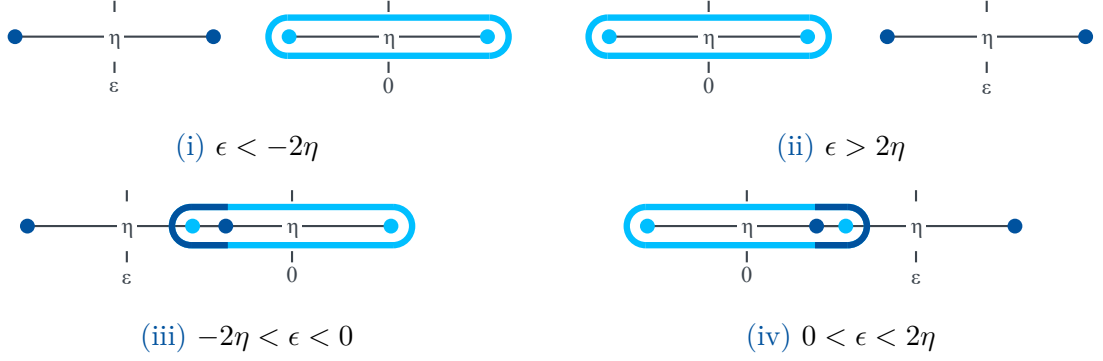
Figure 3.5: The two branch cuts arising in the doublon-holon Green's function g_{dh} are displayed for the four different scenarios that can arise. (i) The driving frequency is significantly larger than the energy difference between the ground state and doublon-holon excitation. In this case, the holon (light blue) and doublon (dark blue) branch cut do not overlap, the Green's function becomes real, and the RPA is comparable to the ORA. (ii) The energy gap $\mathcal{E}_f$ is significantly larger than the driving frequency, which leads to a scenario where the branch cuts do not overlap, and we thus obtain a real Green's function. (iii) and (iv) display the scenario where the energy gap and driving frequency are of comparable magnitude, with the driving frequency being slightly larger/smaller respectively. In this case, the holon and doublon branch cuts overlap, which leads to a complex contribution to g_{dh}. This imaginary part displays the heating due to doublon-holon propagation. In this range, the ORA is invalid and the description with the RPA becomes mandatory.

in Fig. 3.5(iii) and Fig. 3.5(iv). This approach was introduced in the supplemental material of [93], and we proceed in the same manner, with the only exception that we use $z = 3$ as well as omitting the introduction of the dimensionless energy $\tilde{E}$. The convolution integral (3.42) for the four different cases becomes

$$g_{\mathrm{dh}}^{(\mathrm{i})}(\epsilon) = \int_{-\eta}^{\eta} \frac{\mathrm{d}\Omega\, f(\Omega)}{\epsilon - \Omega - 3\left|\sqrt{(\epsilon - \Omega)^2 - \eta^2}\right|} \tag{3.43}$$

$$g_{\mathrm{dh}}^{(\mathrm{ii})}(\epsilon) = \int_{-\eta}^{\eta} \frac{\mathrm{d}\,\Omega f(\Omega)}{\epsilon - \Omega + 3\left|\sqrt{(\epsilon - \Omega)^2 - \eta^2}\right|} \tag{3.44}$$

$$g_{\mathrm{dh}}^{(\mathrm{iii})}(\epsilon) = \int_{-\eta}^{\epsilon+\eta} \frac{\mathrm{d}\Omega\, f(\Omega)}{\epsilon - \Omega - 3\left|\sqrt{(\epsilon - \Omega)^2 - \eta^2}\right|} + \int_{\epsilon+\eta}^{\eta} \frac{\mathrm{d}\,\Omega f(\Omega)}{\epsilon - \Omega - 3i\left|\sqrt{\eta^2 - (\epsilon - \Omega)^2}\right|} \tag{3.45}$$

$$g_{\mathrm{dh}}^{(\mathrm{iv})}(\epsilon) = \int_{-\eta}^{\epsilon-\eta} \frac{\mathrm{d}\,\Omega f(\Omega)}{\epsilon - \Omega + 3\left|\sqrt{(\epsilon - \Omega)^2 - \eta^2}\right|} + \int_{\epsilon-\eta}^{\eta} \frac{\mathrm{d}\,\Omega f(\Omega)}{\epsilon - \Omega + 3i\left|\sqrt{\eta^2 - (\epsilon - \Omega)^2}\right|} \tag{3.46}$$

where we used $f(\Omega) = 3\sqrt{\eta^2 - \Omega^2}/[\pi(9t_h^2 - \Omega^2)]$ and the indices i-iv denote the cases discussed in Fig. 3.5. Scenarios (iii) and (iv) have imaginary contributions. That means if the branch cuts have an overlap, the Green's function becomes imaginary. The imaginary

part of g_{dh} is an indicator for heating arising through doublon-holon propagation in the system. As we see, the condition for nonvanishing heating is $|\epsilon| < \eta$. This mainly depends on the strength of doublon-holon propagation in the excited subspace and the ratio of $\mathcal{E}_f$ and $l\omega$. Close to/at resonance $g_{\mathrm{dh}}(\epsilon)$ thus has major non-real contributions, indicating that for resonant driving, the system tends to heat up and lead to a breakdown of the Floquet formalism [93]. The advantage of the RPA is the capability to capture physics near the resonance and estimate criteria for the ORA. If one can determine t_h, it is consequently easy to conclude a strict condition for frequency ranges that do not lead to heating. Since the determination of t_h is not straightforward in the considered materials and exceeds the content of this thesis, we only treat it as a free parameter and evaluate it qualitatively. The RPA is a good starting point to determine frequency ranges where the ORA, which is easier and faster to evaluate, is a valid description.

4 Tuning possibilities in the J-K-Γ-Γ' model

In this chapter we study the influence of linear and circular polarized light on Kitaev-Heisenberg candidate materials. We consider both the RPA and ORA to derive an effective Floquet-Kitaev-Heisenberg Hamiltonian, introduced in Chap. 3. Via the RPA, we try to capture heating effects to obtain values for the frequency and amplitude of the light where driving with negligible heating is feasible. In these areas, we expect the ORA to be valid. Here, we analyze some of the most prominent materials α-RuCL$_3$, Na$_2$IrO$_3$, and α-Li$_2$IrO$_3$, with ab-initio parameters obtained from [33]. First, we focus only on the influence of linear polarized light with both fixed and arbitrary light angles. Here, we are mainly interested in the distinct influence of the light field on the three bond directions [80, 94]. Afterward, we study the influence of CP, where we primarily consider further NN interactions. Between further and NN interactions we expect a relative tunability for CP.

4.1 Heating

The RPA, introduced in Sec. 3.5.2, can capture heating effects at resonances arising due to doublon-holon propagation. Therefore, we can use this method to determine frequency and amplitude ranges where heating is negligible in the considered material. As potential candidates for the KSL, we focus on α-RuCL$_3$, Na$_2$IrO$_3$, and α-Li$_2$IrO$_3$. For these materials, there have been a multitude of ab initio studies that calculate the necessary parameters for our analysis. We take the hopping parameters t^γ from [33] and onsite parameters, U and J_{H}, for iridates and ruthenates from [100] and [69] respectively. We list the relevant parameters for this section in Tab. 4.1. For the RPA, the holon/doublon propagation t_{h} is kept as a free parameter.

Material	Na_2IrO_3	α-Li_2IrO_3	α-$RuCl_3$
U [eV]	1.7	1.7	3.0
J_H [eV]	0.3	0.3	0.6
t_1^z [meV]	33.1	55.0	50.9
t_2^z [meV]	264.3	219.0	158.2
t_3^z [meV]	26.6	-175.1	-154.0
t_4^z [meV]	-11.8	-124.5	-20.2
$t_1^{x/y}$ [meV]	38.8	76.3	45.4
$t_2^{x/y}$ [meV]	269.3	252.7	162.2
$t_3^{x/y}$ [meV]	-19.4	-108.8	-103.1
$t_4^{x/y}$ [meV]	-23.4	-9.3	-13.0

Table 4.1: Parameters for Na_2IrO_3, α-Li_2IrO_3, and α-$RuCL_3$. NN hopping parameters in meV are taken from [33]. Coulomb repulsion U and Hund's coupling in eV are taken from [100] for iridates and [69] for ruthenates.

ω_P^l	ω_D^l	ω_S^l
$(U - 3J_H)/l$	$(U - J_H)/l$	$(U + 2J_H)/l$

Table 4.2: Resonances for driven d^5 materials, in dependence of Hund's coupling J_H and Coulomb repulsion U. l denotes the number of absorbed (emitted) photons in the virtual hopping process.

With all parameters at hand we can now calculate Heisenberg J, Kitaev K, Γ, and Γ' interactions numerically [(3.25)-(3.28)]. We determine the imaginary and real interaction parts in dependency of the light frequency ω and amplitude E_0. As explained in Sec. 3.5.2, a nonzero imaginary part denotes heating arising from doublon-holon propagation. We expect heating around the resonances, arising from the possible excitation energies $\mathcal{E}_S$, $\mathcal{E}_P$, and $\mathcal{E}_D$ (Tab. 2.1). Possible resonances (Tab. 4.2) then depend on Coulomb repulsion U, Hund's coupling J_H and the number of emitted (absorbed) photons l [see (2.28)]. Therefore, for different materials, we expect different regions where heating is present. In addition to this, we observe that regardless of the material the Heisenberg interaction takes a unique role due to its dependence on (3.29) and (3.30). Other interactions just depend on (3.29) and will, from now on, be referred to as $\mathcal{A}$-interactions. Last but not least we want to stress that due to the $1/l$ dependency in ω_f^l, with $f \in \{P, D, S\}$ and the fact that the sum in (3.25)-(3.28) goes over $l \in \mathbb{Z}$, resonance frequencies condense at low ω. Therefore, we expect heating-free driving to be feasible at higher frequencies, where resonances are separated.

We start our analysis with fixed amplitudes at $E_0 = 7.5\,\mathrm{eV}/(ed)$ and LP parallel to the z-axis for the three candidate materials. It is of note that in this section we focus mainly on the behavior of the imaginary part and not so much on the ratio between the
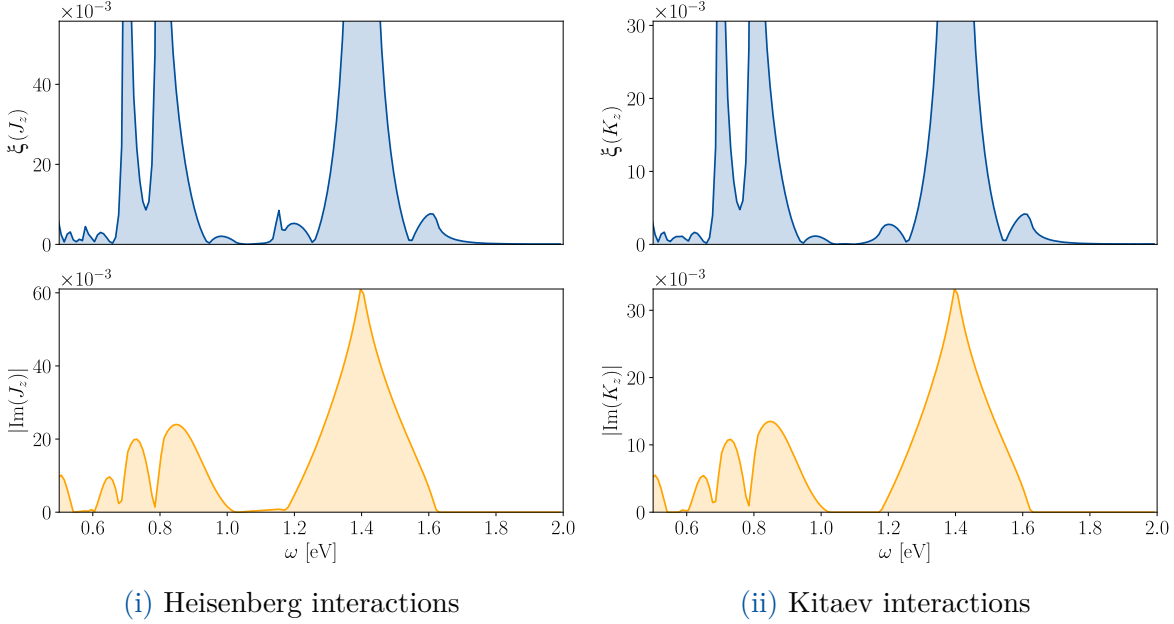
(i) Heisenberg interactions   (ii) Kitaev interactions
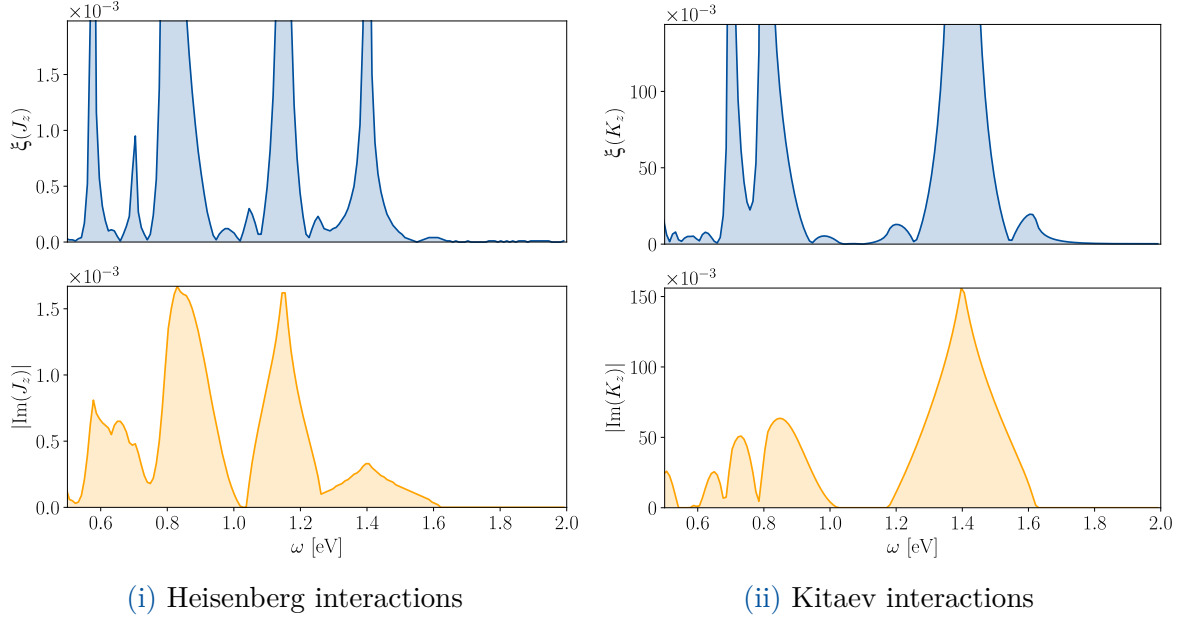
Figure 4.1: Difference between the real part of RPA and ORA (blue) and imaginary part of the RPA (orange) as indicator for heating effects displayed for Na_2IrO_3 at $E_0 = 7.5\,eV/(ed)$. Considered are the z bond Heisenberg (i) and Kitaev (ii) interactions.

single interaction terms, which we will discuss in more detail in Sec. 4.2. The imaginary part represents the heating effects that arise due to resonant driving. The investigation of these heating effects lays the foundation of the discussions in the following sections, as it yields information on how to choose heating-free driving frequencies.

4.1.1 Iridates

For both iridates, resonances are identical because Coulomb repulsion U and Hund's coupling J_H have the same magnitude (see Tab. 4.1). We display the results of the Heisenberg and the Kitaev interaction, representative for the $\mathcal{A}$-interactions, in z direction in Fig. 4.1 and Fig. 4.2. Here, we showcase the difference between the real part of the RPA and the ORA ξ as well as the absolute of the imaginary part. We find frequencies between the resonances $\omega_P^1 = 0.8\,eV$ and $\omega_D^1 = 1.4\,eV$ that yield heating-free driving for $\mathcal{A}$-interactions. From now on, we refer to this frequency range as driving corridor. However, it becomes obvious that due to the additional resonance at ω_S^l in the Heisenberg interaction, there is a resonance arising at $\omega_S^2 = 1.15\,eV$ in between ω_P^1 and ω_D^1, see, e.g., Fig. 4.1(i). This narrows down the driving corridor, where heating-free driving frequencies can be found, to a range of $0.8\,eV < \omega < 1.15\,eV$. Because the ORA neglects the doublon-holon propagation, the results diverge at the resonance points, causing a divergence in ξ. To evaluate where the ORA is valid we have to find areas where ξ is relatively small, which can be found within the driving corridor. Additionally, we also find a good agreement above the ω_D^1 resonance. From now on, these are the two

(i) Heisenberg interactions   (ii) Kitaev interactions

Figure 4.2: Difference between the real part of RPA and ORA (blue) and imaginary part of the RPA (orange) as indicator for heating effects displayed for α-Li$_2$IrO$_3$ at $E_0 = 7.5\,\mathrm{eV}/(ed)$. Considered are the z bond Heisenberg (i) and Kitaev (ii) interactions.

frequency ranges we focus on.

4.1.2 Ruthenates

For the ruthenate compound α-RuCl$_3$ Coulomb repulsion U and Hund's Coupling J_H are significantly larger than in the iridate compound (Tab. 4.1). An increase of Coulomb repulsion U leads to a shift of the resonances to higher frequencies, while the increase of Hund's coupling J_H yields a larger separation of the three resonance peaks (Fig. 4.3). This enhanced resonance splitting causes a broadening of the driving corridor, where the ORA can be valid. Like in iridates, the Heisenberg interaction has an additional resonance within the driving corridor, which arises at $\omega_3^2 = 2.1\,\mathrm{eV}$.

For the ruthenate, we define the driving corridor between $\omega = 1.2\,\mathrm{eV}$ and $\omega = 2.1\,\mathrm{eV}$, which is significantly larger than the driving corridor in iridates. We conclude that driving without heating in ruthenates appears more promising than in iridates due to the larger Hund's coupling J_H. Again, it is also possible to drive without heating above $\omega_D^1 = 2.4\,\mathrm{eV}$. This gives us two possible windows for Floquet engineering like in iridates.

4.1.3 Heating for arbitrary amplitudes

In the previous sections Sec. 4.1.1 and Sec. 4.1.2 we focused on heating effects for a fixed light amplitude $E_0 = 7.5\,\mathrm{eV}/(ed)$. In this section, we want to extend our investigations to arbitrary driving amplitudes E_0. To capture the most important findings we focus

(i) Heisenberg interaction   (ii) Kitaev interaction
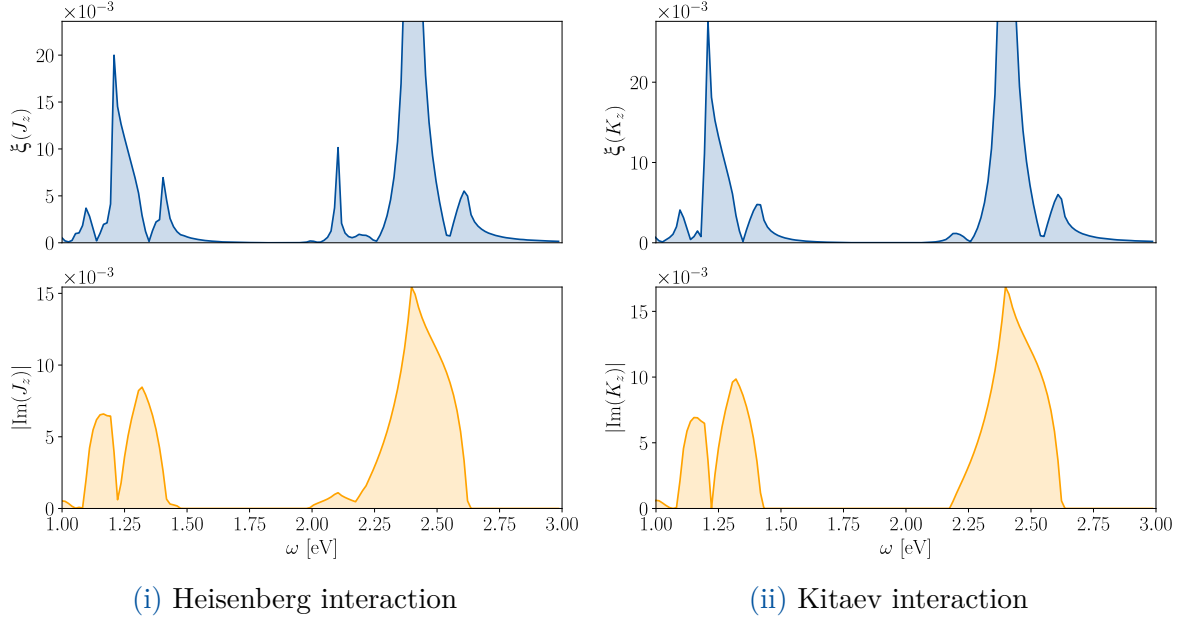
Figure 4.3: Difference between the real part of RPA and ORA (blue) and imaginary part of the RPA (orange) as indicator for heating effects displayed for α-RuCl$_3$ at $E_0 = 7.5\,\text{eV}/(ed)$. Considered are the z bond Heisenberg (i) and Kitaev (ii) interactions.

(i) Im(J_z) in Na$_2$IrO$_3$ (ii) Im(K_z) in Na$_2$IrO$_3$

(iii) Im(J_z) in α-RuCL$_3$ (iv) Im(K_z) in α-RuCL$_3$
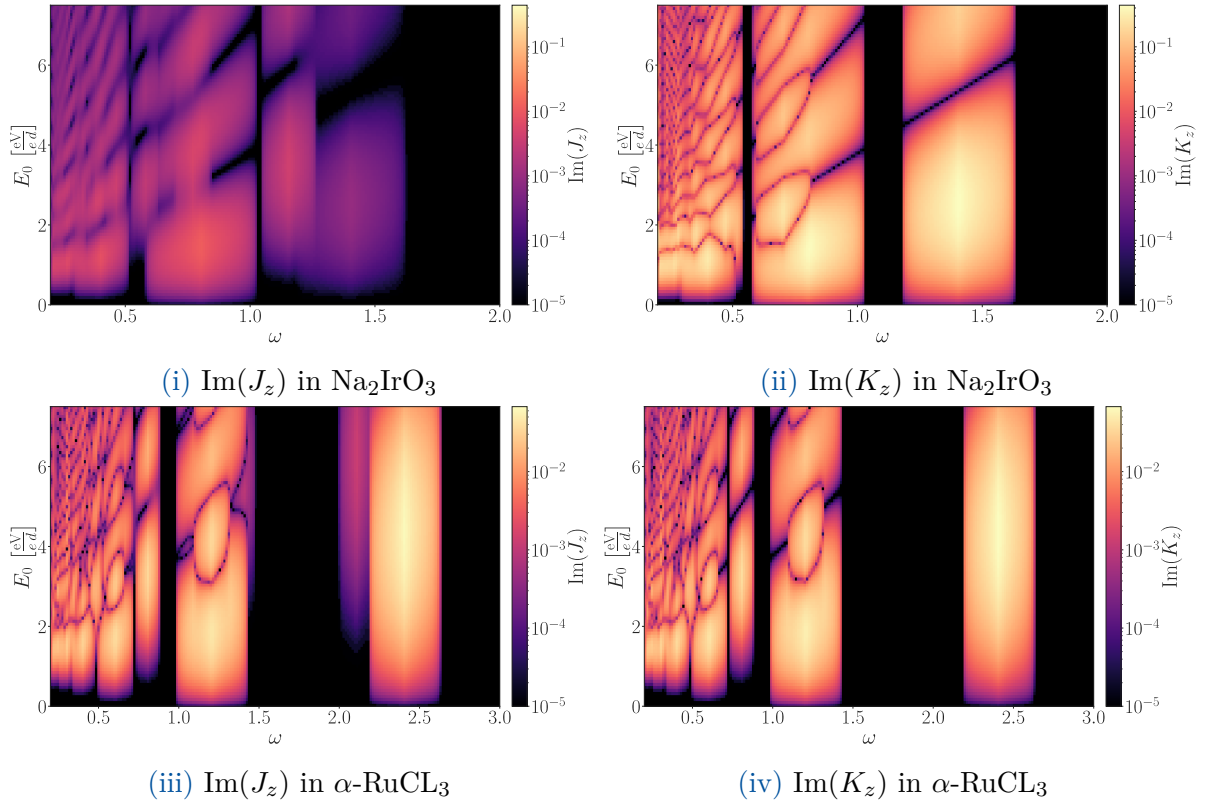
Figure 4.4: The absolute of the imaginary part, representative for the heating due doublon-holon propagation, calculated via the RPA is displayed for Na$_2$IrO$_3$ [(i) and (ii)] and α-RuCl$_3$ [(iii) and (iv)]. We present the z bond Heisenberg interactions in (i) and (iii). The z bond Kitaev interactions interactions, representative for all interactions $\propto \mathcal{A}$, are displayed in (ii) and (iv).

on z bond interactions, which have the strongest contributions of the ω_S^2 peak. This peak, as mentioned, plays a decisive role in determining regions where the ORA is valid because it narrows down the driving corridor. Additionally, we do not study Li_2IrO_3, because heating in iridates is very similar.

In Fig. 4.4 $|Im(K_z)|$, representative for the $\mathcal{A}$-interactions, is displayed for Na_2IrO_3 (ii) and α-$RuCl_3$ (iv). We observe that throughout the whole parameter range of E_0, there is no ω_S^2-heating peak, which arises from (3.30). The different width of the driving corridor for Kitaev interactions in ruthenates and iridates becomes obvious if we compare Fig. 4.4 (ii) and (iv). While in iridates with $t_h = 0.04\,eV$ we obtain a driving corridor of $\approx 0.2\,eV$, for ruthenates we get $\approx 0.8\,eV$. We want to stress that in our calculation the doublon/holon propagation rate t_h is kept as a free parameter, and $t_h = 0.04\,eV$ is the upper limit for t_h so that there is a nonzero driving corridor in all materials. Since $t_h = 0.04\,eV$ has a comparable magnitude as the hopping parameters (Tab. 4.1), we assume that a nonvanishing driving corridor should be feasible in all considered materials.

Looking at the Heisenberg interactions for iridates and ruthenates [Fig. 4.4(i) and (iii)], we observe the emergence of the ω_S^2-peak. As mentioned in Sec. 4.1.1 this narrows down the driving corridor to $\approx 0.04\,eV$ and $\approx 0.6\,eV$ in iridates and ruthenates respectively. Therefore, we set the frequencies where we apply the ORA to $\omega = 1.1\,eV$ and $\omega = 1.6\,eV$ for iridates and ruthenates.

With increasing E_0 the imaginary parts show an oscillating behavior, due to the dependence of the interactions on Bessel functions (3.4). The oscillation of the interactions (3.25)-(3.28) decreases with increasing driving frequency ω. One can explain this behavior with the $1/\omega$ dependence of the Bessel function. Since the driving corridor of iridates arises at lower driving frequencies due to smaller Coulomb repulsion present in these materials than in ruthenates, we expect a higher interaction frequency ν in iridates. As for the scenario with fixed E_0, heating is ubiquitous at low driving frequencies ω. Because of this, heating-free driving in this area is unreasonable independent of the driving amplitude E_0.

4.1.4 Influence of U and J_H

In this section, we explored the impact of Hund's coupling J_H and Coulomb repulsion U on the driving corridor. On the one hand, Hund's coupling determines the width of the driving corridor, i.e., the region where ORA can be valid. This is the case because J_H is responsible for the energy splitting of the excitation energies $\mathcal{E}_S$, $\mathcal{E}_P$, and $\mathcal{E}_D$ (see Tab. 2.1), which determine the possible resonance frequencies. Strong Hund's coupling causes a broadening of the driving corridor and, because of this, is a desirable feature for experiments. Therefore, α-$RuCl_3$ seems more suitable for Floquet engineering than the

(i) $\omega = 1.1\,\text{eV}$

(ii) $\omega = 1.91\,\text{eV}$
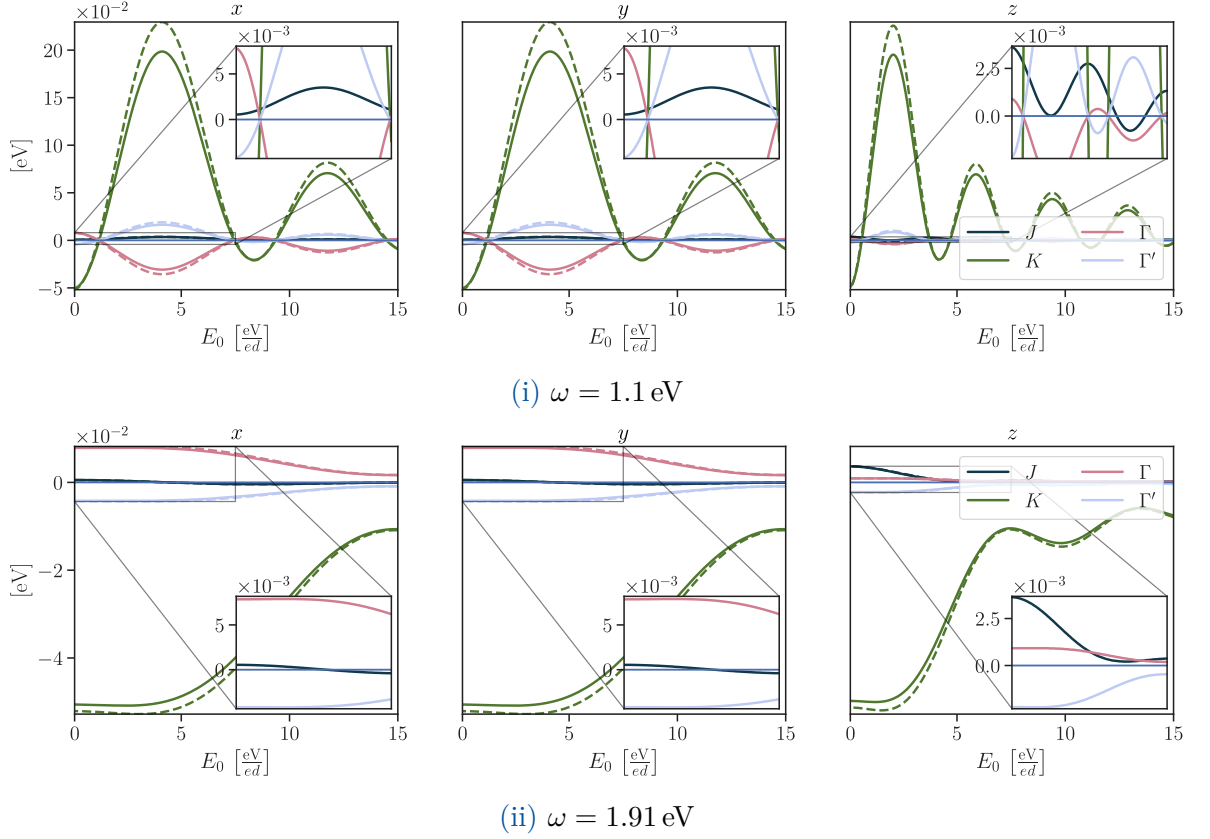
Figure 4.5: J, K, Γ, and Γ' interactions for Na_2IrO_3 in dependence of the driving amplitude E_0 between ω_P^1 and ω_D^1 (i) and above ω_D^1 (ii). Displayed are the results from the ORA (solid line) and the RPA (dashed line) for the three distinct bond directions.

investigated iridate compounds, if one desires to perform Floquet engineering between resonances. On the other hand, Coulomb repulsion U determines the location of the driving corridor. With increasing Coulomb repulsion the driving corridor gets shifted to higher driving frequencies. We will discuss the consequence of this shift in Sec. 4.2.

4.2 Linear Polarized light

In Sec. 4.1, we determined driving frequencies where the ORA can be valid. We found that for iridates $\omega = 1.1\,\text{eV}$ is suitable, while for the ruthenate compound we obtained $\omega = 1.6\,\text{eV}$. In this section, we study the behavior of the interactions relative to each other in more detail. To do so, we set the angle of the light parallel to the z bond and then investigate the interactions as functions of driving amplitude E_0.

4.2.1 Na_2IrO_3

The results for Na_2IrO_3 at $\omega = 1.1\,\text{eV}$ are displayed in Fig. 4.5(i). We observe that all interactions on each bond oscillate with varying E_0 due to the dependency on the Bessel

functions in (3.4). Furthermore, we notice that the z bond has a distinct E_0 dependency than the x and y bonds. This is due to the light angle, which enforces a faster oscillation of z bond interactions, i.e., E_0 dependency of interactions strongly depends on the light angle. If we look at the magnitude of the interactions, we observe dominant Kitaev interactions with significantly smaller J, Γ, and Γ' interactions. We note that with increasing E_0 one can switch the sign of all interactions. As a result of this, the ground state properties change. While a global change of sign is possible, a tuning relative in magnitude for the x and y bonds is possible for the Heisenberg interaction J, see inset Fig. 4.5(i). The reason for that is the contributions from the $\mathcal{B}$-term in the Heisenberg interaction, which has a ω dependence distinct from $\mathcal{A}$-terms. However, the $\mathcal{B}$-term contributions are small for these bond directions, due to the parameter setting of t_1 and t_3, see Tab. 4.1.

As we can see in (3.25) the strength of $\mathcal{B}$ is determined by $(2t_1 + t_3)$, which is almost zero for the x and y direction. Therefore, we observe a shift to $J \geq 0$ within the considered parameter range arising from the $\mathcal{B}$-term. The E_0 dependency of J also shows slightly distinct behavior than the $\mathcal{A}$-interactions.

This effect is far more prominent for the z bond as becomes evident in the inset of Fig. 4.5(i). Here t_1 and t_3 lead to a non-negligible contribution of $\mathcal{B}$, which consequently leads to tunability of the Heisenberg interaction relative to the other interactions. As we see in the inset of Fig. 4.5(i), this means that the Heisenberg interactions can be turned off, with the other interactions prevailing.

We, therefore, conclude that tuning of the Heisenberg interaction relative to the other interactions is, in principle, possible with hopping parameters optimized to enhance the unique feature of J, the $\mathcal{B}$-interaction (3.30). A global change of the sign and a change in magnitude is, in general, possible for all interactions when changing E_0.

After investigating the behavior within the driving corridor, we are now interested in the behavior of the interactions above the ω_2^1-resonance. We display the results for $\omega = 1.91\,\mathrm{eV}$ in Fig. 4.5(ii). Due to the $1/\omega$-dependence of the Bessel functions, interactions no longer show oscillations and are strongly suppressed with increasing E_0. As a result of this, we can not switch the sign for all bonds within the considered parameter range. For the z bond we again observe a distinct behavior for Heisenberg interactions. As becomes evident in the insets of Fig. 4.5(ii) the Heisenberg interaction is far more responsive to E_0 than the other interactions, meaning that for $0\,\mathrm{eV}/(ed) < E_0 < 5\,\mathrm{eV}/(ed)$ one can alter J while the other interactions remain almost constant. It is even possible to suppress J to such a degree that it is smaller than Γ and Γ' interactions. In addition to the distinct behavior on the z bond, we also observe that on the x and y bonds the $\mathcal{B}$-term induces a sign change. Hence, for frequencies above ω_2^1 in $\mathrm{Na_2IrO_3}$ $\mathcal{B}$-terms have a more pronounced effect than within the driving corridor. We still observe a more

(i) $\omega = 1.1\,\text{eV}$

(ii) $\omega = 1.91\,\text{eV}$
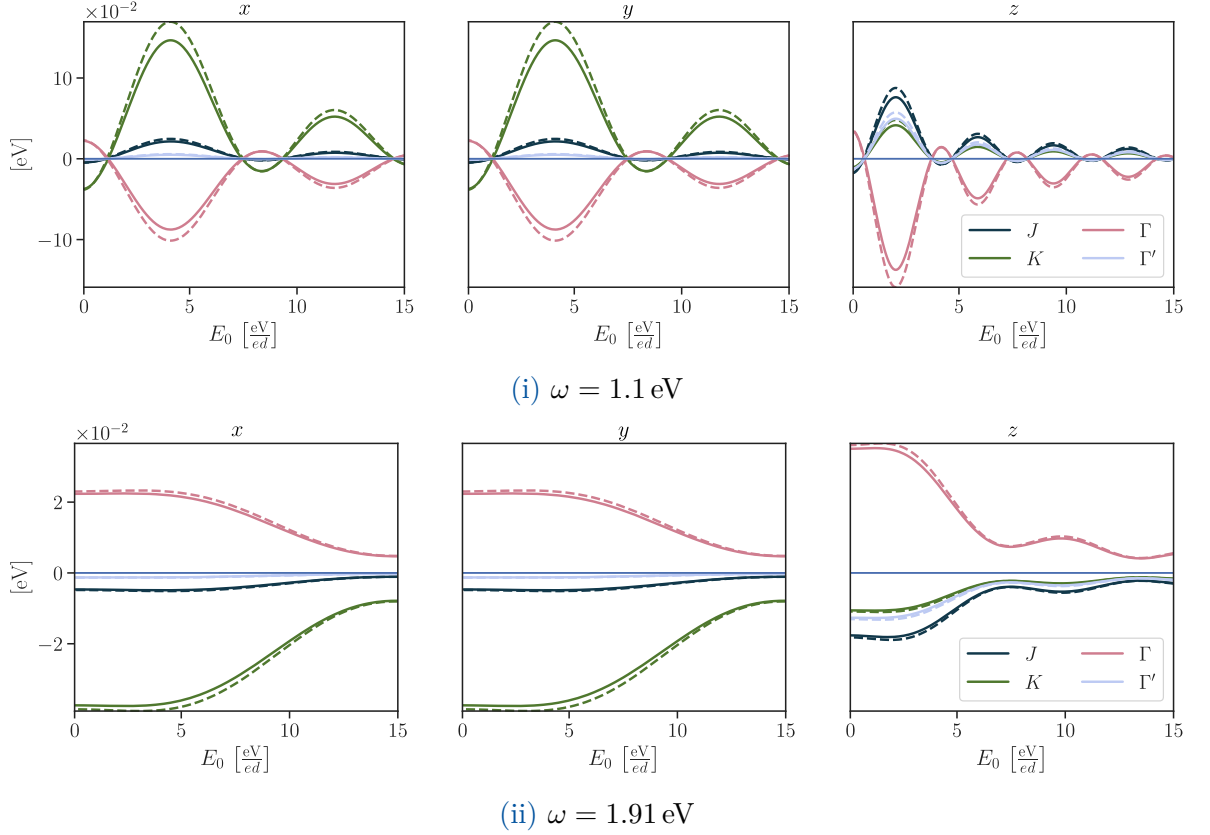
Figure 4.6: J, K, Γ, and Γ' interactions for α-Li$_2$IrO$_3$ in dependence of the driving amplitude E_0 between ω_P^1 and ω_D^1 (i) and above ω_D^1 (ii). Displayed are the results from the ORA (solid line) and the RPA (dashed line) for the three distinct bond directions.

noticeable effect of $\mathcal{B}$ on the z bond than on the x and y bonds. At $E_0 \approx 4\,\text{eV}/(ed)$, Heisenberg interactions on the x and y bonds vanish, while on the z bond J is strongly suppressed. This yields the possibility of almost turning off Heisenberg interactions in all bond directions via Floquet engineering. It is also notable that the difference E_0 dependence between z, x and y bonds at $\omega = 1.91\,\text{eV}$ is strongly reduced compared to the case within the driving corridor at $\omega = 1.1\,\text{eV}$.

Summarizing, we found that in Na$_2$IrO$_3$ we can tune both the magnitude and sign of the interactions present. If one is interested in changing the global sign of the interactions tuning within the driving corridor is suitable, with the drawback that the driving corridor in iridates might be hard to access experimentally. We also showed that the Heisenberg interaction takes a unique role in Floquet engineering because we can change it relative to the other interactions. For a bond-independent suppression of J interactions a driving frequency above ω_2^1 is desirable.

4.2.2 α-Li$_2$IrO$_3$

After investigating Na$_2$IrO$_3$, in this section, we study the other iridate candidate material α-Li$_2$IrO$_3$. Since Coulomb repulsion U and Hund's coupling J_H are expected to be the same as in Na$_2$IrO$_3$, we again investigate the E_0 dependency of the interactions at driving frequencies $\omega = 1.1\,\mathrm{eV}$ and $\omega = 1.91\,\mathrm{eV}$.

The results for $\omega = 1.1\,\mathrm{eV}$ are displayed in Fig. 4.6(i). Contrary to Na$_2$IrO$_3$ the bond anisotropy is sizable in α-Li$_2$IrO$_3$. While on the x and y bonds the Kitaev interactions are dominant, on the z bond the Γ interaction becomes dominant. We also note that, while Kitaev interactions are the strongest interactions on the x and y bonds, the Γ and J interactions are significantly larger than in Na$_2$IrO$_3$. Additionally, all interactions are almost perfectly in phase, including the Heisenberg interaction. Again, we can explain this by taking a look at t_1 and t_3, which in α-Li$_2$IrO$_3$ lead to a strong suppression of the $\mathcal{B}$ contributions. Therefore, tuning of the J interactions relative to the remaining interactions is impossible, and one is limited to switching signs via Floquet engineering. Like in Na$_2$IrO$_3$, with increasing E_0 we observe a decrease of interaction strength.

At $\omega = 1.91\,\mathrm{eV}$ [Fig. 4.6(ii)], we find a scenario comparable to Na$_2$IrO$_3$, where the oscillations of the interactions are suppressed to a point where none of the interactions change the sign. For the x and y bonds, all interactions remain constant up to $E_0 \approx 4\,\mathrm{eV}/(e \cdot d)$ and decrease in strength afterward. The important distinction to Na$_2$IrO$_3$ is, that the J interaction shows the same behavior as the $\mathcal{A}$-interactions. This makes suppression of J impossible. The orbital preserving hopping parameters t_1 and t_3 therefore play a crucial role in whether a material is susceptible to J suppression via Floquet engineering.

4.2.3 α-RuCl$_3$

In the ruthenate compound α-RuCl$_3$ the frequency within the driving corridor is chosen to $\omega = 1.6\,\mathrm{eV}$ and the frequency above ω_2^1 is set to $\omega = 2.9\,\mathrm{eV}$, due to larger Coulomb repulsion U and Hund's coupling J_H present in ruthenates (see Fig. 4.3).

In the case of driving within the driving corridor of α-RuCl$_3$ [Fig. 4.7(i)] the results are qualitatively comparable to α-Li$_2$IrO$_3$. Like for α-Li$_2$IrO$_3$ on the x and y bonds the Kitaev interaction is the strongest, closely followed by the Γ interaction with Heisenberg and Γ' interactions significantly weaker. For the z bond, the Kitaev interaction has the same magnitude as the Heisenberg interaction, both considerably smaller than the Γ interaction. This means that α-RuCl$_3$, like α-Li$_2$IrO$_3$, has strongly anisotropic lattice interactions. However, there are also clear distinctions to the iridate compounds. The Γ interaction is even stronger than in α-Li$_2$IrO$_3$, locating α-RuCl$_3$ even further away from the KSL in the J-K-Γ phase diagram. Furthermore, the higher driving frequency

(i) $\omega = 1.6\,\mathrm{eV}$

(ii) $\omega = 2.9\,\mathrm{eV}$
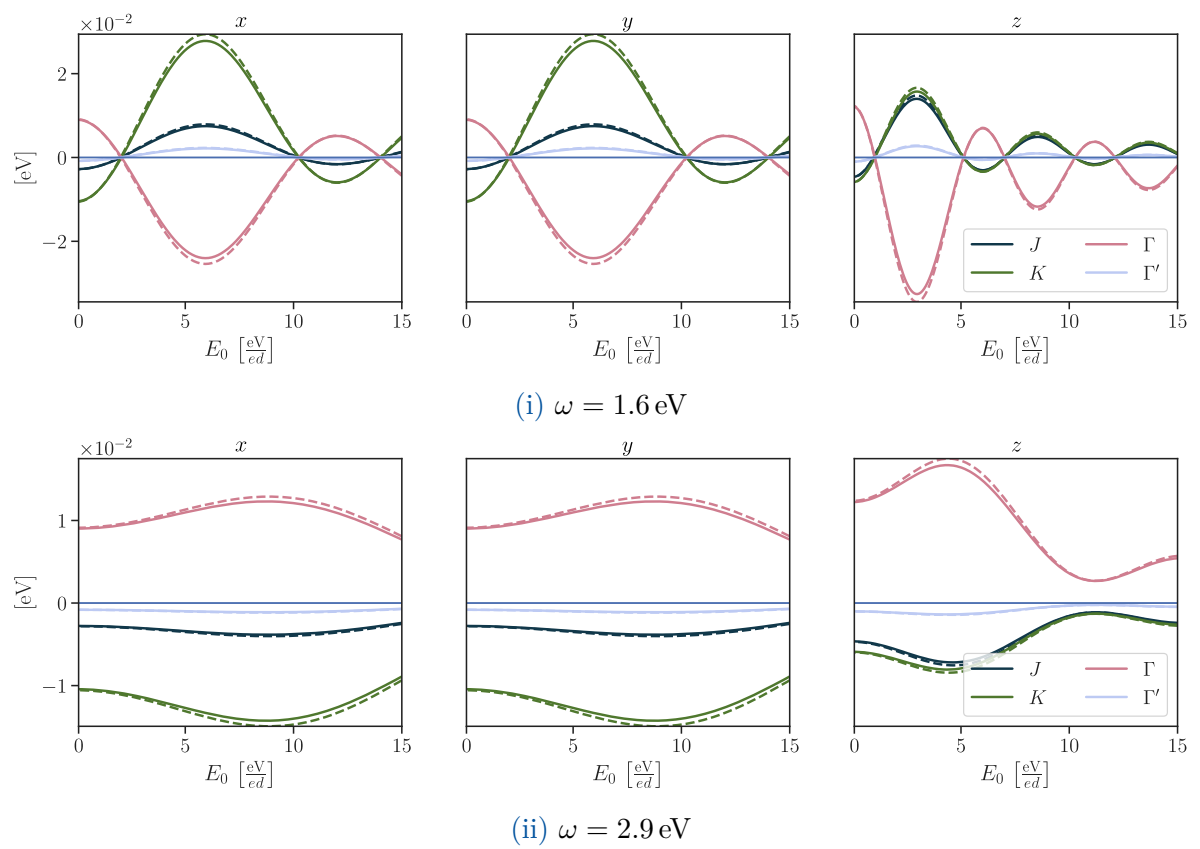
Figure 4.7: J, K, Γ, and Γ' interactions for α-RuCl$_3$ in dependence of the driving amplitude E_0 between ω_P^1 and ω_D^1 (i) and above ω_D^1 (ii). Displayed are the results from the ORA (solid line) and the RPA (dashed line) for the three distinct bond directions.

Material	Na_2IrO_3	α-Li_2IrO_3	α-$RuCl_3$
U [eV]	1.7	1.7	2.0
J_H [eV]	0.3	0.3	0.6
t_1^z [meV]	-9.3	-6.4	-8.2
t_2^z [meV]	-13.8	-13.5	-7.4
t_3^z [meV]	-36.8	-33.3	-39.5
t_4^z [meV]	16.6	16.6	11.7
$t_1^{x/y}$ [meV]	-8.4	-6.3	-7.7
$t_2^{x/y}$ [meV]	-12.7	-13.4	-7.8
$t_3^{x/y}$ [meV]	-35.3	-33.0	-41.4
$t_4^{x/y}$ [meV]	16.0	15.8	11.7

Table 4.3: Parameters for Na_2IrO_3, α-Li_2IrO_3, and α -$RuCL_3$. Third nearest neighbor (TNN) hopping parameters in meV are taken from [33]. Coulomb repulsion U and Hund's coupling J_H in eV taken from [100] for iridates and [69] for ruthenates.

at $\omega = 1.6$ eV, causes a slower oscillation of the interactions (see Sec. 4.1.3). Last but not least, if we look at the RPA results (dashed lines in Fig. 4.7), it becomes evident that the agreement between in ORA and RPA is far superior in the ruthenate than in the iridate compounds. The reason for that is, as mentioned in Sec. 4.1.2, the broader driving corridor. While in iridates the driving corridor is so narrow that, while heating-free driving is possible, a perfect agreement between ORA and RPA is impossible, in the ruthenate compound we can obtain almost identical results within the driving corridor. This is one of the main reasons ruthenates should be experimentally more suitable for Floquet engineering. Similar to α-Li_2IrO_3, the Heisenberg interaction can not be tuned concerning the other interactions, see Fig. 4.7.

Above the ω_D^1-resonance [Fig. 4.7(ii)] at $\omega = 2.9$ eV we observe an enhancement of all interactions for 0 eV$/(ed) < E_0 < 8$ eV$/(ed)$ for the x and y bonds and up to $E_0 \approx 4$ eV$/(ed)$ for the z bond. This is in contrast to the results of the iridates where the interaction strength stayed constant for small amplitudes E_0 instead of increasing. In ruthenates, one can increase the magnitude of all interactions compared to the starting interactions without a change of sign, throughout the considered parameter range. We therefore conclude that with Floquet engineering it is possible to increase the absolute magnitude of all interactions with changing sign (driving corridor) and without changing sign (above $\mathcal{E}_D$).

4.3 Circular polarized light

In Sec. 4.2 we focused on tuning NN interactions with LP and a fixed light angle parallel to the z bond. However, it has been shown [33] that further interactions than NN can

(i) Na$_2$IrO$_3$ (ii) α-Li$_2$IrO$_3$ (iii) α-RuCL$_3$
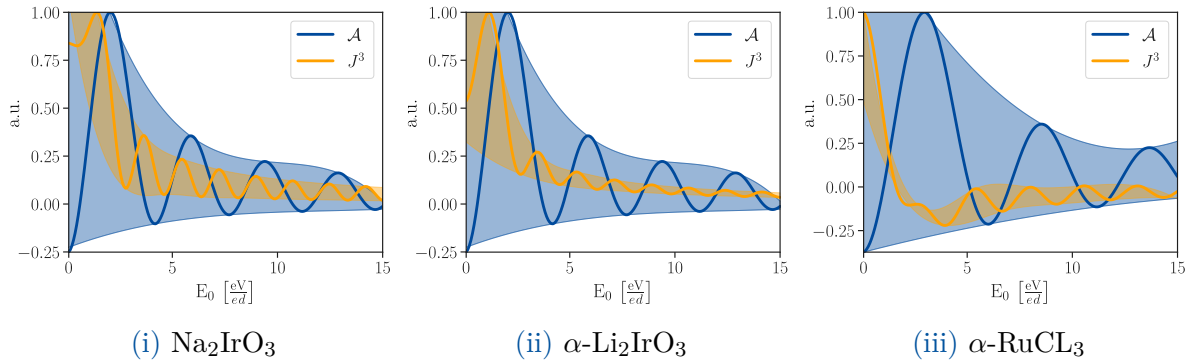
Figure 4.8: NN non-Heisenberg interactions $\mathcal{A}$ (blue) and TNN Heisenberg interactions J^3, normalized with their respective maximal value, are depicted for Na$_2$IrO$_3$ (i), α-Li$_2$IrO$_3$ (ii), and α-RuCl$_3$ (iii). For the iridates the driving frequency is set to $\omega = 1.1\,\mathrm{eV}$, for α-RuCl$_3$ to $\omega = 1.6\,\mathrm{eV}$.

play a decisive role in the nature of the ground state. In particular third nearest neighbor (TNN) Heisenberg interactions have been argued to be a major factor in forming the zig-zag ground state observed in the considered materials [101]. Therefore, in this section, we want to focus on Floquet engineering of the TNN Heisenberg interactions J^3.

Since we want to compare TNN and NN interactions, LP is not suitable due to its distinct effect on different bond directions. Hence, we need a polarization whose influence on the interactions is bond-independent. Hence, we consider CP, where, as shown in Sec. 3.3.2, the Bessel functions just depend on the absolute distance between the considered sites. The NNN hopping terms are obtained from [33], and summarized for all materials in Tab. 4.3. Recalling the condition for a tunability of the J^3 interactions concerning $\mathcal{A}$-interactions, i.e., a nonvanishing $(2t_1 + t_3)^2$, we see (Tab. 4.3) that a tuning in all materials should be possible. We show the results for all considered materials in Fig. 4.8. Here, we consider the NN $\mathcal{A}$-interactions, normalized with the respective absolute maximum in the considered parameter range (blue). The reason why we just investigate NN $\mathcal{A}$-interactions in this discussion is that the effect of $\mathcal{B}$-interactions for NN is rather small. The TNN Heisenberg interactions, normalized with their maximum value, are depicted in orange. For all materials, we set the driving frequency within the driving corridor, i.e., $\omega = 1.1\,\mathrm{eV}$ for iridates and $\omega = 1.6\,\mathrm{eV}$ for ruthenates. For all materials a strong suppression of the J^3 interactions compared to the $\mathcal{A}$-interactions is noticeable. This effect is particularly strong in the ruthenate compound, where J^3 interactions almost vanish even for weak amplitudes E_0. One can attribute the distinct E_0 behavior to the different absolute distances of NN and TNN, which consequently change the argument of the Bessel functions. As we can see, from (3.4) and Fig. 4.8, a higher distance increases the oscillation. It is important to note that because we are using CP, the influence on all bonds is equal, and therefore Heisenberg interactions get suppressed uniformly in all bond directions.
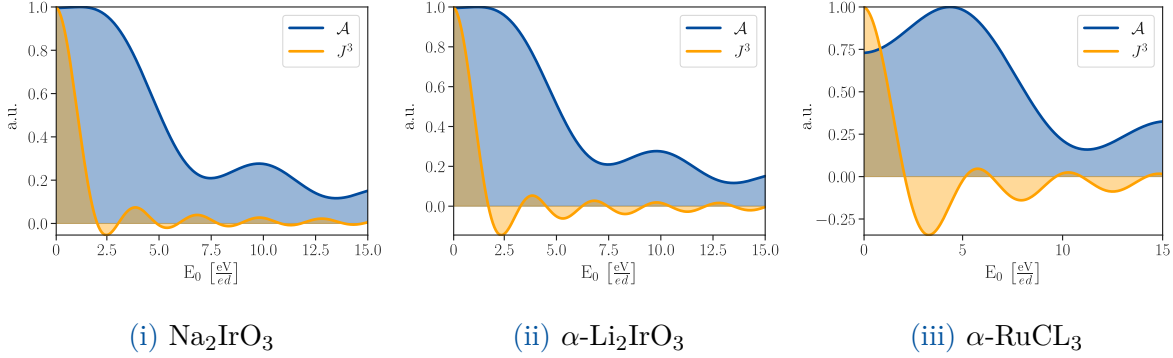
Figure 4.9: NN non-Heisenberg interactions $\mathcal{A}$ (blue) and TNN Heisenberg interactions J^3, normalized with their respective maximal value, are depicted for Na$_2$IrO$_3$ (i), α-Li$_2$IrO$_3$ (ii), and α-RuCl$_3$ (iii). For the iridates the driving frequency is set to $\omega = 1.91$ eV, for α-RuCl$_3$ to $\omega = 2.9$ eV.

Like in Sec. 4.2, we also consider frequencies above the $U - J_\mathrm{H}$ resonance, again we choose $\omega = 1.91$ eV for iridates and $\omega = 2.9$ eV for α-RuCL$_3$, see Fig. 4.9. We observe that above ω_D^1 the suppression of J^3 is even stronger than within the driving corridor. For the iridates, the $\mathcal{A}$ interactions stay constant for small E_0, like already shown in Sec. 4.2.1. Meanwhile, we see a considerable decrease of J^3 even for small E_0. For iridates, we can turn off J^3 interactions while keeping the NN $\mathcal{A}$-interactions at their initial value. For α-RuCl$_3$ the suppression of J^3 is accompanied by an enhancement of $\mathcal{A}$-interactions, like shown in Fig. 4.9. This makes the suppression of J^3-interactions in ruthenates even more pronounced than in iridates.

In this section, we showed that a suppression of TNN Heisenberg interactions is possible via Floquet engineering. This is a significant step in driving the system into a KSL because J^3 interactions are a hindering factor for the KSL in these materials. The reason for this tunability is rooted in the hopping parameters, where the direct hoppings t_1 and t_3 cause sizable $\mathcal{B}$ contributions for J^3 interactions.

4.4 Tuning with the light angle

Going back to LP, we want to investigate the influence of the polarization angle on the interaction parameters. In Sec. 4.2, we focused on the interactions for a fixed light angle at $\varphi = 0$, i.e., parallel to the z bond. Starting from there, we vary the light angle between $0 \leq \varphi \leq \pi$ for all considered materials and bond directions. We restrict ourselves to this parameter range because the dependence of the interactions on φ is π-periodic, see Fig. 3.2. This intuitively makes sense because a light angle of $\varphi = \pi$ describes essentially the same polarization as $\varphi = 0$. Again, we focus on the frequencies within the driving corridor, introduced in Sec. 4.1.3. The results for Na$_2$IrO$_3$, α-Li$_2$IrO$_3$, and α-RuCl$_3$ are displayed in Fig. 4.10, Fig. 4.11, and Fig. 4.12 respectively. We can identify two special

types of light angles for all materials.

First, each bond has a light angle, where the associated interactions decouple from the light field. At these light angles, the light angle is perpendicular to the bond direction, i.e., $\varphi = 5\pi/6$, $\varphi = \pi/6$, and $\varphi = \pi/2$ for the x, y, and z bond respectively. This decoupling consequently means that we can tune the remaining two bond interactions relative to the initial value of the decoupled bond. Therefore, it is possible to decrease the anisotropy in these materials via Floquet engineering. We can observe this, especially in α-RuCl$_3$ at $\varphi = \pi/2$, where we can manipulate x and y bonds K interactions in such a manner that they have the same strength as the formerly distinct z bond. It is important to clarify that increasing the isotropy of all interaction types simultaneously is not necessarily possible. As we see in Fig. 4.12, it is impossible to increase the isotropy of the Γ interaction in ruthenate. The reason for this is that, at $\varphi = \pi/2$, Γ_z is initially larger than $\Gamma_{x/y}$ and we can not increase $\Gamma_{x/y}$ in the considered parameter range. Following the rule of thumb that the initial z-interaction has to be smaller than the initial x/y-interaction to increase the isotropy, we see that for α-RuCl$_3$ we are just able to increase the isotropy of the K interaction at $\varphi = \pi/2$. Turning to iridates we observe that for Na$_2$IrO$_3$ a reduction of anisotropy is possible for Γ- and Γ'-interactions at $\varphi = \pi/2$. Meanwhile, the K interaction intrinsically is almost isotropic and Floquet engineering increases anisotropy. For α-Li$_2$IrO$_3$ (Fig. 4.11), the behavior is comparable to α-RuCl$_3$, where we are just able to decrease anisotropy of the K interactions.

The second type of unique light angle has a polarization parallel to one of the bond directions. This is, e.g., the light angle $\varphi = 0$, extensively discussed in Sec. 4.2. Here, the influence of the light is equal on the two bond directions not parallel to the polarization direction, with a distinct influence on the bond direction parallel to the polarization.

4.5 Tuning Kiteav interactions via light angle

As we have seen in the previous section the anisotropy of the interactions can be decreased with the help of Floquet engineering. In particular, the Kitaev interactions appear susceptible in α-Li$_2$IrO$_3$ and α-RuCl$_3$. To further investigate this effect, in this section, we focus on the ideal case that just Kitaev interactions are present in the materials, i.e., all materials are already in the KSL. To do so, we set all remaining interactions to zero and just study the Kitaev interactions. We then want to investigate the possibilities of Floquet engineering within the KSL phase.

The ground state of the pure Kitaev model can, in general, be divided into a gapped and gapless KSL [6]. The nature of the ground state strongly depends on the ratio of K_x, K_y, and K_z with the criterion for a gapped KSL $|K_\alpha| + |K_\beta| > |K_\gamma|$, with $\alpha, \beta, \gamma \in [x, y, z]$. Since this criterion strongly depends on the degree of anisotropy from
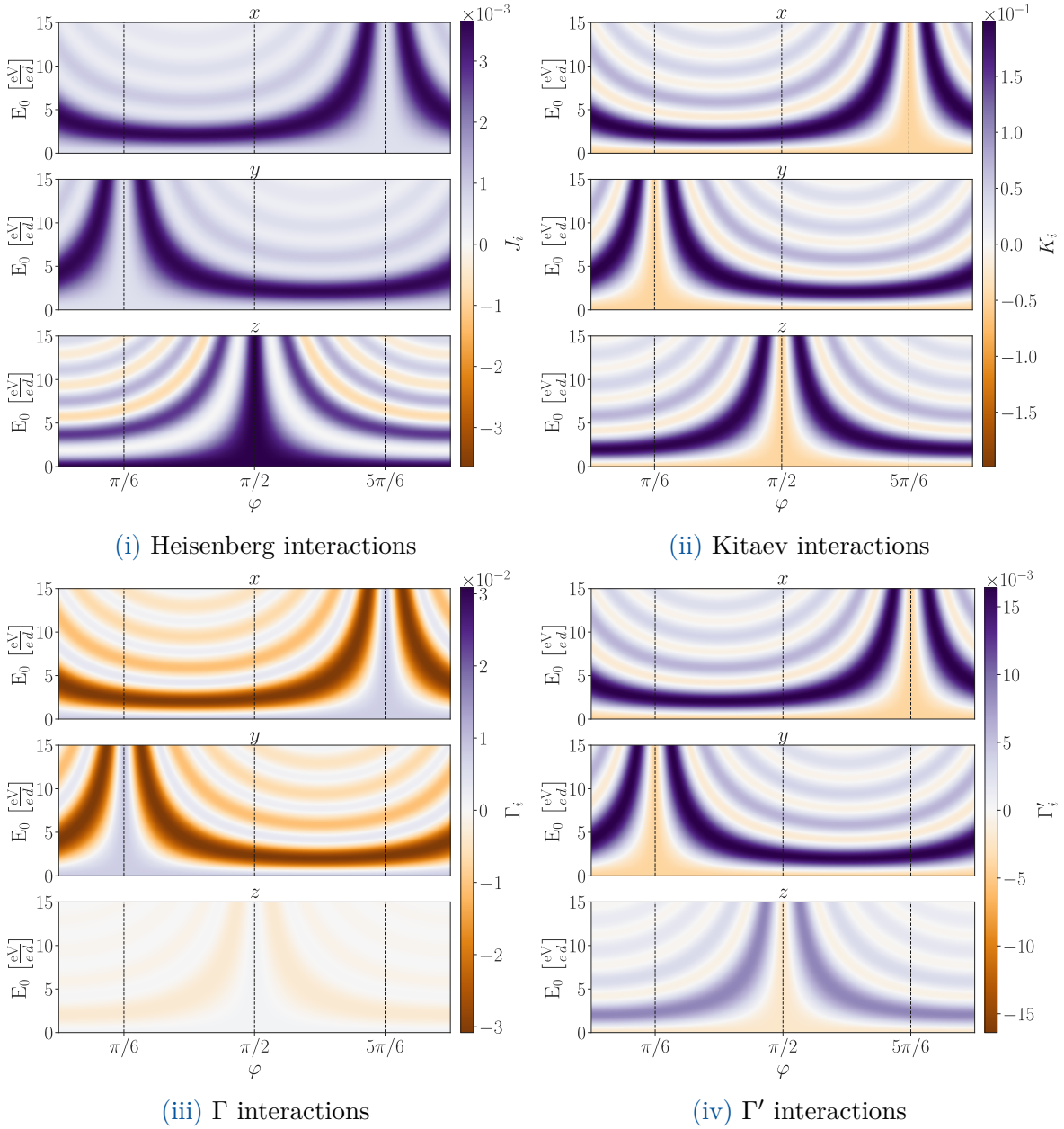
(i) Heisenberg interactions

(ii) Kitaev interactions

(iii) Γ interactions

(iv) Γ' interactions

Figure 4.10: J, K, Γ, and Γ' interactions for $\mathrm{Na_2IrO_3}$ for varied light angle φ and amplitude E_0. Driving frequency is fixed to $\omega = 1.1\,\mathrm{eV}$.
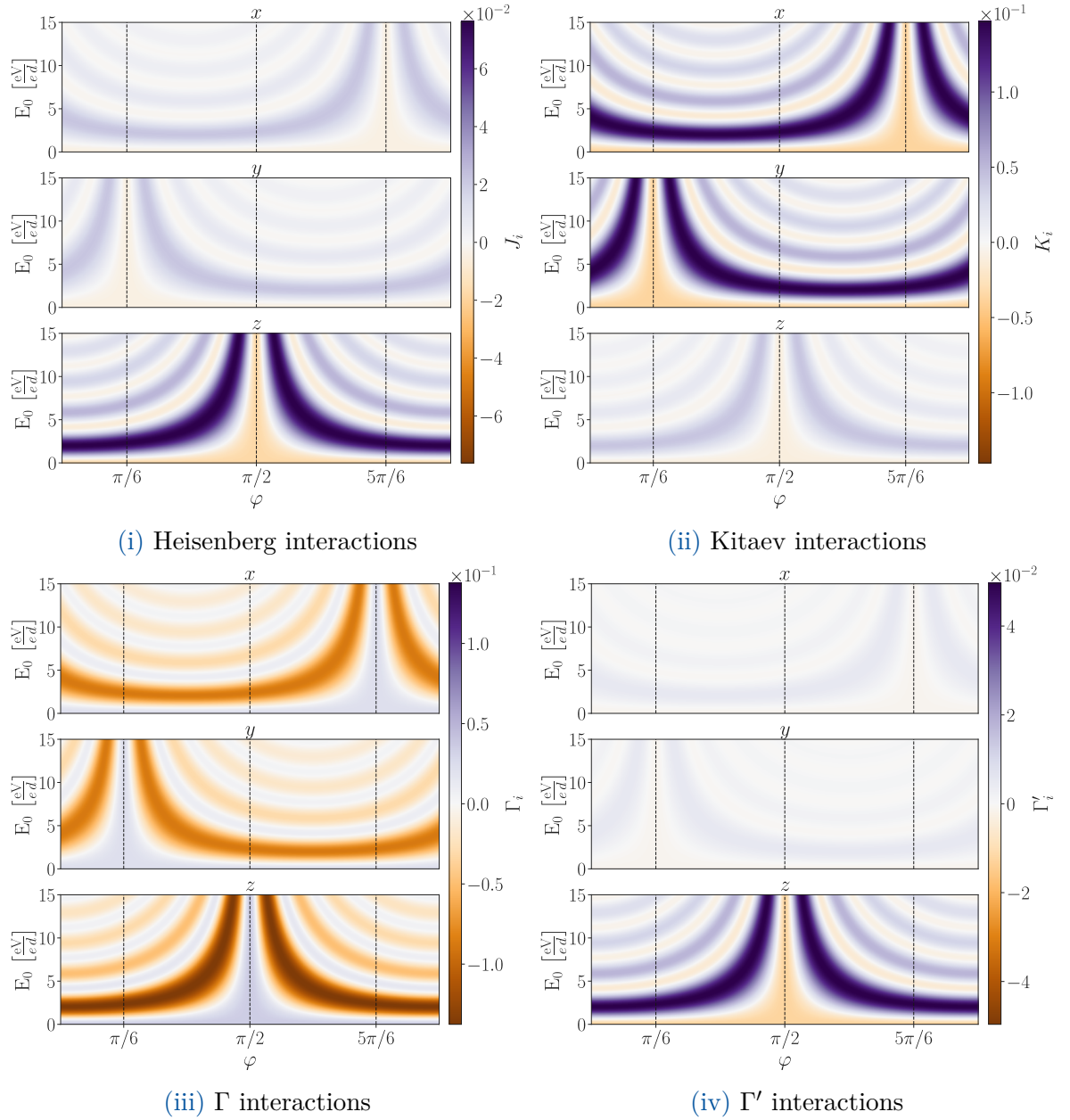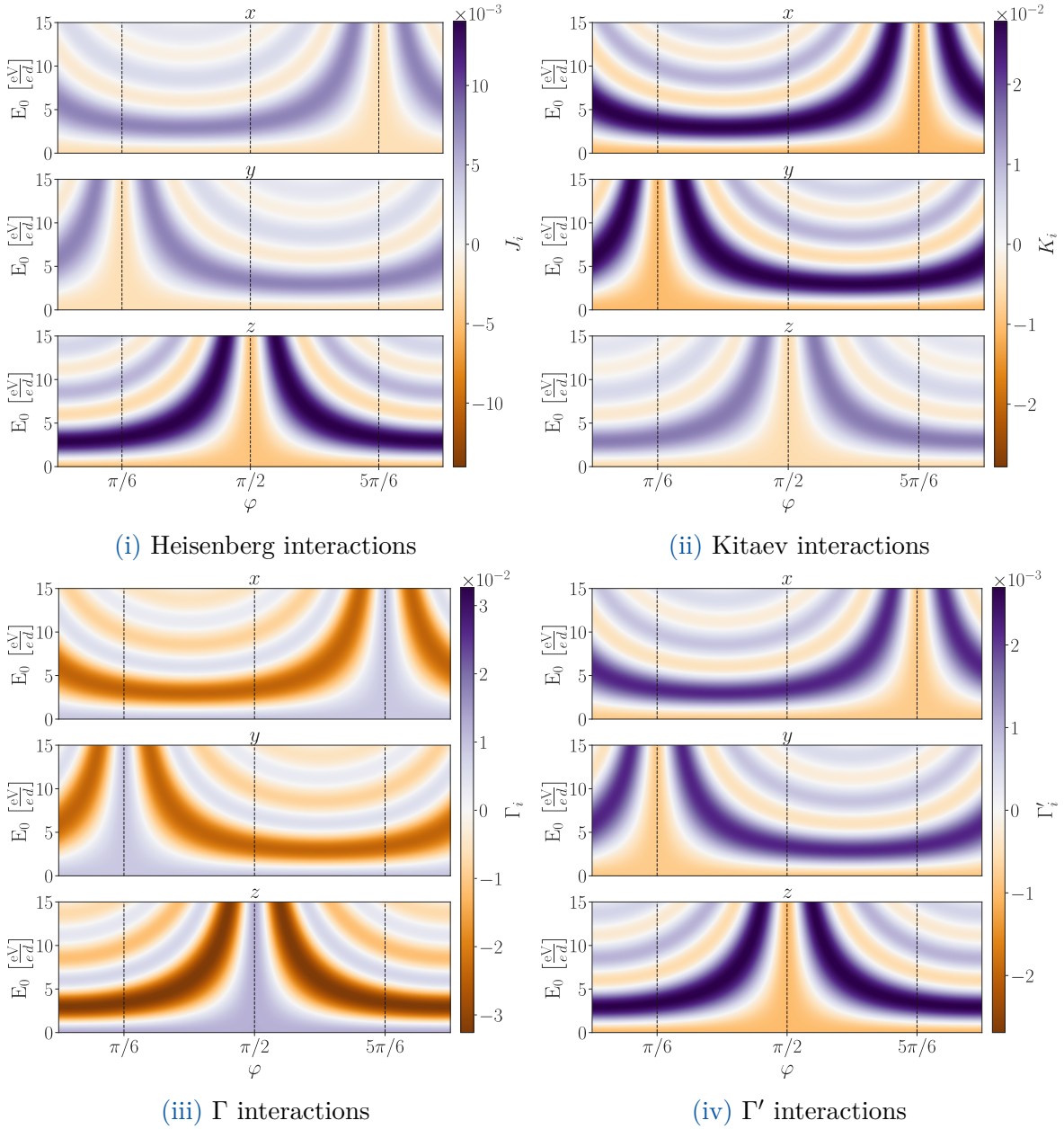
(i) Heisenberg interactions

(ii) Kitaev interactions

(iii) Γ interactions

(iv) Γ' interactions

Figure 4.11: J, K, Γ, and Γ' interactions for α-Li$_2$IrO$_3$ for varied light angle φ and amplitude E_0. Driving frequency is fixed to $\omega = 1.1\,\text{eV}$.

Figure 4.12: J, K, Γ, and Γ' interactions for α-RuCl$_3$ for varied light angle φ and amplitude E_0. Driving frequency is fixed to $\omega = 1.6\,\mathrm{eV}$.

the Kitaev interactions, one can easily imagine that a transition from a gapped to gapless KSL mediated by Floquet engineering and *vice versa* is possible. Additionally we also introduce a criterion for a gapless KSL with isotropic interactions $|K_\alpha - K_\beta| < 10^{-3}$ eV. Applying these conditions to the Kitaev interactions in dependency of the light angle and amplitude from Sec. 4.4, we obtain a phase diagram for all considered materials. The results are displayed in Fig. 4.13 for Na_2IrO_3, α-Li_2IrO_3, and α-$RuCl_3$. Considering the idealized case of just Kitaev interactions being present, all materials start in a gapless KSL. However, already for small amplitudes, gapped regions arise for all materials. Especially the idealized α-Li_2IrO_3 has large regions where a gapped KSL could arise.

For Na_2IrO_3 one observes that for $\varphi = \pi/6$, $\pi/2$, $5\pi/6$ the gapless KSL is more prevalent throughout the considered parameter range of E_0. The phase diagram obeys almost perfect $\pi/3$-periodicity in φ, due to the low anisotropy of Kitaev interactions in Na_2IrO_3. An increase of isotropy up to an isotropic interaction is impossible, as stated in Sec. 4.4. We observe that with increasing amplitude the areas for a gapless phase become narrower and it becomes more difficult to be in a "robust" gapless or gapped phase. This means that when probing this tuning experimentally smaller amplitudes would be advisable because here we expect broad areas of gapped and gapless KSLs.

For α-Li_2IrO_3 and α-$RuCl_3$ the $\pi/3$-periodicity reduces to a π periodicity due to the increased anisotropy in Kitaev interactions for these materials. We observe that for both materials the light angle where the gapless phase is relatively robust respective to E_0 is $\varphi = \pi/2$, i.e., orthogonal to the z-axis. This is a result of the findings in Sec. 4.4, namely that we can decrease the anisotropy of the Kitaev interactions if the light field decouples from the light field (Fig. 4.13). In α-$RuCl_3$ a decrease of the intrinsic anisotropy up to an isotropic phase [purple region in Fig. 4.13 (i)] is possible.

In conclusion, we found that Floquet engineering in a pure Kitaev model can change the ground state properties of the considered model by decreasing or increasing the anisotropy of the system. This opens up the possibility of driving systems formerly considered to be gapless KSL into a gapped KSL and *vice versa.* On the other hand, for materials already considered to be isotropic like, e.g., Na_2IrO_3, one has to pay special attention to amplitude E_0 and light angle φ to preserve the desired ground state.

(i) Na$_2$IrO$_3$ (ii) α-Li$_2$IrO$_3$ (iii) α-RuCl$_3$
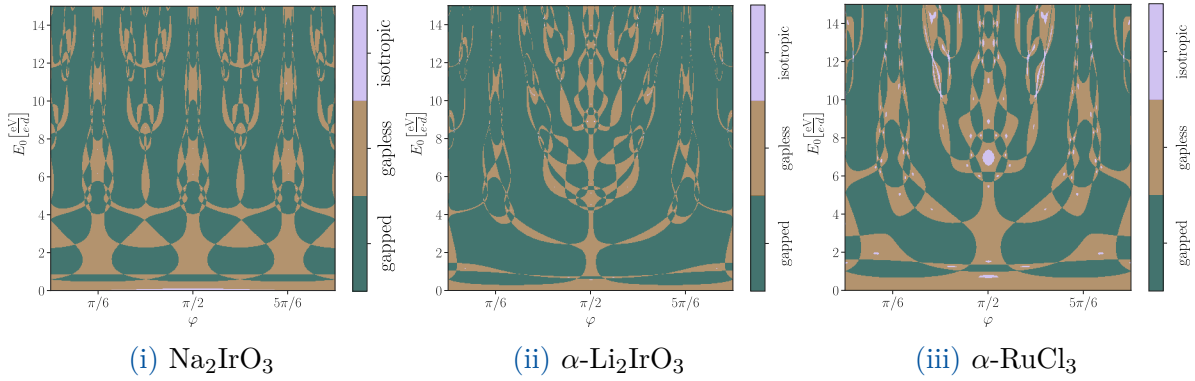
Figure 4.13: KSL phase diagram of Na$_2$IrO$_3$ (i), α-LiIrO$_3$ (ii) , and α-RuCl$_3$ (iii). Phases are determined with the criteria in the text (Sec. 4.5), under the assumption that just Kitaev interactions are present in the considered materials. The gapped KSL is depicted in green while the gapless and the isotropic KSL are depicted in brown and purple respectively.

5

High order effective Floquet-Hamiltonian

Chap. 3 and 4 solely focused on second-order perturbation theory. However, it has been shown that including ligand-mediated processes explicitly via higher-order perturbation theory can have a significant impact in Floquet engineering [31, 32, 89]. Therefore, in this chapter, we introduce ligand-mediated third and fourth-order terms for AP. We start by motivating the necessity of contributions up to the third and fourth order and derive an effective Floquet-Hamiltonian. In this process, we discuss new interactions arising from the inclusion of these high-order terms. Combining these results with the second-order results yields interaction terms, which include all important virtual hopping processes explicitly. We analyze these terms in dependency of ω, E_0, and ϵ for elliptical Lissajous figures. Last but not least, we extend or research to $N > 1$ to see whether the frequency multiplicity N changes interaction terms.

5.1 Why consider ligand contributions explicitly?

Conventionally, the Kitaev-Heisenberg model is derived with second-order perturbation theory in the hopping parameters introduced in Fig. 2.4 (see [1, 3, 34, 97] and Chap. 3). As we have already seen in Sec. 2.2, the t_2 hopping is distinct from the other hoppings as it is the only one including hopping processes via the p ligand atoms. Both the ligand hopping process t_{pd}^2/Δ_{pd}, with the charge transfer gap Δ_{pd}, as well as the direct d-d hopping $(t_{dd\pi} - t_{dd\delta})/2 \equiv t_{dd,2}$ describe an effective hopping between the d_{xz} and the d_{yz} orbital [Fig.5.1(i)]. While it is valid to express these two processes as one effective process t_2 in the model without a light field, this is no longer applicable in the light-driven case. The reason for this is that each hopping process now picks up a complex phase [Fig. 5.1(ii)], which depends on the direction of the bond. Therefore, each bond (d-d and
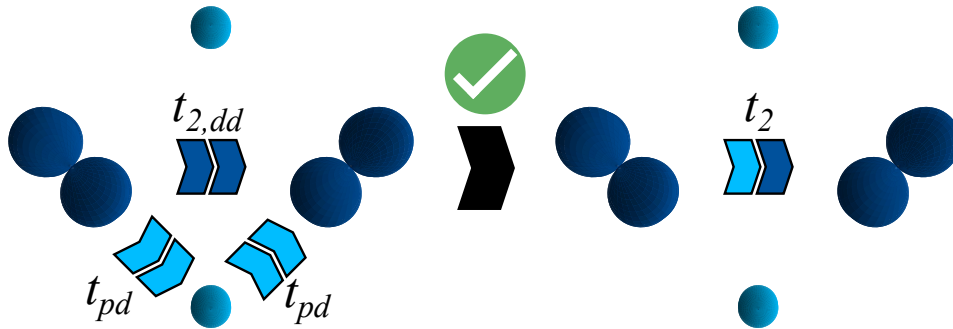
(i) Hopping processes between the d_{xz} and the d_{yz} orbital in the absence of a light field. Hopping via ligands (light blue arrows) and direct hopping (dark blue arrows) can be combined into one effective hopping process t_2 (light and dark blue arrows).
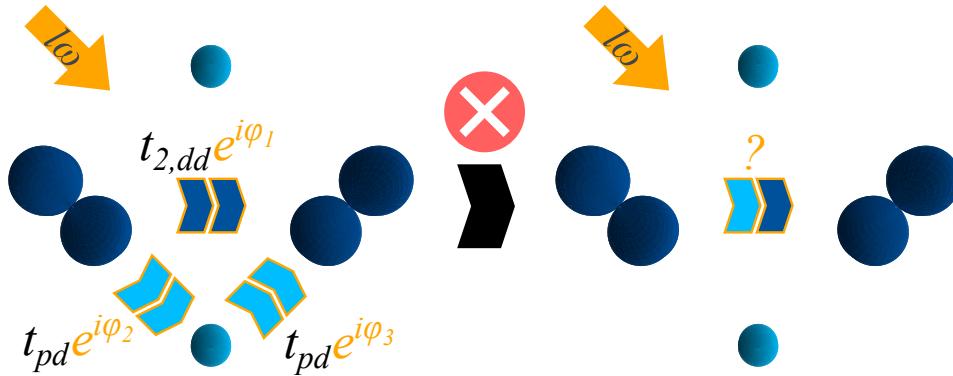
(ii) Hopping processes between the d_{xz} and the d_{yz} orbital in the presence of a light field (orange arrow). Each hopping process picks up a distinct phase φ_i. An expression of the ligand (light blue) and direct hopping (dark blue) processes via one effective hopping is no longer possible.

Figure 5.1: Ligand and direct hopping between adjacent d_{xz} and the d_{yz} orbitals in the absence (i) and presence (ii) of a light field.
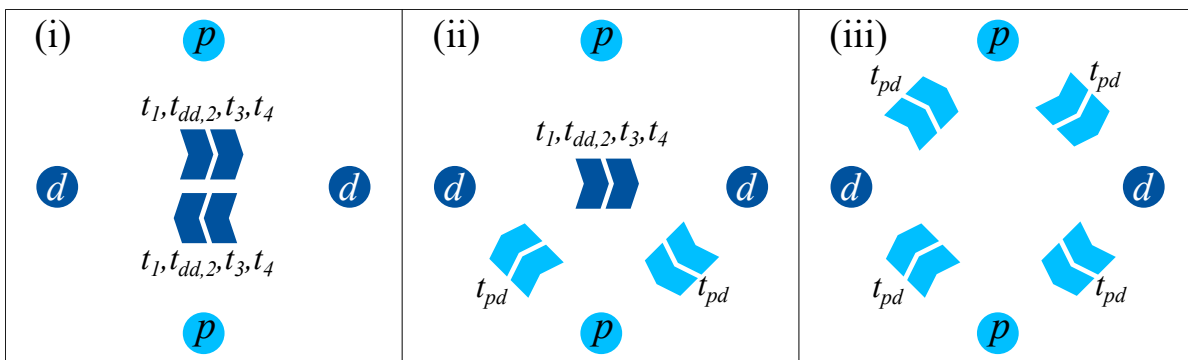
Figure 5.2: Possible hopping process between NN sites including ligands explicitly. Second order hopping $d \to d \to d$ (i), third order ligand hopping $d \to p \to d \to d$ (ii), fourth order ligand hopping $d \to p \to d \to p \to d$ (iii). Depicted third and fourth-order processes are examples of the respective process.

p-d) has a distinct dependence on the light field, which makes an explicit treatment of the ligand hopping process mandatory. Intuitively, this extends the spin-orbital model to third and fourth-order processes, which becomes evident if one inserts the explicit expression of t_2 in (3.26) yielding

$$(t_2)^2 = (t_{dd,2} + \frac{t_{pd}^2}{\Delta_{pd}})^2 = \underbrace{t_{dd,2}^2}_{\mathcal{O}(t^2)} + \underbrace{2t_{dd,2}\frac{t_{pd}^2}{\Delta_{pd}}}_{\mathcal{O}(t^3)} + \underbrace{\frac{t_{pd}^4}{\Delta_{pd}^2}}_{\mathcal{O}(t^4)}. \tag{5.1}$$

Possible hoppings are either $d \to d \to d$ [Fig. 5.2(i)], $d \to p \to d \to d$ [Fig. 5.2(ii)], or $d \to p \to d \to p \to d$ [Fig. 5.2(iii)]. It is important to note that the ligand-mediated hopping process t_{pd}^2/Δ_{pd} can be of comparable magnitude or even stronger than the direct hoppping processes $t_1, t_{dd,2}, t_3, t_4$. Therefore, there are significant third and fourth-order contributions to the Kitaev-Heisenberg interactions.

The consequence of including third-order terms explicitly is an inverse Faraday effect inducing an effective magnetic field within the model [31, 32, 102]. However, these results only consider a CP, and we thus want to extend these results to AP. With a general model, we then can study the fallout for both LP and CP and analyze the changes third-order terms induce for both limiting cases. In addition, we can investigate whether a more unconventional polarization leads to interesting interactions within the Kitaev-Heisenberg model.

Already in the absence of a light field, fourth-order ligand hopping processes are implicitly included in the Kitaev term (3.26) via t_2, see (5.1). That means a neglection of fourth-order terms, like in [31], does not yield an accurate Kitaev interaction strength. Therefore, it is crucial to include these terms in the calculations. In this chapter, we derive fourth-order terms under the influence of a light field. Combining these results with the lower-order terms, we can capture all significant light-induced effects in the Kitaev-Heisenberg model.

5.2 Third order effective Floquet-Hamiltonian

To derive third-order terms, we have to perform perturbation theory of the form

$$H_{\text{eff}}^F = \sum_{l,m} \sum_{\beta,\alpha} \frac{H_{\text{kin}}^{-l-m} |\Psi_\alpha^d\rangle \langle\Psi_\alpha^d| H_{\text{kin}}^m |\Psi_\beta^p\rangle \langle\Psi_\beta^p| H_{\text{kin}}^l}{(\mathcal{E}_\alpha + (m+l)\omega)(\Delta_{pd} + l\omega)}, \tag{5.2}$$

where l is the number of photons absorbed in the first hopping process and m in the second hopping process similar to (2.28). Since at the end of the virtual process, no photons are allowed the third process has to emit the photons absorbed in the first two processes H_{kin}^{-l-m}. Two different processes can have the same denominator. The first one

absorbs l photons in the $d \to p$ and m photons in the $p \to d$ process and emits $m + l$ photons in the $d \to d$ process. The second one absorbs $m + l$ in the $d \to d$ process, emits m photons in the $d \to p$, and l photons in the $p \to d$ process. Both of these virtual hoppings lead to intermediate energies of $\mathcal{E}_\alpha + (m + l)\omega$ and $\Delta_{pd} + l\omega$.

We can decompose the kinetic Hamiltonian in a part, which describes from Ru-atoms to the ligand O-atoms, and a part, which captures the hopping between Ru-atoms $H_{\text{kin}} = H_{dd} + H_{pd}$. With these considerations we can rewrite (5.2) to

$$H_{\text{eff}}^F = \sum_{l,m} \sum_{\beta,\alpha} \frac{\left(H_{dd}^{-l-m} P_{d,\alpha} H_{pd}^m P_{p,\beta} H_{pd}^l\right) + \left(H_{pd}^{-l} P_{p,\alpha} H_{pd}^{-m} P_{d,\beta} H_{dd}^{l+m}\right)}{\mathcal{E}_{l+m}^\alpha(\omega)\mathcal{E}_l^{\Delta_{pd}}(\omega)}, \tag{5.3}$$

with $\mathcal{E}_l^\alpha(\omega) = \mathcal{E}_\alpha + l\omega$, $\mathcal{E}_l^{\Delta_{pd}}(\omega) = \Delta_{pd} + l\omega$, and the projectors P on the subspaces $|\Psi_\alpha^d\rangle$ and $|\Psi_\beta^p\rangle$. The formula used in [31] to determine third-order terms neglects hoppings of the form $d \to d \to p \to d$. That leads to significant changes in the interaction terms derived. Using the projection onto $j = 1/2$ from [31], we obtain the following matrix elements

$$J = 2\,\text{Re}\left(\left\langle \frac{1}{2}, -\frac{1}{2}\middle| H_{\text{eff}}\middle| -\frac{1}{2}, \frac{1}{2}\right\rangle\right) \tag{5.4}$$

$$D = 2\,\text{Im}\left(\left\langle \frac{1}{2}, -\frac{1}{2}\middle| H_{\text{eff}}\middle| -\frac{1}{2}, \frac{1}{2}\right\rangle\right) \tag{5.5}$$

$$h = \frac{1}{2}\left(\left\langle \frac{1}{2}, \frac{1}{2}\middle| H_{\text{eff}}\middle| \frac{1}{2}, \frac{1}{2}\right\rangle - \left\langle -\frac{1}{2}, -\frac{1}{2}\middle| H_{\text{eff}}\middle| -\frac{1}{2}, -\frac{1}{2}\right\rangle\right) \tag{5.6}$$

$$K = \left\langle \frac{1}{2}, \frac{1}{2}\middle| H_{\text{eff}}\middle| \frac{1}{2}, \frac{1}{2}\right\rangle + \left\langle -\frac{1}{2}, -\frac{1}{2}\middle| H_{\text{eff}}\middle| -\frac{1}{2}, -\frac{1}{2}\right\rangle - 2\left\langle -\frac{1}{2}, \frac{1}{2}\middle| H_{\text{eff}}\middle| -\frac{1}{2}, \frac{1}{2}\right\rangle - J \tag{5.7}$$

$$\Gamma = -2\,\text{Im}\left(\left\langle \frac{1}{2}, \frac{1}{2}\middle| H_{\text{eff}}\middle| -\frac{1}{2}, -\frac{1}{2}\right\rangle\right) \tag{5.8}$$

$$\mu = 2\,\text{Re}\left(\left\langle \frac{1}{2}, \frac{1}{2}\middle| H_{\text{eff}}\middle| -\frac{1}{2}, -\frac{1}{2}\right\rangle\right). \tag{5.9}$$

As expected, there are finite contributions for a magnetic field h arising from the inverse Faraday effect [103] and contributions for J, K, and Γ. However, we find two new interactions, distinct from the former interactions, which we define as D and μ. As we will see later, these interactions vanish in the limes of CP, which is why they have not been reported yet. Calculating these matrix elements then yields the effective extended Kitaev-Heisenberg Hamiltonian

$$H_{\text{eff}}^3 = \sum_{\gamma,\langle i,j\rangle_\gamma} J_\gamma^3 \mathbf{S}_i \mathbf{S}_j + K_\gamma^3 S_i^\gamma S_j^\gamma + \Gamma_\gamma^3\left(S_i^\alpha S_j^\beta + S_i^\beta S_j^\alpha\right)$$
$$+ D_\gamma^3 \mathbf{e}_\gamma\left(\mathbf{S}_i \times \mathbf{S}_j\right) + \mu_\gamma^3\left(S_i^\alpha S_j^\alpha - S_i^\beta S_j^\beta\right) + h_\gamma^3\left(S_i^\gamma + S_j^\gamma\right) \tag{5.10}$$

which in addition to the Kitaev-Heisenberg interactions (KHI) J, K, and Γ has light

induced interactions (LI) h, D and μ. The physical interpretation of D and μ in (5.10) arises from a projection of the respective matrix element into the spin-1/2 basis

$$\frac{1}{2i}\left(S_i^- S_j^+ - S_i^+ S_j^-\right) = (\mathbf{S}_i \times \mathbf{S}_j)_z = S_i^x S_j^y - S_i^y S_j^x \tag{5.11}$$

$$\frac{1}{2}\left(S_i^+ S_j^+ + S_i^- S_j^-\right) = S_i^x S_j^x - S_i^y S_j^y. \tag{5.12}$$

D (5.11) has a Dzyaloshinskii–Moriya form and breaks inversion symmetry while μ (5.12) induces further anisotropies. Both these interactions preserve time-reversal symmetry. That is the opposite behavior of h, which breaks time-reversal symmetry (but keeps inversion symmetry intact). Since we know that CP preserves inversion symmetry, we expect μ and D to vanish for CP. With this, we can now derive the expression for the interaction terms in (5.10) expressed as functions of Coulomb repulsion U, Hund's coupling J_H, hopping strengths, and excitation energies $\mathcal{E}_\alpha$ introduced in Tab. 2.1. The terms for the z-bond are

$$K_z^3 = \sum_{m,l} \frac{t_{pd}^2}{\mathcal{E}_m^{\Delta_{pd}}(\omega)}\left[\mathrm{Re}\left(\mathfrak{B}_{l,m}^3 + \mathfrak{B}_{m,l}^3\right)\frac{12}{9}\left(\frac{t_2}{\mathcal{E}_{l+m}^D(\omega)} - \frac{t_2}{\mathcal{E}_{l+m}^P(\omega)}\right)\right.$$
$$\left. + \mathrm{Im}\left(\mathfrak{B}_{l,m}^3 - \mathfrak{B}_{m,l}^3\right)\frac{8}{27}\left(\frac{t_1 - t_3}{\mathcal{E}_{l+m}^D(\omega)} + \frac{2t_1 + t_3}{\mathcal{E}_{l+m}^S(\omega)} + \frac{6t_2}{\mathcal{E}_{l+m}^P(\omega)}\right)\right] \tag{5.13}$$

$$\Gamma^3 = \sum_{m,l} \frac{t_{pd}^2}{\mathcal{E}_m^{\Delta_{pd}}(\omega)}\mathrm{Re}\left(\mathfrak{B}_{l,m}^3 + \mathfrak{B}_{l,m}^3\right)\frac{4}{9}\left(\frac{t_1 - t_3}{\mathcal{E}_{l+m}^P(\omega)} - \frac{t_1 - t_3}{\mathcal{E}_{l+m}^D(\omega)}\right) \tag{5.14}$$

$$\mu_z^3 = \sum_{m,l} \frac{-t_{pd}^2}{\mathcal{E}_m^{\Delta_{pd}}(\omega)}\mathrm{Re}\left(\mathfrak{B}_{l,m}^3 - \mathfrak{B}_{m,l}^3\right)\frac{4}{9}\left(\frac{t_2}{\mathcal{E}_{l+m}^P(\omega)} + \frac{t_2}{\mathcal{E}_{l+m}^D(\omega)}\right) \tag{5.15}$$

$$D_z^3 = \sum_{m,l} \frac{t_{pd}^2}{\mathcal{E}_m^{\Delta_{pd}}(\omega)}\mathrm{Re}\left(\mathfrak{B}_{l,m}^3 - \mathfrak{B}_{m,l}^3\right)\frac{8}{27}\left(\frac{2t_1 + t_3}{\mathcal{E}_{l+m}^S(\omega)} + \frac{t_1 - t_3}{\mathcal{E}_{l+m}^D(\omega)} + \frac{3(t_1 + t_3)}{\mathcal{E}_{l+m}^P(\omega)}\right) \tag{5.16}$$

$$h_z^3 = \sum_{m,l} \frac{-t_{pd}^2}{\mathcal{E}_m^{\Delta_{pd}}(\omega)}\mathrm{Im}\left(\mathfrak{B}_{l,m}^3 - \mathfrak{B}_{m,l}^3\right)\frac{2}{9}\left(\frac{t_1 - t_3}{\mathcal{E}_{l+m}^D(\omega)} + \frac{t_1 - t_3}{\mathcal{E}_{l+m}^P(\omega)}\right), \tag{5.17}$$

with

$$\mathfrak{B}_{l,m}^3 = \mathcal{B}_{-l-m}(0, \mathbf{A})\,\mathcal{B}_{-l}^*\left(\pi/4, \mathbf{A}/\sqrt{2}\right)\mathcal{B}_{-m}^*\left(-\pi/4, \mathbf{A}/\sqrt{2}\right), \tag{5.18}$$

and $\mathcal{B}(\vartheta, \mathbf{A})$ introduced in (3.22). We again emphasize that the distinct calculation in (5.3) leads to considerably different interaction terms than in [31]. That is especially true for the Heisenberg interaction, which does not have third-order contributions, contrary to the statement of [31]. We observe that for CP, i.e. $\mathfrak{B}_{m,l}^3 = \mathfrak{B}_{l,m}^{3*}$, both D and μ indeed vanish.

5.3 Fourth order effective Floquet-Hamiltonian

As mentioned in Sec. 5.1 fourth-order terms might have significant contributions to Kitaev interactions, which is why, in this section, we want to derive the contributions to the Kitaev-Heisenberg model within fourth-order perturbation theory. We proceed in the same way as in the previous section, i.e., we calculate the matrix elements (5.4)-(5.9), with the distinction that we now use the effective Hamiltonian arising for fourth-order perturbation theory. We find that three different interactions have non-vanishing contributions in the fourth-order

$$
\begin{aligned}
J^4 = \sum_{n,l,m,k} &\frac{t_{pd}^4 \, \delta_{n,-l-k-m}}{\mathcal{E}_{l+k+m}^{\Delta_{pd}}(\omega)\mathcal{E}_m^{\Delta_{pd}}(\omega)} \frac{2}{27} \left(\mathfrak{B}_{n,l}^4 - \mathfrak{B}_{l,n}^4 \right) \left(\mathfrak{B}_{-m,-k}^{4*} - \mathfrak{B}_{-k,-m}^{4*} \right) \\
&\times \left(\frac{1}{\mathcal{E}_{l+m}^D(\omega)} + \frac{3}{\mathcal{E}_{l+m}^P(\omega)} + \frac{2}{\mathcal{E}_{l+m}^S(\omega)} \right)
\end{aligned}
\tag{5.19}
$$

$$
\begin{aligned}
K^4 = \sum_{n,l,m,k} &\frac{t_{pd}^4 \, \delta_{n,-l-k-m}}{\mathcal{E}_{l+k+m}^{\Delta_{pd}}(\omega)\mathcal{E}_m^{\Delta_{pd}}(\omega)} \left[\frac{2}{3} \left(\mathfrak{B}_{l,n}^4 \mathfrak{B}_{-m,-k}^{4*} + \mathfrak{B}_{n,l}^4 \mathfrak{B}_{-k,-m}^{4*} \right) \right. \\
&\times \left(\frac{1}{\mathcal{E}_{l+m}^P(\omega)} - \frac{1}{\mathcal{E}_{l+m}^D(\omega)} \right) - \frac{2}{27} \left(\mathfrak{B}_{n,l}^4 - \mathfrak{B}_{l,n}^4 \right) \left(\mathfrak{B}_{-m,-k}^{4*} - \mathfrak{B}_{-k,-m}^{4*} \right) \\
&\left. \times \left(\frac{2}{\mathcal{E}_{l+m}^S(\omega)} + \frac{3}{\mathcal{E}_{l+m}^P(\omega)} + \frac{4}{\mathcal{E}_{l+m}^D(\omega)} \right) \right]
\end{aligned}
\tag{5.20}
$$

$$
\begin{aligned}
\mu^4 = \sum_{n,l,m,k} &\frac{t_{pd}^4 \, \delta_{n,-l-k-m}}{\mathcal{E}_{l+k+m}^{\Delta_{pd}}(\omega)\mathcal{E}_m^{\Delta_{pd}}(\omega)} \frac{2}{18} \left(\mathfrak{B}_{n,l}^4 \mathfrak{B}_{-m,-k}^{4*} - \mathfrak{B}_{l,n}^4 \mathfrak{B}_{-k,-m}^{4*} \right) \\
&\times \left(\frac{1}{\mathcal{E}_{l+m}^D(\omega)} - \frac{1}{\mathcal{E}_{l+m}^P(\omega)} \right),
\end{aligned}
\tag{5.21}
$$

where l, m, k are the photons absorbed and emitted in the virtual hopping process, and the fourth-order equivalent of (5.18) is given as

$$
\mathfrak{B}_{n,l}^4 = \mathcal{B}_n \left(\pi/4, \mathbf{A}/\sqrt{2} \right) \mathcal{B}_l \left(-\pi/4, \mathbf{A}\sqrt{2} \right),
\tag{5.22}
$$

with $\mathcal{B}_l(\vartheta, \mathbf{A})$ defined in (3.22). Both Heisenberg and μ-interactions vanish for $E_0 = 0\,\mathrm{eV}/(ed)$, i.e., in the absence of light. That is expected, due to the absence of fourth-order contributions in the Heisenberg term and no reported μ terms in the conventional Kitaev-Heisenberg model. However, the Kitaev term has significant contributions at $E_0 = 0\,\mathrm{eV}/(ed)$, which is expected due to the reasons explained in Sec. 5.1. For a light field with finite amplitude, i.e., $E_0 > 0\,\mathrm{eV}/(ed)$, and CP both Heisenberg and Kitaev interactions have contributions, while μ-interactions, as for third order, vanish. However, for non-CP, μ can have non-vanishing contributions. To obtain the complete effective Floquet-Kitaev-Heisenberg Hamiltonian we have to add up the results of the second

t_1	t_2	t_3	t_{pd}	Δ_{pd}	U	J_H
$0.044\,\text{eV}$	$0.08\,\text{eV}$	$-0.109\,\text{eV}$	$-0.8\,\text{eV}$	$5.0\,\text{eV}$	$3.0\,\text{eV}$	$0.45\,\text{eV}$

Table 5.1: Hopping strengths for α-RuCl$_3$ obtained via density functional theory (DFT) [104] and photoemission measurements [105].

(App.B), third (Sec. 5.2), and fourth-order (Sec. 5.3), which yields, for the z-bond

$$H_{\text{eff}}^F = (J_z^2 + J_z^4)\mathbf{S}_i\mathbf{S}_j + (K_z^2 + K_z^3 + K_z^4)S_i^z S_j^z + (\Gamma_z^2 + \Gamma_z^3)(S_i^x S_j^y + S_i^y S_j^x)$$
$$+ (\mu_z^3 + \mu_z^4)(S_i^x S_j^x - S_j^y S_j^y) + D_z^3\mathbf{e}_z(\mathbf{S}_i \times \mathbf{S}_j) + h_z^3(S_i^z + S_j^z). \tag{5.23}$$

5.4 Parameters

In this chapter, we use the same hopping parameters [104], Coloumb repulsion and Hund's coupling [105] as in [31], to compare our extended fourth-order effective model with the existing third-order results, see Tab. 5.1. Contrary to the parameters in Chap.4, the initial hopping parameters are isotropic. We want to emphasize that, in principle, the model obtained in Sec. 5.1-5.3 can also capture anisotropic hopping parameters.

5.5 Special cases of elliptical Lissajous figures

We start our analysis of the high-order Floquet Kitaev-Heisenberg model for the limiting cases $\epsilon = \pi/2$ and $\epsilon = 0$. Especially LP was discussed extensively in Sec. 4.2, while CP has been discussed in [31, 32]. Therefore, it is convenient, to begin with these cases to elaborate changes third and fourth order induce.

5.5.1 Linear polarized light

As discussed in Sec. 4.2 for second-order perturbation theory, we find that LP has an anisotropic influence on the three different bond types in the honeycomb lattice. It was argued that with the change of the light angle, one can change the influence on the distinct bonds, including a possible decoupling of the light from one bond. The explicit inclusion of third and fourth-order terms introduces new bonds, namely the ones connecting d and p atoms (see Fig. 5.3). Therefore, one can deduce that a complete decoupling from light is impossible for linear polarization if there are contributions from higher-order terms.

As an example, we set the light angle to the z bond $\varphi = \pi/2$, which causes a decoupling from the d-d bond. However, there are still contributions depending on E_0 and ω arising from the d-p bonds belonging to the z bond, enclosing an angle of $\pi/4$ and $-\pi/4$ with the light, see Fig. 5.3(ii).

(i) LP with $\varphi = \pi/4$ (ii) LP with $\varphi = \pi/2$ (iii) CP
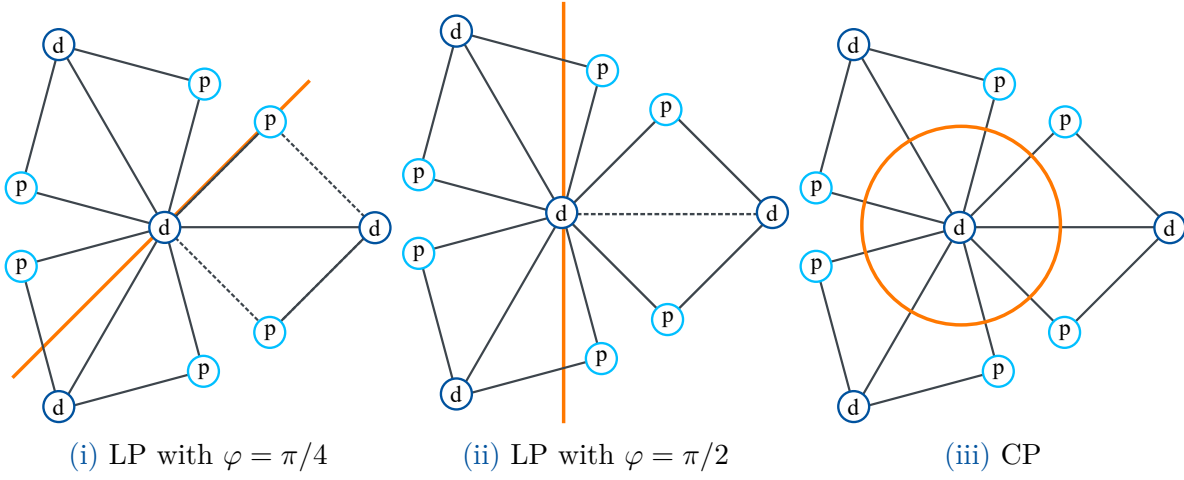
Figure 5.3: Different polarizations discussed in the text. For LP (i) and (ii), there is the possibility of light decoupling from a certain bond direction (dashed lines), and the influence on the bonds is, in general, strongly anisotropic. CP (iii) has an isotropic influence on all bonds.
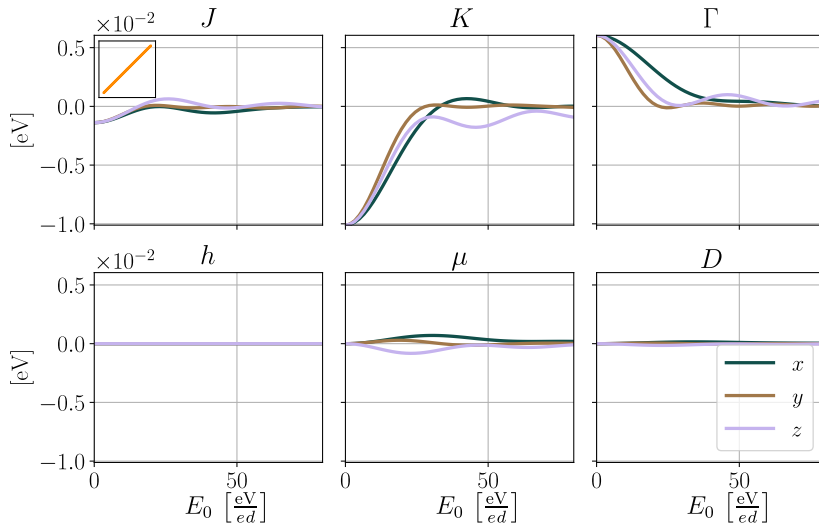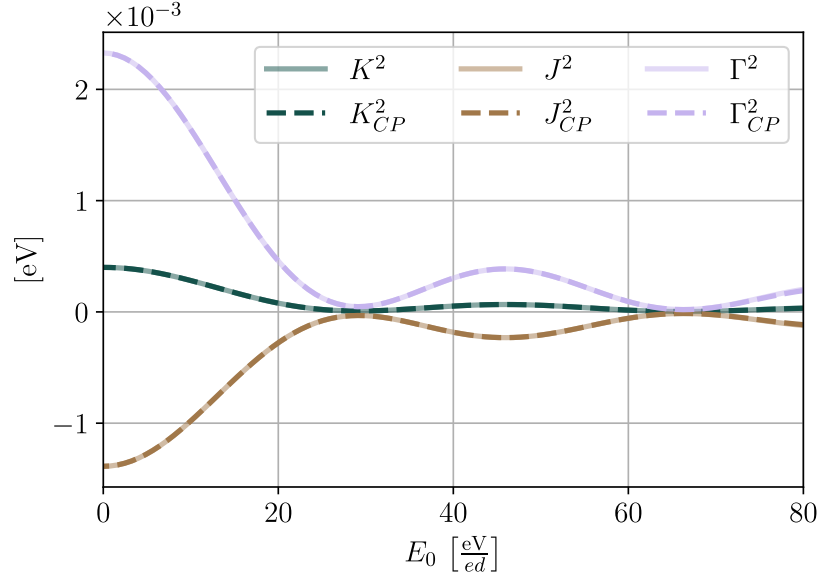

Figure 5.4: J, K, Γ, D, μ, and h interactions in x, y, and z direction in dependency of light amplitude E_0 for $\omega = 12.0$ eV. We display the results for frequency multiplicity $N = 1$ and LP with $\varphi = \pi/4$ (see inset).

Figure 5.5: Comparison of the model for CP (dashed lines) with the second-order results for AP, calculated like in (B.6), in the limit of $N = 1$ and $\epsilon = \pi/2$ (solid lines) for $\omega = 12.0\,\text{eV}$.

For the remainder of the chapter, we set the light angle to $\pi/4$ [see Fig. 5.3(i)], i.e. $E_x = E_y = E_0$. The results for all interaction parameters obtained in Tab. 5.1 at driving frequency $\omega = 12.0\,\text{eV}$ are depicted in Fig. 5.4. As for the second-order results, the influence on the bond directions x, y, and z is strongly anisotropic. As expected, there is no induced magnetic field for LP (Fig. 5.4) due to the absence of time-reversal symmetry breaking. However, contributions from the inversion symmetry-breaking term D and the term μ (Fig. 5.4) exist, which both induce anisotropies. We can attribute this induced anisotropy to the fact that, for LP, it makes a difference if the hopping path goes over the "upper" d-p-d connection or the "lower" one Fig. 5.3. These two connections have inverted angles between light polarization and bond directions for the absorption of m and n photons.

for the former m photons get absorbed for light angle φ_1 and n photons for φ_2 while for the latter one it is exactly inverse. Last but not least, we observe that, due to third-order contributions, the E_0 dependency for the KHI is no longer perfectly in phase. That arises from (5.13)-(5.17) in addition to the fact that there are no third-order contributions for J. Therefore, tuning the different parameters relative to each other seems possible even for LP. These newly discovered properties make the explicit inclusion of third and fourth order mandatory for LP.
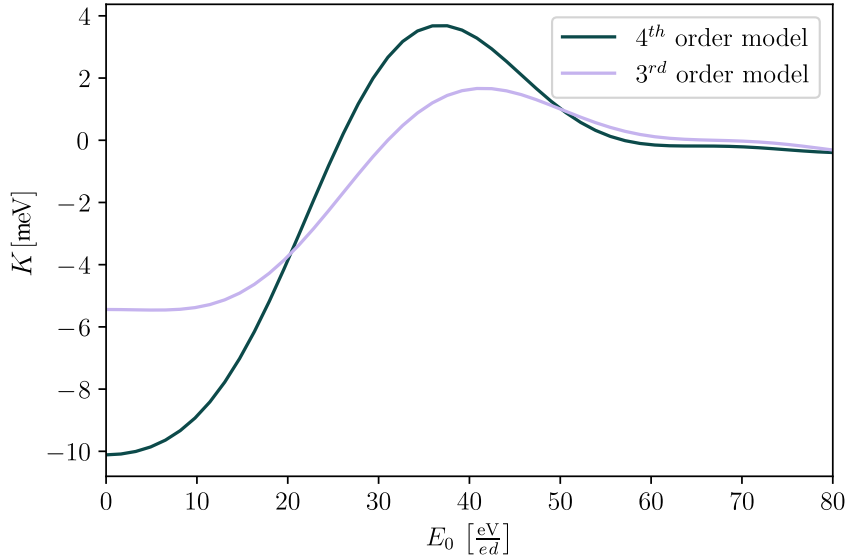
Figure 5.6: Comparison of the third- (mauve) and fourth-order model (dark green) for Kitaev interactions, at $N = 1$ for $\omega = 12.0\,\text{eV}$, in dependency of E_0.

5.5.2 Circular polarized light

The influence of CP has been heavily discussed in the context of the inverse Faraday effect [103]. To compare the results of our extended model in the limit of $\epsilon = \pi/2$ with the third order results of [31], we set the driving frequency to $\omega = 12.0\,\text{eV}$, which is the only frequency where both analytical and numerical results exist [31]. We depict the results from our model in Fig. 5.7. As predicted from second-order results Sec. 4.3, all bond directions experience the same modulation. However, like for LP, we note that K and Γ are not in phase anymore, giving the possibility of relative tuning between KHI (as already discussed in [31,80]). We also note that there is a nonzero contribution to h for $E_0 > 0\,\text{eV}/(ed)$, which is a result of broken time-reversal symmetry. Both D and μ vanish due to the preservation of space isotropy. Comparing our results with the results of [31], we notice that the results of our extended model fit the numerical results far better. Especially the behavior of the Kitaev interaction with a maximum at $E_0 \approx 40\,\text{ev}/(ed)$, which is not reproduced by the analytic results of [31] shows good agreement with our analytic results. The reason for that is most likely the negligence of fourth-order terms and alternative hopping paths, discussed in Sec. 5.2, in third-order terms. We attribute the minor difference between numerical and our analytic results to a different sign in the Bessel functions used for the ED calculations in [31]. While this results in a minor difference far from resonances, the effect might be more pronounced closer to the resonances. We, therefore, emphasize the importance of the index signs chosen in (5.18) of Sec. 5.2, which we believe to be the correct ones. Still, the relatively good agreement with the numerical results at $\omega = 12.0\,\text{eV}$ encourages the validity of our extended model.
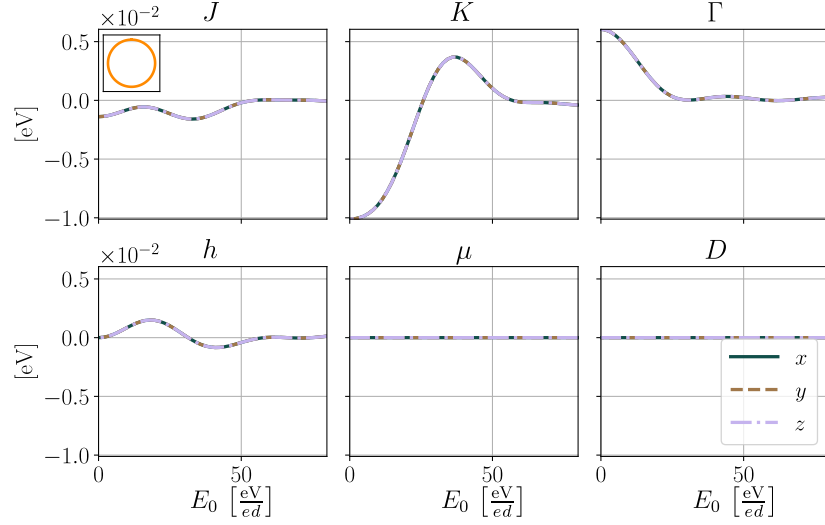
Figure 5.7: J, K, Γ, D, μ, and h interactions in x, y, and z direction in dependency of light amplitude E_0 for $\omega = 12.0\,\text{eV}$. We display the results for frequency multiplicity N=1 and CP (see inset).

To further confirm the model for AP, we want to compare the results from second-order perturbation theory for CP with our model at $\epsilon = \pi/2$, see Fig. 5.5. We observe that the CP model agrees with the AP model at $\epsilon = \pi/2$. Like for LP, inclusion of third-order correction terms is crucial for CP because second-order perturbation theory can not capture the induced magnetic field. Since we want to obtain the correct magnitudes for the interactions and capture a realistic influence of E_0, inclusion of fourth-order terms is mandatory, as they can have significant contributions. That is especially true for the Kitaev interaction see Fig. 5.6. With our model, we can capture all relevant effects for both LP and CP and are also able to continuously vary ϵ as discussed in Sec. 3.3.3.

5.6 Elliptical Lissajous figures

5.6.1 Above resonances

The main advantage of the Lissajous model derived in Sec. 5.3 is its capability to capture the E_0 and ω dependency for AP. That means we are no longer limited to the cases of CP and LP but can extend our research to more exotic polarization cases. In this section, we explore the influence of the parameter ϵ, which changes the phase between x and y polarized light (see Sec. 3.3.3), on the high-order Kitaev-Heisenberg interactions. We start our analysis with a fixed driving frequency set above resonances at $\omega = 12.0\,\text{eV}$.

As discussed in Sec. 5.5, for driving frequencies above all resonances, we generally expect a considerable suppression of KHI with increasing E_0. The results for all interactions with $0 < \epsilon < \pi$ are displayed in Fig. 5.8. We observe that J, K, and Γ interactions get strongly suppressed for $E_0 > 70\,\text{eV}/(ed)$ [Fig. 5.8(i)]. While the suppression of Γ is

(i) KHI J, K, and Γ

(ii) LI D, μ, and h
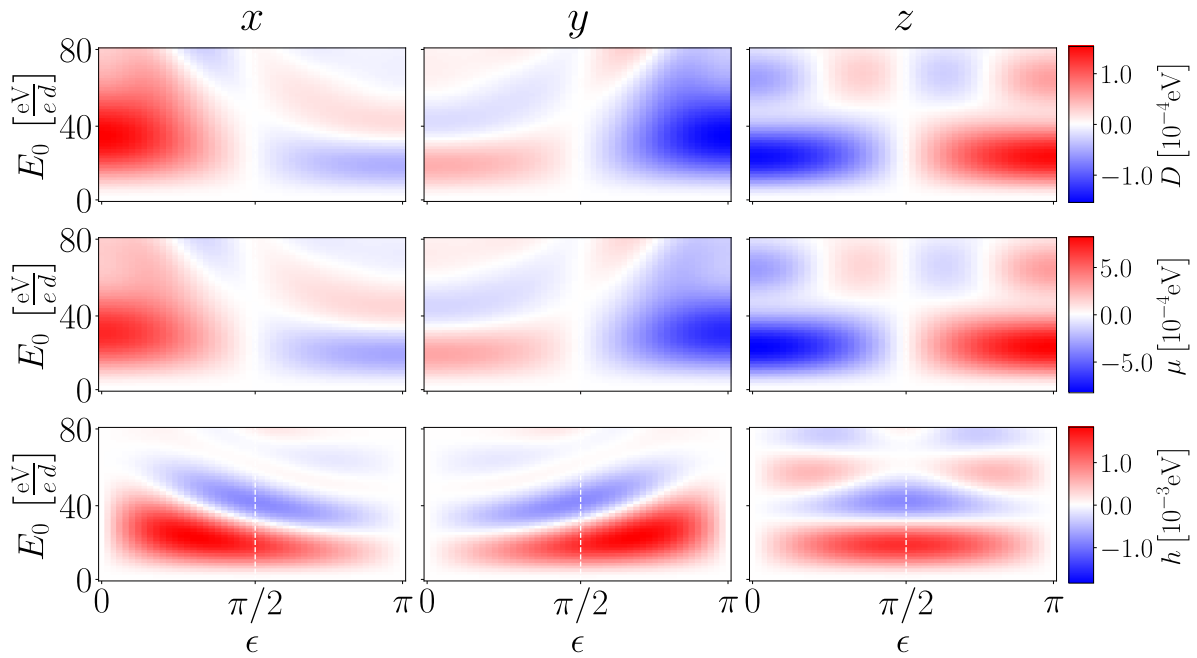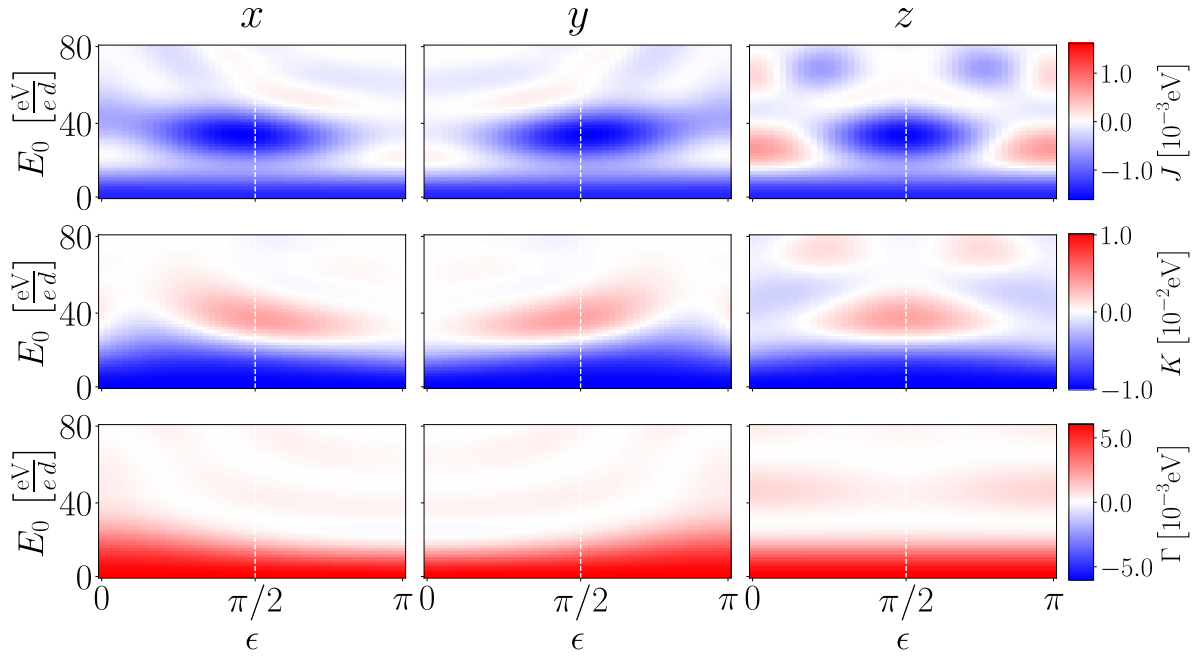
Figure 5.8: Interactions in x, y, and z direction in dependency of light amplitude E_0 and phase shift ϵ for $\omega = 12.0\,\text{eV}$. Displayed are the results for frequency multiplicity N=1.

sizable, Kitaev and Heisenberg interaction have considerable contributions for finite E_0, compared to their values at $E_0 = 0\,\text{eV}/(ed)$. That is especially true for CP, where the Heisenberg interaction experiences an increase before getting suppressed for large E_0. We also observe a change in a sign for Kitaev interaction at $E_0 \approx 40\,\text{eV}/(ed)$, switching from a negative to a positive sign. For LP, we a suppression of both effects. The transition between LP and CP appears smooth with no significant new properties. We observe that z is symmetric around $\pi/2$, and the results for x at ϵ and y at $\epsilon + \pi$ are the same.

The results for LI h, D, and μ at $\omega = 12.0\,\text{eV}$ are showcased in Fig. 5.8(ii). As expected at $E_0 = 0$ all interactions vanish for arbitrary ϵ. The induced magnetic field h arises for finite E_0 and $\epsilon \neq n\pi$ with $n \in \mathbb{N}$. At $\epsilon = \pi/2$ contributions are isotropic, which is analogous to a magnetic field pointing in the $\mathbf{n} = (1, 1, 1)$ direction, as predicted by [32]. If we move away from $\epsilon = \pi/2$, contributions become anisotropic, which causes a change in the direction of the induced magnetic field. In addition, the maximal x and y contributions of h are between CP and LP. Therefore, with more unconventional Lissajous figures, we can manipulate the direction and strength of the induced magnetic field. For D and μ we observe finite contributions at $E_0 > 0$ and non-CP. Contrary to the previously discussed interactions, D and μ do not obey the symmetry rules as the KHI. As we see z-interactions are antisymmetric around $\epsilon = \pi/2$, while x-interactions at ϵ coincide with y-interactions at $\epsilon + \pi$ multiplied with a factor of -1. We can attribute this antisymmetric behavior of all bonds to the fact that both D and μ break the interaction isotropy [(5.10) in Sec. 5.2]. Otherwise, D and μ behave similarly, with μ having significantly stronger contributions. The contributions of both interactions are relatively weak compared to the symmetric interactions, which are approximately a magnitude stronger.

5.6.2 In-between resonances

After discussing driving above resonances in Sec. 5.6.1, in this section, we focus on driving in-between resonances. That is motivated by the second-order results of Sec. 4.2, as well as the numerical results of [30, 31, 94], which both show a significant enhancement of interactions at finite E_0, which is desirable because ideally we want to increase Kitaev interactions significantly. We choose a driving frequency of $\omega = 2.1\,\text{eV}$ which is between the resonances at $\mathcal{E}_S/2$, $\mathcal{E}_D$, and $\Delta_{pd}/2$. Since the $\mathcal{E}_D$ and $\Delta_{pd}/2$ resonance almost coincide, we expect quite significant heating effects, discussed in Sec. 4.1, close to these resonances, while heating effects close to $E_S/2$ are likely to be less pronounced. Therefore, we choose the driving frequency closer to $E_S/2$ instead of a driving frequency exactly between the resonances.

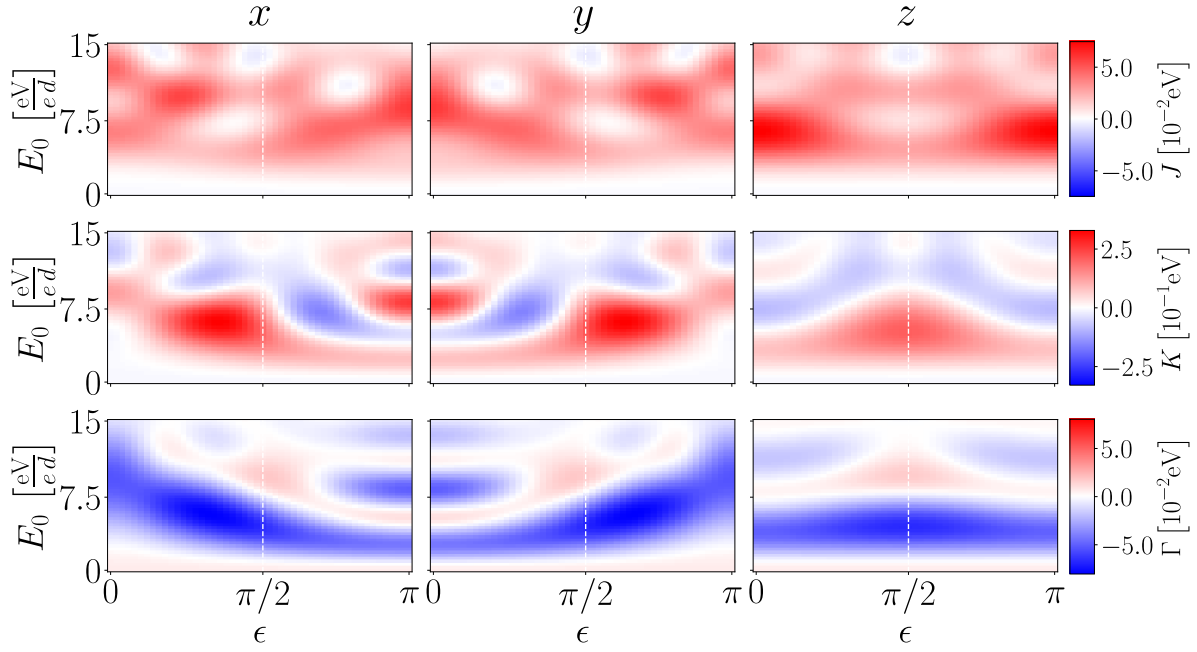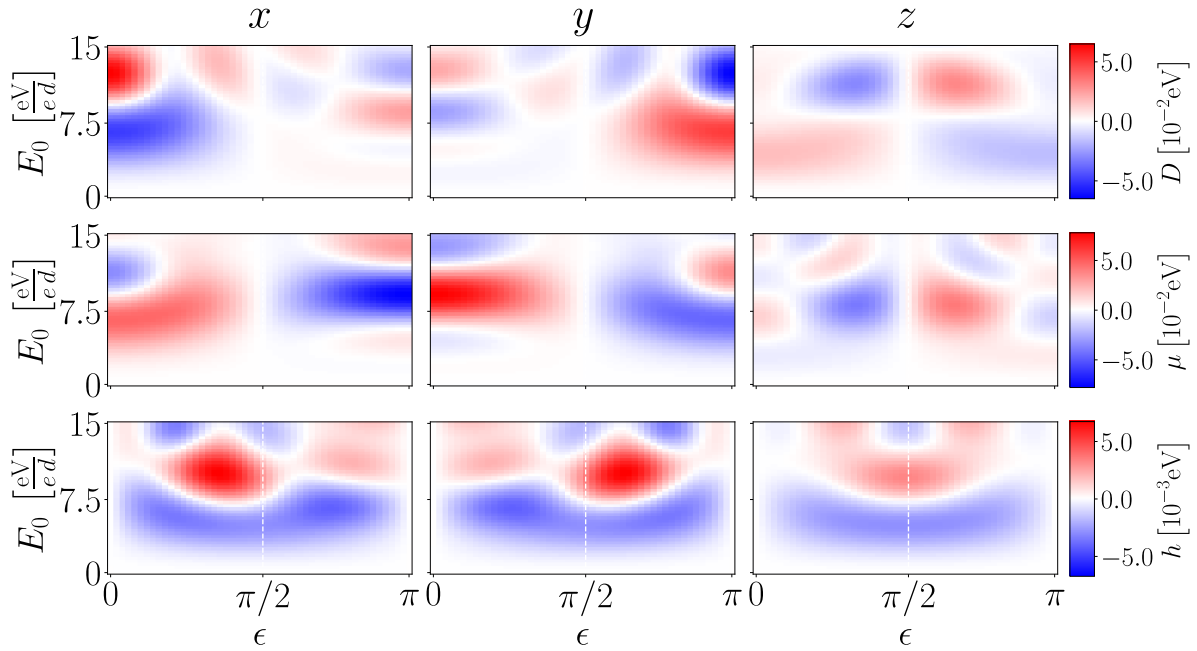We start our analysis with the KHI J, K, and Γ, displayed in Fig. 5.9(i). First,
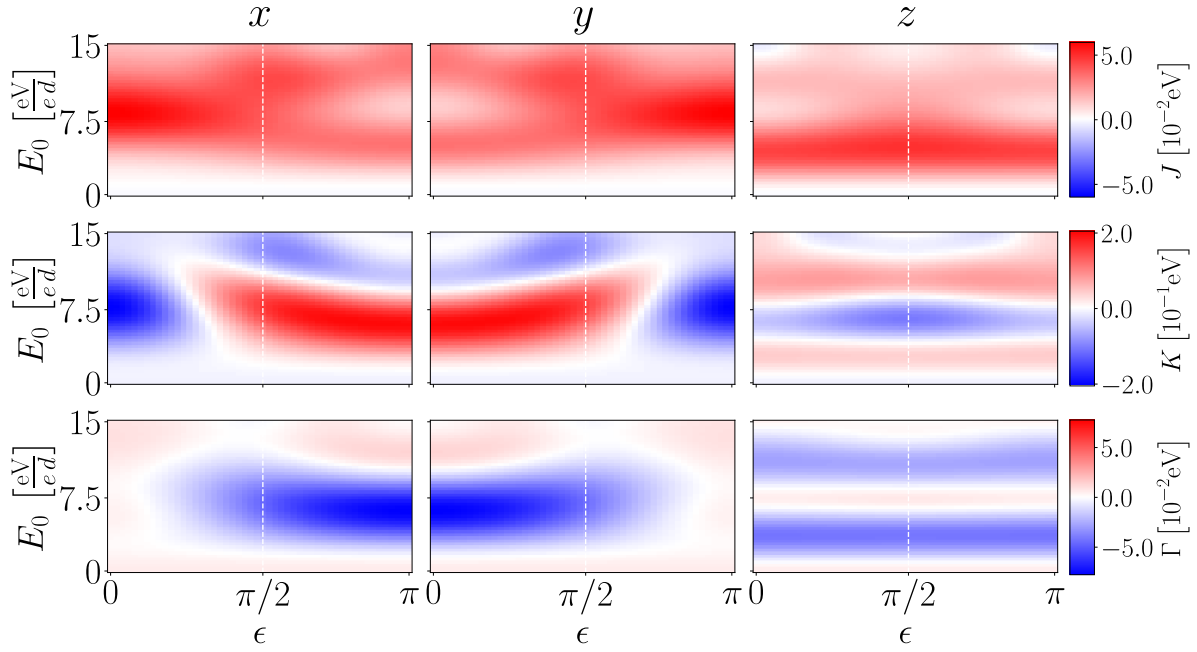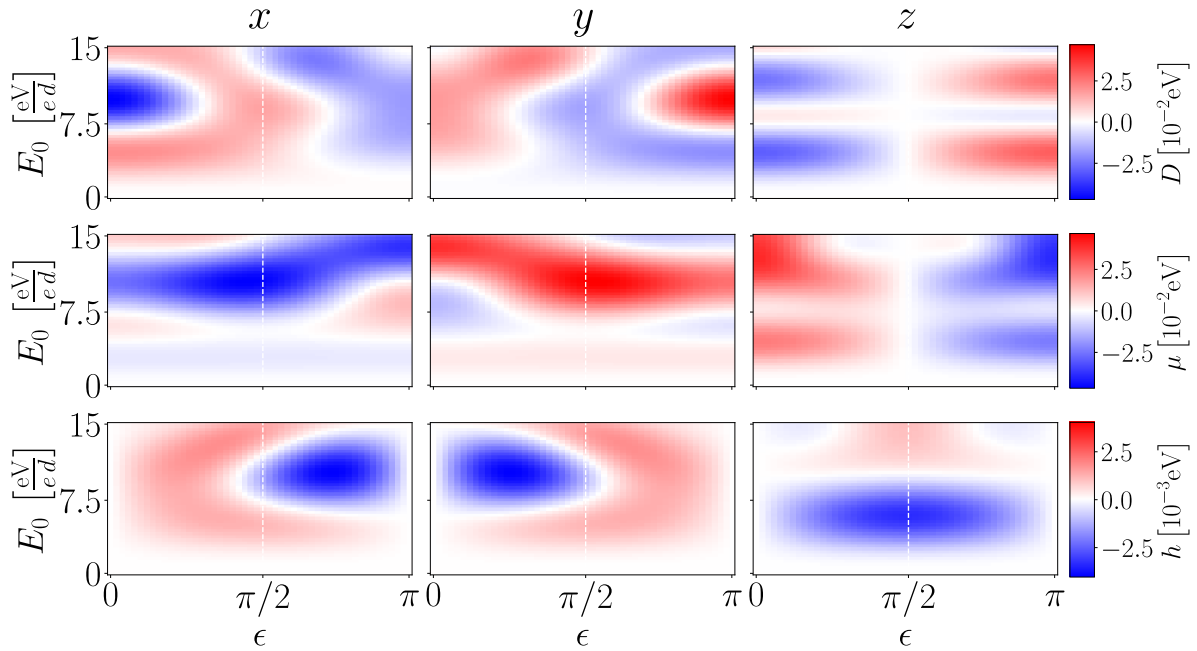
(i) KHI J, K, and Γ

(ii) LI D, μ, and h

Figure 5.9: Interactions in x, y, and z direction in dependency of light amplitude E_0 and phase shift ϵ for $\omega = 2.1\,\mathrm{eV}$. Displayed are the results for frequency multiplicity N=1.

we note that, compared to Fig. 5.8, all interactions increase significantly for finite E_0. That was already reported for second-order results (Sec. 4.2). However, the ϵ and E_0 dependency becomes far more intricate if we include third and fourth-order terms. We especially want to point out the Kitaev interactions, which have maximal x and y contributions between CP and LP. That is in strong contrast to the results of $\omega = 12.0\,\text{eV}$, where maximal contributions (outside of $E_0 = 0$) are at $\epsilon = \pi/2$. Therefore, a significant change in the driving frequency changes the interaction properties on top of the overall interaction magnitude. We want to emphasize that values of the interactions at $E_0 = 0$ have to be the same as for $\omega = 12.0\,\text{eV}$.

The LI interactions are displayed in Fig. 5.9(ii). D and μ interactions vanish at $\epsilon = \pi/2$, while the induced magnetic field vanishes at $\epsilon = 0$ and $\epsilon = \pi$. We observe that the strength of the anisotropic interactions is increased significantly from $\propto 10^{-4}$ to $\propto 10^{-2}$, making them comparable in magnitude to the KHI interactions. We again observe the typical antisymmetric behavior for D and μ in dependency of ϵ, as explained in Sec. 5.6.1. Interactions appear to be stronger in-plane. Maxima at $\epsilon = 0$ and $\epsilon = \pi$ can be found at $E_0 \approx 8.0\,\text{eV}/(ed)$ for μ and $E_0 \approx 12.0\,\text{eV}/(ed)$ for D. We also note that D and μ are of comparable magnitude, contrary to $\omega = 12.0\,\text{eV}$. Meanwhile h has the same magnitude ($\propto 10^{-3}$) as driving above resonances. Therefore, a change of the frequency to $\omega = 2.1\,\text{eV}$ reduces the overall influence of the magnetic field because all other interactions increase significantly. The overall maximum of h is, like $\omega = 12.0\,\text{eV}$, in-between CP and LP. This maximum for x and y interactions, in combination with relatively weak contributions from the z direction, results in an induced magnetic field mainly pointing in the x and y directions.

5.7 $N > 1$ Lissajous figures

We want to focus on the frequency multiplicity N, which we fixed to $N = 1$ in the previous sections. N describes the ratio of frequencies of light polarized in x and y direction in the Lissajous figures (see Tab. 3.1). Since driving in-between resonances has proven to enhance KHI interactions in this section we use the driving frequency $\omega = 2.1\,\text{eV}$ as in Sec. 5.6.2.

We start our analysis with $N = 2$ Lissajous figures (Fig. 5.10). The KHI interactions again show a sizable increase from their starting value at $E_0 = 0\,\text{eV}/(ed)$ [Fig. 5.10(i)]. Comparing these results to the results of Sec. 5.6, we notice some qualitative changes. The z interactions show a weak dependence on ϵ in Fig. 5.10, while in Fig. 5.9 the influence of ϵ appears to be far more pronounced. This trend is also visible for x and y interactions. We want to instance the behavior of K_x at $E_0 = 6.0\,\text{eV}/(ed)$ with changing ϵ. For $N = 1$ we observe multiple changes of sign and magnitude with changing ϵ

(i) KHI J, K and Γ

(ii) LI D, μ, and h

Figure 5.10: Interactions in x, y, and z direction in dependency of light amplitude E_0 and phase shift ϵ for $\omega = 2.1\,\text{eV}$. Displayed are the results for frequency multiplicity N=2.

(i) $N = 1$, $E_0 = 6\,\mathrm{eV}/(ed)$ (ii) $N = 2$, $E_0 = 6\,\mathrm{eV}/(ed)$
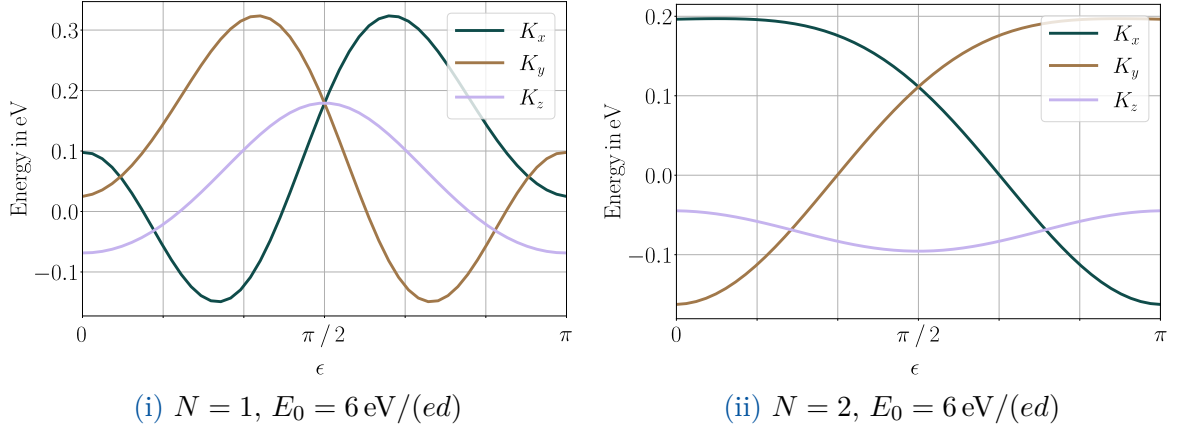
Figure 5.11: x, y, and z bond Kitaev interactions in dependency of the Lissajous phase shift ϵ for $\omega = 2.1\,\mathrm{eV}$ and $E_0 = 6.0\,\mathrm{eV}/(ed)$. We display the results for $N = 1$ (i) and $N = 2$ (ii).

from 0 to π [Fig. 5.11(i)]. Meanwhile, for $N = 2$ there is just one sign change, and the magnitude stays relatively unaffected [Fig. 5.11(ii)]. In addition, the sign at $\epsilon = 0$ differs from the one at $\epsilon = \pi$ for $N = 2$. With this, we can switch signs of Kitaev interactions in x and y interactions while preserving z interactions. In Fig. 5.11(ii), it also becomes obvious that $N = 2$ interactions are not isotropic for finite E_0 regardless of ϵ. That is intuitively the case because, for $N = 2$, there is no pendant to CP of the $N = 1$ Lissajous figures.

For the LI, we notice that D and μ have finite contributions at $\epsilon = \pi/2$ for x and y bonds. Again, the reason for these contributions is that the $N = 2$, $\epsilon = \pi/2$ polarization no longer preserves the isotropy [see Fig. 5.10(ii)] of the system and therefore allows finite D and μ interactions. z interactions still vanish for $\epsilon = \pi/2$, due to the antisymmetric behavior of D and μ. For the induced magnetic field, we do not observe significant changes in the z interaction. On the other hand, x and y interactions show some significant changes, most prominently the change of sign of the global extremum. That means that the in-plane magnetic field discussed in [31, 32, 102] changes direction with the change from $N = 1$ to $N = 2$. Like for $N = 1$, the magnetic field still vanishes at $\epsilon = 0$ and $\epsilon = \pi$.

In principle, there is an infinite number of distinct Lissajous figures due to $N \in \mathbb{N}$. However, if N becomes sufficiently large we do not expect a significant change in the resulting interactions. The reason is that with increasing frequency multiplicity N the phase shift ϵ becomes less important, see Tab. 3.1. To explore the behavior for these large N Lissajous figures, we set $N = 5$, which is, as we will see in the remainder of the chapter, a decent representative for $\lim_{N \to \infty}$ Lissajous figures. The KHI and LI are shown in Fig. 5.12(i) and Fig. 5.12(ii) respectively.

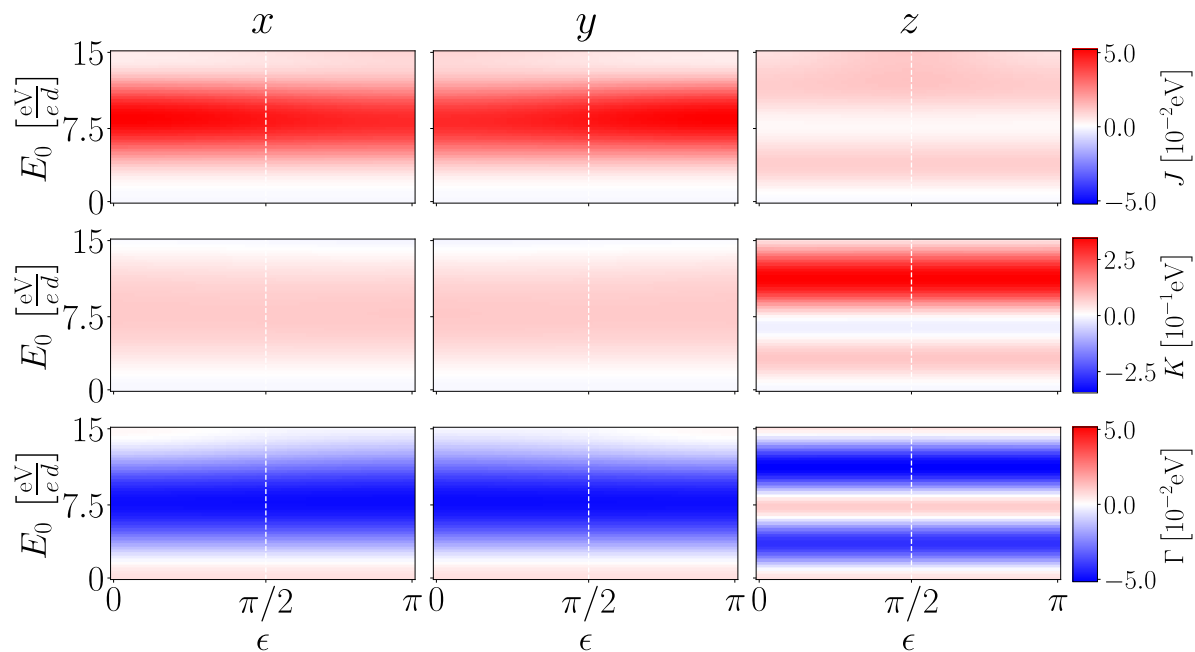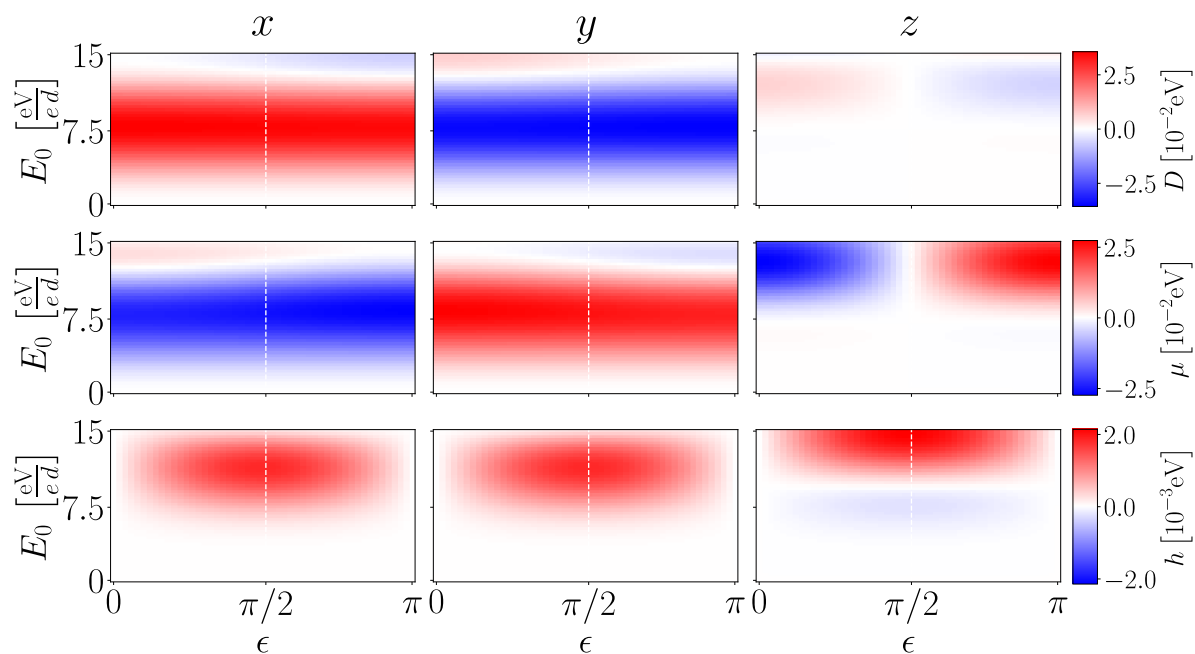All KHI interactions decouple almost completely from ϵ, with isotropic x and y in-

(i) KHI J, K, and Γ

(ii) LI D, μ, and h

Figure 5.12: Interactions in x, y, and z direction in dependency of light amplitude E_0 and phase shift ϵ for $\omega = 2.1\,\text{eV}$. Displayed are the results for frequency multiplicity N=5.

teractions and a distinct z interaction. While the Heisenberg interaction has dominant x and y contributions, Kitaev interactions are dominant in the z direction with comparably weak contributions for the x and y directions. Last but least, Γ interactions are comparable in magnitude for all bond directions.

While for KHI, all interactions show a quasi-decoupling from ϵ, this is not the case for the LI. For D and μ, z interactions still switch sign at $\epsilon = \pi/2$, with a weak ϵ dependence for x and y interactions. Last but not least, the magnetic field vanishes at $\epsilon = 0$ and $\epsilon = \pi$, like in Sec. 5.6 and 5.7, for all bond directions. That makes high-order Lissajous figures a promising playground for manipulating the magnetic field because changing ϵ only affects the z components of D and μ interactions. Therefore, one can finetune the induced magnetic field while keeping KHI interactions intact. The direction of the magnetic field also does not change significantly with changing ϵ pointing approximately in the $\mathbf{n}$ direction for $E_0 \approx 14\,\mathrm{eV}/(ed)$.

II

Magnetic phase transitions in t_{2g}^4 square lattice models

6 Kugel-Khomskii model

In this chapter we derive an effective spin-orbit model for t_{2g}^4 square lattice compounds with sizable Hund's coupling J_H, which can be applied to the debated compound Ca_2RuO_4. In our derivation, we include anisotropic hopping processes, Hund's coupling J_H and further neighbor interactions. This model is the foundation for the discussions in Chap. 7.

6.1 Motivation

As mentioned in Sec. 1.2, the nature of the paramagnetic ground state in Ca_2RuO_4 is, up until now, still not entirely explained. To shine light on this topic, we want to derive an effective spin-orbit Hamiltonian following the approach of Sec. 2.3.1, giving us the possibility to explore the ground state properties of Ca_2RuO_4. There have been derivations of effective spin-orbit models for Ca_2RuO_4 [39, 71]. However, they do not consider anisotropic hopping processes or Hund's coupling J_H. Density functional theory (DFT) calculations imply that the hopping processes in Ca_2RuO_4 have distinct strength with regards to the orbital flavor, Tab. 6.1. The convention for the hopping parameters used from here on is $t_{\alpha,m}$ with α the orbital flavor and m the bond type, see also Tab. 6.1. In addition to that x-ray scattering results have shown sizable Hund's coupling, meaning that we must not neglect it in the derivation. In the following, we will discuss the

$t_{\alpha,m}$	$t_{xy,1}$	$t_{xy,2}$	$t_{xy,3}$	$t_{zx,1}$	$t_{zx,2}$	$t_{zx,3}$	$t_{yz,1}$	$t_{yz,2}$	$t_{yz,3}$
	t_{xy}	t_{xy}	t_{NNN}	t_{zx}	0	0	0	t_{yz}	0
[eV]	0.2	0.2	0.1	0.137	0	0	0	0.137	0

Table 6.1: Hopping strengths for Ca_2RuO_4 obtained via density functional theory (DFT) from [106]. Here, we set the labels of the hopping parameters according to Fig. 6.1.
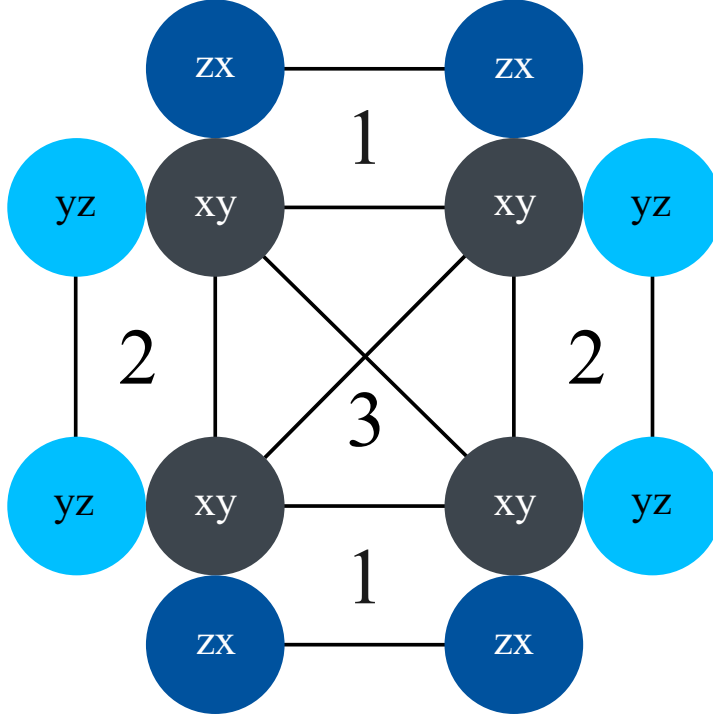
Figure 6.1: Possible hopping paths on the square lattice. d_{yz} and d_{zx} orbital are just active on bond 1 and 2 respectively and do not show significant hopping amplitudes further than NN interactions. The d_{xy} orbital is active on both NN bonds 1 and 2, and furthermore has a non negligible hopping amplitude on the NNN bond 3.

derivation of the model qualitatively and focus on the discussion of the single interaction terms arising in perturbation theory. For a detailed derivation, we want to point the interested reader to App.C.

6.2 Derivation

The kinetic Hamiltonian for Ca_2RuO_4 is given in (2.1). However, the hopping processes possible on the square lattice are distinct from the processes on the hexagonal lattice (Tab. 4.1), as discussed in Sec. 2.2.1. Fig. 6.1 illustrates the significant NN and NNN hopping processes in Ca_2RuO_4. For NN interactions, we observe that the xy orbital is active in both bond directions, while the xz and yz orbital are just active on bond 1 and 2 respectively. In addition to NN, the xy orbital also has non-zero NNN interactions, denoted by 3 in Fig. 6.1. These are the hoppings possible in a square lattice of t_{2g}^4 atoms see Fig. 2.5(iii).

The on-site Hamiltonian is, as introduced in Chap. 2, given by the Kanamori Hamiltonian (2.2). In the Mott insulating phase, the number of holes is fixed to two holes per site. In addition, because Hund's coupling is large, of the possible states with two holes per site, we only consider those where holes occupy different orbitals and the total spin is

(i) $\Delta\mathcal{E}_1$, $\Delta\mathcal{E}_2$ (ii) $\Delta\mathcal{E}_2$, $\Delta\mathcal{E}_3$ (iii) $\Delta\mathcal{E}_3$
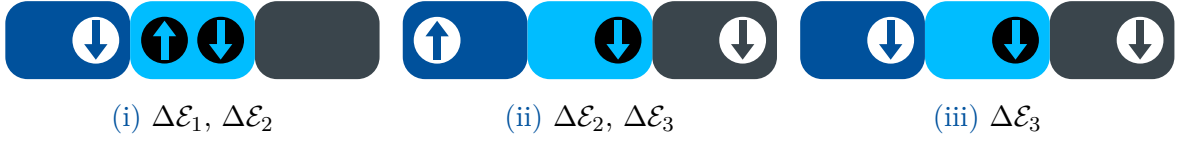
Figure 6.2: Possible energy differences for the $d^4 d^4 \rightarrow d^3 d^5$ excitation. One can in general distinct between three different d^3 configurations: One double occupation with the remaining electron residing in a distinct orbital having an overlap with $f = 1$ and 2 of Tab. 2.2, all particles in different orbital and two having the same spin with the last spin in opposite direction having an overlap with $f = 3$, 4, and 5 of Tab. 2.2, and lastly three particles in distinct orbitals with spins aligned in the same direction, referring to $f = 6$ of Tab. 2.2.

maximized. This restriction decreases the Hilbert space to three possible states per site, which are the states with $\mathcal{E}_P$ see Tab. 2.1. The three triplet spin states have one orbital occupied by two electrons (indicated by 0 in Tab.2.1). Therefore, these states have three different orbital configurations, with the double electron configuration residing in one of the T_{2g} orbitals. If we combine orbital and spin degrees of freedom we obtain nine possible degenerated initial states. We name the orbital configurations according to the orbital with the double electron occupation and can map the orbital configurations to a pseudo angular momentum with

$$
\begin{aligned}
L^x &= \mathcal{L}_{yz} = \mathrm{i}(|xy\rangle\langle zx| - |zx\rangle\langle xy|) \\
L^y &= \mathcal{L}_{xz} = \mathrm{i}(|yz\rangle\langle xy| - |xy\rangle\langle yz|) \\
L^z &= \mathcal{L}_{xy} = \mathrm{i}(|zx\rangle\langle yz| - |yz\rangle\langle zx|).
\end{aligned}
\tag{6.1}
$$

Here, $\mathcal{L}_\alpha$ is a convenient labeling for the effective spin-orbit Hamiltonian, and L^α is the conventional notation in the framework of the angular momentum $\mathbf{L}$.

The effective spin-orbit Hamiltonian can then be obtained via second-order perturbation theory, describing the virtual $d^2 d^2 \rightarrow d^3 d^1 \rightarrow d^2 d^2$ hopping processes, see App.C. For this, we need the possible excitation energies and states of the $d^3 d^1$ configuration. Tab. 2.2 lists the d^3 states with corresponding energies, while the on-site energies for one hole per site d^1 are 0. The energy difference in the denominator of (2.8) can be calculated via $\Delta\mathcal{E}_f = 2\mathcal{E}_P - \mathcal{E}_{3,f}$.

6.2.1 Kanamori energies

For the d^3 states we have to distinguish three different cases. First, there are states with two holes occupying the same orbital and the remaining one residing in one of the other two orbitals. In this case the eigenstates of H_{int} can be symmetric $f = 1$ in Tab. 2.2 or antisymmetric $f = 2$. This yields an energy difference of $\Delta\mathcal{E}_1 = -(U + 2J_H)$ and
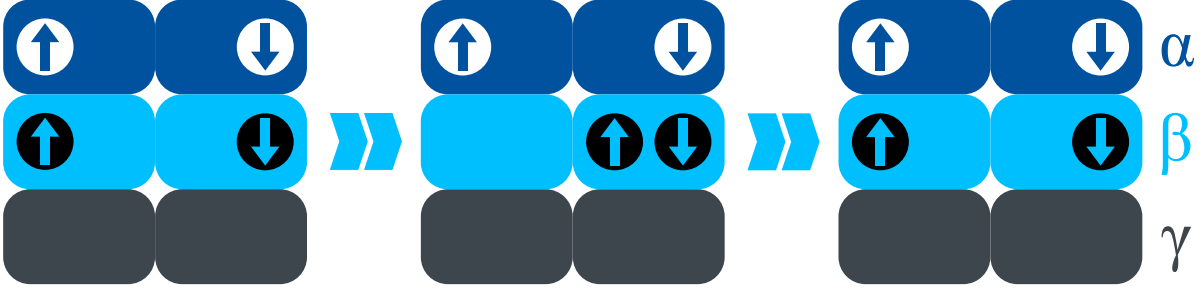
Figure 6.3: Example for an orbital preserving hopping process (6.2). The hole in the β orbital on-site i hops to site j, which causes a double occupation, and then immediately hops back to site i, which completes the virtual process. Initial and final orbital configurations are identical.
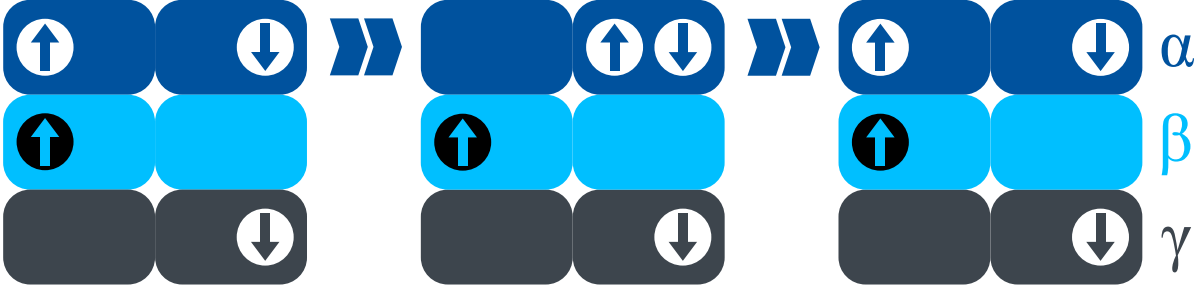

Figure 6.4: Example for an orbital preserving hopping process where the electron double occupation resides in different orbitals for site i and j. In contrast to Fig. 6.3 all orbitals can contribute to the hopping process.

$\Delta\mathcal{E}_2 = -U$ for $f = 1$ and $f = 2$ respectively.

In the second case, all three holes reside in distinct orbitals with their spins combined to a total spin of $S_{\text{tot}} = 1/2$. Again there are symmetric $f = 3$ in Tab. 2.2 and antisymmetric $f = 4$ and 5 solutions yielding energy differences of $\Delta\mathcal{E}_3 = -(U - 3J_H)$ and $\Delta\mathcal{E}_4 = \Delta\mathcal{E}_5 = \Delta\mathcal{E}_2 = -U$ respectively.

Lastly, three holes in three different orbitals can also form a spin $S_{\text{tot}} = 3/2$ by aligning their spins all in the same direction $f = 6$ this like $f = 3$ yields an energy difference of $\Delta\mathcal{E}_6 = \Delta\mathcal{E}_3 = -(U - 3J_H)$. This gives us, in total, three excitation energies to consider in the perturbation theory, which we summarize in Fig. 6.2. If we perform the perturbation theory and project the result in the spin-orbit basis, introduced in [39], we arrive at an effective spin-orbit Hamiltonian. This approach is supported by results of similar Hamiltonians [65–67].

6.2.2 Effective interactions

In the following, we will discuss the single terms occurring in the Hamiltonian in more detail, where our calculations yield terms with orbital and spin-orbital interactions. We separate the Hamiltonian into three different types of interactions. First, some terms
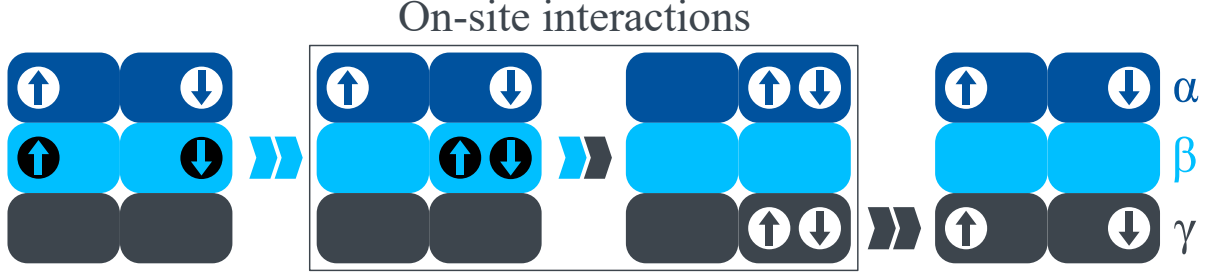
On-site interactions

Figure 6.5: Example for a pair flip process (6.3). A hole from site i in the β orbital hops to site j. On-site Kanamori interactions induce a flip of the double occupation from β to γ. Subsequently, one of the holes in the γ orbital hops back to site i, which results in a so-called pair flip, where the two holes formally residing in β orbitals now reside in the γ orbitals.
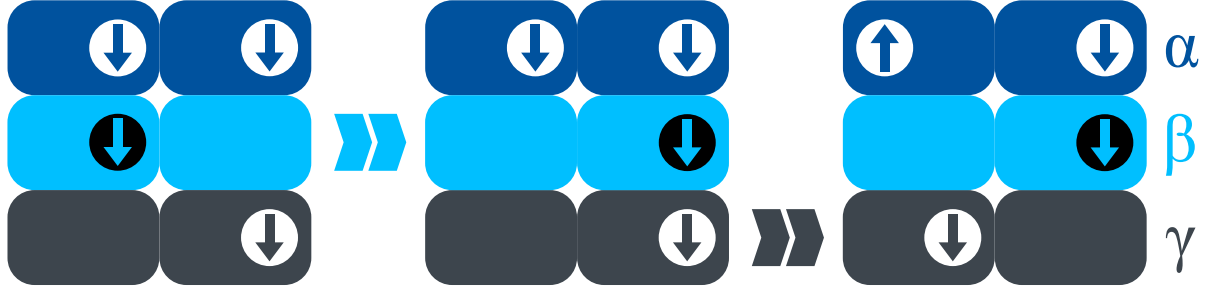

Figure 6.6: Example for the orbital swap process. A hole in the β orbital on-site j hops to site i, afterward the hole in the γ orbital hops from the site i to j, which results in a final configuration that has the orbital configurations of β and γ orbital reversed compared to the initial configuration.

preserve the orbital flavor in the virtual excitation process

$$
\begin{aligned}
H_{\mathrm{OP}} = & \left[t_{\gamma \neq (\alpha, \beta), m}^2 \frac{(U + J_H)}{U(U + 2J_H)} - \frac{(t_{\alpha,m}^2 + t_{\beta,m}^2)J_H}{U(U - 3J_H)} \right] (\mathbf{S}_i \mathbf{S}_j - 1) \left(1 - \mathcal{L}_\alpha^2 \right)_i \left(1 - \mathcal{L}_\beta^2 \right)_j \\
& + t_{\beta,m}^2 \frac{U + J_H}{U(U + 2J_H)} (\mathbf{S}_i \mathbf{S}_j - 1) \left(1 - \mathcal{L}_\alpha^2 \right)_i \left(1 - \mathcal{L}_\alpha^2 \right)_j .
\end{aligned}
\tag{6.2}
$$

Here, we can distinguish between a hopping process where the double occupation of electrons resides in an orbital with the same flavor on both sides (Fig. 6.3) and a scenario where the double occupations of the two sites reside in orbitals with different flavors (Fig. 6.4). In the first case, just orbitals with a single occupation can contribute to the virtual hopping process, while in the second case, all orbitals are involved.

The second type of interactions prevalent in the Hamiltonian are terms that change

the orbital flavor throughout the virtual excitation

$$H_{\text{OF}} = \frac{t_{\alpha,m}t_{\beta,m}}{U}\left[\frac{U - J_H}{U - 3J_H}(\mathbf{S}_i\mathbf{S}_j + 1)(\mathcal{L}_\beta\mathcal{L}_\alpha)_i(\mathcal{L}_\alpha\mathcal{L}_\beta)_j\right.$$
$$\left. - \frac{J_H}{U + 2J_H}(\mathbf{S}_i\mathbf{S}_j - 1)(\mathcal{L}_\beta\mathcal{L}_\alpha)_i(\mathcal{L}_\beta\mathcal{L}_\alpha)_j\right]. \tag{6.3}$$

Again, we can distinguish two types of orbital interactions. If the initial configuration has a double occupation with the same flavor on both sites, virtual hopping, which changes the orbital flavor, is mediated via on-site interactions (Fig. 6.5). The Kanamori Hamiltonian (2.2) can change the orbital flavor of a double occupation on-site i, consequently the active orbitals change. In the sketch, we see that first a hole in the β orbital hops from the site i to j via the kinetic part of the Hamiltonian, the on-site Kanamori Hamiltonian then flips the orbital flavor of the double occupation on-site i from β to γ. Subsequently, the active orbital for the hopping back is the γ orbital. In total this causes a flip of the occupation from β to γ on both sites, which is why we refer to them as "pair-flip" processes. In the second scenario, the initial setup has double occupations in different orbitals on the two sites. Here, the hopping process is pretty straightforward, see Fig. 6.6, leading to a so-called orbital "swap" process. Here, the sites exchange the flavor of the double occupation.

Last but not least, we have terms with just orbital interactions

$$H_{\text{LL}} = \frac{t_{\alpha,m}t_{\beta,m}}{U - 3J_H}\frac{2J_H}{U}(\mathcal{L}_\beta\mathcal{L}_\alpha)_i(\mathcal{L}_\alpha\mathcal{L}_\beta)_j - \frac{t_{\alpha,m}^2 + t_{\beta,m}^2}{U - 3J_H}\left(1 - \mathcal{L}_\alpha^2\right)_i\left(1 - \mathcal{L}_\beta^2\right)_j, \tag{6.4}$$

where the first term is the "flip" process and the second is the orbital preserving term of Fig. 6.4.

The total effective Hamiltonian is achieved by adding (6.2)-(6.4) and performing the summation over all bonds and orbital flavors

$$H_{\text{eff}} = \sum_{m=1}^{3}\sum_{\langle i,j\rangle_m}\sum_{\alpha\neq\beta}(H_{\text{OF}} + H_{\text{OP}} + H_{\text{LL}}). \tag{6.5}$$

Plugging in the hoppings from Tab. 6.1, one then derives at the spin-orbit Hamiltonian, which applies to Ca_2RuO_4. Adding SOC (2.3) and CF (2.6) yields the complete Hamiltonian

$$H = H_{\text{eff}} + H_{\text{SOC}} + H_{\text{CF}}, \tag{6.6}$$

which can be analyzed via ED (Sec. 2.4.1) and Monte-Carlo (Sec. 2.4.2) to determine the ground state properties in dependence of Δ and λ.

7

Δ-λ phase diagram

In this chapter we discuss the influence CF Δ and SOC λ have in t_{2g}^4 square lattice transition metal compounds. In particular, we are interested in the compound Ca_2RuO_4. We begin the analysis in the limiting cases, i.e., dominant λ, implying Van-Vleck magnetism [39], and dominant Δ, supporting a conventional spin-orbit Hamiltonian. From there, we vary λ and Δ to obtain a phase diagram, depending on the strength of CF and SOC. ED on a $\sqrt{8} \times \sqrt{8}$ cluster yields the occurring phases for the entire considered parameter range. We supplement these results with calculations of the triplon model [39], for strong SOC, and semi-classical MC analysis, for weak SOC. To compare the theoretical results with the results of inelastic neutron scattering [5], we analyze the dynamics for the parameters of Ca_2RuO_4. Last but not least, we study dynamic properties in the framework of Ca_2RuO_4 with varied Δ and λ.

7.1 Parameters

The hopping parameters for Ca_2RuO_4 are derived via DFT in [106] and given in Tab. 6.1. As we see the NN interaction hopping parameters have different magnitudes for distinct orbitals, i.e., $t_{xy} > t_{zx} = t_{yz}$. This makes the derivation of a Kugel-Khomskii type model with arbitrary hopping amplitudes for different orbitals, as is done in 6.2, mandatory. X-ray scattering results [107] yield Hund's coupling $J_H = 0.34\,\text{eV}$ and Coulomb repulsion $U = 2.0\,\text{eV}$. The sizable J_H shows the importance of including it in the second-order perturbation theory in Sec. 6.2, it also justifies the restriction to d^2 states with $\mathcal{E}_P$. DFT calculations [106] determined the CF strength to $\Delta = 0.25\,\text{eV}$. Lastly SOC $\lambda = 0.065\,\text{eV}$ is obtained from [107]. Since we are mainly interested in the effect of Δ and λ on Ca_2RuO_4, from now we keep them as free parameters to obtain a $\Delta - \lambda$ phase diagram in which we can locate Ca_2RuO_4.
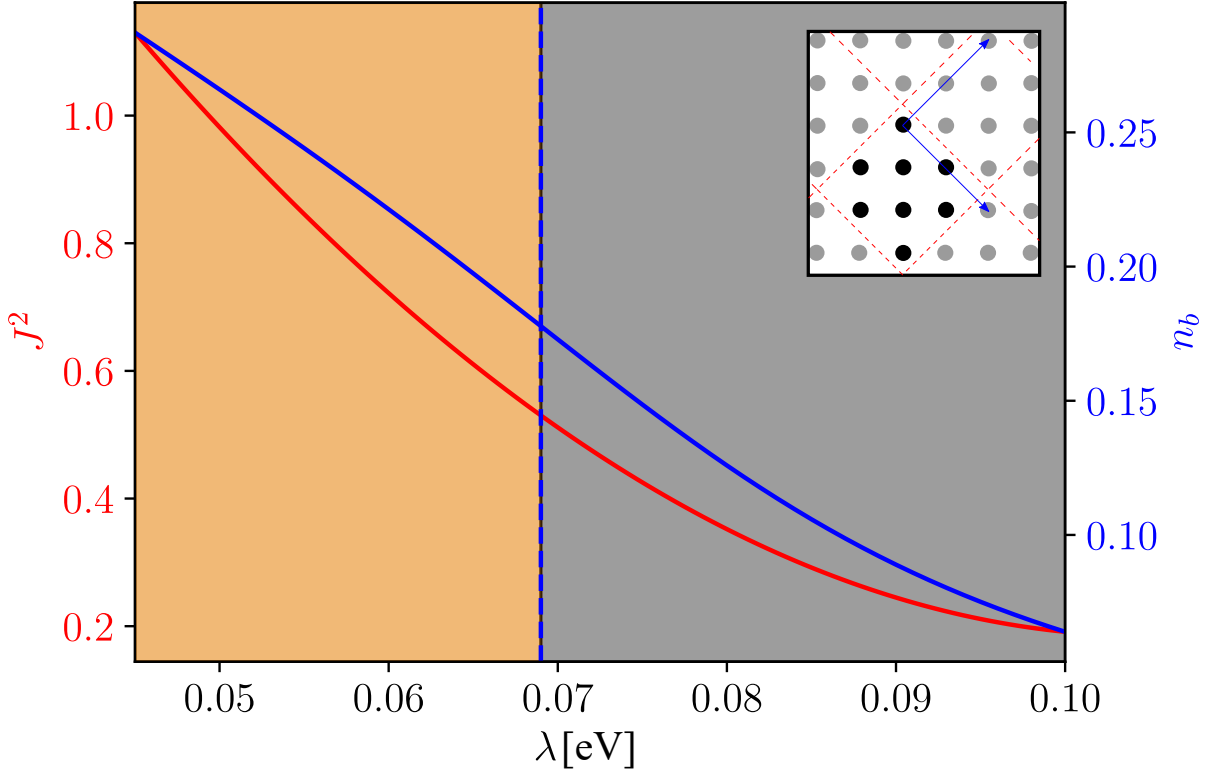
Figure 7.1: Total angular angular momentum J^2 of the spin-orbit model and triplon density n_b of the triplon model calculated via ED and plotted as functions of SOC λ. The dashed vertical line denotes the inflection point of the triplon density n_b, which we interpret as the crossover point into the paramagnet (PM). $\frac{\partial^2 n_b}{\partial \lambda^2} = 0$ determines the location of this inflection point. The parameters are set to $t_{xy} = 0.2\,\text{eV}$, $t_{yz} = t_{xz} = 0.137\,\text{eV}$, $t_{\text{NNN}} = 0.1\,\text{eV}$, $U = 2\,\text{eV}$, $J_{\text{H}} = 0.34\,\text{eV}$, and $\Delta = 0.1\,\text{eV}$. The inset displays the cluster geometry of the $\sqrt{8} \times \sqrt{8}$ cluster used for ED.

7.2 Limiting cases

To gain an impression of the influence Δ and λ have in t_{2g}^4 compounds, we study some important limiting cases. First, we consider the case of $\lambda \gg \Delta$, where we expect the triplon model [39] to hold Sec. 2.2.3. Afterward, we investigate ground state properties for either fixed λ or Δ. Since we do not restrict ourselves to $\lambda \gg \Delta$, it is mandatory to work in the framework of the spin-orbital model, with $S = 1$ and $L = 1$, see App. C. Last but not least, we consider weak λ where we can analyze the spin-orbital model with the semi-classical MC approach. Here, we consider snapshots (fixed Δ and λ) to complement the ED spin-orbit results.

7.2.1 ED for the triplon model

For dominant SOC, spin and orbital degree of freedom couple to the total angular momentum J (Sec. 2.2.3). In case of t_{2g}^4 materials this yields a non-magnetic $J = 0$ ground state [39]. In the limit of strong SOC, the triplon model introduced in 2.2.3 is

	Γ	**X**	**M**	**Y**	**M/2**
k_x	0	π	π	0	$\frac{\pi}{2}$
k_y	0	0	π	π	$\frac{\pi}{2}$

Table 7.1: Possible k vectors on the $\sqrt{8} \times \sqrt{8}$ cluster for exact diagonalization.

valid and one can quantify magnetism of the ground state via the number of triplons in the system, where the absence of $J = 1$ triplons points towards paramagnetism while a high triplon number is an indicator of a magnetic ground state. Mitigating λ, superexchange, which drives the transition from $J = 0$ to $J = 1$ states, becomes non-negligible. This leads to a condensation of triplons [39] (Sec. 2.3.3), resulting in a magnetic ground state.

The crossover to the magnetic state can be captured by the triplon number n_b in dependency of λ, calculated via ED for the triplon model [77] on a $\sqrt{8} \times \sqrt{8}$ cluster. For the calculations we choose a CF of $\Delta = 0.1\,\mathrm{eV}$, see Fig. 7.1. To determine the phase boundary of the paramagnet (PM) ground state, we calculate the inflection point of n_B ($\lambda \approx 0.07\,\mathrm{eV}$). In addition to the triplon number, we display the expectation value of $\langle J^2 \rangle$ (red) calculated via the spin-orbit model in Fig. 7.1. As we can see, $\langle J^2 \rangle$ does not show any inflection, making it difficult to determine a phase boundary with the spin-orbit model (Sec. 6.2). The quantifiable phase transition via the inflection point showcases the advantage of the triplon model for $\lambda \gg \Delta$. Therefore, we use the triplon model to capture physics for dominant λ while the spin-orbit model is applicable for intermediate values of $\lambda \approx 0.08\,\mathrm{eV}$.

7.2.2 ED for the spin-orbit model

We analyze ground state properties of the spin-orbit model via the static spin structure factor (SSF) in momentum space

$$S^\gamma(\mathbf{k}) = \sum_{i,j} e^{i\mathbf{k}(\mathbf{r}_i - \mathbf{r}_j)} \langle \Phi_0 | S_i^\gamma S_j^\gamma | \Phi_0 \rangle , \qquad (7.1)$$

with $\gamma \in [x, y, z]$ and $|\Phi_0\rangle$ the ground state determined via ED. Like for the triplon model, we consider a cluster of $\sqrt{8} \times \sqrt{8}$ geometry, which yields five unique possible values of $\mathbf{k}$ listed in Tab. 7.1. We measure both in-plane ($\gamma \in [x, y]$) and out-of-plane ($\gamma = z$) moments, if both in-plane moments coincide we display just the S^x moment. One can infer the spin-order of the ground state from the SSF. A strong signal at **M** hints an AFM, while a strong signal at **X** signifies a stripy order with ferromagnet (FM) order in one bond direction and AFM order in the other one. Last but not least, a strong signal at Γ implies ferromagnetic order.
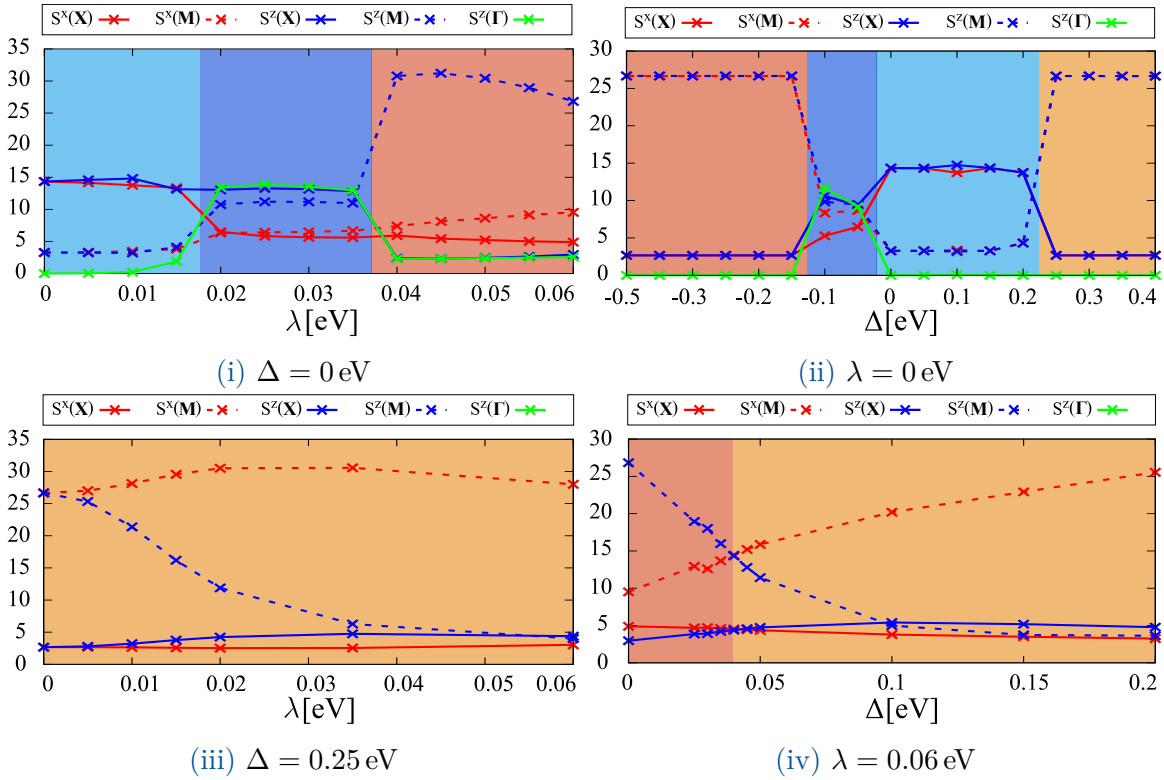
(i) $\Delta = 0\,\mathrm{eV}$

(ii) $\lambda = 0\,\mathrm{eV}$

(iii) $\Delta = 0.25\,\mathrm{eV}$

(iv) $\lambda = 0.06\,\mathrm{eV}$

Figure 7.2: in-plane (x) and out-of-plane static spin structure factor (SSF) measured at $\mathbf{\Gamma}$, $\mathbf{M}$, and $\mathbf{X}$. Displayed are the scenarios for fixed CF at $\Delta = 0.0\,\mathrm{eV}$ (i) and $\Delta = 0.25\,\mathrm{eV}$ (iii) and varied λ as well as scenarios for fixed SOC at $\lambda = 0\,\mathrm{eV}$ (ii) and $\lambda = 0.06\,\mathrm{eV}$ (iv). The background is shaded according to the respective phase, i.e., out-of-plane AFM (dark orange), in-plane AFM (light orange), stripy (light blue), and "3-up-1-down" (3U1D) (dark blue).

We want to analyze the limiting cases of vanishing and dominant Δ, with λ as a free parameter and *vice versa.* Fig. 7.2(i)-(iv) displays the results for these cases. At $\Delta = 0\,\text{eV}$, we can identify two sharp phase transitions in the considered parameter range. The dominant signals at **X** indicate a stripy phase for weak SOC $\lambda < 0.018\,\text{eV}$. An increase of SOC suppresses the in-plane Ş (red) while strongly enhancing the out-of-plane SSF's Γ and **M**. Since all out-of-plane contributions are of comparable magnitude it is difficult to unambiguously identify the nature of the ground state in the $0.018 < \lambda < 0.037\,\text{eV}$ parameter range with ED. We discuss the nature of this phase with FM contributions in more detail in the context of MC simulations (Sec. 7.2.3). Lastly, increasing SOC up to $\lambda > 0.037\,\text{eV}$ causes yet another phase transition into what appears to be an out-of-plane AFM, due to the dominant out-of-plane **M** contributions.

For vanishing SOC $\lambda = 0\,\text{eV}$, Fig. 7.2(ii), we observe three phase transitions in the considered parameter range. An isotropic AFM arises for $-0.5 < \Delta < -0.12\,\text{eV}$. As we will show later, this phase is continuously connected with the out-of-plane AFM identified previously (Fig. 7.1). Increasing Δ yields the yet unidentified phase with dominant out-of-plane FM contributions in the range of $-0.12 < \Delta < -0.02\,\text{eV}$. For $-0.02 < \Delta < 0.23\,\text{eV}$ the ground state becomes an isotropic stripy phase in agreement with the phase identified for small SOC and vanishing Δ [Fig. 7.2(i)]. In case the CF gets further enhanced, the ground state is again an isotropic AFM. However, this AFM state is not continuously connected with the out-of-plane AFM (dark orange in Fig. 7.2), like for strong negative CF, but appears to be connected with an in-plane AFM for finite SOC (light orange in Fig. 7.2).

The smooth transition from the isotropic AFM to the in-plane AFM at dominant CF $\Delta = 0.25\,\text{eV}$ becomes obvious in Fig. 7.2(iii). Increasing SOC from $0 < \lambda < 0.06\,\text{eV}$ we observe the suppression of the out-of-plane moment going hand in hand with an enhancement of the in-plane AFM moment indicating an in-plane AFM for finite values of SOC.

Last but not least, we study the ground states for strong SOC at $\lambda = 0.06\,\text{eV}$. As discussed previously, for a negative CF the ground state is an out-of-plane AFM prevailing up to $\Delta \approx 0.04\,\text{eV}$. The ground state becomes an in-plane AFM for larger CF's.

Summarizing, we found that finite SOC and strong CF favor the formation of an AFM. The orientation of this AFM depends on the sign of Δ, with $\Delta \ll 0$ yielding an out-of-plane and $\Delta \gg 0$ an in-plane AFM. For small values of both CF and SOC ED results yield a stripy phase for $\Delta > 0\,\text{eV}$ in agreement with [63]. In addition, the ED calculations gave rise to phase with significant out-of-plane FM contributions for small $\Delta < 0\,\text{eV}$, not yet reported.

7.2.3 MC for the spin-orbit model

If multiple signals have comparable magnitude it is complicated to unambiguously identify the ground state via ED. Therefore, we supplement ED with MC calculations. We focus on the phase with FM out-of-plane contributions, which is ambiguous in the ED analysis.

We perform semi-classical MC calculations on a 4×4 square lattice cluster with periodic boundary conditions. One advantage of MC calculations is the capability of calculating larger cluster sizes. In addition, our calculations yield a visual picture of the ground state on the 4×4 cluster in position space, which yields a convenient way to identify magnetic orders. However, MC in the spin-orbit basis has limitations going to strong SOC, being incapable of capturing the PM observed for strong SOC [77]. MC is therefore mainly used to confirm the stripy, AFM, and yet undetermined phase arising for weak SOC. To compare ED and MC results, we take "snapshots" at fixed Δ and λ with MC. We choose the values of Δ and λ for these snapshots, which solidly locates them in one of the four distinct phases found with ED. Fig. 7.3 shows the four resulting MC "snapshots" are displayed.

The out-of-plane AFM Fig. 7.3(i), stripy (iii), and in-plane AFM phases are confirmed by the Monte-Carlo simulations. The spin components in momentum space [lower pictures in Fig. 7.3(i)-(iv)] coincide with the static SSF of the ED calculations. Meanwhile, the results displayed in the location domain [upper pictures in Fig. 7.3(i)-(iv)] give a clear impression of the spin patterns. The yet ambiguous phase with FM contributions can also be put into context with the help of the spatial SSF. As can be seen in Fig. 7.3, the momentum space spin-components shows finite signals at $\mathbf{X}$, $\mathbf{Y}$, $\mathbf{M}$, and $\mathbf{\Gamma}$. However, the spatial SSF makes an interpretation of the results of both ED and MC possible. The phase arising appears to be a mixture between out-of-plane stripy and AFM phase, where stripes with FM order alternate with AFM stripes, yielding a spin pattern which can we describe as "3-up-1-down" (3U1D) on a 2×2 cluster. Therefore, with the MC calculations, we have an interpretation of all four phases arising for small values of SOC λ.

7.3 Phase diagram

After considering the limiting cases for fixed values of either Δ or λ and identifying the five distinct ground states arising within the considered parameter range we now want to derive a complete Δ-λ phase diagram. To obtain the phase boundaries, we perform sweeps for multiple values of CF Δ and SOC λ. To capture both the magnetic phases as well as the PM, we perform sweeps for both the triplon as well as the spin-orbit model.
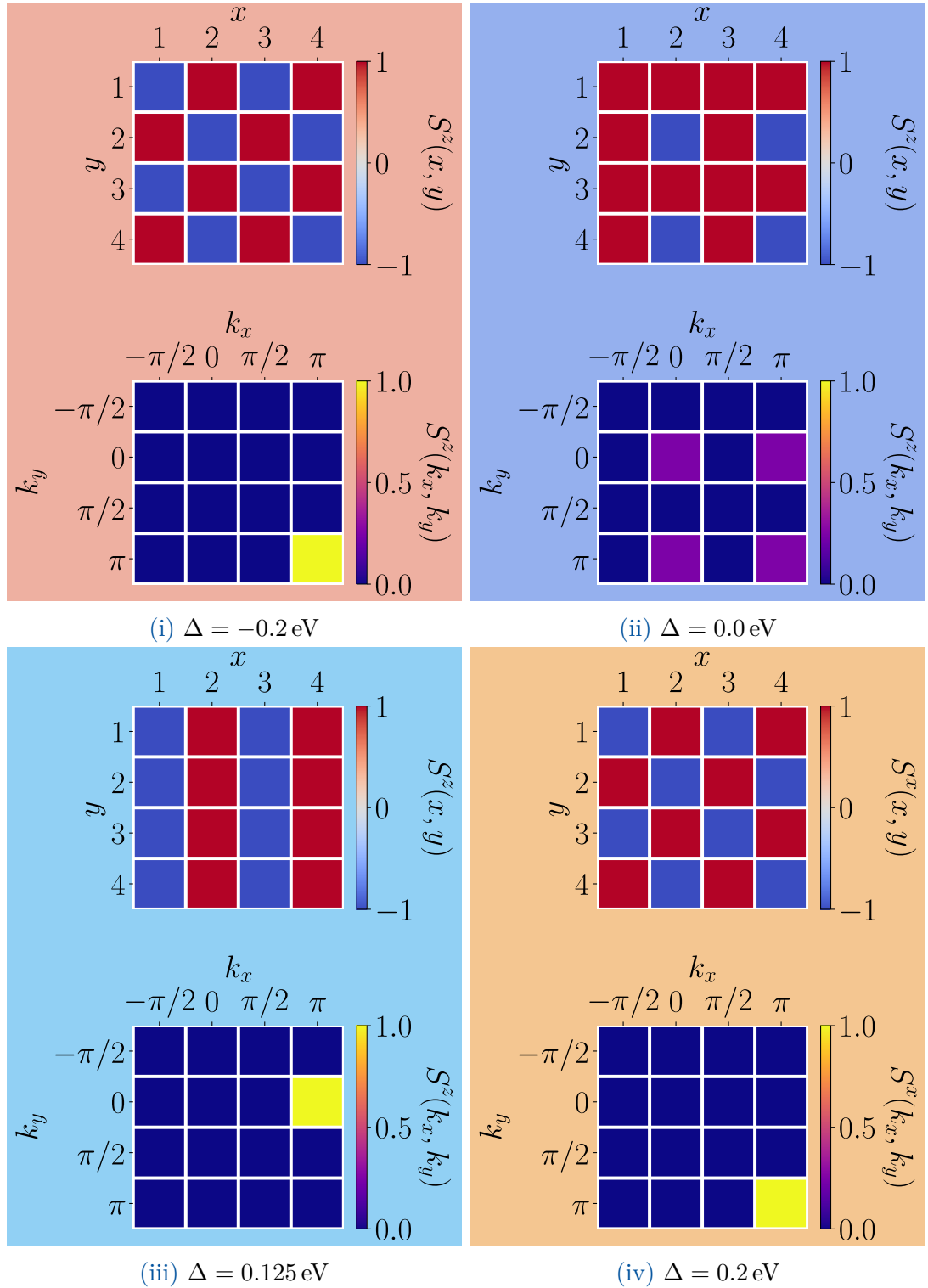
Figure 7.3: x and z spin component calculated via semi-classical MC on a 4×4 cluster are displayed in both position and momentum space at $\lambda = 0.01\,\text{eV}$ and $\Delta = -0.2\,\text{eV}$ (i), $0.0\,\text{eV}$ (ii), $0.125\,\text{eV}$ (iii), and $0.2\,\text{eV}$ (iv). Each plot displays the spin component with the most dominant spin contribution. The top of (i)-(iv) displays the strength of the respective spin component on each site of the considered cluster. The bottom plot displays the spin components for all calculated wave vectors $\mathbf{k}$.
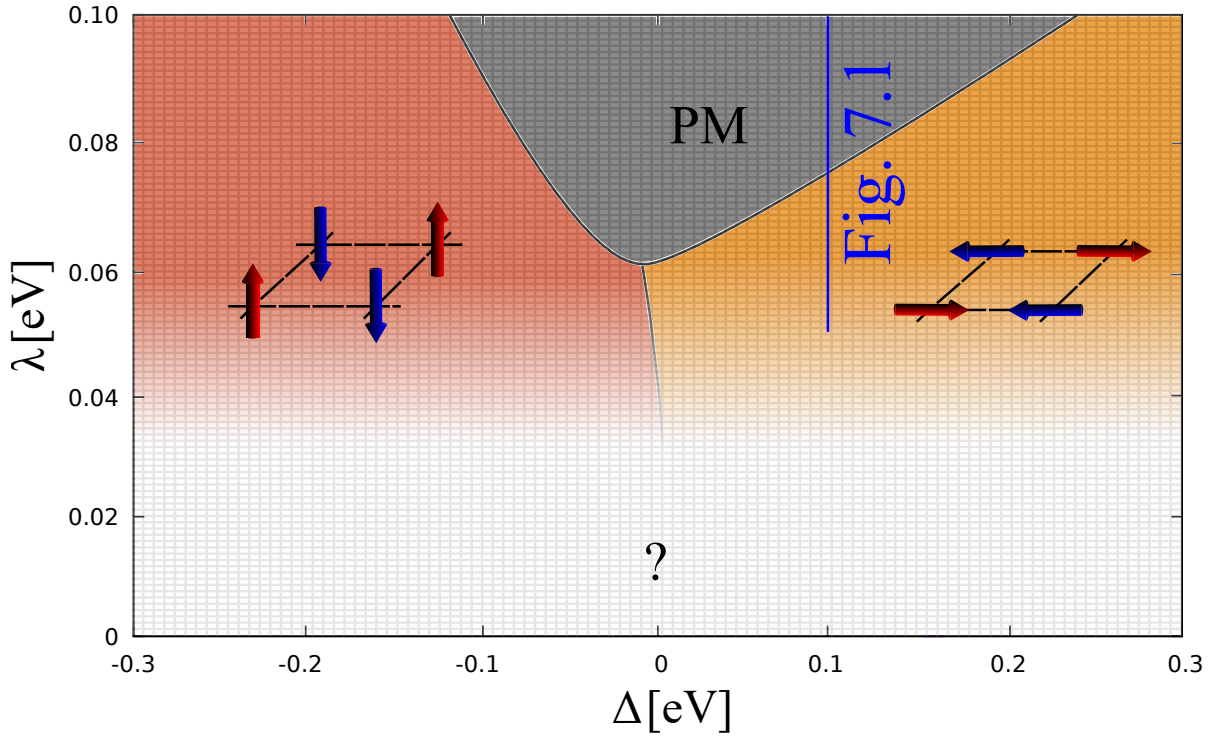
Figure 7.4: Phase diagram of the triplon model calculated via ED on a $\sqrt{8} \times \sqrt{8}$ cluster. Out-of-plane and in-plane AFM phases are colored in dark and light orange respectively. In addition, we display cartoons of the respective AFM ordering. The PM determined via the inflection point in the second derivative (see Fig. 7.1) is displayed in grey. The blue line denotes the parameter setting used for Fig. 7.1. Finally, the fading of all phases for weak SOC signifies the incapability of the triplon model to capture the correct ground state in this parameter range.

7.3.1 ED for the triplon model

The triplon model is analyzed via ED and gives rise to the phase transition to the PM, as described in Sec. 7.2.1. Fig. 7.4 depicts the Δ-λ phase diagram of the triplon model. While for sizable SOC, the triplon model is feasible and the PM can be identified via the inflection point (Fig. 7.1), at small SOC the triplon picture breaks down and results are no longer valid. However, the results for $\lambda > 0.04$ eV agree with the findings of Sec. 7.2.2, that a negative CF induces an out-of-plane AFM while $\Delta > 0$ favors an in-plane AFM arrangement. It also becomes obvious that the presence of a CF counteracts the formation of PM. The phase transition to the PM for $\Delta \approx 0$ eV is at $\lambda \approx 0.06$ eV. Introducing a finite Δ then increases λ at which the phase transition occurs. The phase boundary between in-plane and out-of-plane AFM is at $\Delta \approx 0$ eV and not very susceptible to a change of λ. With these results, we can locate the PM within the spin-orbit model and give a complete phase diagram for sizable λ.
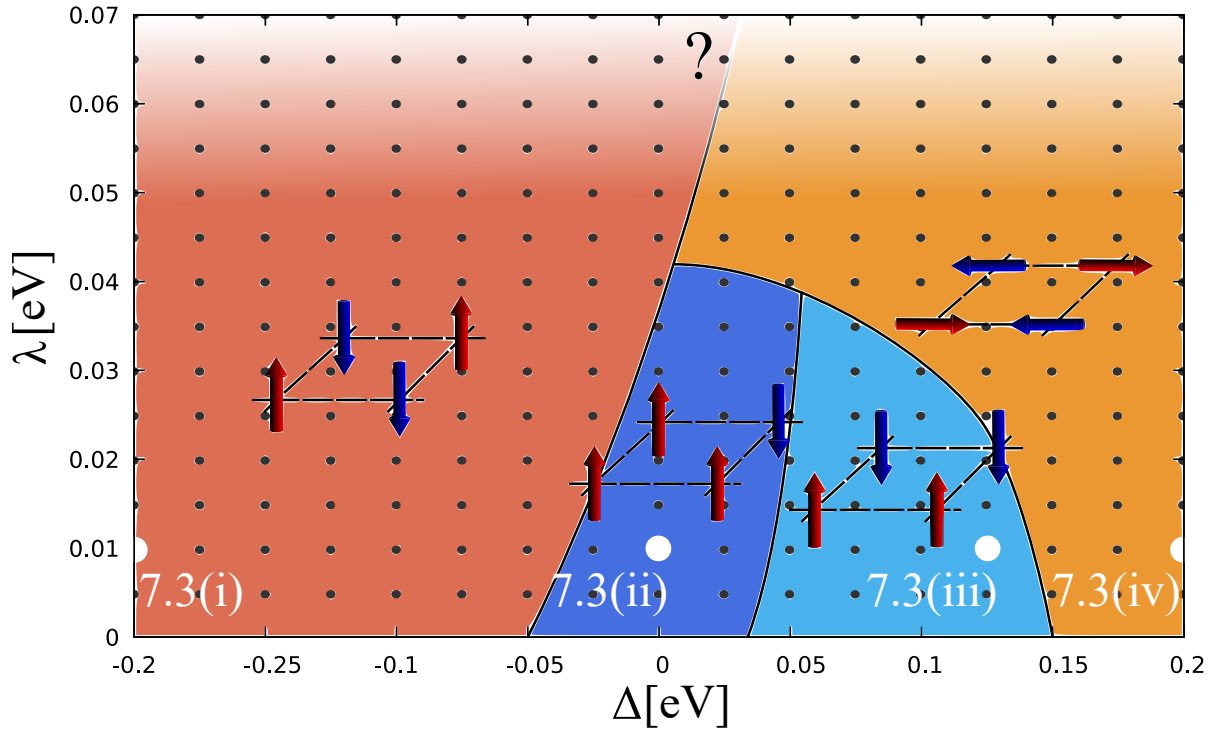
Figure 7.5: Phase diagram of the spin-orbital model calculated via semi-classical MC simulations on a 4×4 cluster. The four distinct phases found, i.e., out-of-plane AFM, "3-up1-down", Zig-Zag, and in-plane AFM are displayed in dark orange, dark blue, light blue, and light orange respectively. Insets show sketches of the ground state spin arrangements on a 2×2 cluster of all phases. The white dots denote the location of the snapshots taken in Fig. 7.3. The fading for strong SOC, like in Fig. 7.4, displays the incapability of the MC simulations to correctly predict the ground state properties (see Sec. 7.3.2).

7.3.2 MC for the spin-orbit model

To analyze the phases arising for small SOC λ we have to analyze the spin-orbit model introduced in Sec. 6.2. Like for the single sweeps in Sec. 7.2.2, we perform both ED and semi-classical MC simulations.

Here, we start with the MC analysis, which gives rise to the phase diagram depicted in Fig. 7.5. The grey grid denotes the Δ-λ parameters used to calculate ground state properties. The snapshots of Fig. 7.3 are marked with white dots and annotated accordingly. For large SOC, the incapability of MC to calculate the accurate ground state is denoted with a "?" in Fig. 7.5. For small SOC, we can identify the four distinct phases found in Sec. 7.2.3. Cartoons of a 2×2 cluster visualize the phases in Fig. 7.5. A sizable negative CF $\Delta < -0.05$ eV induces an out-of-plane AFM phase. Increasing λ leads to an expansion of this phase up to even positive values of Δ. Therefore, strong SOC and strong negative CF favor the out-of-plane AFM.

In the range of $-0.05 < \Delta < 0.03$ eV and $\lambda \approx 0$ eV the 3U1D phase arises. Unlike the

out-of-plane AFM, it gets superseded by an in-plane AFM ordering beyond $\lambda \approx 0.04\,\text{eV}$. We observe a similar behavior for the stripy phase arising within $0.03 < \Delta < 0.15\,\text{eV}$ and weak SOC. If we increase SOC, the stripy phase narrows until it vanishes at $\lambda \approx 0.04\,\text{eV}$. Both, 3U1D and stripy, are therefore favored by small SOC and CF. Therefore, we can attribute their origin to the nature of spin-orbit exchange interactions, because these become dominant for vanishing Δ and λ.

variational cluster approach (VCA) calculations on a 2×2 cluster [63] already documented the stripy phase. However, there are no reports of the 3U1D phase in the context of VCA. The reason is that, in VCA, one has to set the order of the potential ground state. VCA then gives information on whether the chosen order is a good choice. The 3U1D order was not a candidate order in [63] and was therefore not discussed as the potential ground state. However, there have been ED calculations on Ca-based Ru-compounds [108], which also discuss the potential of a 3U1D phase.

Lastly, for large positive CF $\Delta > 0.15\,\text{eV}$, the MC simulations give rise to the in-plane AFM. Like the out-of-plane AFM, the in-plane AFM expands upon increasing λ and suppresses both the stripy and 3U1D phase beyond $\lambda \approx 0.04\,\text{eV}$. Therefore, at $\lambda \gg 0\,\text{eV}$ only AFM phases prevail, with the orientation (in-plane our out-of-plane) depending on the sign of the CF. That is in agreement with the results of the triplon model and Fig. 7.2(iv).

7.3.3 ED for spin-orbit model

Up until now, we investigated the phase diagram for strong SOC via ED of the triplon model and for weak SOC via MC of the spin-orbit model. To piece together these findings, we analyze the spin-orbit model via ED, which is valid for the entire considered parameter range of λ. Fig. 7.6 shows the resulting Δ-λ phase diagram. We take the phase boundaries of the PM from the triplon model Fig. 7.4. We observe a good qualitative agreement between the ED and MC simulations.

The 3U1D and stripy phase are more expanded concerning Δ compared to the MC results. Reasons for this difference can be both the difference in cluster size of the calculations and quantum fluctuations near orbital degeneracy neglected by the MC calculations. Like for the MC results a negative CF Δ favors an out-of-plane AFM prevailing up to $\Delta \approx -0.12\,\text{eV}$ and $\lambda \approx 0\,\text{eV}$. Upon increasing λ the out-of-plane AFM phase broadens at the cost of the 3U1D phase. Spatial SSFs hint a 3U1D formation within $-0.12 < \Delta < -0.05\,\text{eV}$. These phase boundaries are significantly different from the findings of MC calculations. The 3U1D phase shifts to higher CF $\Delta \approx 0\,\text{eV}$ for finite λ. Like in MC, this phase is absent for large SOC $\lambda > 0.04\,\text{eV}$.

The stripy phase arises at $-0.05 < \Delta < 0.22\,\text{eV}$, and is, therefore, significantly broader as in the MC calculations. Increasing SOC narrows down the stripy phase,
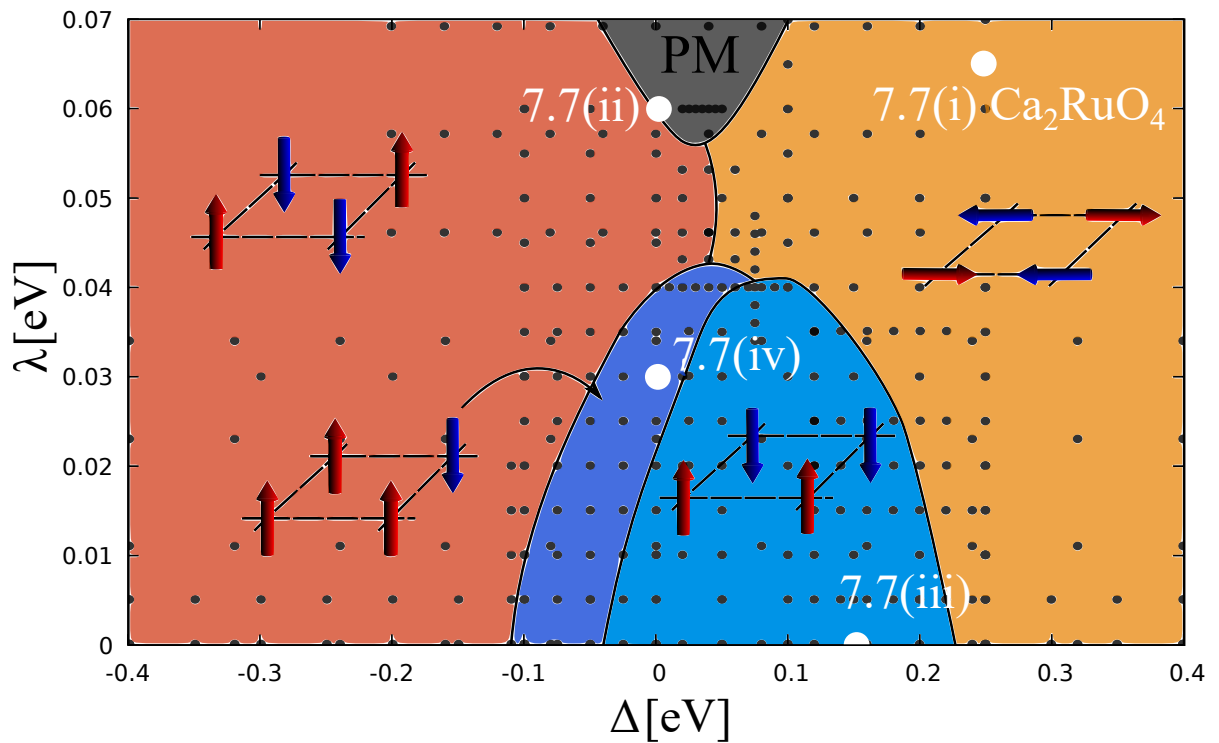
Figure 7.6: λ-Δ phase diagram of the spin-orbit model calculated via ED on a $\sqrt{8} \times \sqrt{8}$ cluster. Color coding of the phases is the same as in Fig. 7.4 and Fig. 7.5. Like in Fig. 7.5, cartoons of a 2×2 illustrate the phases as a cluster spin configuration. The results of the triplon model yield the PM. White dots denote the snapshots taken to calculate the dynamic spin structure factor (DSSF) of the four magnetic phases in Fig. 7.7. Grey dots denote parameters for numerical calculations.
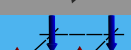
$\|\Delta\| \gg t^2/U, \lambda$ and $\Delta \gg 0$	$\rightarrow$	in-plane AFM
$\|\Delta\| \gg t^2/U, \lambda$ and $\Delta \ll 0$	$\rightarrow$	out-of-plane AFM
$\lambda \gg t^2/U, \Delta$	$\rightarrow$	paramagnet
$t^2/U \gg \lambda, \Delta$ and $\Delta \geq -0.02\,\mathrm{eV}$	$\rightarrow$	stripy
$t^2/U \gg \lambda, \Delta$ and $\Delta < -0.02\,\mathrm{eV}$	$\rightarrow$	3-up-1-down

Table 7.2: Ratio of Δ, λ, and t^2/U for the five distinct phases found in the Δ-λ phase diagram. Cartoons show an illustration of the respective phase on a 2×2 cluster.

upon $\lambda = 0.04\,\mathrm{eV}$ where it completely vanishes.

Between $0.04 < \lambda < 0.06\,\mathrm{eV}$, the only phases present are the in-plane and out-of-plane AFM, with the latter expanding to small positive values of Δ. For $\lambda > 0.06\,\mathrm{eV}$ the PM arises at small CF's broadening further with increasing λ (see also Fig. 7.4).

With the help of ED and MC for the spin-orbit and triplon model, we were able to arrive at a complete Δ-λ phase diagram capturing physics for both weak and sizable SOC λ. We found that for dominant CF, the ground state is an AFM arrangement with either in-plane ($\Delta > 0$) or out-of-plane ($\Delta < 0$) orientation. Spin-orbit coupling favors the formation of a $J = 0$ nonmagnetic state, while the superexchange $\propto t^2/U$ favors a nonzero magnetization. Superexchange favors the stripy phase as the magnetic ground state. However, this state is highly susceptible to the influence of Δ, e.g., already a weak negative CF induces the 3U1D phase.

7.4 Dynamics

One of the key questions arising after analyzing the ground state properties theoretically is how to connect these results with experimental measurements. A common experimental method to determine ground state properties for the considered material family is inelastic neutron scattering (INS) [5], which measures magnetic excitations. Therefore we analyze the dynamic spin structure factor (DSSF)

$$O^\alpha(\mathbf{k}, \omega) = -\frac{1}{\pi}\mathrm{Im}\,\langle\phi_0|\,O^\alpha(-\mathbf{k})\frac{1}{\omega - H + i0^+}O^\alpha(\mathbf{k})\,|\phi_0\rangle, \qquad (7.2)$$

with $\mathbf{O} = \mathbf{S}$ and $\alpha \in \{x, y, z\}$, of all four magnetic phases found. In addition to the DSSF, with (7.2), we can also calculate the dynamic orbital structure factor (DOSF) ($\mathbf{O} = \mathbf{L}$) and the magnetic structure factor ($\mathbf{O} = \mathbf{m}$). We can obtain a frequency-resolved DSSF $S^\alpha(\mathbf{k}, \omega)$, which can be compared with the experimental results of INS [5].

(i) $\Delta = 0.25\,\text{eV}$ and $\lambda = 0.065\,\text{eV}$

(ii) $\Delta = 0.0\,\text{eV}$ and $\lambda = 0.06\,\text{eV}$

(iii) $\Delta = 0.15\,\text{eV}$ and $\lambda = 0.0\,\text{eV}$

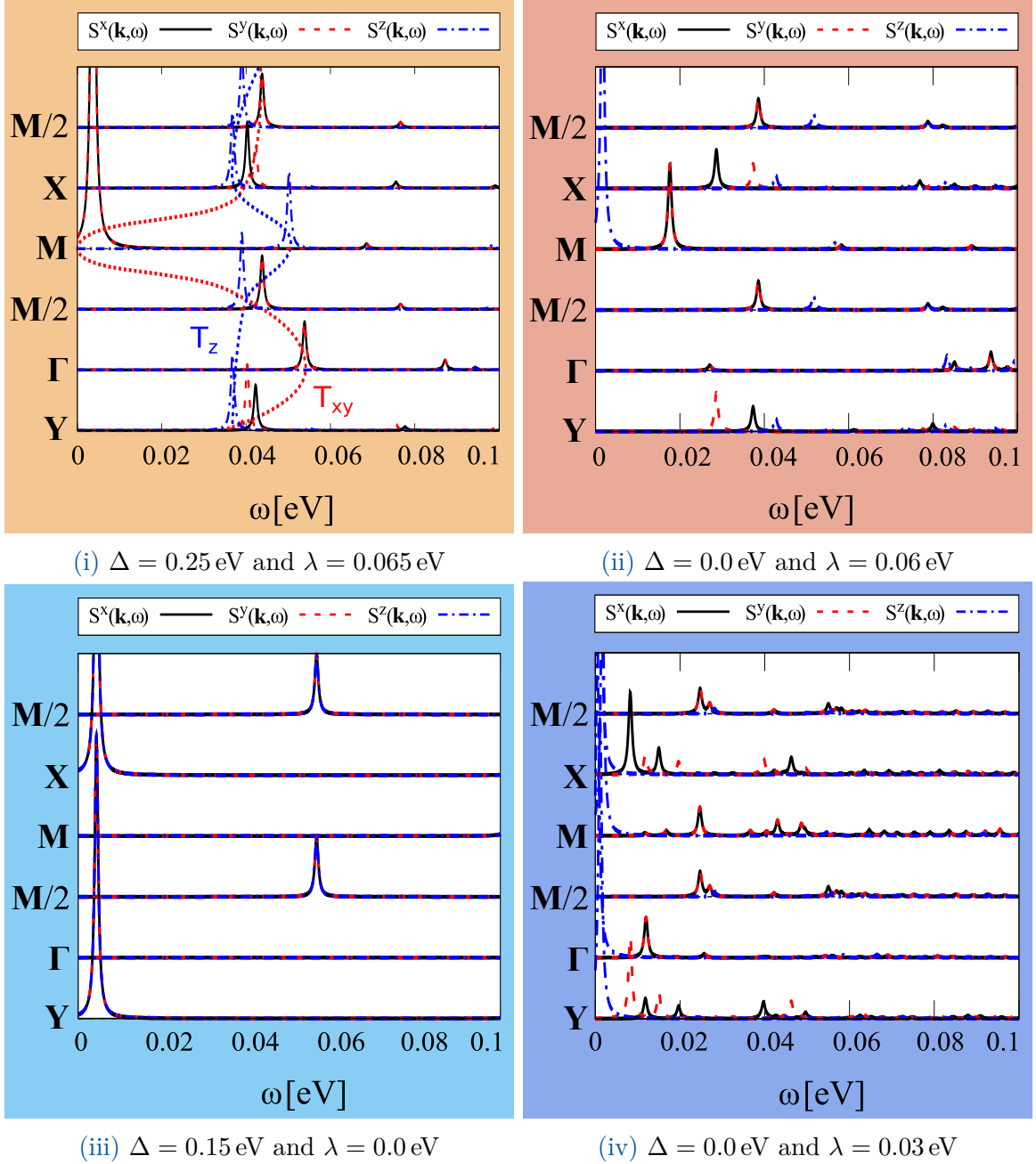(iv) $\Delta = 0.0\,\text{eV}$ and $\lambda = 0.03\,\text{eV}$

Figure 7.7: Dynamic spin structure factor (DSSF) calculated with ED on a $\sqrt{8} \times \sqrt{8}$ cluster via (7.2). The results for the in-plane AFM (i), out-of-plane AFM (ii), stripy (iii), and "3-up-1down" (iv) phase are displayed. The parameters used in (i) are expected for Ca_2RuO_4 [63] and are in good agreement with the inelastic neutron scattering (INS) measurements of [5]. The red and blue dashed lines in (i) are a guideline for the in-plane and out-of-plane transverse modes respectively.
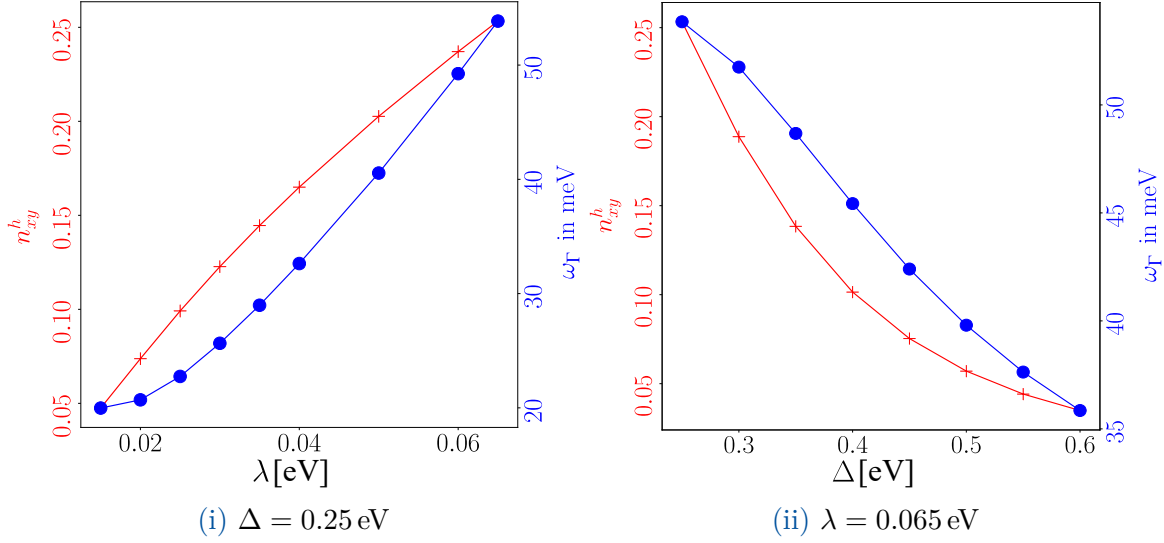
Figure 7.8: Hole density in the d_{xy} orbital n^h_{xy} (red crosses) and excitation energy at the $\mathbf{\Gamma}$-point $\omega_{\mathbf{\Gamma}}$ (blue dots) in dependency of λ (i) and Δ (ii). The parameter which is not varied, Δ and λ for (i) and (ii) respectively, is fixed at the value of Ca_2RuO_4 taken from Sec. 7.1.

To analyze the DSSF, we took snapshots at fixed Δ and λ, with the results for the four distinct phases displayed in Fig. 7.7. White dots denote the location of the snapshots in the phase diagram in Fig. 7.6. In the following, we will analyze the results for each phase separately, especially focusing on the in-plane AFM snapshot, which is the expected ground state of Ca_2RuO_4.

7.4.1 In-plane AFM excitations - Ca_2RuO_4

To compare the DSSF of ED calculations with INS results, we calculate the DSSF for realistic values for Ca_2RuO_4. DFT calculations [106] and X-ray scattering results [107] yield $\lambda = 0.065\,\text{eV}$ and $\Delta = 0.25\,\text{eV}$, for SOC and CF. The results for all available wavevectors $\mathbf{k}$ are displayed in Fig. 7.7(i). We can identify an in-plane Goldstone mode at $\mathbf{M}$. This indicates the presence of an in-plane AFM as found in Fig. 7.6. In addition to the Goldstone mode, we can extrapolate both the in-plane and out-of-plane transverse modes, indicated as dashed lines in Fig. 7.7(i). The maximum of the in-plane transverse mode at $\mathbf{\Gamma}$ is reminiscent of the transverse mode measured in INS experiments [5]. If we compare the excitation energies measured in experiments with our results, we find a very good agreement. The maximum at $\omega_{\mathbf{\Gamma}} = 54\,\text{meV}$ is reproduced by our calculations, which solidifies the validity of the spin-orbit model, derived in Sec. 6.2. This maximum is indicative of the isotropic in-plane orientation of the magnetic moments.

Hereafter, we want to discuss the connection between $\omega_{\mathbf{\Gamma}}$ and the hole density in the xy orbital n^h_{xy}. The hole density is intertwined with the ratio between Δ and λ.

That is the case, because strong SOC favors equal hole distributions in all t_{2g} orbitals, while Δ enforces a vanishing n_{xy}^h. This competition of Δ and λ is the focal point of the discussions revolving around Ca_2RuO_4, as explained in Sec. 1.2. Investigating the behavior of n_{xy}^h might help to clarify the role λ and Δ play in Ca_2RuO_4.

Starting from the Ca_2RuO_4 parameters, we gradually decrease SOC while keeping the CF fixed Fig. 7.8(i). Decreasing λ reduces the hole density (red crosses) significantly to a point where n_{xy}^h almost vanishes $n_{xy}^h \approx 0.05\,\text{eV}$. This behavior seems to be closely connected to the excitation energy $\omega_{\boldsymbol{\Gamma}}$ at $\boldsymbol{\Gamma}$, as we observe a drastic decrease of $\omega_{\boldsymbol{\Gamma}}$. Starting from the maximum measured in the experiment for $\lambda = 0.065\,\text{eV}$, the excitation energy turns into a minimum at $\omega_{\boldsymbol{\Gamma}} = 20\,\text{meV}$ for $\lambda = 0.02\,\text{eV}$, not resembling the experimental transversal mode anymore. We conclude that n_{xy}^h, and therefore λ, has a decisive influence on the magnetic excitations observed in Ca_2RuO_4. Meanwhile, the value of $n_{xy}^h = 0.25$ at $\lambda = 0.065\,\text{eV}$, still implies an almost fully occupied xy orbital, justifying the picture of an orbital ordered ground state.

To complement the results of Fig. 7.8(i), we also increase Δ [Fig. 7.8(ii)] with a fixed λ. As expected, we observe a decrease of n_{xy}^h from $n_{xy}^h = 0.25$ at $\Delta = 0.25\,\text{eV}$ to $n_{xy}^h \approx 0.05\,\text{eV}$ at $\Delta = 0.6\,\text{eV}$. Like for Fig. 7.8(i), this decrease goes hand in hand with a decrease of the excitation energy, from a maximum at $\omega_{\boldsymbol{\Gamma}} = 54\,\text{meV}$ to a minimum at $\omega_{\boldsymbol{\Gamma}} \approx 35\,\text{meV}$. We can conclude that the excitation energy $\omega_{\boldsymbol{\Gamma}}$ is closely connected with the hole density of the xy orbital n_{xy}^h.

Comparing the influence of Δ and λ (Fig. 7.8) we see that while the effect on $\omega_{\boldsymbol{\Gamma}}$ is qualitatively the same, there are also some clear distinctions. In both cases, the hole density goes to a minimum of $n_{xy}^h \approx 0.05$ at $\lambda \approx 0.02\,\text{eV}$ or $\Delta \approx 0.6\,\text{eV}$ respectively. Meanwhile $\omega_{\boldsymbol{\Gamma}}$ differs for small SOC [Fig. 7.8(i)] $\omega_{\boldsymbol{\Gamma}} \approx 20\,\text{meV}$ and strong CF [Fig. 7.8(ii)] $\omega_{\boldsymbol{\Gamma}} \approx 36\,\text{meV}$. From this, we deduce that SOC and CF appear to have a direct influence on the excitation energy at $\boldsymbol{\Gamma}$, in addition to the indirect influence via the hole density. We conclude that while the ground state is quite robust against perturbations in both Δ and λ, the excitation spectra are quite sensitive towards these perturbations. With this knowledge, the good agreement of the excitation spectra in Fig. 7.7(i) with the INS results appears quite remarkable. These results also imply that both SOC and CF have a sizable influence on the dynamics in Ca_2RuO_4.

7.4.2 Excitations for other magnetic orders

In addition to the results of Sec. 7.4.1, we want to analyze the dynamics of the other magnetic phases found in the ground state analysis of Sec. 7.3.3. We start at a vanishing CF $\Delta = 0.0\,\text{eV}$ and finite SOC $\lambda = 0.06\,\text{eV}$. Fig. 7.7(ii) shows the results of the DSSF's. The Goldstone mode arising at $\mathbf{M}$ has a clear out-of-plane signal. If we increase SOC to $\lambda = 0.12\,\text{eV}$ and keep $\Delta = 0.0\,\text{eV}$ [Fig. 7.9(i)], a transition into the PM (Sec. 7.3.3)

(i) $\lambda = 0.12\,\text{eV}$, $\Delta = 0.0\,\text{eV}$

(ii) $\lambda = 0.12\,\text{eV}$, $\Delta = 0.25\,\text{eV}$
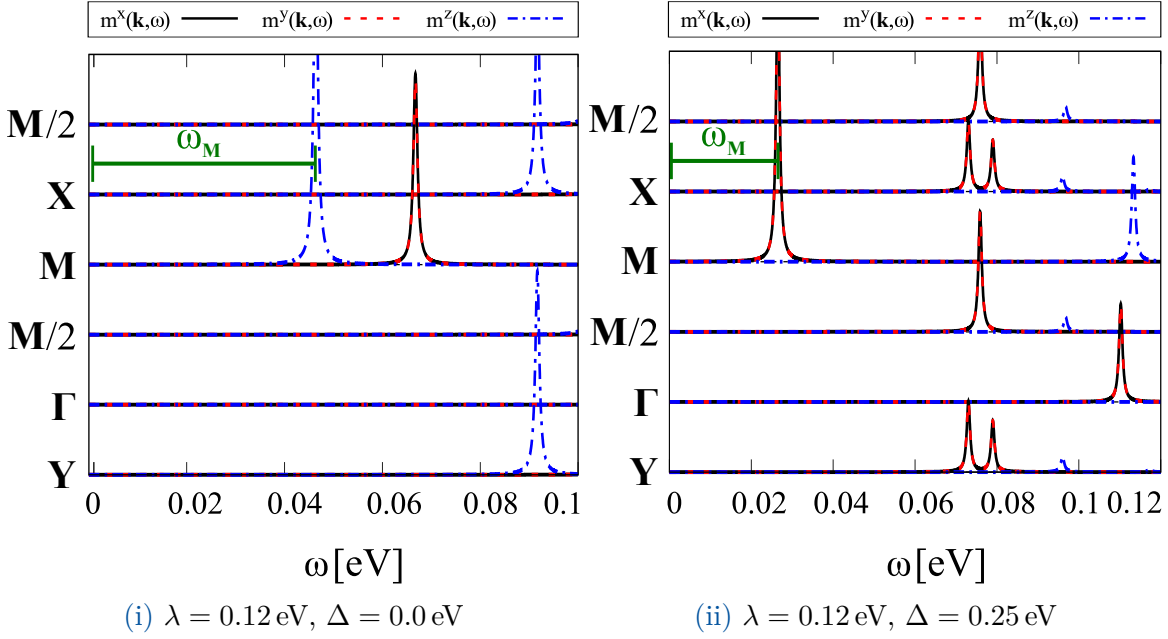
Figure 7.9: Dynamic magnetic structure factor $m^\alpha(\mathbf{k}, \omega)$ for significant SOC $\lambda = 0.12\,\text{eV}$ at $\Delta = 0.0\,\text{eV}$ (i) and $\Delta = 0.25\,\text{eV}$ (ii). The excitation energy $\omega_\mathbf{M}$ at $\mathbf{M}$ is denoted with a green bar in (i) and (ii) and is indicative of the possibility of triplon condensation.

occurs. Indicative for this is the finite excitation energy $\omega_\mathbf{M} \approx 0.046\,\text{eV}$ at $\mathbf{M}$, indicated with a green bar in Fig. 7.9(i). The absence of a Goldstone mode indicates a lack of magnetic ordering in the ground state, as predicted by the triplon model (Fig. 7.1).

Increasing CF up to $\Delta = 0.25\,\text{eV}$, Fig. 7.9(ii), the excitation energy at $\mathbf{M}$ decreases significantly up to a value of $\omega_\mathbf{M} \approx 0.027\,\text{eV}$, which is in concordance with the fact that a finite CF favors the condensation of triplons and therefore a magnetic ground state (Sec. 7.2.1). The importance of a finite CF also becomes evident in the phase diagram (Fig. 7.6) where Ca_2RuO_4 would be in the PM ground state if CF would be absent.

The DSSF's of the other two phases, stripy and 3U1D found in the phase diagram, Fig. 7.6, are displayed in Fig. 7.7(iii) and (iv) respectively. We take the snapshots at weak SOC, $\lambda = 0.0\,\text{eV}$ (iii) and $\lambda = 0.03\,\text{eV}$ (iv), and therefore we find the characteristic Goldstone modes for these two phases. For the stripy phase, we identify two Goldstone modes arising at $\mathbf{X}$ and $\mathbf{Y}$, yielding a degeneracy between the x and y stripy phase. Furthermore, these Goldstone modes have equal contributions from x, y, and z DSSF's, which indicates an isotropic stripy phase. The 3U1D phase [Fig. 7.7(iv)] shows four Goldstone modes, which arise at the $\mathbf{k}$ vectors previously discussed in Tab. 7.1. In contrast to the stripy phase, all Goldstone modes have an out-of-plane nature with dominant $S^z(\mathbf{k}, \omega)$ contributions.

Last but not least, we want to analyze the DSSF in case of a negative CF, yielding an out-of-plane checkerboard pattern, discussed in [77]. We set the CF to $\Delta = -0.3\,\text{eV}$, which is sufficient to fix the xy orbital at half filling and a double occupancy in either

(i) DSSF $\lambda = 0.2\,\mathrm{meV}$

(ii) DOSF $\lambda = 0.2\,\mathrm{meV}$

(iii) DSSF $\lambda = 0.01\,\mathrm{eV}$

(iv) DOSF $\lambda = 0.01\,\mathrm{eV}$
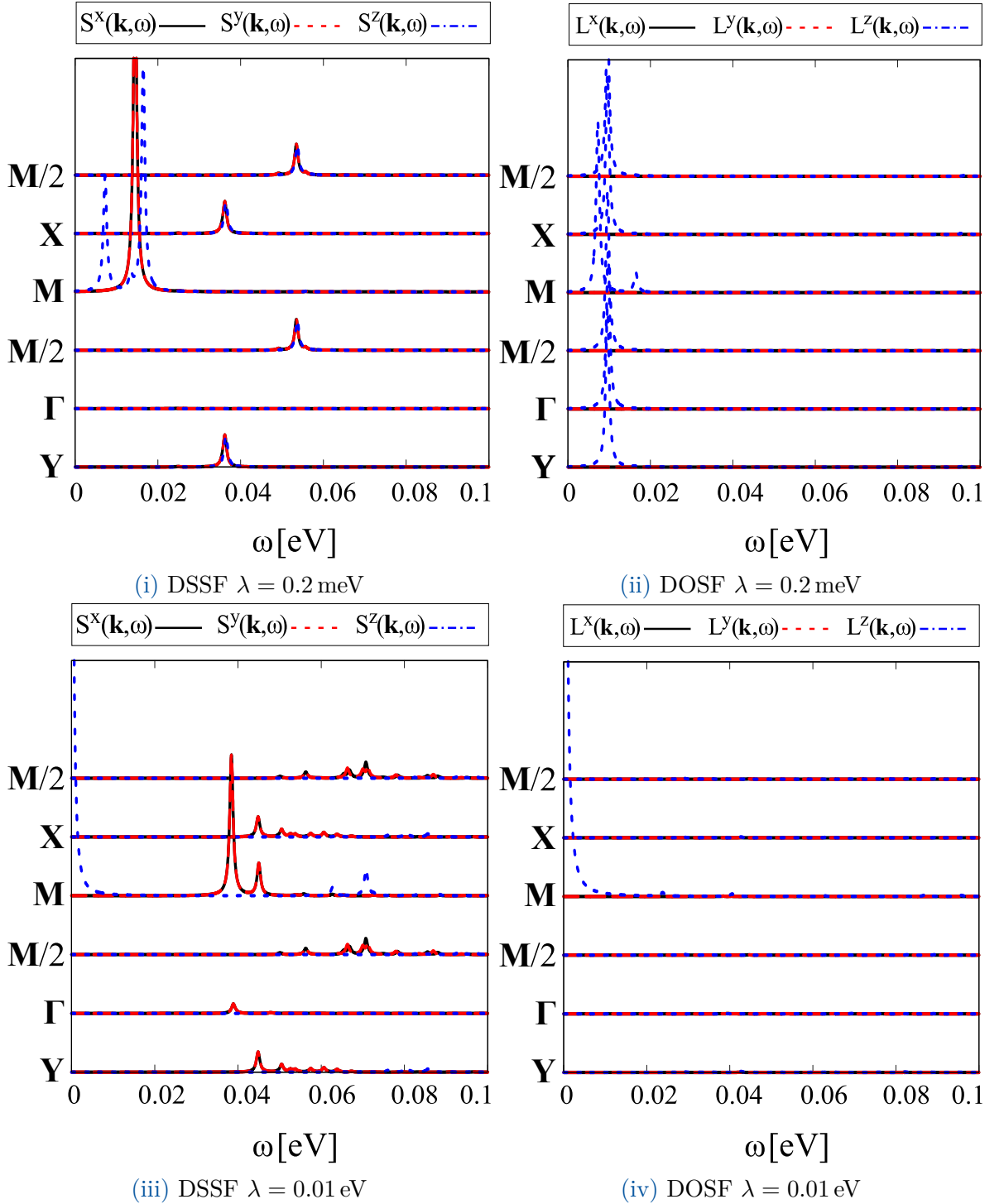
Figure 7.10: DSSF and DOSF at negative CF $\Delta = -0.3\,\mathrm{eV}$ for $\lambda = 0.2\,\mathrm{meV}$ (i)-(ii) and $\lambda = 0.01\,\mathrm{eV}$ (iii)-(iv). We performed calculations with ED. The DOSF is calculated via (7.2), with $\mathbf{O} = \mathbf{L}$.

the xz or yz orbital at vanishing SOC $\lambda = 0.0\,\text{eV}$. We expect that these two configu-
rations alternate on the lattice in a checkerboard manner, with the same unit cell as
the Heisenberg spin AFM. Fig. 7.10(i) shows the results for almost vanishing SOC at
$\lambda = 20^{-4}\,\text{eV}$. As we see, the small SOC already induces a slight anisotropy in the al-
most isotropic DSSF, yielding that the AFM is only purely isotropic at $\lambda = 0.0\,\text{eV}$. For
the DOSF, which can be obtained similarly as the DSSF setting $\mathbf{O} = \mathbf{L}$ in (7.2), we
obtain the results shown in Fig. 7.10(ii). The DOSF, in contrast to the DSSF, does
not show any clear ordering preference and remains featureless. While at first glance,
this appears to be contradicting the expected checkerboard pattern expected, we have
to keep in mind that alternating orbital order is quadrupolar, i.e., features would show
up in the $(L^x)^2 - (L^y)^2 \propto n_{xy}^h - n_{yz}^h$ channel. Since we do not measure this channel
in our calculations we do not observe any features. The spin isotropy gets completely
lifted for more sizable SOC. As an example, we show the DSSF for $\lambda = 0.01\,\text{eV}$, in
Fig. 7.10(iii), where we observe a pronounced ordered moment along the z-axis with a
significant excitation gap. Furthermore, the orbital order clearly shows dipolar nature
[Fig. 7.10(iv)] with a peak at $\mathbf{M}$. An increase of SOC thus causes coupling between the
spin and orbital sector, which leads to a checkerboard pattern with $L^z = 1$, $S^z = -1$ on
one sublattice, and $L^z = -1$, $S^z = 1$ on the other. If we compare the influence of SOC
on the magnetic order with the behavior for $\Delta > 0$, we see that rather than a continuous
transition from the isotropic to the anisotropic AFM, like displayed in Fig. 7.2(iii), the
transition for $\Delta < 0$ is very sharp.

8

Finite temperature analysis

Chap. 7 solely focuses on the ground state properties and dynamics at $T = 0$. In this chapter, we want to investigate the effective model of Chap. 6 for finite temperatures. With the semiclassical MC method introduced in Sec. 2.4.2, we can capture finite temperature properties such as magnetization $M(T)$ and heat capacity $C(T)$. We start our numerical analysis by investigating the impact of cluster sizes on the Néel temperature T_N. We then introduce the feedback optimized parallel tempering (FOPT) method [109] to our system to see whether it improves the MC results. Last but not least, we study the effect of SOC λ and CF Δ on the Néel temperature determined via $M(T)$ and $C(T)$.

8.1 Magnetization and specific heat

The model derived in Chap. 6 can be used to obtain finite temperature results, which can be compared qualitatively to well-known experimental commodities of Ca_2RuO_4, such as the Néel temperature. Ca_2RuO_4 undergoes a phase transition from a paramagnetic phase into the ordered in-plane at a Néel temperature of $T_N \approx 113\,K$ [42, 43]. This phase transition manifests itself as a peak in the specific heat $C(T) = \partial_T E(T)$, with ground state energy E, as well as the magnetic susceptibility $\chi(T) = \partial_T M(T)$, with magnetization $M(T)$. Both $\chi(T)$ and $C(T)$ can be calculated via the semi-classical MC approach used for $T \approx 0$ in Sec. 7.2.3. A caveat in calculating Néel temperatures via MC is the finite size of the cluster, which is why one should be cautious comparing T_N from MC quantitatively with experimental results. However, general trends of T_N, like, e.g., dependence on parameters like CF and SOC, should be captured qualitatively well by the MC simulations.

(i) Energy
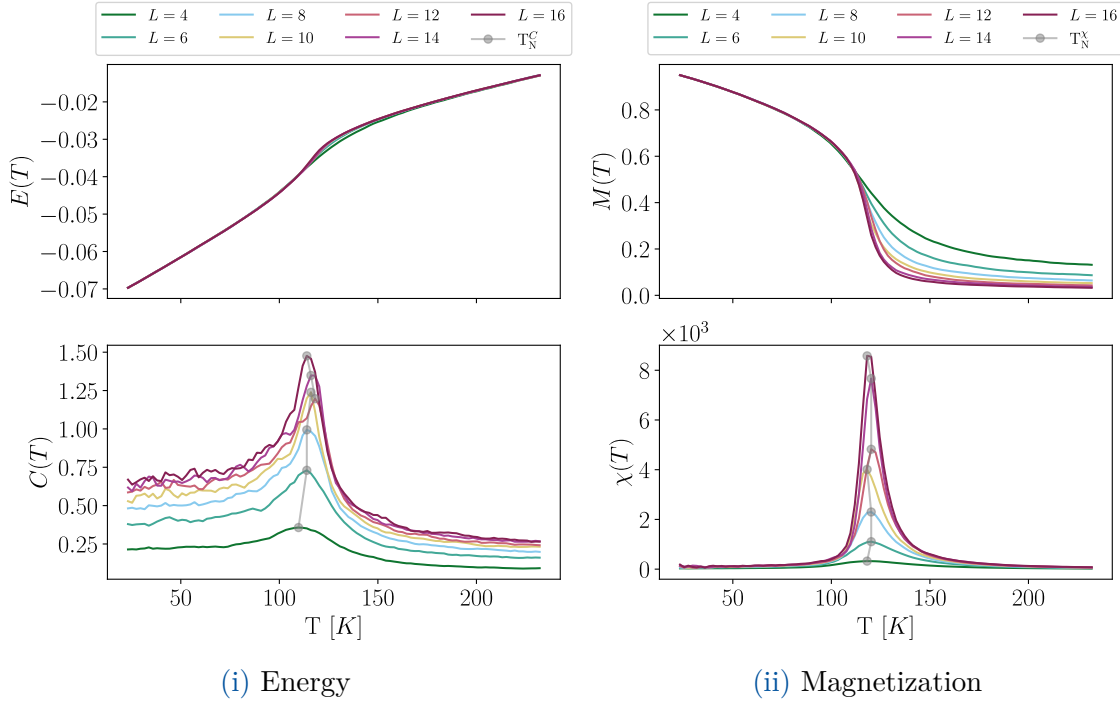
(ii) Magnetization

Figure 8.1: Ground state energy $E(T)$ and specific heat $C(T)$ as function of the temperature T (i), and magnetization $M(T)$ and susceptibility $\chi(T)$ as function of T (ii) for different $L \times L$ cluster sizes. The simulations are done for 100 temperatures arranged in an equidistant manner. The Néel temperature is indicated with grey dots in $C(T)$ and $\chi(T)$. The grey line is a guideline for the evolution of T_N as a function of cluster size. We choose parameters according to Tab. 8.2 A.

L	4	6	8	10	12	14	16
$C\,[a.u.]$	0.36	0.73	0.99	1.24	1.20	1.35	1.48
$T_N^C\,[K]$	109.7	113.9	113.9	116.1	118.2	116.1	113.9
$\chi\,[a.u.]$	322.7	1104.4	2298.9	4009.5	4821.5	7664.9	8578.4
$T_N^\chi\,[K]$	118.1	120.2	120.2	118.1	120.2	120.2	118.1

Table 8.1: Néel temperature T_N in dependency of cluster size L^2 determined via specific heat $C(T)$ and susceptibility $\chi(T)$.
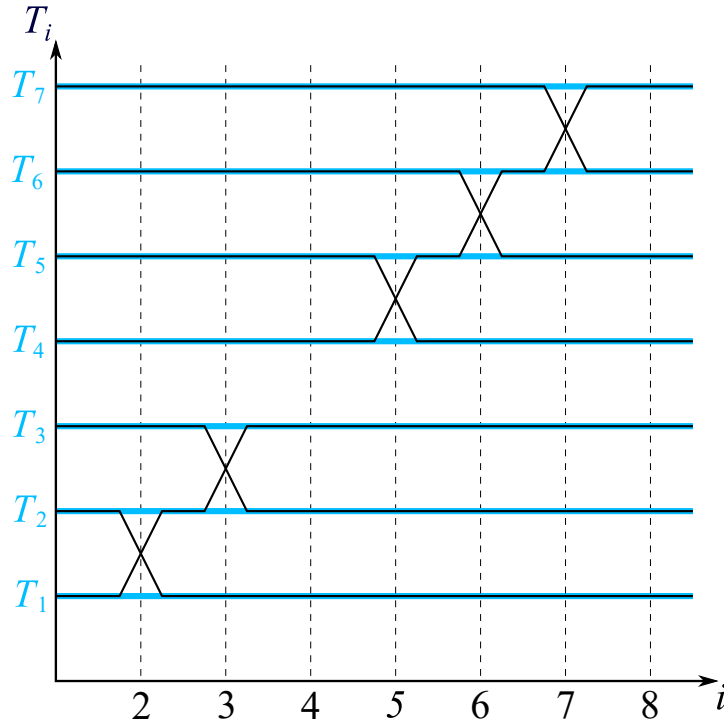
Figure 8.2: Sketch of the PTMC simulation. Black lines denote replicas with T_i, which can swap with the replica at T_{i-1} at the i-th iteration step of the swap process.

8.2 Finite size scaling of T_N

In order to determine the Néel temperature T_N for Ca_2RuO_4 with our effective model we set $\lambda = 0.065\,\text{eV}$ and $\Delta = 0.25\,\text{eV}$ (see Sec. 8.1). Fig. 8.1 shows the results for χ and C for different cluster sizes. The Néel temperature is determined as the maximum of χ (C) and denoted with grey circles in Fig. 8.1 (i) and (ii). With the increase of the cluster size L^2 the maximum in χ (C) gets more pronounced, which is expected [110]. The Néel temperature is almost unaffected by the increase of the cluster from $L = 4$ to $L = 16$, see Tab. 8.1. We determine the Néel temperature of Ca_2RuO_4 on a 16×16 cluster to $T_N^\chi = 118.1\,\text{K}$ and $T_N^C = 113.9\,\text{K}$ via the maximum in susceptibility χ and specific heat C respectively. These are both in very good agreement with the experimental measurements [50]. We again want to stress that finite-size effects could still play a decisive role in these calculations. Therefore, we do not claim that our model is appropriate to predict exact T_N for real materials. Since the Néel temperature stays relatively unaffected within the considered cluster sizes, we use a $L = 8$ cluster for further calculations in this chapter, keeping in mind that it probably slightly overestimates T_N.

8.3 Parallel tempering Monte Carlo

PTMC has become a reliable numerical method for a multitude of applications [111–113]. The main advantage of PTMC compared to conventional MC is the higher probability of escaping from local minima at low T. In a conventional Metropolis algorithm, the probability of accepting a new state at a temperature T is

$$P = \min\left\{1, e^{-\Delta E/T}\right\}, \tag{8.1}$$

where ΔE is the energy difference between the old and new state. It is evident that for low temperatures the probability of changing configurations decreases if the new configuration has a higher energy than the old one. This can cause a convergence towards a local minimum, which is not desired. PTMC attempts to solve this issue by using m replicas of the system at different temperatures T, which can exchange after a certain amount of MC steps. This means that copies at low temperatures can move to higher T, where it is easier to escape local minima. An exchange of temperatures T_i and T_{i-1} is accepted with the probability

$$A_i = \min\left\{1, \exp\left[(\beta_i - \beta_{i-1})(U_i - U_{i-1})\right]\right\} \tag{8.2}$$

with $\beta_i = 1/k_B T_i$ the inverse temperature and U_i the potential energy of replica i as introduced in [111]. One then goes iteratively over all replicas i to obtain the setting for the next MC run see Fig. 8.2. These two steps, Monte Carlo steps and exchange of replica i and $i-1$, are then repeated until convergence. In the end, one obtains the ground state configuration for m different temperatures, including a replica at $T \approx 0\,\mathrm{K}$, which we can compare to ED results (like done in Sec. 7.2.3). PTMC is therefore especially suited for finite temperature analysis.

8.4 Feedback optimized parallel tempering

As we can see in (8.2), the choice of the temperature distribution $\mathbf{T} = (T_1, T_2, T_3, ..., T_m)$ for the m replicas is of crucial importance for the exchange probability. Most commonly $\mathbf{T}$ is either linear in T or β. However, it has been argued [109] that for problems, with a diverging specific heat, this distribution might not be suitable to guarantee a fast equilibration of the m replicas [109]. The reason is that the acceptance rate of a swap process depends on the inverse of the specific heat, i.e., a high specific heat causes a low acceptance rate A. Therefore, for temperature replicas below T_N it is unlikely to swap with replicas above T_N, which is not desirable because the replicas are supposed to cover a large part of the energy landscape. To circumvent this Katzgraber *et al.* proposed
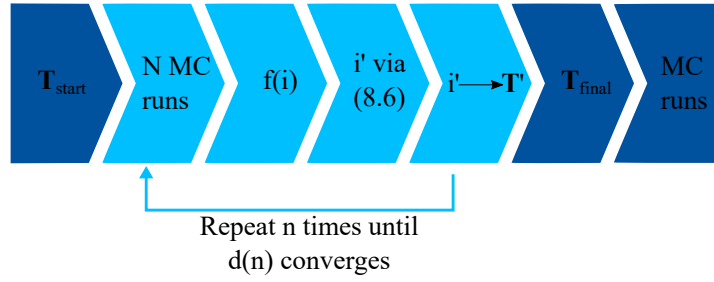
Figure 8.3: Sketch of the FOPT iteration.

the FOPT method, which aims to obtain $\mathbf{T}$ with high acceptance rates around the bottlenecks. As it turns out, this results in a $\mathbf{T}$ condensed around T_N. That additionally guarantees a high resolution of the phase transition, so T_N can be determined precisely. Since Ca_2RuO_4 has a finite temperature of $T_N \approx 113\,K$ [42, 43], the FOPT method should, in theory, be suitable here and lead to faster equilibration. To see whether FOPT is advantageous for our model, we discuss the implementation of the FOPT and its application to our problem.

8.4.1 Theory

One can find a detailed description of the FOPT in [109, 114]. In this section, we will briefly discuss the method and the details important for the implementation of our problem. One goal of the FOPT is to adjust $\mathbf{T}$ to expedite the equilibration time for all temperature replicas. This is realized by minimizing the time a replica needs to travel from the minimal temperature $T_{\min}$ to the maximal temperature $T_{\max}$ and back (see Fig. 1 in [109]). This consequently reduces the time of the replica, especially those with temperatures below T_N, to cover the phase space and converge towards the global minimum. Like in [109], we first introduce $u(i)$ and $d(i)$, which count the number of replicas at T_i, that have last visited $T_{\min}$ and $T_{\max}$ respectively. This is done after a certain number of Monte-Carlo steps, to guarantee reliable statistics. To obtain reliable statistics, a sizable number of Monte-Carlo steps is mandatory, so most of the replicas have either visited $T_{\min}$ or $T_{\max}$. This comes at a high computational cost, the impact of which we will discuss later. With reliable values for $u(i)$ and $d(i)$ we can define the flow

$$f_u(i) = \frac{u(i)}{u(i) + d(i)}, \tag{8.3}$$

describing the fraction of replicas which have visited $T_{\min}$ most recently. This can be defined analogous for $T_{\max}$ as $f_d(i)$. In the remainder of this chapter, we consider the flow coming from $T_{\min}$ and therefore set $f_u(i) = f(i)$.

Contrary to [109], we defined the flow as a function of the index i instead of the

associated temperature T_i. In our simulations, we found that this approach yields better results. For $T_i = T_{\min}$ the flow trivially becomes $f(i) = 1$, because all replicas traveling through $T_{\min}$ most recently have visited $T_{\min}$. *Vice versa* for $T_i = T_{\max}$ the flow becomes 0 independently of the number of Monte-Carlo steps used to obtain $u(i)$ and $d(i)$. The density $\eta(T_i)$, introduced in (5) of [109], in our framework becomes constant $\eta(i) = C$, because all indexes are equidistant with a distance 1 between them. The constant becomes $C = 1/m$ due to the normalization condition $\sum_{i=1}^{m} \eta(i) = 1$. The optimized density distribution can be obtained via $\eta'(i) = C' \sqrt{\partial_i f(i)}$ with C' guaranteeing the normalization of $\eta'(i)$. Similar to (11) in [109], we then can obtain an optimized index distribution via

$$m \sum_{j=1}^{i} \eta'(j) = i', \tag{8.4}$$

where the sum goes over the initial indexes up to the index of interest i and i' is the associated optimized index. With this, we can obtain an optimized index for each replica. It is of note that i' is no longer an integer. However, we still can map the set of optimized indexes $\mathbf{i}' = (1', 2', 3', ..., m')$ back to a set of temperatures $\mathbf{T}'$ via linear interpolation. Therefore, we obtain a set of optimized temperatures, which we assign with the original index set $\mathbf{i}$ so that $\mathbf{T}' = (T'_1, T'_2, ...T'_m)$. With $\mathbf{T}'$ we can restart the process of calculating an improved flow. One repeats this process until the flow function $f(i)$ becomes linear as a function of the replica index i. A linear $f(i)$ guarantees a minimal time to cover the phase space. The flowchart in Fig. 8.3 summarizes the FOPT process.

As a criterion for the linearity of $f(i)$, we introduce the deviation from a linear function

$$d(n) = \frac{1}{m} \sum_{i=1}^{m} \left| (f_n(i) - \max f_n) \left(1 - \frac{i}{m}\right) \right|, \tag{8.5}$$

where the sum goes over the number of the replicas m, and n is the iteration index. As an abort criterion for the FOPT iterations, we demand $d(n) < 0.05$ to guarantee a sufficient $\mathbf{T}$. As mentioned earlier, the FOPT proves to be significantly more efficient and accurate for the index i instead of the temperature T like in [109] for our implementation.

8.4.2 Ising model

To benchmark the FOPT implementation we start with a toy model introduced in [109], the ferromagnetic Ising model

$$H = -J \sum_{\langle i,j \rangle} S_i S_j, \tag{8.6}$$

(i) $T(n)$

(ii) $d(n)$
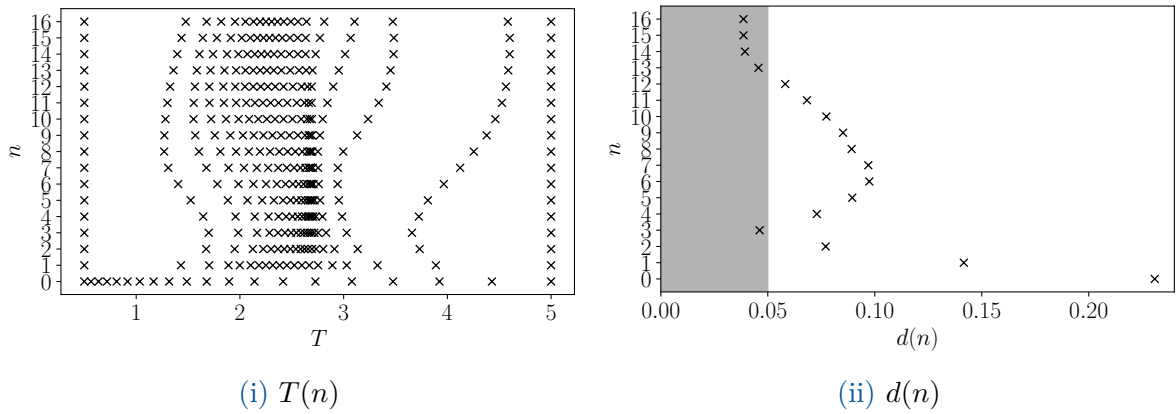
Figure 8.4: Temperature distribution $\mathbf{T}(n)$ (i) and deviation $d(n)$ (ii) for $n = 16$ FOPT iterations and $\mathbf{T}_\beta$ in the Ising model.
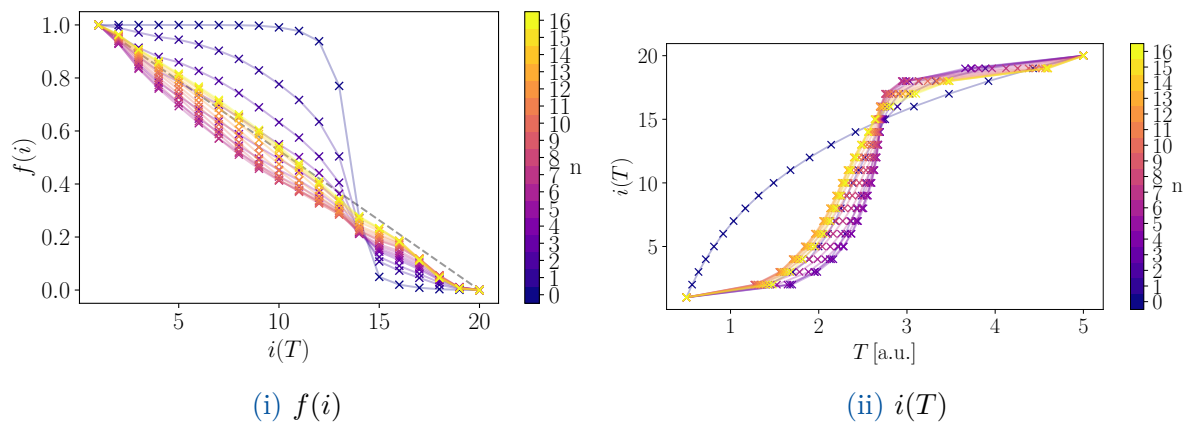

(i) $f(i)$

(ii) $i(T)$

Figure 8.5: Flow $f(i)$ (i) and replica index $i(T)$ (ii) for $n = 16$ FOPT iterations and $\mathbf{T}_\beta$ in the Ising model. Iteration step n is indicated by the respective colormap.
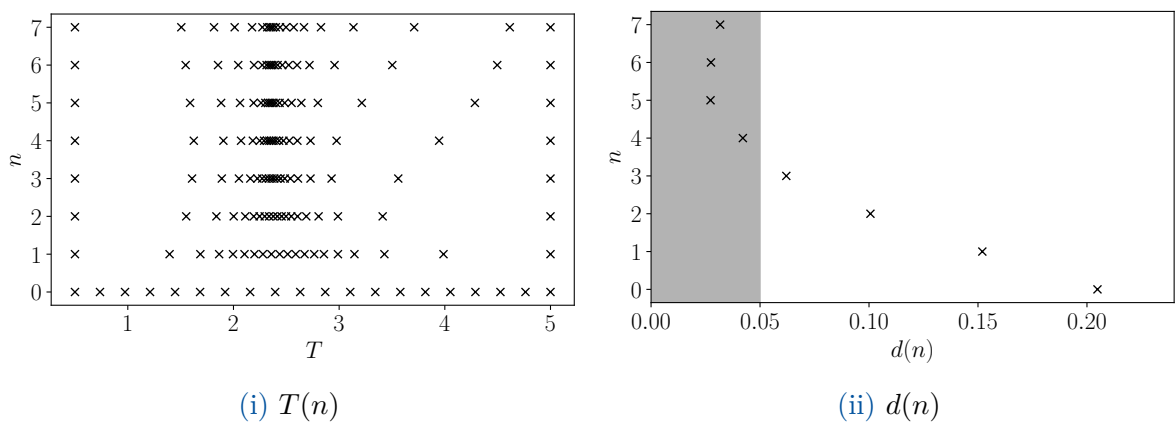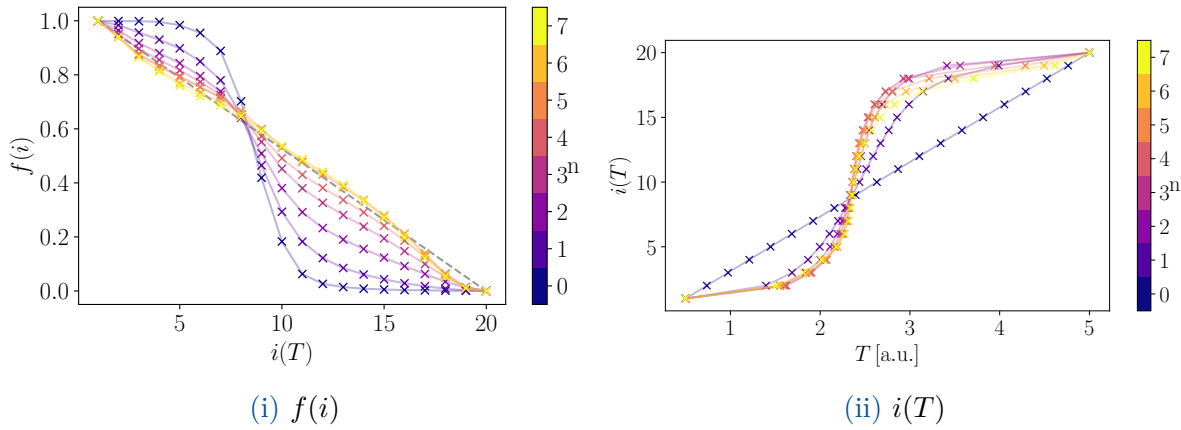

(i) $T(n)$

(ii) $d(n)$

Figure 8.6: Temperature distribution $\mathbf{T}(n)$ (i) and deviation $d(n)$ (ii) for $n = 7$ FOPT iterations and $\mathbf{T}_\mathrm{T}$ in the Ising model.

(i) $f(i)$ (ii) $i(T)$

Figure 8.7: Flow $f(i)$ (i) and replica index $i(T)$ (ii) for $n = 7$ FOPT iterations and $\mathbf{T}_{\mathrm{T}}$ in the Ising model. Iteration step n is indicated by the respective colormap.

with a coupling strength J and $\langle i, j \rangle$ the NN's. We perform the calculations of the model on a $L = 12$ cluster. The initial $\mathbf{T}$ is set to either equidistant for temperatures ($\mathbf{T}_{\mathrm{T}}$) or $\beta = 1/(k_B T)$ ($\mathbf{T}_\beta$).

In Fig. 8.4 and Fig. 8.6 we display the results starting from $\mathbf{T}_{\mathrm{T}}$ and $\mathbf{T}_\beta$ respectively. We display the flow $f(i)$ and the temperature $T(i)$ as functions of the replica index i in Fig. 8.5 and Fig. 8.7, where the color indicates the FOPT iteration step n. The flow $f(i)$ shows a fast convergence towards a linear behavior in the case of $\mathbf{T}_{\mathrm{T}}$. The results after $n = 7$ FOPT iterations fulfill the condition of $d(n)$ see Fig. 8.6(ii). The resulting $\mathbf{T}$ of the n FOPT iterations are displayed in Fig. 8.6(i). Here, we observe a condensation of replicas around the bottleneck at $T = 2.5$ (with T in arbitrary units). This is a result of the linearized flow $f(i)$ but bears additional value because the resolution around T_{N} gets enhanced with FOPT.

Starting with $\mathbf{T}_\beta$ [see Fig. 8.4(ii)], we see that the system needs significantly more iterations ($N = 16$) to match the criteria of a linearized flow (8.5). The resulting $\mathbf{T}$ is again condensed around the critical temperature and is comparable to the result of Fig. 8.4(i). For the Ising model $\mathbf{T}_{\mathrm{T}}$ is superior to $\mathbf{T}_\beta$, due to faster convergence towards a linear flow. The results of the FOPT for the Ising model are indeed promising, especially the condensation around T_{N} is of note because it reduces the number of replicas required to get a high resolution around the Néel temperature.

8.4.3 Ca$_2$RuO$_4$

After the successful application to the Ising model, we want to extend our analysis of the FOPT to the spin-orbit model of Ca$_2$RuO$_4$, introduced in Chap. 6. Again we use $\mathbf{T}_{\mathrm{T}}$ and $\mathbf{T}_\beta$ as starting $\mathbf{T}$. In Fig. 8.9 and Fig. 8.8 we show results of the FOPT iterations necessary to obtain a suitable $\mathbf{T}$ for $\mathbf{T}_\beta$ and $\mathbf{T}_{\mathrm{T}}$ respectively. Like for the Ising model,
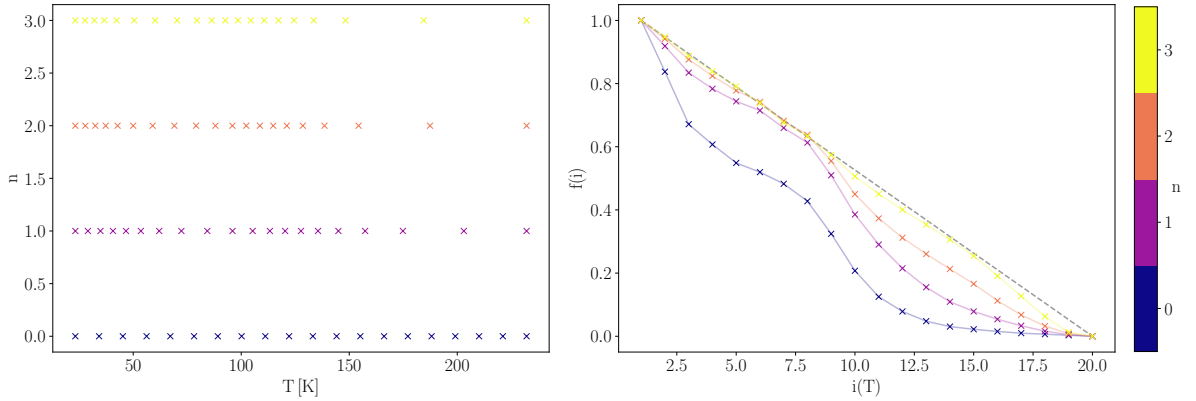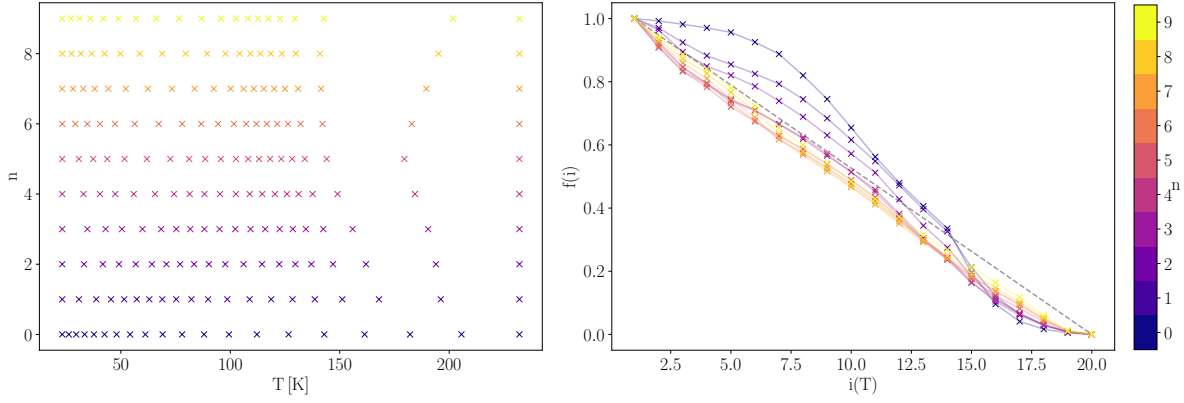
Figure 8.8: FOPT for Ca_2RuO_4 A (Tab. 8.2) for $\Delta = 0.3\,\text{eV}$ and $\mathbf{T}_T$. Displayed are temperature distribution $\mathbf{T}$ as a function of FOPT iteration index n (left-hand side) and flow $f(i)$ as a function of replica index i and n (right-hand side).

we observe a significantly faster convergence of $f(i)$ for $\mathbf{T}_T$, with only $n = 3$ iterations necessary to obtain an optimized $f(i)$. We also observe a condensation of $\mathbf{T}$ around the Néel temperature T_N see Fig. 8.8. The motivation of the FOPT applied to our effective model was to increase the convergence speed of the MC calculations while keeping the resolution around T_N as high as possible. However, in our implementation of the FOPT the convergence of the flow, i.e., obtaining a high resolution around T_N, took longer than the convergence of the ground states for $\mathbf{T}$, with PTMC. The reason is that our problem does not require a linearized flow to converge. This contradicts the premise of FOPT, which is to tackle complicated problems where a linearized flow would significantly increase the efficiency of PTMC. In our case, the linearized flow is more of a neat feature, in the form of a resolution around T_N, than an essential part of solving the problem.

Concluding, while the FOPT method seemed promising for Ca_2RuO_4, the fast convergence of the initial problem makes our problem a suboptimal candidate for the FOPT. We found that to guarantee a high resolution around T_N, an equidistant temperature distribution $\mathbf{T}_T$ with a higher m is sufficient.

8.5 Effect of SOC and CF

To evaluate the stability of the phases determined in [77] towards an increase of temperature we study the behavior of the Néel temperature T_N in dependency of the CF Δ and the magnitude of SOC λ.

Figure 8.9: FOPT for Ca_2RuO_4 A (Tab. 8.2) for $\Delta = 0.3\,eV$ and $\mathbf{T}_\beta$. Displayed are temperature distribution $\mathbf{T}$ as a function of FOPT iteration index n (left-hand side) and flow $f(i)$ as a function of the replica index i and n (right-hand side).

	t_z [eV]	$t_{x/y}$ [eV]	t_{NNN} [eV]	U [eV]	J_{H} [eV]	Section
A	0.2	0.2	0.0	2.5	0.5	8.5.1
B	0.2	0.137	0.1	2.0	0.34	8.5.2

Table 8.2: Parameter sets used for the finite temperature analysis. Parameter set A is idealized for a faster MC convergence (see Fig. 8.1) and therefore has isotropic hopping with no NNN interactions. We used set B, obtained via DFT [106], in the $T = 0$ analysis (Ch. 7).
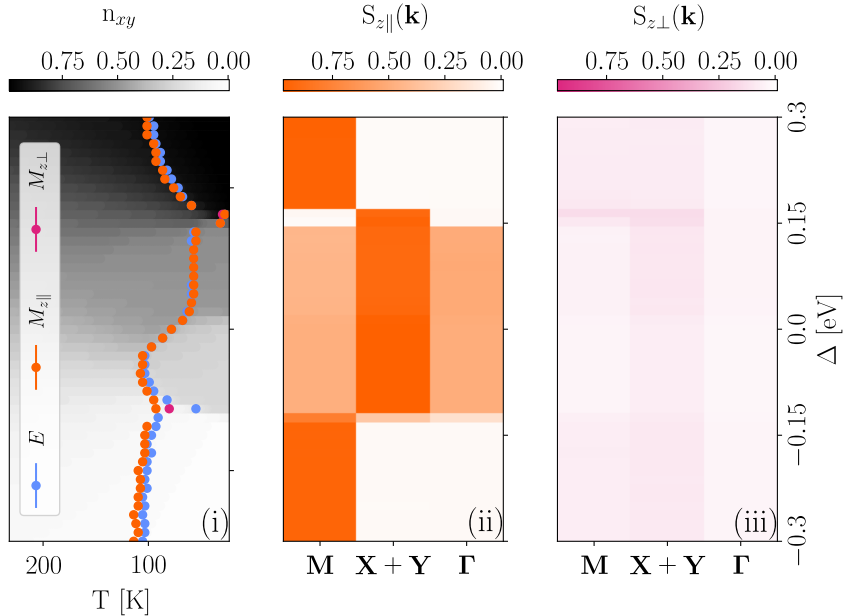
Figure 8.10: (i) Néel temperature of Ca_2RuO_4 (A in Tab. 8.2) calculated via in-plane magnetization (pink), out-of-plane magnetization (orange), and ground state energy (blue) for varied Δ and T at $\lambda = 0.01\,eV$. In the background, the double-occupation density in the d_{xy} orbital n_{xy} is displayed (grey colormap). We calculate out-of-plane (ii) and in-plane (iii) SSF at wave vector $\boldsymbol{\Gamma}$, $\mathbf{X} + \mathbf{Y}$ (superposition of $\mathbf{X}$ and $\mathbf{Y}$ results), and $\mathbf{M}$ as function of Δ at the minimal temperature of $\mathbf{T}$.
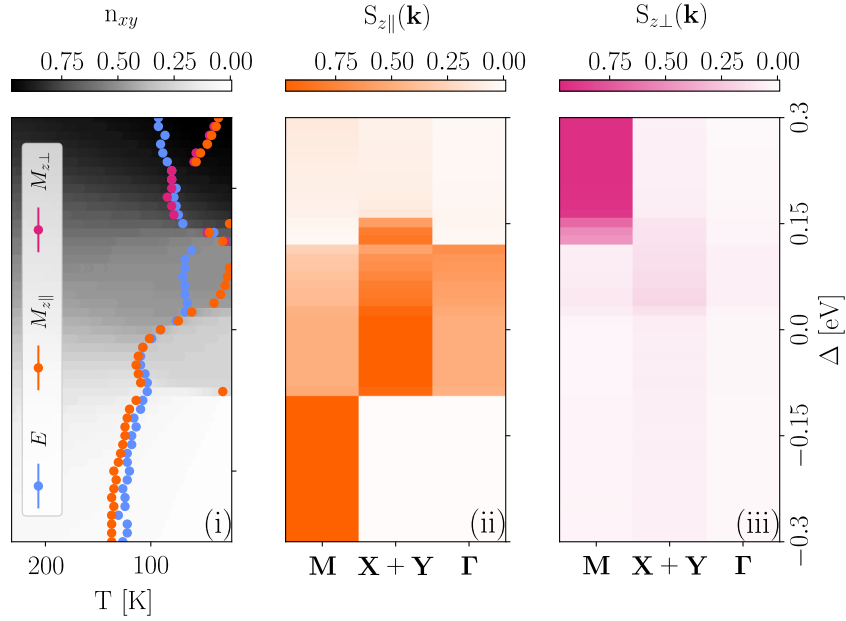
Figure 8.11: (i) Néel temperature of Ca_2RuO_4 (A in Tab. 8.2) calculated via in-plane magnetization (pink), out-of-plane magnetization (orange), and ground state energy (blue) for varied Δ and T at $\lambda = 0.03$ eV. In the background, the double-occupation density in the d_{xy} orbital n_{xy} is displayed (grey colormap). We calculate out-of-plane (ii) and in-plane (iii) SSF at wave vector $\mathbf{\Gamma}$, $\mathbf{X} + \mathbf{Y}$ (superposition of $\mathbf{X}$ and $\mathbf{Y}$ results), and $\mathbf{M}$ as function of Δ at the minimal temperature of $\mathbf{T}$.
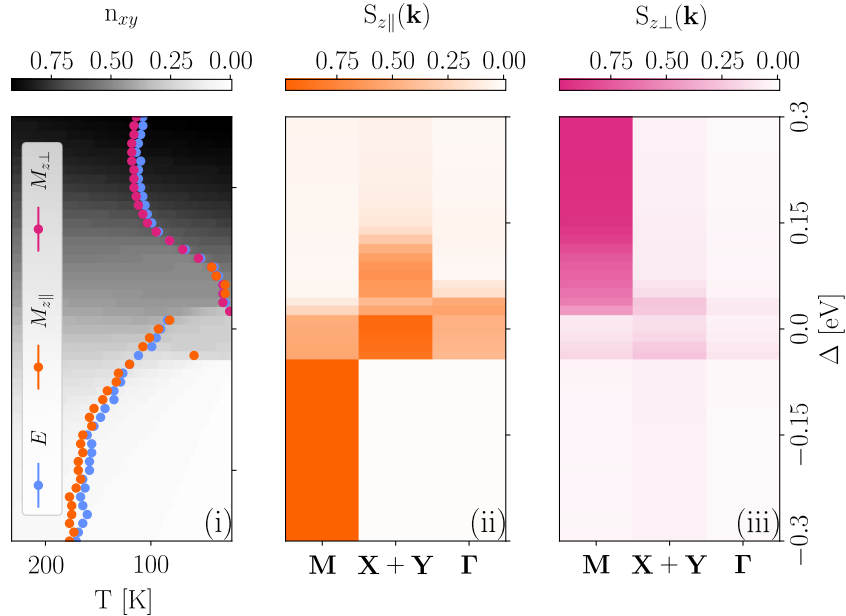
Figure 8.12: (i) Néel temperature of Ca_2RuO_4 (A in Tab. 8.2) calculated via in-plane magnetization (pink), out-of-plane magnetization (orange), and ground state energy (blue) for varied Δ and T at $\lambda = 0.06$ eV. In the background the double-occupation density in the d_{xy} orbital n_{xy} is displayed (grey colormap). We calculate out-of-plane (ii) and in-plane (iii) SSF at wave vector $\mathbf{\Gamma}$, $\mathbf{X} + \mathbf{Y}$ (superposition of $\mathbf{X}$ and $\mathbf{Y}$ results), and $\mathbf{M}$ as function of Δ at the minimal temperature of $\mathbf{T}$.

8.5.1 Idealized Parameters

We start our analysis of Ca_2RuO_4 with idealized hopping parameters (Introduction in Tab. 8.2). NN hopping is here assumed to be isotropic, NNN hopping is neglected, and Coulomb repulsion U and Hund's coupling J_H are set to $U = 2.5\,\mathrm{eV}$ and $J_H = 0.5\,\mathrm{eV}$ respectively. While in Sec. 8.1 this simplification was mainly used to guarantee convergence for larger cluster sizes, in this section we want to carve out the effect these simplifications have on ground state properties at $T = 0$. In addition, we study the influence of Δ and λ on the Néel temperature determined in Sec. 8.1.

We present the results for parameter set A (Tab. 8.2) in Fig. 8.10-8.12 for different values of λ. We determined the Néel temperature via in-plane magnetization $M_{z\perp}$ (pink), out-of-plane magnetization $M_{z\perp}$ (orange), and energy (blue) in dependence of the crystal field within $|\Delta| < 0.3\,\mathrm{eV}$ and fixed λ. Furthermore, we showcase the double-occupation density of electrons in the d_{xy} orbital n_{xy} as a function of Δ and T indicating orbital ordering. Fig. 8.10-8.12 (ii) and (iii) displays the in- and out-of-plane SSF for wavevectors $\mathbf{M}$, $\mathbf{X} + \mathbf{Y}$, and $\mathbf{\Gamma}$ (see also Tab. 8.1) as a function of CF Δ. The SSF $S(\mathbf{k})$ is calculated for the lowest temperature of $\mathbf{T}_T$ used for the Monte-Carlo simulation.

We observe that for small λ [Fig. 8.10] and large $|\Delta|$ the system is in a out-of-plane AFM. The out-of-plane AFM at $\Delta \ll 0\,\mathrm{eV}$ agrees with the results found in Sec. 7.3.3. Meanwhile, the out-of-plane ordering at $\Delta \gg 0\,\mathrm{eV}$ arises because for weak SOC in- and out-of-plane AFM order are quasi-degenerated, and the Monte-Carlo picks one spin arrangement. This changes if we move to larger values of λ, which prefers an in-plane AFM ordering. The ED results for more realistic parameters agree with this result. However, for weak positive CF the ground state properties for the idealized parameter set A differ drastically from the predicted stripy order, with significant $S(\mathbf{k})$ contributions at $\mathbf{\Gamma}$ and $\mathbf{M}$ leading to an incommensurate spin ordering comparable to the 3U1D phase found in Fig. 7.3. We attribute this disagreement to the lack of NNN interactions, which play an important role in the formation of the stripy spin arrangement in Fig. 7.5. We conclude that, while A comes at a lower computational cost it is mandatory to use a more realistic parameter set to capture ground state properties accurately. We can also identify the 3U1D phase at $\Delta < 0$. However it appears far more extended than in Fig. 7.5, prevailing up to values of $\lambda = 0.06\,\mathrm{eV}$ [Fig. 8.12].

As we can see in Fig. 8.10-8.12 (i), the Néel temperature depends heavily on both Δ and λ. Starting with the AFM phases at $|\Delta| \gg 0$ we observe that an increase of $|\Delta|$ within these phases leads to a saturating increase of T_N. Similarly, an increase of λ also tends to stabilize these phases against temperature fluctuations, which leads to higher Néel temperatures. We observe a contrary behavior of the two intermediate phases at weaker CF Δ. Here, an increase of λ leads to a significant decrease in T_N, which makes these phases very susceptible to "thermal" fluctuations and therefore potentially

unstable.

Last but not least, for n_{xy}, we see a clear dependence on the respective ground state, while there is only a weak temperature dependence. In particular, at T_N, we do not observe any unconventional behavior, leading to the conclusion that orbital ordering prevails above T_N as was already predicted by [51].

8.5.2 DFT parameters [106]

Since A did not reproduce the ground state properties found in Sec. 7.3.2 correctly, it is mandatory to use the parameters set used for ED [77] and VCA [63]. Hence, we set the parameters to B (Tab. 8.2), and evaluate T_N in dependence on both Δ and λ. As we can see in Fig. 8.13-8.15, the phases found in Sec. 7.3.2 are now correctly reproduced, emphasizing the importance of the choice of parameters. We observe a relatively narrow 3U1D phase around $\Delta \approx 0\,\mathrm{eV}$, which gets suppressed increasing λ. The phase arising for weak positive Δ now shows clear signs of a stripy spin arrangement like predicted in Sec. 7.3.2. However, it prevails up to $\lambda = 0.06\,\mathrm{eV}$, which disagrees with the results of the 4×4 cluster of Sec. 7.3.2. We attribute this disagreement to the difference in cluster sizes, as we use a $L = 8$ cluster for the finite temperature studies. Barring this discrepancy, it is still obvious that the choice of parameters changes the phase boundaries and the phases arising drastically. In particular, the lack of the stripy phase, which is also supported by VCA results [63], makes parameter set A a poor choice.

Like in Sec. 8.5.1, the Néel temperature depends heavily on the respective phase, with quite sizable Néel temperatures for the 3U1D, in-plane, and out-of-plane AFM phases. The stripy phase shows an almost vanishing T_N. Again, an increase of λ leads to an increase of T_N in the AFM phase. Meanwhile, T_N of the stripy phase decreases even more when increasing λ. As for the 3U1D phase, T_N appears unchanged if we change λ, while at $\lambda = 0.06\,\mathrm{eV}$ this phase vanishes entirely as predicted in Sec. 7.3.2. Since one expects sizable SOC in $\mathrm{Ca_2RuO_4}$, the stripy phase appears to only exist at very low temperatures. This would make the stripy phase very hard to realize in experiments. In addition, we observe that the Néel temperature of $\mathrm{Ca_2RuO_4}$ predicted by B appears to be further away from the experiment than the Néel temperature obtained via A, while it is still at $T_N \approx 100\,\mathrm{K}$ which is very close to experimental data. Therefore, the anisotropic effective Hamiltonian (Ch. 6) seems to not only describe results at $T = 0$ very well but additionally yields reasonable finite temperature results.

n_{xy} has a similar behavior as observed for A. NNN and anisotropic interactions affect neither the orbital ordering above T_N [51] nor the dependence on the temperature.

In conclusion, choosing the right parameter set is crucial to get the correct $T \approx 0\,\mathrm{K}$ properties and has a noticeable effect on finite temperature properties. However, we observed a few general trends for both A and B. Increasing λ and Δ stabilizes AFM
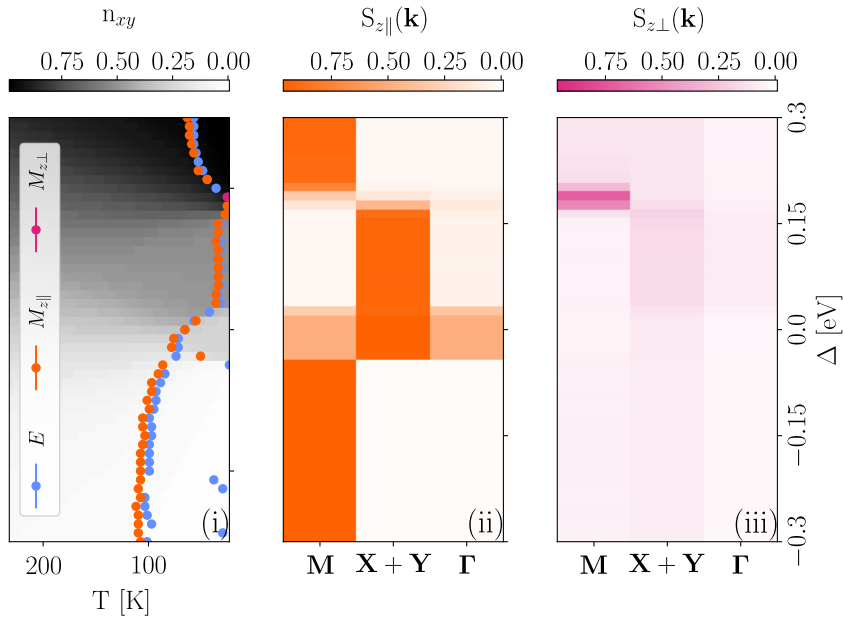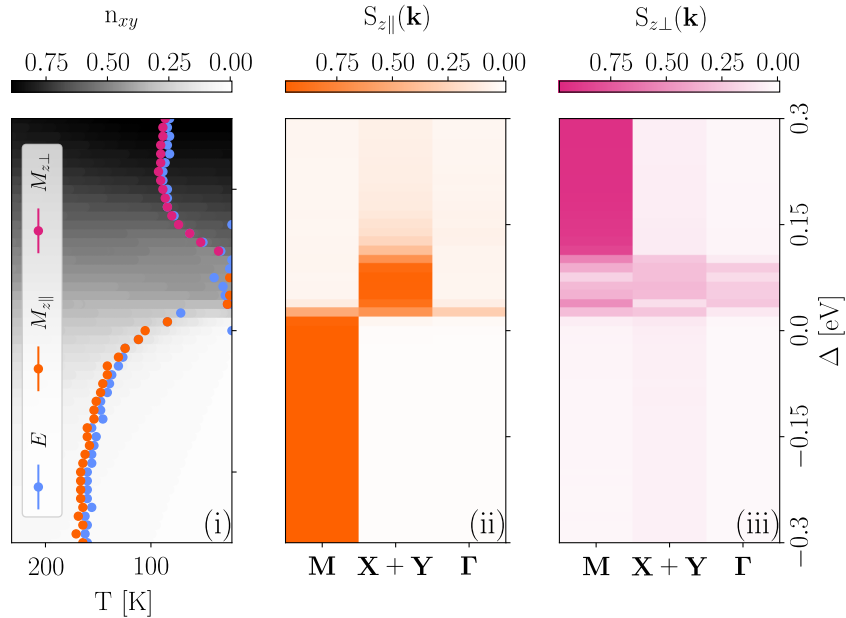
Figure 8.13: (i) Néel temperature of Ca_2RuO_4 (B in Tab. 8.2) calculated via in-plane magnetization (pink), out-of-plane magnetization (orange), and ground state energy (blue) for varied Δ and T at $\lambda = 0.01\,\text{eV}$. In the background, the double-occupation density in the d_{xy} orbital n_{xy} is displayed (grey colormap). We calculate out-of-plane (ii) and in-plane (iii) SSF at wave vector $\mathbf{\Gamma}$, $\mathbf{X} + \mathbf{Y}$ (superposition of $\mathbf{X}$ and $\mathbf{Y}$ results), and $\mathbf{M}$ as function of Δ at the minimal temperature of $\mathbf{T}$.

towards the influence of T. Meanwhile, increasing λ destabilizes the stripy phase found for B. Last but not least, orbital ordering is not affected by the loss of magnetic order and prevails up to high temperatures.
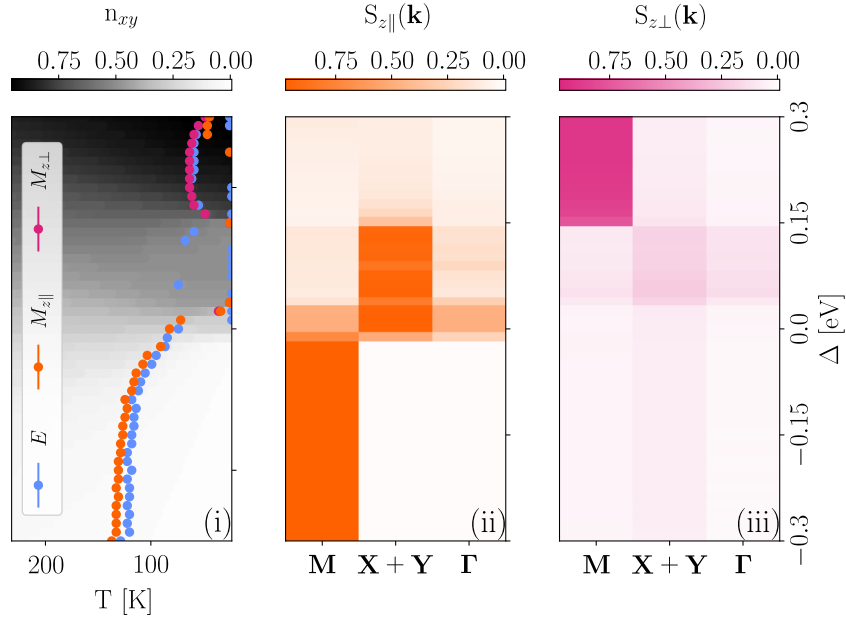
Figure 8.14: (i) Néel temperature of Ca_2RuO_4 (B in Tab. 8.2) calculated via in-plane magnetization (pink), out-of-plane magnetization (orange), and ground state energy (blue) for varied Δ and T at $\lambda = 0.03\,\text{eV}$. In the background, the double-occupation density in the d_{xy} orbital n_{xy} is displayed (grey colormap). We calculate out-of-plane (ii) and in-plane (iii) SSF at wave vector $\mathbf{\Gamma}$, $\mathbf{X} + \mathbf{Y}$ (superposition of $\mathbf{X}$ and $\mathbf{Y}$ results), and $\mathbf{M}$ as function of Δ at the minimal temperature of $\mathbf{T}$.

Figure 8.15: (i) Néel temperature of Ca_2RuO_4 (B in Tab. 8.2) calculated via in-plane magnetization (pink), out-of-plane magnetization (orange), and ground state energy (blue) for varied Δ and T at $\lambda = 0.06\,\text{eV}$. In the background, the double-occupation density in the d_{xy} orbital n_{xy} is displayed (grey colormap). We calculate out-of-plane (ii) and in-plane (iii) SSF at wave vector $\mathbf{\Gamma}$, $\mathbf{X} + \mathbf{Y}$ (superposition of $\mathbf{X}$ and $\mathbf{Y}$ results), and $\mathbf{M}$ as function of Δ at the minimal temperature of $\mathbf{T}$.

9 Conclusion and Outlook

In this thesis, we derived effective Kugel-Khomskii models for different types of Mott-insulating transition metal compounds. We focused on d^4 and d^5 materials with strong spin-orbit coupling, like Ca_2RuO_4 and α-$RuCl_3$ respectively. This thesis was divided into two main parts, discussing the different properties of the Ru t_{2g}^4 and the t_{2g}^5 Kitaev-Heisenberg compounds.

In the first part, we solely focused on d^5 Kitaev-Heisenberg-type materials. Here, the effective Kugel-Khomskii model is a well-known commodity and yields, for materials with strong spin-orbit coupling, an effective model with Kitaev-, Heisenberg-, Γ-, and Γ'-interactions. A large field of research for these materials is concerned with driving the system into a pure Kitaev material. This is desirable due to the exactly solvable spin liquid ground state in the Kitaev limit [6]. In this thesis, we took a relatively unexplored approach to tuning interaction parameters via a light field periodic in time. Via the Floquet formalism, we found new expressions for the interactions, depending on frequency and amplitude and the polarization of the incoming light.

We showed that ruthenates like α-$RuCl_3$ are more suited for Floquet engineering than iridates, both of which are proximate to the Kitaev spin liquid ground state. This is the case because heating plays a less pronounced role in ruthenates due to stronger Hund's coupling J_H and Coulomb repulsion U causing a broader range of frequencies where heating is absent. Within these frequency corridors, the effective Floquet-Kitaev-Heisenberg model is feasible. Linear polarized light then induces anisotropies in the interactions, depending on the angle of the light concerning the respective bond. We argue that this could make linear polarized light a potential tool to tune an already existing Kitaev spin liquid from a gapped to a gapless ground state and *vice versa*.

Circular polarized light, on the other hand, preserves the isotropy of the system but breaks time-reversal symmetry. This leads to the inverse Faraday effect reported in [31, 32]. One can capture this effect if one considers an effective Floquet-Kitaev-Heisenberg model, which includes third-order ligand processes explicitly. It is mandatory

to include explicit fourth-order ligand terms in perturbation theory if one wants to obtain the accurate magnitudes of the single interactions. The inclusion of third and fourth-order terms does have a significant impact on circularly and linearly polarized light. Linear polarization induces two novel terms breaking inversion symmetry absent for circularly polarized light. Since linear polarization preserves time-reversal symmetry, the induced magnetic field vanishes and we do not observe an inverse Faraday effect. We can bridge the gap between linearly and circularly polarized light via Lissajous figures. In this thesis, we presented an effective Floquet-Heisenberg model for arbitrary polarization, connecting the limiting cases continuously via elliptical Lissajous figures. More complex Lissajous figures move away from the conventional limiting cases, linearly and circularly polarized light. Lissajous figures with a large difference of frequencies in x and y direction show a decoupling of the Kitaev-Heisenberg interaction parameters from the relative phase ϵ. However, the induced magnetic field still can be switched on and off via ϵ. Therefore, one could, in principle, tune the induced magnetic field relative to the remaining parameters.

The Floquet formalism introduces a plethora of pathways to manipulate the properties of Kitaev-Heisenberg materials of which we have only scratched the surface in this thesis. However, our effective model provides a solid foundation to discover more of these possibilities. The immediate next step could be an implementation of our model for an optical cavity, which has been discussed in the context of Floquet engineering recently [115]. In addition, numerical studies of the ground state properties for the fourth-order model (similar to the second-order model in App.A) could be desirable. Ground state properties could be dimers, a gapped or gapless quantum spin liquid, or some of the ordered states discussed in the context of the conventional Kitaev-Heisenberg model.

The second part of this thesis discussed d^4 transition metal Mott insulators in a square lattice arrangement, in particular Ca_2RuO_4. Contrary to the Kitaev-Heisenberg model of part I, the effective Kugel-Khomskii model for these materials is yet relatively unexplored. In this thesis we present an effective spin-orbit Hamiltonian, considering Hund's coupling, anisotropic nearest, and third nearest neighbor interactions, which has been lacking in the context of Ca_2RuO_4. With this model a detailed analysis of the ground state properties via a Δ-λ phase diagram is possible.

We found that a large crystal field induces an antiferromagnetic spin order, with the orientation changing from in-plane for $\Delta \gg 0$ to out-of-plane $\Delta \ll 0$ with changing the sign of the crystal field. Between these two AFM phases, at weak spin-orbit coupling, a stripy AFM phase arises for a weak positive crystal field. For a weak negative crystal field and weak spin-orbit coupling, we find a novel phase, which we designate 3U1D. Like the stripy phase, this phase vanishes for larger values of λ. For large λ, the system

eventually becomes paramagnetic, where finite Δ pushes the phase transition to larger λ. We locate Ca_2RuO_4 well into the in-plane AFM regime, within this phase diagram, in agreement with both experimental [5] and VCA results [63].

Concerning dynamics, we found that the results of the dynamical spin structure factor are in excellent agreement with experimental results of neutron scattering [5], reproducing signature properties of Ca_2RuO_4, like the maximum of the transverse mode. The dynamical properties are susceptible to change in Δ and λ and appear to depend strongly on the hole density in the xy orbital. We found that n_{xy}^h has nonvanishing contributions for Ca_2RuO_4. That is a signature for a prominent role of SOC in Ca_2RuO_4. The strong n_{xy}^h dependence of the dynamics makes the correspondence with experimental results even more remarkable.

Last but not least, we analyzed finite temperature properties of the effective spin-orbit model, in particular for Ca_2RuO_4. Monte-Carlo simulations yield the specific heat $C(T)$ and susceptibility $\chi(T)$, which we can qualitatively compare with experimental measurements. With this, we identified the Néel temperature of Ca_2RuO_4, signifying the phase transition from an AFM ordered Mott insulator to a PM Mott insulator. Our numerical results are in good qualitative agreement with experimental data. The Néel temperature in Ca_2RuO_4 appears to be susceptible to changes in Δ and λ. Meanwhile, T_N increases gradually with increasing λ, changing Δ induces more abrupt changes in T_N depending on the magnetic order of the ground state. The orbital ordering does not show significant changes at T_N and therefore prevails in the PM Mott insulating phase.

In our attempts to determine the Néel temperature accurately, we explored the possibilities of applying FOPT. It turned out that our system is not a candidate for FOPT because it converges fast with PTMC, while FOPT becomes useful for problems that have long PTMC convergence time. For systems, like ours, we recommend a traditional parallel tempering approach with a large temperature set.

The effective spin-orbital model for d^4 transition metal Mott insulators derived in this thesis is an excellent starting point for future studies. First, Monte-Carlo results for the ground state properties could be extended to larger clusters comparable to the cluster sizes used for finite temperatures, to estimate the influence of finite size effects on the phase boundaries in Sec. 7.2.3. In addition, like for the Kitaev-Heisenberg model, a light-matter interaction study via the Floquet formalism would be interesting. Here, the effect on the interaction parameters in the triplon model, introduced in Sec. 2.3.3, would be particularly compelling, due to the possibility of enhancing/suppressing triplon condensation. Furthermore, the model in this thesis might easily be applied to similar materials like, e.g., vanadates [116]. Here, one would have to adjust the model to three dimensions to study the influence of Δ and λ.

A Ground state properties driving with CP

A.1 Materials

As we have argued in Chap. 4, of the considered materials so far, α-RuCl$_3$ is suited the best for Floquet engineering, due to the broad driving corridor and the possibility to strongly decrease the anisotropy of the Kitaev interactions. α-RuCL$_3$ is widely considered one of the more promising candidate materials to realize the Kitaev spin liquid. However, recently, studies on ruthenates have been extended to materials with other ligand atoms, namely iodine and bromine, which both show promising features. While α-RuBr$_3$ is in a Mott insulating state [118], α-RuI$_3$ appears to be metallic [119, 120]. However, recently it has been shown [121], that the metallic behavior of α-RuI$_3$ is mainly attributed to impurities of the probe, and pristine samples should be insulating. We therefore consider both α-RuBr$_3$ and α-RuI$_3$ for Floquet engineering. We use the second-order Kitaev-Heisenberg model, introduced in Chap. 4, for both materials. Notably, we did these studies before we derived the fourth-order model, hence we considered the second-order model. While there are some essential differences, we still feel that a ground-state analysis yields some useful insight, which is why we discuss the results in this appendix.

Material	α-RuCl$_3$	α-RuBr$_3$	α-RuI$_3$
t_1 [eV]	0.035	0.024	0.009
t_2 [eV]	0.184	0.169	0.170
t_3 [eV]	-0.054	-0.030	0.007

Table A.1: Hopping strengths t_1, t_2, and t_3, introduced in Sec. 3.2, for α-RuCl$_3$, α-RuBr$_3$, and α-RuIr$_3$ obtained from [117]. Like in Sec. 4.1 Coulomb repulsion is $U = 3.0\,\text{eV}$ and Hund's coupling is $J_\text{H} = 0.6\,\text{eV}$.

Material	α-RuCl$_3$	α-RuBr$_3$	α-RuI$_3$
J [eV]	$-9.1 \cdot 10^{-4}$	$-2.70 \cdot 10^{-4}$	$1.76 \cdot 10^{-4}$
K [eV]	$-1.73 \cdot 10^{-2}$	$-1.53 \cdot 10^{-2}$	$-1.61 \cdot 10^{-2}$
Γ [eV]	$6.07 \cdot 10^{-3}$	$3.38 \cdot 10^{-3}$	$1.26 \cdot 10^{-4}$

Table A.2: J, K, and Γ calculated with the hopping parameters from [117]. Coulomb repulsion is $U = 3.0$ eV and Hund's coupling is $J_\mathrm{H} = 0.6$ eV.

In Tab. A.1, we list the DFT hopping parameters for α-RuBr$_3$ and α-RuI$_3$ from [117], which we used in this thesis. We are well aware that, unlike [33], these parameters neglect anisotropies and t_4 hoppings, but since, to our knowledge, these are the only DFT results for all three ruthenates, we will use them in this section to compare the different materials.

As becomes evident in [117] both α-RuBr$_3$ and α-RuI$_3$ show a strong suppression of J and Γ interactions compared to α-RuCl$_3$, locating these materials closer to the KSL or even in the KSL [121]. This proximity to the KSL can lead to a distinct phase for a switched sign of the interactions, which we will discuss in more detail in Sec. A.2. Last but not least, we observe that changing the material can lead to a change of sign in the J interaction, as α-RuI$_3$ has AFM Heisenberg interactions while Heisenberg interactions in α-RuBr$_3$ and α-RuCl$_3$ are FM (Tab. A.2).

A.2 Exact diagonalization

As we have seen previously in Sec. 3.2, Floquet engineering with Lissajous figures can change the magnitude and sign of all interactions. The effect on the different bond directions is not uniform for most Lissajous figures. This induces anisotropies, as explained in Sec. 3.2, which means that the description with an idealized J-K-Γ model is no longer possible. However, in this section, we want to focus on circularly polarized light, which keeps the J-K-Γ model intact. We start to locate all three materials in the J-K-Γ model and determine their initial ground state properties. Thereupon, we introduce a non-zero light field to investigate the change of ground state properties in dependence of E_0.

To study ground state properties of the considered materials we perform exact diagonalization on 16 site and 24 site clusters (see Fig. A.1) with periodic boundary conditions. We use the WEINBE58 package [123, 124] to implement the J-K-Γ Hamiltonian in Python. We start our analysis with the conventional Kitaev-Heisenberg model as discussed in [33, 34]. As a benchmark, we calculate Kitaev, non-Kitaev, and traditional spin structure factors for $\Gamma = 0$ like done for a 24-site cluster in [122]. The result (Fig. A.2) qualitatively shows an overall good agreement with the results of Fig. 5(a) and Fig. 2(b) in [122]. Like in [122], we are able to identify the distinct phases as AFM

(i) 16 site cluster   (ii) 24 site cluster
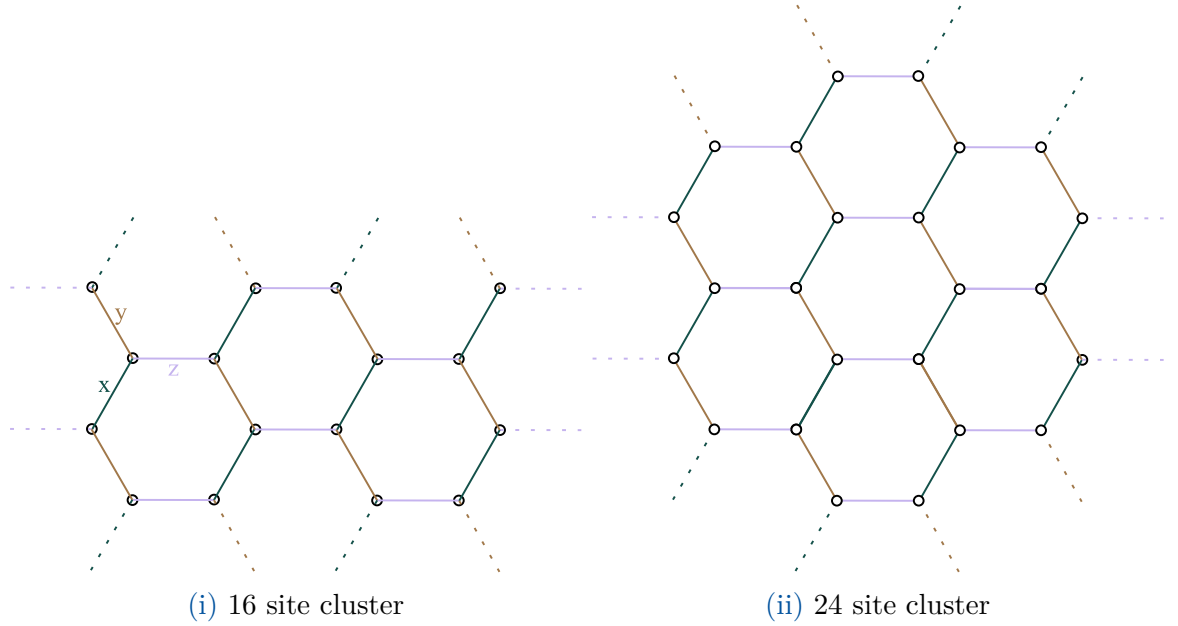
Figure A.1: Lattice geometry of α-RuCl$_3$. x, y, and z bonds are colored green, purple, and brown respectively. Solid lines display the 16 site (i) and 24 site (ii) clusters with periodic boundary conditions (dashed lines) used for the exact diagonalization calculations in Sec. A.2.
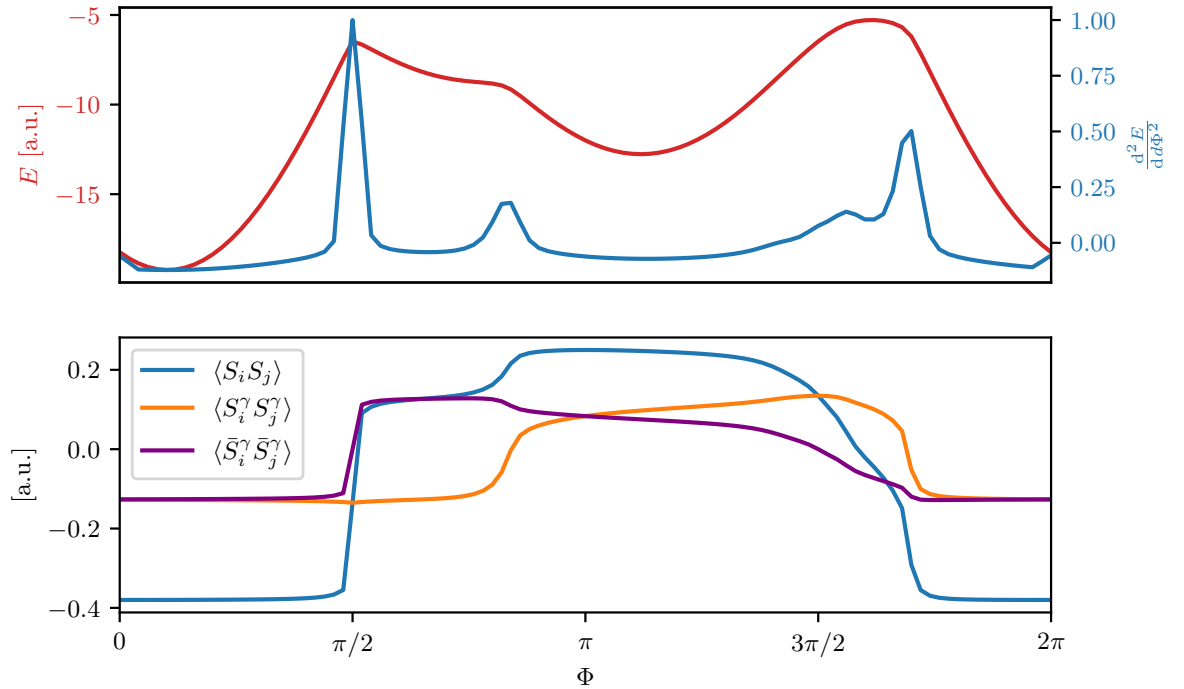
Figure A.2: Tuning between the Kitaev ($\Phi = \pi/2$) and Heisenberg ($\Phi = 0$) limit in the J-K-model. Ground state energy E and second derivative $d^2E/d\Phi^2$ in dependency of Φ. Spin- (blue), Kitaev- (orange), and non-Kitaev-correlations (purple) for varied Φ. The results are in concordance with the results of [122] calculated on a 24-site cluster.
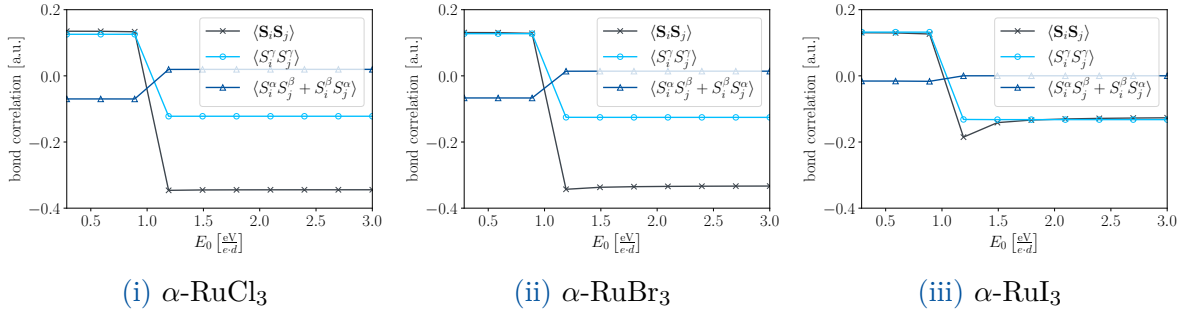
Figure A.3: Kitaev (light blue), Heisenberg (anthracite) and Γ (dark blue) correlations for varied E_0 and $\omega = 1.6\,\text{eV}$. Results for parameters of α-RuCl$_3$ (i), α-RuBr$_3$ (ii), and α-RuI$_3$ (iii) (obtained from [117]) are displayed.

, KSL, zig-zag, and stripy.

After we confirm that the code is reproducing the J-K-Γ model correctly, we want to locate the three considered ruthenates within this model. The results for α-RuCl$_3$, α-RuBr$_3$, α-RuI$_3$ are displayed in Fig. A.3. Here, we calculate the Heisenberg, Kitaev, and Γ nearest neighbor bond correlations via ED on a 24-site cluster in dependence of the field strength E_0 at $\omega = 1.6\,\text{ev}$. We average the bond correlations over the cluster.

For small E_0 all materials have Kitaev correlations with almost identical strength as the Heisenberg correlations. This indicates weak Heisenberg interactions and dominant Kitaev interactions. In addition, we observe weak negative Γ correlations, which hint at a non-KSL ground state. We observe that Γ interactions become weaker if we change from Cl to I. Therefore, substituting the ligand atoms pushes the ground state closer to the KSL found in Fig. A.2 with $\Gamma = 0$.

Increasing E_0 we observe a relatively sharp phase transition into the AFM phase for Cl and Br ligands. The AFM is indicated by the Heisenberg correlations at $\langle \mathbf{S}_i \mathbf{S}_j \rangle \approx -0.34$. We attribute this phase transition to the change of sign in the interactions discussed in Sec. 4.2. Meanwhile, for α-RuI$_3$ the phase arising does not show signatures of an AFM ground state. The fact that Heisenberg and Kitaev interactions coincide and almost vanishing Γ correlations furthermore hints that the ground state might indeed be a KSL or at least very close to realizing a KSL. While α-RuI$_3$, in reality, appears to be metallic and more DFT studies on these materials would be favorable, one can still infer two meaningful observations from these results. First, a phase transition via Floquet engineering is possible, due to the global sign flip of all interactions. Second, it seems possible to drive a system from the AFM into the AFM Kitaev spin liquid in principle.

As we discussed in Chap. 5, including higher order terms allows for the possibility to tune K and Γ respective to the other parameters, which would open new pathways in driving a system towards the KSL. The results of this appendix should thus be viewed

as a rough starting point in the analysis of ground-state behavior, with the second-order model.

B Perturbation theory

B.1 Second order perturbation theory

B.1.1 Circular polarized light

We can simplify the kinetic Hamiltonian for CP via the relation

$$\sin(\vartheta)\cos(\omega t) + \cos(\vartheta)\sin(\omega t) = \sin(\vartheta + \omega t), \tag{B.1}$$

where ϑ is the bond angle relative to the z-bond (Fig. 5.3). The simplified kinetic Hamiltonian then reads

$$H_{\text{kin}} = \sum_n \sum_{\langle i,j \rangle} \sum_{\alpha,\beta} t_{\alpha\beta} \mathcal{J}_n(A_0) e^{\sin(\vartheta + \omega t)} d_{i,\alpha}^\dagger d_{j,\beta} + h.c., \tag{B.2}$$

with $A_0 = E_0/\omega$, α, β the orbital flavor $\alpha, \beta \in [xy, yz, xz]$ and $t_{\alpha\beta}$ the associated hopping strength. The Floquet Hamiltonian describes the absorption of l photons that we can derive via averaging over time as described in the main text (Sec. 2.3.4). This then yields

$$\mathcal{H}_l = \frac{1}{2\pi} \int_0^{2\pi} H_{\text{kin}} e^{-il\omega t} \mathrm{d}t = \sum_{\langle i,j \rangle} \sum_{\alpha,\beta} t_{\alpha\beta} \left[\mathcal{J}_l(A_0) e^{il\vartheta} d_{i,\alpha}^\dagger d_{j,\beta} + \mathcal{J}_{-l}(A_0) e^{il\vartheta} d_{j,\alpha}^\dagger d_{i,\beta} \right], \tag{B.3}$$

as expected.

B.1.2 Arbitrarily polarized light

For AP the kinetic Hamiltonian becomes more complicated as (B.1) is no longer applicable, therefore it reads

$$
H_{\text{kin}} = \sum_{\langle i,j \rangle} \sum_{\alpha,\beta} t_{\alpha\beta} \exp\left[iA_0\left(\sin(\omega t)\cos(\alpha) + \frac{1}{N}\sin(N\omega t + \epsilon)\sin(\alpha)\right)\right] d_{i,\alpha}^\dagger d_{j,\beta} + h.c..
$$

(B.4)

To derive the Floquet Hamiltonian we proceed as in (B.2), simplifying the Hamiltonian with the Jacobi-Anger expansion then yields an expression with multiple Bessel functions $\mathcal{J}$

$$
\mathcal{H}_l = \sum_{\langle i,j \rangle} \sum_{\alpha,\beta} \sum_n t_{\alpha\beta} \mathcal{J}_n\left[\frac{A_0}{N}\sin(\alpha)\right] \left\{ \mathcal{J}_{l-Nn}\left[A_0\cos(\alpha)\right] e^{i\epsilon n} d_{i,\alpha}^\dagger d_{j,\beta}\right.
$$
$$
\left. + \mathcal{J}_{-l-Nn}\left[A_0\cos(\alpha)\right] e^{-i\epsilon n} d_{j,\alpha}^\dagger d_{i,\beta}\right\}.
$$

(B.5)

To derive the second-order Hamiltonian we have to calculate $\mathcal{H}_{-l}\mathcal{H}_l$. A general second-order hopping process including only d-orbitals absorbing and emitting l photons becomes

$$
\mathcal{H}_{-l}\mathcal{H}_l = \sum_{\langle i,j \rangle} \sum_{\alpha,\beta} \sum_{\gamma,\delta} t_{\gamma\delta} t_{\alpha\beta} \left[\left(\sum_n \mathcal{J}_{-l-Nn}\left[A_0\cos(\alpha)\right] \mathcal{J}_n\left[\frac{A_0}{N}\sin(\vartheta)\right]\cos(\epsilon n)\right)^2\right.
$$
$$
\left. + \left(\sum_n \mathcal{J}_{-l-Nn}\left[A_0\cos(\alpha)\right] \mathcal{J}_n\left[\frac{A_0}{N}\sin(\vartheta)\right]\sin(\epsilon n)\right)^2 \right] d_{i,\gamma}^\dagger d_{j,\delta} d_{j,\alpha}^\dagger d_{i,\alpha},
$$

(B.6)

with γ, δ the orbital flavor $\gamma, \delta \in [xy, yz, xz]$.

B.2 Third order perturbation theory

B.2.1 Circular polarized light

To take into account third-order processes in the effective Hamiltonian we have to include p-d hopping terms in the kinetic Hamiltonian, which for an arbitrary bond type and CP reads

$$
H_{\text{kin}} = \sum_{\langle i,j \rangle} \sum_{\alpha,\beta} t_{\alpha\beta} e^{iA_0\sin(\vartheta+\omega t)} d_{i,\alpha}^\dagger d_{j,\beta}
$$
$$
+ t_{pd}\left\{ e^{i\frac{A_0}{\sqrt{2}}\sin\left(\vartheta+\frac{\pi}{4}+\omega t\right)} p_{1,\langle i,j \rangle}^\dagger + e^{i\frac{A_0}{\sqrt{2}}\sin\left(\vartheta-\frac{\pi}{4}+\omega t\right)} p_{2,\langle i,j \rangle}^\dagger \right\} d_{j,\beta}
$$
$$
+ t_{pd}\left\{ e^{-i\frac{A_0}{\sqrt{2}}\sin\left(\vartheta-\frac{\pi}{4}+\omega t\right)} p_{1,\langle i,j \rangle}^\dagger + e^{-i\frac{A_0}{\sqrt{2}}\sin\left(\vartheta+\frac{\pi}{4}+\omega t\right)} p_{2,\langle i,j \rangle}^\dagger \right\} d_{i,\alpha} + h.c.,
$$

(B.7)

with $p^\dagger_{1/2,\langle i,j\rangle}$ the creation operators for the p-ligand atoms belonging to the bond $\langle i,j\rangle$ (see Fig. 5.3). Third-order processes include one hopping process mediated via the p ligands and one hopping process directly between the d orbital. To understand this mechanism, we consider a minimal example, where we consider one of the three d orbitals, which means $d_{i,\alpha} \to d_i$. Here we consider the process $d^\dagger_2 d_1 d^\dagger_1 p_1 p^\dagger_1 d_2$. We can directly transfer the prefactor that arises from this hopping process to the multiple orbital model. We first consider the Floquet Hamiltonians for the three processes, which we can write as

$$\mathcal{H}_m = \frac{1}{T}\int_0^T \sum_n \mathcal{J}_n\left(\frac{A_0}{\sqrt{2}}\right)e^{i(\alpha+\frac{\pi}{4}+\omega t)n}e^{-im\omega t}p^\dagger_1 d_2 \mathrm{d}t = \mathcal{J}_m\left(\frac{A_0}{\sqrt{2}}\right)e^{im(\alpha+\frac{\pi}{4})}p^\dagger_1 d_2 \quad \text{(B.8)}$$

$$\mathcal{H}_k = \frac{1}{T}\int_0^T \sum_n \mathcal{J}_n\left(\frac{A_0}{\sqrt{2}}\right)e^{i(\alpha-\frac{\pi}{4}+\omega t)n}e^{-ik\omega t}d^\dagger_1 p_1 \mathrm{d}t = \mathcal{J}_k\left(\frac{A_0}{\sqrt{2}}\right)e^{ik(\alpha-\frac{\pi}{4})}d^\dagger_1 p_1 \quad \text{(B.9)}$$

$$\mathcal{H}_{-m-k} = \frac{1}{T}\int_0^T \sum_n \mathcal{J}_n\left(A_0\right)e^{-i(\alpha+\omega t)n}e^{i(k+m)\omega t}d^\dagger_2 d_1 \mathrm{d}t = \mathcal{J}_{m+k}\left(A_0\right)e^{-i(k+m)\alpha}d^\dagger_2 d_1,$$

$$\text{(B.10)}$$

where p-d hopping processes absorb m and k photons which then get emitted in the d-d hopping. If we combine these processes we obtain the third order process over the p_1 ligand

$$\mathcal{H}_{-m-k}\mathcal{H}_k\mathcal{H}_m = \mathcal{J}_{m+k}\left(A_0\right)\mathcal{J}_m\left(\frac{A_0}{\sqrt{2}}\right)\mathcal{J}_k\left(\frac{A_0}{\sqrt{2}}\right)e^{-i(k-m)\frac{\pi}{4}}. \quad \text{(B.11)}$$

The hopping over the p_2 ligand is exactly the complex conjugate.

B.2.2 Hermiticity of H_l

It is important to note that the Floquet Hamiltonian describing the absorption of l photons is not Hermitian itself. As an example H_l for CP reads

$$\begin{aligned}
H_l =\Big(&\mathcal{J}_l(A_0)d^\dagger_1 d_2 + \mathcal{J}_{-l}(A_0)d^\dagger_2 d_1 + \mathcal{J}_l(A_0/\sqrt{2})d^\dagger_1 p_1 e^{-il\pi/4} + \mathcal{J}_{-l}(A_0/\sqrt{2})p^\dagger_1 d_1 e^{-il\pi/4} \\
&+ \mathcal{J}_l(A_0/\sqrt{2}))d^\dagger_1 p_2 e^{il\pi/4} + \mathcal{J}_{-l}(A_0/\sqrt{2})p^\dagger_2 d_1 e^{il\pi/4} - \mathcal{J}_l(A_0/\sqrt{2})p^\dagger_1 d_2 e^{il\pi/4} \\
&- \mathcal{J}_{-l}(A_0/\sqrt{2})d^\dagger_2 p_1 e^{il\pi/4} - \mathcal{J}_l(A_0/\sqrt{2})p^\dagger_2 d_2 e^{-il\pi/4} - \mathcal{J}_{-l}(A_0/\sqrt{2})d^\dagger_2 p_2 e^{-il\pi/4}\Big) \\
&\otimes |n+l\rangle\langle n|.
\end{aligned} \quad \text{(B.12)}$$

Of course, the total Floquet Hamiltonian is again Hermitian. It is important to keep this property in mind, especially if one wants to calculate the third-order correction terms.

B.2.3 Reversed path

To obtain an accurate third-order Hamiltonian it is crucial to take into account all hopping processes with the same intermediate energies. While this is unambiguous for the second order, for the third order, things become more complicated due to the nature of the hopping process. For third order, it is essential to be aware that, in principle, two different processes can lead to the same intermediate energies, which is not the case for second-order processes. First, there is the process described in Sec. B.2.1, where the d-p hopping processes absorb m and k photons respectively, which then get emitted in the d-d process completing the virtual excitation. In the second case, the d-d process takes place first, absorbing $m + k$ photons, and then the d-p processes emit m and k photons respectively, which is the reverse of the first process. To obtain the third-order correction terms one has to calculate

$$
\begin{aligned}
H_{\text{eff}}^{\alpha,\beta} &= |\beta\rangle \langle\alpha| \otimes \sum_{l,k,m} \sum_{\delta,\gamma} \langle\beta,0| H_l \frac{|\delta,m+k\rangle \langle\delta,m+k|}{\mathcal{E}_{\delta,m+k}} H_k \frac{|\gamma,m\rangle \langle\gamma,m|}{\mathcal{E}_{\gamma,m}} H_m |\alpha,0\rangle \\
&= |\beta\rangle \langle\alpha| \otimes \sum_{l,k,m} \sum_{\delta,\gamma} \langle\beta,0| \left(H_{-m-k}^{dd} \frac{|\delta,m+k\rangle \langle\delta,m+k|}{\mathcal{E}_{\delta,m+k}} H_k^{pd} \frac{|\gamma,m\rangle \langle\gamma,m|}{\mathcal{E}_{\gamma,m}} H_m^{pd} \right. \\
&\left. + H_{-m}^{pd} \frac{|\gamma,m\rangle \langle\gamma,m|}{\mathcal{E}_{\gamma,m}} H_{-k}^{pd} \frac{|\delta,m+k\rangle \langle\delta,m+k|}{\mathcal{E}_{\delta,m+k}} H_{m+k}^{dd} \right) |\alpha,0\rangle ,
\end{aligned}
\tag{B.13}
$$

with δ,β possible intermediate excited states and α,β the possible initial states. Neglecting the reversed path would lead to an incomplete and thus inaccurate effective Hamiltonian.

B.2.4 Arbitrary polarization

For AP (B.7) has more complicated Peierls terms, which we introduced in (B.4). Again, we want to consider an exemplary hopping process leading to the prefactors arising from a coupling to a time-periodic light field. Here, we consider a hopping over the p_2 ligand atom. The three important parts of the kinetic Hamiltonian are

$$
H^1 = \exp\left\{-i\frac{A_0}{\sqrt{2}}\left[\sin(\omega t)\cos\left(\alpha + \frac{\pi}{4}\right) + \frac{1}{N}\sin\left(N\omega t + \epsilon\right)\sin\left(\alpha + \frac{\pi}{4}\right)\right]\right\} p_2^\dagger d_1 \tag{B.14}
$$

$$
H^2 = \exp\left\{-i\frac{A_0}{\sqrt{2}}\left[\sin(\omega t)\cos\left(\alpha - \frac{\pi}{4}\right) + \frac{1}{N}\sin(N\omega t + \epsilon)\sin\left(\alpha - \frac{\pi}{4}\right)\right]\right\} d_2^\dagger p_2 \tag{B.15}
$$

$$
H^3 = \exp\left\{iA_0\left[\sin(\omega t)\cos(\alpha) + \frac{1}{N}\sin(N\omega t + \epsilon)\sin(\alpha)\right]\right\} d_1^\dagger d_2 . \tag{B.16}
$$

Again, we can use the Jacobi anger expansion in contrast to CP, we have to apply it twice, which yields

$$H^1 = \sum_{m,n} \mathcal{J}_m \left[\frac{A_0}{\sqrt{2}} \cos(\alpha + \frac{\pi}{4}) \right] e^{-i\omega t m} \mathcal{J}_n \left[\frac{A_0}{\sqrt{2}N} \sin\left(\alpha + \frac{\pi}{4}\right) \right] e^{-i(N\omega t + \epsilon)n} p_2^\dagger d_1 \quad (B.17)$$

$$H^2 = \sum_{m,n} \mathcal{J}_m \left[\frac{A_0}{\sqrt{2}} \cos(\alpha - \frac{\pi}{4}) \right] e^{-i\omega t m} \mathcal{J}_n \left[\frac{A_0}{\sqrt{2}N} \sin\left(\alpha - \frac{\pi}{4}\right) \right] e^{-i(N\omega t + \epsilon)n} d_2^\dagger p_2 \quad (B.18)$$

$$H^3 = \sum_{m,n} \mathcal{J}_m \left[A_0 \cos(\alpha) \right] e^{i\omega t m} \mathcal{J}_n \left[\frac{A_0}{N} \sin(\alpha) \right] e^{i(N\omega t + \epsilon)n} d_1^\dagger d_2. \quad (B.19)$$

Averaging over time yet again yields the effective Floquet term

$$\mathcal{H}_l^1 = \sum_n \mathcal{J}_n \left[\frac{A_0}{\sqrt{2}N} \sin(\alpha + \frac{\pi}{4}) \right] \mathcal{J}_{-l-Nn} \left[\frac{A_0}{\sqrt{2}} \cos(\alpha + \frac{\pi}{4}) \right] e^{-i\epsilon n} p_2^\dagger d_1 \quad (B.20)$$

$$\mathcal{H}_l^2 = \sum_n \mathcal{J}_n \left[\frac{A_0}{\sqrt{2}N} \sin(\alpha - \frac{\pi}{4}) \right] \mathcal{J}_{-l-Nn} \left[\frac{A_0}{\sqrt{2}} \cos(\alpha - \frac{\pi}{4}) \right] e^{-i\epsilon n} d_2^\dagger p_2 \quad (B.21)$$

$$\mathcal{H}_l^3 = \sum_n \mathcal{J}_{l-Nn} \left[A_0 \cos(\alpha) \right] \mathcal{J}_n \left[\frac{A_0}{N} \sin(\alpha) \right] e^{i\epsilon n} d_1^\dagger d_2. \quad (B.22)$$

Combining these hopping processes yields the factor for the virtual third-order hopping process

$$\mathfrak{B}_{l,m}^3 = \left\{ \sum_n \mathcal{J}_{-m-k-Nn} \left[A_0 \cos(\alpha) \right] \mathcal{J}_n \left[\frac{A_0}{N} \sin(\alpha) \right] e^{i\epsilon n} \right\}$$

$$\times \left\{ \sum_n \mathcal{J}_n \left[\frac{A_0}{\sqrt{2}N} \sin(\alpha - \frac{\pi}{4}) \right] \mathcal{J}_{-k-Nn} \left[\frac{A_0}{\sqrt{2}} \cos(\alpha - \frac{\pi}{4}) \right] e^{-i\epsilon n} \right\}$$

$$\times \left\{ \sum_n \mathcal{J}_n \left[\frac{A_0}{\sqrt{2}N} \sin(\alpha + \frac{\pi}{4}) \right] \mathcal{J}_{-m-Nn} \left[\frac{A_0}{\sqrt{2}} \cos(\alpha + \frac{\pi}{4}) \right] e^{-i\epsilon n} \right\}. \quad (B.23)$$

With this, we can calculate the complete effective Hamiltonian, with which we can determine the Kitaev-Heisenberg interactions introduced in Sec. 2.3.2 to

$$J = 2 \operatorname{Re} \left(\langle \uparrow_i \downarrow_j | H_{\text{eff}} | \downarrow_i \uparrow_j \rangle \right) \quad (B.24)$$

$$D = 2 \operatorname{Im} \left(\langle \uparrow_i \downarrow_j | H_{\text{eff}} | \downarrow_i \uparrow_j \rangle \right) \quad (B.25)$$

$$h = \frac{1}{2} \left(\langle \uparrow_i \uparrow_j | H_{\text{eff}} | \uparrow_i \uparrow_j \rangle - \langle \downarrow_i \downarrow_j | H_{\text{eff}} | \downarrow_i \downarrow_j \rangle \right) \quad (B.26)$$

$$K = \langle \uparrow_i \uparrow_j | H_{\text{eff}} | \uparrow_i \uparrow_j \rangle + \langle \downarrow_i \downarrow_j | H_{\text{eff}} | \downarrow_i \downarrow_j \rangle - 2 \langle \downarrow_i \uparrow_j | H_{\text{eff}} | \downarrow_i \uparrow_j \rangle - J \quad (B.27)$$

$$\Gamma = - 2 \operatorname{Im} \left(\langle \uparrow_i \uparrow_j | H_{\text{eff}} | \downarrow_i \downarrow_j \rangle \right) \quad (B.28)$$

$$\mu = 2 \operatorname{Re} \left(\langle \uparrow_i \uparrow_j | H_{\text{eff}} | \downarrow_i \downarrow_j \rangle \right). \quad (B.29)$$

where $\uparrow, \downarrow$ are the effective $j = 1/2$ moments. To calculate these matrix elements, we need to know how the annihilation and creation operators introduced in (B.12) act

	$\mathcal{E}_S\left[t_{pd}^2/(54(\Delta_{pd}+m\omega))\right]$	$\mathcal{E}_P\left[t_{pd}^2/(54(\Delta_{pd}+m\omega))\right]$	$\mathcal{E}_D\left[t_{pd}^2/(54(\Delta_{pd}+m\omega))\right]$
$\langle\uparrow_i\uparrow_j\lvert H_{\text{eff}}\rvert\uparrow_i\uparrow_j\rangle$	$4i(2t_1+t_3)\operatorname{Re}\left[\mathfrak{B}_{l,m}^3-\mathfrak{B}_{m,l}^3\right]$	$12i(t_1+t_3)\operatorname{Re}\left[\mathfrak{B}_{l,m}^3-\mathfrak{B}_{m,l}^3\right]$	$4i(t_1-t_3)\operatorname{Re}\left[\mathfrak{B}_{l,m}^3-A_2\right]$
$\langle\uparrow_i\uparrow_j\lvert H_{\text{eff}}\rvert\uparrow_i\uparrow_j\rangle$	0	$-6\left((t_1-t_3)\operatorname{Im}\left[\mathfrak{B}_{l,m}^3-\mathfrak{B}_{m,l}^3\right]+t_2\operatorname{Re}\left[\mathfrak{B}_{l,m}^3+\mathfrak{B}_{m,l}^3\right]\right)$	$-6\left((t_1-t_3)\operatorname{Im}\left[\mathfrak{B}_{l,m}^3-\mathfrak{B}_{m,l}^3\right]-t_2\operatorname{Re}\left[\mathfrak{B}_{l,m}^3+\mathfrak{B}_{m,l}^3\right]\right)$
$\langle\downarrow_i\downarrow_j\lvert H_{\text{eff}}\rvert\downarrow_i\downarrow_j\rangle$	0	$6\left((t_1-t_3)\operatorname{Im}\left[\mathfrak{B}_{l,m}^3-\mathfrak{B}_{m,l}^3\right]-5t_2\operatorname{Re}\left[\mathfrak{B}_{l,m}^3+\mathfrak{B}_{m,l}^3\right]\right)$	$6\left((t_1-t_3)\operatorname{Im}\left[\mathfrak{B}_{l,m}^3-\mathfrak{B}_{m,l}^3\right]-t_2\operatorname{Re}\left[\mathfrak{B}_{l,m}^3+\mathfrak{B}_{m,l}^3\right]\right)$
$\langle\downarrow_i\uparrow_j\lvert H_{\text{eff}}\rvert\downarrow_i\uparrow_j\rangle$	$-4(2t_1+t_3)\operatorname{Im}\left[\mathfrak{B}_{l,m}^3-\mathfrak{B}_{m,l}^3\right]$	$-6\left(4t_1\operatorname{Im}\left[\mathfrak{B}_{l,m}^3-\mathfrak{B}_{m,l}^3\right]+2t_2\operatorname{Re}\left[\mathfrak{B}_{l,m}^3+\mathfrak{B}_{m,l}^3\right]\right)$	$-6\left(4t_1\operatorname{Im}\left[\mathfrak{B}_{l,m}^3-\mathfrak{B}_{m,l}^3\right]+2t_2\operatorname{Re}\left[\mathfrak{B}_{l,m}^3+\mathfrak{B}_{m,l}^3\right]\right)$
$\langle\uparrow_i\downarrow_j\lvert H_{\text{eff}}\rvert\downarrow_i\uparrow_j\rangle$	0	$-6\left(i(t_1-t_3)\operatorname{Re}\left[\mathfrak{B}_{l,m}^3+\mathfrak{B}_{m,l}^3\right]+t_2\operatorname{Re}\left[\mathfrak{B}_{l,m}^3-\mathfrak{B}_{m,l}^3\right]\right)$	$6\left(i(t_1-t_3)\operatorname{Re}\left[\mathfrak{B}_{l,m}^3+\mathfrak{B}_{m,l}^3\right]-t_2\operatorname{Re}\left[\mathfrak{B}_{l,m}^3-\mathfrak{B}_{m,l}^3\right]\right)$
$\langle\uparrow_i\downarrow_j\lvert H_{\text{eff}}\rvert\uparrow_i\downarrow_j\rangle$	0	0	0

Table B.1: $j=1/2$ matrix elements of H_{eff} for an intermediate $\mathcal{E}_S$, $\mathcal{E}_P$, and $\mathcal{E}_D$. H_{eff} is derived in third order perturbation theory.

	$\mathcal{E}_S\,[1/54]$	$\mathcal{E}_P\,[1/54]$	$\mathcal{E}_D\,[1/54]$
$\langle\downarrow_i\uparrow_j\lvert H_{\text{eff}}\rvert\uparrow_i\downarrow_j\rangle$	$2\left(\mathfrak{B}_{n,l}^4\mathfrak{B}_{-m,-k}^{4*}-\mathfrak{B}_{n,l}^4\mathfrak{B}_{-k,-m}^{4*}+\mathfrak{B}_{l,n}^4\mathfrak{B}_{-k,-m}^{4*}-\mathfrak{B}_{l,n}^4\mathfrak{B}_{-m,-k}^{4*}\right)$	$3\left(\mathfrak{B}_{n,l}^4\mathfrak{B}_{-m,-k}^{4*}-\mathfrak{B}_{n,l}^4\mathfrak{B}_{-k,-m}^{4*}+\mathfrak{B}_{l,n}^4\mathfrak{B}_{-k,-m}^{4*}-\mathfrak{B}_{l,n}^4\mathfrak{B}_{-m,-k}^{4*}\right)$	$\left(\mathfrak{B}_{n,l}^4\mathfrak{B}_{-m,-k}^{4*}-\mathfrak{B}_{n,l}^4\mathfrak{B}_{-k,-m}^{4*}+\mathfrak{B}_{l,n}^4\mathfrak{B}_{-k,-m}^{4*}-\mathfrak{B}_{l,n}^4\mathfrak{B}_{-m,-k}^{4*}\right)$
$\langle\uparrow_i\uparrow_j\lvert H_{\text{eff}}\rvert\uparrow_i\uparrow_j\rangle$	0	$3\left(3\mathfrak{B}_{n,l}^4\mathfrak{B}_{-k,-m}^{4*}+3\mathfrak{B}_{l,n}^4\mathfrak{B}_{-k,-m}^{4*}+2\mathfrak{B}_{l,n}^4\mathfrak{B}_{-m,-k}^{4*}\right)$	$3\left(\mathfrak{B}_{n,l}^4\mathfrak{B}_{-m,-k}^{4*}+\mathfrak{B}_{l,n}^4\mathfrak{B}_{-k,-m}^{4*}\right)$
$\langle\uparrow_i\downarrow_j\lvert H_{\text{eff}}\rvert\uparrow_i\downarrow_j\rangle$	0	$3\left(3\mathfrak{B}_{n,l}^4\mathfrak{B}_{-m,-k}^{4*}+3\mathfrak{B}_{l,n}^4\mathfrak{B}_{-m,-k}^{4*}+2\mathfrak{B}_{l,n}^4\mathfrak{B}_{-k,-m}^{4*}\right)$	$3\left(\mathfrak{B}_{n,l}^4\mathfrak{B}_{-m,-k}^{4*}+\mathfrak{B}_{l,n}^4\mathfrak{B}_{-k,-m}^{4*}\right)$
$\langle\downarrow_i\downarrow_j\lvert H_{\text{eff}}\rvert\downarrow_i\downarrow_j\rangle$	0	$3\left(3\mathfrak{B}_{n,l}^4A_2^*+2\mathfrak{B}_{l,n}^4\mathfrak{B}_{-m,-k}^{4*}+2\mathfrak{B}_{n,l}^4\mathfrak{B}_{-k,-m}^{4*}\right)$	$3\left(\mathfrak{B}_{n,l}^4\mathfrak{B}_{-m,-k}^{4*}+\mathfrak{B}_{l,n}^4\mathfrak{B}_{-k,-m}^{4*}\right)$
$\langle\downarrow_i\uparrow_j\lvert H_{\text{eff}}\rvert\uparrow_i\downarrow_j\rangle$	$2\left(\mathfrak{B}_{n,l}^4\mathfrak{B}_{-m,-k}^{4*}+3\mathfrak{B}_{l,n}^4\mathfrak{B}_{-k,-m}^{4*}-\mathfrak{B}_{n,l}^4\mathfrak{B}_{-k,-m}^{4*}-\mathfrak{B}_{l,n}^4\mathfrak{B}_{-m,-k}^{4*}\right)$	$3\left(3\mathfrak{B}_{n,l}^4\mathfrak{B}_{-m,-k}^{4*}+3\mathfrak{B}_{l,n}^4\mathfrak{B}_{-k,-m}^{4*}-\mathfrak{B}_{n,l}^4\mathfrak{B}_{-k,-m}^{4*}-\mathfrak{B}_{l,n}^4\mathfrak{B}_{-m,-k}^{4*}\right)$	$\left(7\mathfrak{B}_{n,l}^4\mathfrak{B}_{-m,-k}^{4*}+7\mathfrak{B}_{l,n}^4\mathfrak{B}_{-k,-m}^{4*}+5\mathfrak{B}_{n,l}^4\mathfrak{B}_{-k,-m}^{4*}+5\mathfrak{B}_{l,n}^4\mathfrak{B}_{-m,-k}^{4*}\right)$
$\langle\uparrow_i\downarrow_j\lvert H_{\text{eff}}\rvert\uparrow_i\downarrow_j\rangle$	$2\left(\mathfrak{B}_{n,l}^4\mathfrak{B}_{-k,-m}^{4*}-\mathfrak{B}_{n,l}^4\mathfrak{B}_{-m,-k}^{4*}\right)$	$3\left(\mathfrak{B}_{n,l}^4\mathfrak{B}_{-k,-m}^{4*}-\mathfrak{B}_{n,l}^4\mathfrak{B}_{-m,-k}^{4*}\right)$	$3\left(-\mathfrak{B}_{n,l}^4\mathfrak{B}_{-k,-m}^{4*}+\mathfrak{B}_{n,l}^4\mathfrak{B}_{-m,-k}^{4*}\right)$
$\langle\uparrow_i\downarrow_j\lvert H_{\text{eff}}\rvert\downarrow_i\uparrow_j\rangle$	0		

Table B.2: $j=1/2$ matrix elements of H_{eff} for an intermediate $\mathcal{E}_S$, $\mathcal{E}_P$, and $\mathcal{E}_D$ energy, where $n=-l-k-m$. H_{eff} is derived in fourth order perturbation theory.

on the $|\sigma_i, \sigma_j\rangle$ states. This is well documented in the supplemental material of [31]. With this, we can calculate the desired matrix elements, which include ligand atoms and the reversed path for each bond. In the calculations we proceed as follows, we determine contributions to the matrix elements with a virtual excitation energy $\mathcal{E}_{\mathrm{S}}$, $\mathcal{E}_{\mathrm{P}}$, and $\mathcal{E}_{\mathrm{D}}$ separately and then combine them to obtain the interactions (B.24)-(B.29). We list the results for the different virtual excitations in Tab. B.1. The results in Tab. B.1 were the first indicator that there have to be interactions beyond the J, K, and Γ interactions, since contributions for the $\langle \uparrow_i \downarrow_j | H_{\mathrm{eff}} | \downarrow_i \uparrow_j \rangle$ are purely imaginary, while Heisenberg interactions would be completely real. Hence, we can not attribute these matrix elements to the Heisenberg interaction. This necessitates the introduction of the new Dzyaloshinskii–Moriya type interaction type D

$$(S_i \times S_j)_z = S_i^x S_j^y - S_i^y S_j^x = -\frac{i}{2}(S_i^- S_j^+ - S_i^+ S_j^-). \tag{B.30}$$

Similarly the μ interaction

$$S_i^x S_j^x - S_i^y S_j^y = \frac{1}{2}\left(S_i^+ S_j^+ + S_i^- S_j^-\right), \tag{B.31}$$

arises from the real parts of $\langle \uparrow_i \uparrow_j | H_{\mathrm{eff}} | \downarrow_i \downarrow_j \rangle$, where the imaginary part of this matrix element yields the Γ-interactions. These new interactions vanish for circular polarization, which is why they have not yet been documented.

It is important to note that the inclusion of the reversed path has a tremendous effect on the interactions. The omission of the reversed path in [31] yielded non-zero third-order Heisenberg interactions for CP, which vanish if we take the reversed path into account. As becomes evident in (B.27), this also has an effect on the Kitaev interactions, which explains the discrepancy between numerical and analytical results in [31].

B.3 Fourth order

For fourth-order processes, we consider parts of the kinetic Hamiltonian describing a *p-d* hopping. As for third-order processes, we evaluate the prefactors arising from the influence of the light field via a simple example. Here, we consider a hopping from site 1 to site 2 mediated via the p_2 ligand and back. This then yields

$$
\begin{aligned}
\mathfrak{B}^4_{-m-l-k,l}\mathfrak{B}^{4*}_{-m,-k} = & \left\{ \sum_n \mathcal{J}_n \left[\frac{A_0}{\sqrt{2}N} \sin(\alpha + \frac{\pi}{4}) \right] \mathcal{J}_{-m-l-k-Nn} \left[\frac{A_0}{\sqrt{2}} \cos(\alpha + \frac{\pi}{4}) \right] e^{i\epsilon n} \right\} \\
& \times \left\{ \sum_n \mathcal{J}_n \left[\frac{A_0}{\sqrt{2}N} \sin(\alpha - \frac{\pi}{4}) \right] \mathcal{J}_{l-Nn} \left[\frac{A_0}{\sqrt{2}} \cos(\alpha - \frac{\pi}{4}) \right] e^{i\epsilon n} \right\} \\
& \times \left\{ \sum_n \mathcal{J}_n \left[\frac{A_0}{\sqrt{2}N} \sin(\alpha - \frac{\pi}{4}) \right] \mathcal{J}_{-k-Nn} \left[\frac{A_0}{\sqrt{2}} \cos(\alpha - \frac{\pi}{4}) \right] e^{-i\epsilon n} \right\} \\
& \times \left\{ \sum_n \mathcal{J}_n \left[\frac{A_0}{\sqrt{2}N} \sin(\alpha + \frac{\pi}{4}) \right] \mathcal{J}_{-m-Nn} \left[\frac{A_0}{\sqrt{2}} \cos(\alpha + \frac{\pi}{4}) \right] e^{-i\epsilon n} \right\}
\end{aligned}
$$

$$\tag{B.32}$$

as a prefactor for fourth-order virtual excitations. We can then calculate the matrix elements for the Kitaev-Heisenberg Hamiltonian in the same fashion as in Sec. B.2.4. Tab. B.2 displays the results for all relevant matrix elements. Combining these results then yields the interactions (5.19)-(5.21). Again, considering the reverse path is essential to obtain accurate interaction strengths.

C
The Hamiltonian

C.1 Two particle eigenstates of the Kanamori Hamiltonian

Tab. 2.1 lists the possible states for two particles distributed on the three d-orbitals. Since Hund's coupling is sizable in Ca_2RuO_4, we can only consider the states with $\mathcal{E}_P$ for the ground state manifold. Therefore, we have three possible states per site labeled as $|T_{-1}\rangle$, $|T_0\rangle$, and $|T_1\rangle$ according to their total spin.

C.2 Three particle eigenstates of the Kanamori Hamiltonian

In case of double occupancy in one orbital, the eigenstates are given as $\Psi_{3,1}$ and $\Psi_{3,2}$ in Tab. 2.2, with corresponding eigenenergies $\mathcal{E}_{3,1}$ and $\mathcal{E}_{3,2}$. One can derive these energies via diagonalization of the Kanamori Hamiltonian Tab. C.1. The hopping processes including such an intermediate state are either orbital preserving $|\beta_i\beta_j\rangle\langle\beta_i\beta_j|$ Fig. 6.3 or pair flip $|\beta_i\beta_j\rangle\langle\alpha_i\alpha_j|$ Fig. 6.3 processes. Here, β_i denotes the orbital with no hole occupation. For the orbital preserving process, we obtain energy corrections of the form

$$\mathcal{A} = -\left(\frac{1}{U + 2J_\mathrm{H}} + \frac{1}{U}\right) = -2\frac{U + J_\mathrm{H}}{U(U + 2J_\mathrm{H})}, \tag{C.1}$$

where the two energies in the denominator arise from the energy difference between the triplet state manifold and the excited three-particle states $\Psi_{3,1}$ and $\Psi_{3,2}$ respectively. In the same fashion, we can obtain the energy correction for the pair flip terms, which

	$|\uparrow_\alpha\downarrow_\alpha\uparrow_\beta\rangle$	$|\uparrow_\beta\uparrow_\gamma\downarrow_\gamma\rangle$
$\langle\uparrow_\alpha\downarrow_\alpha\uparrow_\beta|$	$3U - 5J_\mathrm{H}$	J_H
$\langle\uparrow_\beta\uparrow_\gamma\downarrow_\gamma|$	J_H	$3U - 5J_\mathrm{H}$

Table C.1: Matrix elements of the Kanamori Hamiltonian for a three-particle state with an electron double occupancy.

	$\lvert\uparrow_\alpha\downarrow_\beta\uparrow_\gamma\rangle$	$\lvert\downarrow_\alpha\uparrow_\beta\uparrow_\gamma\rangle$	$\lvert\uparrow_\alpha\uparrow_\beta\downarrow_\gamma\rangle$
$\langle\uparrow_\alpha\downarrow_\beta\uparrow_\gamma\rvert$	$3U - 7J_\mathrm{H}$	$-J_\mathrm{H}$	$-J_\mathrm{H}$
$\langle\downarrow_\alpha\uparrow_\beta\uparrow_\gamma\rvert$	$-J_\mathrm{H}$	$3U - 7J_\mathrm{H}$	$-J_\mathrm{H}$
$\langle\uparrow_\alpha\uparrow_\beta\downarrow_\gamma\rvert$	$-J_\mathrm{H}$	$-J_\mathrm{H}$	$3U - 7J_\mathrm{H}$

Table C.2: Matrix elements of the Kanamori Hamiltonian for a three-particle state with no electron double occupancy.

include doubly occupied intermediate states

$$\mathcal{A}_F = -\frac{1}{2}\left(\frac{1}{U + 2J_\mathrm{H}} - \frac{1}{U}\right) = -\frac{-J_\mathrm{H}}{U(U + 2J_\mathrm{H})}. \tag{C.2}$$

Hopping processes with an intermediate state with three electrons occupying all three distinct orbitals can be distinguished into the states with total spin $S = 1/2$ ($\lvert\Psi_{t,3}\rangle$, $\lvert\Psi_{t,4}\rangle$, $\lvert\Psi_{t,5}\rangle$) and $S = 3/2$ states ($\lvert\psi_{t,6}\rangle$). We can obtain the former ones via diagonalization of the Kanamori Hamiltonian Tab. C.2. Processes including the intermediate $S = 3/2$ state $\lvert\Psi_{t,6}\rangle$ yield a energy correction of

$$\mathcal{B} = -\frac{1}{U - 3J_\mathrm{H}}. \tag{C.3}$$

Hopping processes, which include the $S = 1/2$ intermediate states, either are spin preserving with a correction term

$$\mathcal{C} = -\frac{1}{3}\frac{1}{U - 3J_\mathrm{H}} - \frac{2}{3}\frac{1}{U} = -\frac{(U - 2J_\mathrm{H})}{U(U - 3J_\mathrm{H})}, \tag{C.4}$$

or induce a spin-flip

$$\mathcal{D} = -\frac{1}{3}\frac{1}{U - 3J_\mathrm{H}} + \frac{1}{3}\frac{1}{U} = -\frac{J_\mathrm{H}}{U(U - 3J_\mathrm{H})}. \tag{C.5}$$

Again, the energies arising in the denominators of these expressions arise from the energy difference between the d^4 ground state manifold defined in Sec. C.1 and the respective excited state.

C.3 Initial state $\lvert\beta_i\beta_j\rangle$

To obtain the complete Hamiltonian it is advisable to consider the virtual hopping processes for different scenarios and then combine them. First, we want to distinguish between the initial orbital configurations of two d^4 sites. We start the analysis of hopping processes with initial states $\lvert\beta_i\beta_j\rangle$ where the double occupation resides in the same orbital

	$\lvert\uparrow_\alpha\uparrow_\gamma,\uparrow_\alpha\downarrow_\gamma\rangle$	$\lvert\uparrow_\alpha\downarrow_\gamma,\uparrow_\alpha\uparrow_\gamma\rangle$	$\lvert\downarrow_\alpha\uparrow_\gamma,\uparrow_\alpha\uparrow_\gamma\rangle$	$\lvert\uparrow_\alpha\uparrow_\gamma,\downarrow_\alpha\uparrow_\gamma\rangle$
$\langle\uparrow_\alpha\uparrow_\gamma,\uparrow_\alpha\downarrow_\gamma\rvert$	$t_\gamma^2\mathcal{A}$	$-t_\gamma^2\mathcal{A}$	0	0
$\langle\uparrow_\alpha\downarrow_\gamma,\uparrow_\alpha\uparrow_\gamma\rvert$	$-t_\gamma^2\mathcal{A}$	$t_\gamma^2\mathcal{A}$	0	0
$\langle\downarrow_\alpha\uparrow_\gamma,\uparrow_\alpha\uparrow_\gamma\rvert$	0	0	$t_\alpha^2\mathcal{A}$	$-t_\alpha^2\mathcal{A}$
$\langle\uparrow_\alpha\uparrow_\gamma,\downarrow_\alpha\uparrow_\gamma\rvert$	0	0	$-t_\alpha^2\mathcal{A}$	$t_\alpha^2\mathcal{A}$

Table C.3: Interactions arising through virtual hopping processes in the $m_S = 1$ spin sector for an initial orbital state $|\beta_i\beta_j\rangle$. We write the interactions in the spin basis.

	$\lvert\uparrow_\alpha\uparrow_\gamma,\downarrow_\alpha\downarrow_\gamma\rangle$	$\lvert\downarrow_\alpha\downarrow_\gamma,\uparrow_\alpha\uparrow_\gamma\rangle$	$\lvert\downarrow_\alpha\uparrow_\gamma,\uparrow_\alpha\downarrow_\gamma\rangle$	$\lvert\uparrow_\alpha\downarrow_\gamma,\downarrow_\alpha\uparrow_\gamma\rangle$
$\langle\uparrow_\alpha\uparrow_\gamma,\downarrow_\alpha\downarrow_\gamma\rvert$	$(t_\gamma^2+t_\alpha^2)\mathcal{A}$	0	$-t_\gamma^2\mathcal{A}$	$-t_\alpha^2\mathcal{A}$
$\langle\downarrow_\alpha\downarrow_\gamma,\uparrow_\alpha\uparrow_\gamma\rvert$	0	$(t_\gamma^2+t_\alpha^2)\mathcal{A}$	$-t_\alpha^2\mathcal{A}$	$-t_\gamma^2\mathcal{A}$
$\langle\downarrow_\alpha\uparrow_\gamma,\uparrow_\alpha\downarrow_\gamma\rvert$	$-t_\gamma^2\mathcal{A}$	$-t_\alpha^2\mathcal{A}$	$(t_\gamma^2+t_\alpha^2)\mathcal{A}$	0
$\langle\uparrow_\alpha\downarrow_\gamma,\downarrow_\alpha\uparrow_\gamma\rvert$	$-t_\alpha^2\mathcal{A}$	$-t_\gamma^2\mathcal{A}$	0	$(t_\gamma^2+t_\alpha^2)\mathcal{A}$

Table C.4: Interactions arising through virtual hopping processes in the $m_S = 0$ spin sector for an initial orbital state $|\beta_i\beta_j\rangle$. We write the interactions in the spin basis.

on both sites. Since the kinetic Hamiltonian (2.1) preserves the total spin of the two sites combined we can further dissect the manifold of initial states with $|\beta_i\beta_j\rangle$ into spin sectors. Since two holes reside on each site, the total magnetic spin quantum number can take values $m_S = -2, -1, 0, 1, 2$. H_{kin} has the same hopping amplitudes for $\uparrow$ and $\downarrow$, hence $\pm m_s$ are calculated completely analogous. This reduces the spin sectors we have to consider to $m_s = 0, 1, 2$.

The initial state with the electron double occupancy in orbital β on both states and $\uparrow$ for each hole does not allow for any hopping processes due to the Pauli principle thus, we obtain $H_2 = 0$. Tab. C.3 and Tab. C.4 display the virtual hopping processes for the $m_s = 0, 1$ spin sectors. From Tab. C.3 we deduce the Hamiltonian for spin sector $m_S = 1$

$$
\begin{aligned}
H_{i,j}^1 = \frac{\mathcal{A}}{2}\left(t_\alpha^2 + t_\gamma^2\right)\Big(&|T_i^1 T_j^0\rangle\langle T_i^1 T_j^0| - |T_i^1 T_j^0\rangle\langle T_i^0 T_j^1| + |T_i^{-1} T_j^0\rangle\langle T_i^{-1} T_j^0| \\
&- |T_i^{-1} T_j^0\rangle\langle T_i^0 T_j^{-1}| + i\leftrightarrow j\Big)\otimes|\beta_i\beta_j\rangle\langle\beta_i\beta_j|,
\end{aligned}
\tag{C.6}
$$

where we projected the spin states into the triplet basis via

$$|\uparrow, \uparrow\rangle = |T_1\rangle \tag{C.7}$$

$$|\downarrow, \downarrow\rangle = |T_{-1}\rangle \tag{C.8}$$

$$|\downarrow, \uparrow\rangle = \frac{1}{\sqrt{2}}(|T^0\rangle + |S\rangle) \tag{C.9}$$

$$|\uparrow, \downarrow\rangle = \frac{1}{\sqrt{2}}(|T^0\rangle - |S\rangle). \tag{C.10}$$

We neglect the singlet states $|S\rangle$ because they are not part of the ground state manifold $\mathcal{E}_P$. In the same fashion, we obtain the effective Hamiltonian for the $m_S = 0$ spin sector

$$H_{i,j}^0 = - \left(t_\alpha^2 + t_\gamma^2\right) \frac{U + J_{\mathrm{H}}}{U(U + 2J_{\mathrm{H}})} \left(2 |T_i^1 T_j^{-1}\rangle \langle T_i^1 T_j^{-1}| - |T_i^1 T_j^{-1}\rangle \langle T_i^0 T_j^0| \right.$$
$$\left. - |T_i^0 T_j^0\rangle \langle T_i^1 T_j^{-1}| + i \leftrightarrow j + |T_i^0 T_j^0\rangle \langle T_i^0 T_j^0| \right) \otimes |\beta_i \beta_j\rangle \langle \beta_i \beta_j| . \tag{C.11}$$

Combining the results of the different spin sectors and including $H_{i,j}^{-1}$, we derive at the spin-orbit Hamiltonian for orbital preserving hopping processes

$$H_{\beta\beta}^{\mathrm{OP}} = - \sum_{i,j} \frac{U + J_{\mathrm{H}}}{U(U + 2J_{\mathrm{H}})} \left(t_\alpha^2 + t_\gamma^2\right) \left(|T_i^1 T_j^0\rangle \langle T_i^1 T_j^0| - |T_i^1 T_j^0\rangle \langle T_i^0 T_j^1| \right.$$
$$+ 2 |T_i^1 T_j^{-1}\rangle \langle T_i^1 T_j^{-1}| + \frac{1}{2} |T_i^0 T_j^0\rangle \langle T_i^0 T_j^0| + |T_i^{-1} T_j^0\rangle \langle T_i^{-1} T_j^0| - |T_i^{-1} T_j^0\rangle \langle T_i^0 T_j^{-1}|$$
$$\left. - |T_i^1 T_j^{-1}\rangle \langle T_i^0 T_j^0| - |T_i^0 T_j^0\rangle \langle T_i^1 T_j^{-1}| + i \leftrightarrow j \right) \otimes |\beta_i \beta_j\rangle \langle \beta_i \beta_j| . \tag{C.12}$$

We now can project the Hamiltonian from the triplet basis into a $S = 1$ basis via

$$n_i = \left(|T_i^1\rangle \langle T_i^1| + |T_i^{-1}\rangle \langle T_i^{-1}| + |T_i^0\rangle \langle T_i^0| \right)$$
$$S_i^z = \left(|T_i^1\rangle \langle T_i^1| - |T_i^{-1}\rangle \langle T_i^{-1}| \right)$$
$$S_i^x = \frac{1}{2} (S_i^+ + S_i^-)$$
$$S_i^y = \frac{i}{2} (-S_i^+ + S_i^-)$$
$$S_i^+ = \sqrt{2} (|T_i^1\rangle \langle T_i^0| + |T_i^0\rangle \langle T_i^{-1}|)$$
$$S_i^- = \sqrt{2} (|T_i^{-1}\rangle \langle T_i^0| + |T_i^0\rangle \langle T_i^1|), \tag{C.13}$$

which yields

$$H_{\beta\beta}^{\mathrm{OP}} = \sum_{i,j} \frac{U + J_{\mathrm{H}}}{U(U + 2J_{\mathrm{H}})} \left(t_\alpha^2 + t_\gamma^2\right) (S_i S_j - 1) \otimes |\beta_i \beta_j\rangle \langle \beta_i \beta_j| . \tag{C.14}$$

The orbital flip processes in the $|\beta_i \beta_j\rangle$ manifold can be derived completely analogous to

	$\|T_i^1 T_j^1\rangle \otimes \|\beta_i\gamma_j\rangle$	$\|T_i^1 T_j^1\rangle \otimes \|\gamma_i\beta_j\rangle$
$\langle\beta_i\gamma_j\| \otimes \langle T_i^1 T_j^1\|$	$(t_\gamma^2 + t_\beta^2)\mathcal{B}$	$-2t_\gamma t_\beta \mathcal{B}$
$\langle\gamma_i\beta_j\| \otimes \langle T_i^1 T_j^1\|$	$-2t_\gamma t_\beta \mathcal{B}$	$(t_\gamma^2 + t_\beta^2)\mathcal{B}$

Table C.5: Interactions arising through virtual hopping processes in the $m_S = 2$ spin sector for an initial orbital state $|\beta_i\gamma_j\rangle$. We write the interactions in the triplet basis defined in Sec. C.1.

the orbital preserving terms yielding

$$
H_{\beta\beta}^{\mathrm{OF}} = \sum_{i,j} \frac{-J_{\mathrm{H}}}{U(U + 2J_{\mathrm{H}})} t_\alpha t_\beta \left(S_i S_j - 1 \right) \otimes \left(|\alpha_i\alpha_j\rangle \langle\beta_i\beta_j| + |\beta_i\beta_j\rangle \langle\alpha_i\alpha_j| \right). \tag{C.15}
$$

The total Hamiltonian for the $|\beta_i\beta_j\rangle$ then is $H_{\beta\beta} = H_{\beta\beta}^{\mathrm{OP}} + H_{\beta\beta}^{\mathrm{OF}}$.

C.4 Initial state $|\beta_i\gamma_j\rangle$

We now consider the initial states with the electron double occupations residing in distinct orbitals for the adjacent sites i and j. Like in Sec. C.3, we consider the three spin sectors $m_S = 0, 1, 2$. We summarize the virtual hopping processes, projected into the triplet basis, in Tab. C.5, Tab. C.6, and Tab. C.7. Therefore, we obtain the $m_S = 2$ Hamiltonian

$$
H_2 = -\sum_{i,j} |T_i^1 T_j^1\rangle \langle T_i^1 T_j^1| \otimes \left(\frac{t_\gamma^2 + t_\beta^2}{U - 3J_{\mathrm{H}}} |\beta_i\gamma_j\rangle \langle\beta_i\gamma_j| - \frac{2t_\gamma t_\beta}{U - 3J_{\mathrm{H}}} |\beta_i\gamma_j\rangle \langle\gamma_i\beta_j| + i \leftrightarrow j \right). \tag{C.16}
$$

The $m_S = 1$ Hamiltonian is given by

$$
\begin{aligned}
H_1 = &\left\{ \left[t_\alpha^2 \mathcal{A}/2 - (t_\beta^2 + t_\gamma^2)\mathcal{D} \right] \left(|T_i^1 T_j^0\rangle \langle T_i^1 T_j^0| - |T_i^1 T_j^0\rangle \langle T_i^0 T_j^1| - |T_i^0 T_j^1\rangle \langle T_i^1 T_j^0| \right. \right. \\
&\left. + |T_i^0 T_j^1\rangle \langle T_i^0 T_j^1| \right) + (t_\gamma^2 + t_\beta^2)\mathcal{B} \left(|T_i^1 T_j^0\rangle \langle T_i^1 T_j^0| + |T_i^0 T_j^1\rangle \langle T_i^0 T_j^1| \right) \Bigg\} \otimes |\beta_i\gamma_j\rangle \langle\beta_i\gamma_j| \\
&+ t_\gamma t_\beta \left[(\mathcal{B} - \mathcal{D}) \left(|T_i^1 T_j^0\rangle \langle T_i^1 T_j^0| - |T_i^1 T_j^0\rangle \langle T_i^0 T_j^1| - |T_i^0 T_j^1\rangle \langle T_i^1 T_j^0| \right. \right. \\
&\left. + |T_i^0 T_j^1\rangle \langle T_i^0 T_j^1| \right) - 2\mathcal{B} \left(|T_i^1 T_j^0\rangle \langle T_i^1 T_j^0| + |T_i^0 T_j^1\rangle \langle T_i^0 T_j^1| \right) \Bigg] \\
&\otimes |\beta_i\gamma_j\rangle \langle\gamma_i\beta_j| + i \leftrightarrow j, \tag{C.17}
\end{aligned}
$$

	$\lvert T_i^1 T_j^0\rangle \otimes \lvert\beta_i\gamma_i\rangle$	$\lvert T_i^0 T_j^1\rangle \otimes \lvert\beta_i\gamma_i\rangle$	$\lvert T_i^1 T_j^0\rangle \otimes \lvert\gamma_i\beta_i\rangle$	$\lvert T_i^0 T_j^1\rangle \otimes \lvert\gamma_i\beta_i\rangle$
$\langle T_i^1 T_j^0\rvert \otimes \langle\beta_i\gamma_i\rvert$	$t_\alpha^2 A/2 - (t_\beta^2 + t_\gamma^2)(D - B)$	$(t_\beta^2 + t_\gamma^2)D - t_\alpha^2 A/2$	$-t_\gamma t_\beta(B + D)$	$-t_\gamma t_\beta(B - D)$
$\langle T_i^0 T_j^1\rvert \otimes \langle\beta_i\gamma_i\rvert$	$(t_\beta^2 + t_\gamma^2)D - t_\alpha^2 A/2$	$t_\alpha^2 A/2 - (t_\beta^2 + t_\gamma^2)(D - B)$	$-t_\gamma t_\beta(B - D)$	$-t_\gamma t_\beta(B + D)$
$\langle T_i^1 T_j^0\rvert \otimes \langle\gamma_i\beta_i\rvert$	$-t_\gamma t_\beta(B + D)$	$-t_\gamma t_\beta(B - D)$	$t_\alpha^2 A/2 - (t_\beta^2 + t_\gamma^2)(D - B)$	$(t_\beta^2 + t_\gamma^2)D - t_\alpha^2 A/2$
$\langle T_i^0 T_j^1\rvert \otimes \langle\gamma_i\beta_i\rvert$	$-t_\gamma t_\beta(B - D)$	$-t_\gamma t_\beta(B + D)$	$(t_\beta^2 + t_\gamma^2)D - t_\alpha^2 A/2$	$t_\alpha^2 A/2 - (t_\beta^2 + t_\gamma^2)(D - B)$

Table C.6: Interactions arising through virtual hopping processes in the $m_S = 1$ spin sector for an initial orbital state $\lvert\beta_i\gamma_j\rangle$. We write the interactions in the triplet basis defined in Sec. C.1.

	$\lvert T_i^1 T_j^{-1}\rangle \otimes \lvert\beta_i\gamma_i\rangle$	$\lvert T_i^{-1} T_j^1\rangle \otimes \lvert\beta_i\gamma_i\rangle$	$\lvert T_i^0 T_j^0\rangle \otimes \lvert\beta_i\gamma_i\rangle$	$\lvert T_i^1 T_j^{-1}\rangle \otimes \lvert\gamma_i\beta_i\rangle$	$\lvert T_i^{-1} T_j^1\rangle \otimes \lvert\gamma_i\beta_i\rangle$	$\lvert T_i^0 T_j^0\rangle \otimes \lvert\gamma_i\beta_i\rangle$
$\langle T_i^1 T_j^{-1}\rvert \otimes \langle\beta_i\gamma_i\rvert$	$\left(t_\alpha^2 A - (t_\beta^2 + t_\gamma^2)(2D - B)\right)$	0	$(t_\beta^2 + t_\gamma^2)D - t_\alpha^2 A/2$	$-2t_\beta t_\gamma D$	0	$-t_\gamma t_\beta(B - D)$
$\langle T_i^{-1} T_j^1\rvert \otimes \langle\beta_i\gamma_i\rvert$	0	$\left(t_\alpha^2 A - (t_\beta^2 + t_\gamma^2)(2D - B)\right)$	$(t_\beta^2 + t_\gamma^2)D - t_\alpha^2 A/2$	0	$-2t_\beta t_\gamma D$	$-t_\gamma t_\beta(B - D)$
$\langle T_i^0 T_j^0\rvert \otimes \langle\beta_i\gamma_i\rvert$	$(t_\beta^2 + t_\gamma^2)D - t_\alpha^2 A/2$	$(t_\beta^2 + t_\gamma^2)D - t_\alpha^2 A/2$	$t_\alpha^2 A/2 - (t_\beta^2 + t_\gamma^2)(D - B)$	$-t_\gamma t_\beta(B - D)$	$-t_\gamma t_\beta(B - D)$	$(t_\beta^2 + t_\gamma^2)D - t_\alpha^2 A/2$
$\langle T_i^1 T_j^{-1}\rvert \otimes \langle\gamma_i\beta_i\rvert$	$-2t_\beta t_\gamma D$	0	$-t_\gamma t_\beta(B - D)$	$t_\alpha^2 A - (t_\beta^2 + t_\gamma^2)(2D - B)$	0	$(t_\beta^2 + t_\gamma^2)D - t_\alpha^2 A/2$
$\langle T_i^{-1} T_j^1\rvert \otimes \langle\gamma_i\beta_i\rvert$	0	$-2t_\beta t_\gamma D$	$-t_\gamma t_\beta(B - D)$	0	$t_\alpha^2 A - (t_\beta^2 + t_\gamma^2)(2D - B)$	$(t_\beta^2 + t_\gamma^2)D - t_\alpha^2 A/2$
$\langle T_i^0 T_j^0\rvert \otimes \langle\gamma_i\beta_i\rvert$	$-t_\gamma t_\beta(B - D)$	$-t_\gamma t_\beta(B - D)$	$(t_\beta^2 + t_\gamma^2)D - t_\alpha^2 A/2$	$(t_\beta^2 + t_\gamma^2)D - t_\alpha^2 A/2$	$(t_\beta^2 + t_\gamma^2)D - t_\alpha^2 A/2$	$t_\alpha^2 A/2 - (t_\beta^2 + t_\gamma^2)(D - B)$

Table C.7: Interactions arising through virtual hopping processes in the $m_S = 0$ spin sector for an initial orbital state $\lvert\beta_i\gamma_j\rangle$. We write the interactions in the triplet basis defined in Sec. C.1.

and last but not least, for $m_S = 0$, we obtain

$$
\begin{aligned}
H_0 =& \Bigg\{ \left[t_\alpha^2 \mathcal{A}/2 - (t_\beta^2 + t_\gamma^2)\mathcal{D} \right] \Bigg(2\,|T_i^1 T_j^{-1}\rangle \langle T_i^1 T_j^{-1}| + 2\,|T_i^{-1}T_j^1\rangle \langle T_i^{-1}T_j^1| + |T_i^0 T_j^0\rangle \langle T_i^0 T_j^0| \\
& - |T_i^1 T_j^{-1}\rangle \langle T_i^0 T_j^0| - |T_i^{-1}T_j^1\rangle \langle T_i^0 T_j^0| - |T_i^0 T_j^0\rangle \langle T_i^1 T_j^{-1}| - |T_i^0 T_j^0\rangle \langle T_i^{-1}T_j^1| \Bigg) \\
& + (t_\gamma^2 + t_\beta^2)\mathcal{B} \left(|T_i^1 T_j^{-1}\rangle \langle T_i^1 T_j^{-1}| + |T_i^{-1}T_j^1\rangle \langle T_i^{-1}T_j^1| + |T_i^0 T_j^0\rangle \langle T_i^0 T_j^0| \right) \Bigg\} \\
& \otimes |\beta_i \gamma_j\rangle \langle \beta_i \gamma_j| \\
& + \Bigg[t_\gamma t_\beta (\mathcal{B} - \mathcal{D}) \Bigg(2\,|T_i^1 T_j^{-1}\rangle \langle T_i^1 T_j^{-1}| + 2\,|T_i^{-1}T_j^1\rangle \langle T_i^{-1}T_j^1| + |T_i^0 T_j^0\rangle \langle T_i^0 T_j^0| \\
& - |T_i^1 T_j^{-1}\rangle \langle T_i^0 T_j^0| - |T_i^{-1}T_j^1\rangle \langle T_i^0 T_j^0| - |T_i^0 T_j^0\rangle \langle T_i^1 T_j^{-1}| - |T_i^0 T_j^0\rangle \langle T_i^{-1}T_j^1| \Bigg) \\
& - 2t_\gamma t_\beta \mathcal{B} \left(|T_i^1 T_j^{-1}\rangle \langle T_i^1 T_j^{-1}| + |T_i^{-1}T_j^1\rangle \langle T_i^{-1}T_j^1| + |T_i^0 T_j^0\rangle \langle T_i^0 T_j^0| \right) \Bigg] \\
& \otimes |\beta_i \gamma_j\rangle \langle \gamma_i \beta_j| + i \leftrightarrow j.
\end{aligned}
\tag{C.18}
$$

Again, to obtain the effective Hamiltonian for the $|\beta_i \gamma_j\rangle$ manifold, we add up the interactions of the spin sectors. Projecting this into the $S = 1$, like in Sec. C.3, then yields

$$
\begin{aligned}
H_{\beta\gamma} =& \Big\{ \left[(t_\beta^2 + t_\gamma^2)\mathcal{D} - t_\alpha^2 \mathcal{A}/2 \right] (S_i S_j - 1) + (t_\gamma^2 + t_\beta^2)\mathcal{B} \Big\} \otimes |\beta_i \gamma_j\rangle \langle \beta_i \gamma_j| \\
& - t_\gamma t_\beta \left[(\mathcal{B} - \mathcal{D})(S_i S_j - 1) + 2\mathcal{B} \right] \otimes |\beta_i \gamma_j\rangle \langle \gamma_i \beta_j|.
\end{aligned}
\tag{C.19}
$$

C.5 Complete Hamiltonian

We can obtain the complete effective Hamiltonian by combining the results of Sec. C.3 and Sec. C.4. This yields an effective spin-orbit Hamiltonian including both anisotropic hopping $t_\alpha \neq t_\beta \neq t_\gamma$ as well as finite Hund's coupling J_{H}

$$
\begin{aligned}
H =& H_{\beta\beta} + H_{\beta\alpha} \\
=& \sum_{\alpha \neq \beta} t_\beta^2 (S_i S_j - 1) \frac{U + J_{\mathrm{H}}}{U(U + 2J_{\mathrm{H}})} \otimes |\alpha_i \alpha_j\rangle \langle \alpha_i \alpha_j| \\
& - t_\alpha t_\beta (S_i S_j - 1) \frac{J_{\mathrm{H}}}{U(U + 2J_{\mathrm{H}})} \otimes |\alpha_i \alpha_j\rangle \langle \beta_i \beta_j| \\
& + \left[(S_i S_j - 1)t_{\gamma \neq (\alpha,\beta)}^2 \frac{(U + J_{\mathrm{H}})}{U(U + 2J_{\mathrm{H}})} - (S_i S_j - 1)\frac{(t_\alpha^2 + t_\beta^2)J_{\mathrm{H}}}{U(U - 3J_{\mathrm{H}})} - \frac{(t_\alpha^2 + t_\beta^2)}{(U - 3J_{\mathrm{H}})} \right] \\
& \otimes |\alpha_i \beta_j\rangle \langle \alpha_i \beta_j| + \frac{t_\alpha t_\beta}{U(U - 3J_{\mathrm{H}})} \left[(U - J_{\mathrm{H}})(S_i S_j + 1) + 2J_{\mathrm{H}} \right] \otimes |\alpha_i \beta_j\rangle \langle \beta_i \alpha_j|. \tag{C.20}
\end{aligned}
$$

The expressions (6.2)-(6.4) in the main text can be derived via the mapping (6.1). To compare our model with the Hamiltonian of [39] we set $J_{\mathrm{H}} = 0$ and consider isotropic NN hopping. This then yields for a c bond (like defined in [39])

$$
\begin{aligned}
H =& \frac{t^2}{U}\Bigg[-(S_i S_j + 1) \otimes \Bigg(|B_i C_j\rangle \langle B_i C_j| + |C_i A_j\rangle \langle C_i A_j| + |A_i B_j\rangle \langle B_i A_j| + i \leftrightarrow j \\
& + 2\,|C_i C_j\rangle \langle C_i C_j| + |B_i B_j\rangle \langle B_i B_j| + |A_i A_j\rangle \langle A_i A_j| \Bigg) \\
& + 3\,|B_i C_j\rangle \langle B_i C_j| + 3\,|C_i A_j\rangle \langle C_i A_j| + 2\,|A_i B_j\rangle \langle A_i B_j| + i \leftrightarrow j \\
& + 4\,|C_i C_j\rangle \langle C_i C_j| + 2\,|B_i B_j\rangle \langle B_i B_j| + 2\,|A_i A_j\rangle \langle A_i A_j| \Bigg] \\
=& -\frac{t^2}{U}\Bigg[(S_i S_j + 1) \otimes \mathcal{O}_{ij} + (L_i^z)^2 + \left(L_j^z\right)^2 \Bigg],
\end{aligned}
\tag{C.21}
$$

with

$$
\mathcal{O}_{ij} = (L_i^x L_j^x)^2 + (L_i^y L_j^y)^2 + L_i^x L_i^y L_j^y L_j^x + L_i^y L_i^x L_j^x L_j^y.
\tag{C.22}
$$

Here we used the definition $L_i^x = -i(|B_i\rangle \langle C_i| - |C_i\rangle \langle B_i|)$, with $|A_i\rangle$, $|B_i\rangle$, and $|C_i\rangle$ describing an electron double occupancy in the yz, zx, and xy orbital respectively. Since we chose a specific bond direction, the beforehand general double occupancy states $|\alpha_i\rangle$, $|\beta_i\rangle$, and $|\gamma_i\rangle$ now become $|A_i\rangle$, $|B_i\rangle$, and $|C_i\rangle$. Comparing (C.21) with the result of [39] [in the text before (1)], we see a perfect agreement solidifying the validity of the model.

List of Figures

List of Tables

Deutsche Zusammenfassung

In dieser Thesis haben wir effektive Kugel-Khomskii-Modelle für verschiedene Mott-isolierende Übergangsmetalle hergeleitet und diese analysiert. Hierbei haben wir uns auf d^4 und d^5 Materialien mit beträchtlicher Spin-Bahn Kopplung, wie u.a. Ca_2RuO_4 und α-$RuCl_3$, konzentriert. Diese Thesis war in zwei Hauptsegmente eingeteilt, die die verschiedenen Eigenschaften von Ru t_{2g}^4 und t_{2g}^5 Kitaev-Heisenberg Materialien diskutieren.

Im ersten Teil haben wir lediglich d^5 Kitaev-Heisenberg Materialien untersucht. Der effektive Kugel-Khomskii Hamiltonian für diese ist weitläufig bekannt und liefert, für starke Spin-Bahn Kopplung, ein Modell mit Kitaev, Heisenberg, Γ und Γ' Interaktionen. Ein großes Feld der Forschung für diese Materialien ist darauf ausgerichtet Wege zu finden diese Materialien in ein pures Kitaev-Modell zu treiben. Dies ist wünschenswert, da dieses Modell einen exakt lösbaren Grundzustand hat, welcher eine Spinflüssigkeit beschreibt [6]. In dieser Thesis haben wir einen relativ unerforschten Ansatz, die Beeinflussung von Interaktionsparametern durch ein zeitperiodisches Lichtfeld, untersucht. Durch den Floquet Formalismus, haben wir neue Ausdrücke für Interaktionen gefunden, die von der Frequenz und Amplitude des Lichts abhängen.

Wir haben gezeigt, dass Ruthenate, wie α-$RuCl_3$, geeigneter für Floquet-Engineering sind als Iridate, welche beide nah am Kitaev Spinflüssigkeitzustand sind. Ruthenate sind von Vorteil, da das Erhitzen des Materials während des Engineerings eine kleinere Rolle spielt. Dies ist der Fall, da Hund's Kopplung J_H und Coulomb Abstoßung U hier einen weiteren Frequenzbereich in dem Erhitzen abwesend ist erlaubt. In diesen Frequenzbereichen ist das effektive Floquet-Kitaev-Heisenberg-Modell plausibel. Linear polarisiertes Licht induziert hier Anisotropie in den Interaktionen, welche vom Winkel des Lichts zur betreffenden Verbindung abhängt. Wir argumentieren, dass dies ein mögliches Werkzeug sein könnte, welches es uns erlaubt Phasenübergänge innerhalb einer bestehenden Kitaev Spinflüssigkeit zu induzieren.

Zirkular polarisiertes Licht, auf der anderen Seite, erhält die Isotropie des Systems, bricht jedoch die Zeitumkehrsymmetrie. Dies führt zu einem inversen Faraday Effekt [31, 32]. Dieser Effekt kann beobachtet werden, wenn man ein Floquet-Kitaev-Heisenberg-Modell betrachtet, welches Prozesse dritter Ordnung über die Liganden ex-

plizit berücksichtigt. Um die akkuraten Stärken der einzelnen Interaktionen zu erhalten, ist es hierbei auch notwendig Ligandprozesse vierter Ordnung zu inkludieren. Die Inklusion von Prozessen dritter und vierter Ordnung hat nicht nur einen Effekt auf zirkular, sondern auch linear polarisiertes Licht. Für linear polarisiertes Licht induzieren diese Terme zwei neue Interaktionen, welche die Inversionssymmetrie des Systems brechen. Auf der anderen Seite verschwindet das induzierte Magnetfeld für lineare Polarisation, da die Zeitumkehrinvarianz hier nicht gebrochen wird. Die Lücke zwischen linearer und zirkularer Polarisation kann mithilfe elliptischer Lissajous Figuren gefüllt werden. In dieser Thesis haben wir eine effektiven Floquet-Hamiltonian für beliebige Polarisationen präsentiert, welcher die beiden Grenzfälle verbinden kann. Komplexere Lissajous Figuren entfernen sich dann weiter von den Grenzfällen, lineare und zirkulare Polarisation. Lissajous Figuren mit einer großen Frequenzdifferenz in x und y Richtung zeigen eine Entkopplung der Kitaev-Heisenberg Interaktionen von der relativen Phase ϵ. Das induzierte Magnetfeld kann jedoch nach wie vor durch ϵ an- und ausgeschaltet werden. Daher könnte man im Prinzip das Magnetfeld relativ zu den anderen Parametern abstimmen.

Der Floquet Formalismus führt eine Vielzahl an Möglichkeiten ein, Eigenschaften von Kitaev-Heisenberg Materialien ein, von denen wir lediglich einige wenige betrachtet haben. Unser effektives Modell liefert jedoch ein solides Fundament, um weitere Möglichkeiten zu erkunden. Ein erster nächster Schritt wäre die Implementation unseres Modells für eine optische Kavität, welche kürzlich im Kontext von Floquet Engineering diskutiert wurde [115]. Des Weiteren könnte man sich mit numerischen Kalkulationen zu Grundzustandseigenschaften für das Modell mit Termen vierter Ordnung befassen. Grundzustände könnten hierbei Dimere, verschiedene Spinflüssigkeiten, sowie einige der geordneten Zustände, die im Kontext von konventionellen Kitaev-Heisenberg Materialien diskutiert wurden, sein.

Der zweite Teil dieser Thesis befasste sich mit d^4 Übergangsmetall basierter Mott Isolatoren, welche eine Quadratgitterordnung haben. Besonderer Fokus lag hierbei auf dem Material Ca_2RuO_4. Im Gegensatz zu den Kitaev-Heisenberg Materialien im ersten Teil sind die Kugel-Khomskii-Modelle hier relativ unerforscht. In dieser Thesis haben wir einen effektiven Spin-Bahn Hamiltonian präsentiert, welcher Hund's Kopplung J_H, anisotrope Interaktionen nächster Nachbarn, sowie dritt-nächster Nachbarn berücksichtigt. Ein solcher Hamiltonian wurde im Kontext von Ca_2RuO_4, unseres Wissens, bisher nicht hergeleitet. Mit diesem Modell war es uns möglich eine detaillierte Analyse der Grundzustandseigenschaften, in Form eines $\Delta - \lambda$ Phasendiagramms, durchzuführen.

Wir haben festgestellt, dass ein beträchtliches Kristallfeld eine antiferromagnetische Ordnung induziert. Hierbei ändert sich die Orientierung der Spins von orthogonal zur Ebene, $\Delta \ll 0$, zu in der Ebene $\Delta \gg 0$ mit einem Vorzeichenwechsel des Kristallfelds.

Zwischen diesen beiden antiferromagnetischen Phasen existiert eine stripy Phase, für schwache Spin-Bahn Kopplung und schwaches positives Δ. Für schwaches negatives Kristallfeld Δ und schwache Spin-Bahn Kopplung, haben wir zudem eine neue Phase gefunden, welche wir mit 3U1D bezeichnet haben. Wie die stripy Phase verschwindet diese für beträchtliche Spin-Bahn Kopplung. Für sehr starke Spin-Bahn Kopplung wird das System paramagnetisch, wobei der Phasenübergang hier mit größerem Δ zu stärkerem λ wandert. Wir verordnen Ca_2RuO_4 eindeutig in der antiferromagnetischen Phase mit Spinorientierung in der Ebene. Dies ist in Übereinstimmung mit sowohl experimentellen [5] als auch VCA Resultaten [63].

Betreffend Anregungen, haben wir festgestellt, dass die Resultate des dynamische Spinstrukturfaktors unseres Modells exzellente Übereinstimmung mit experimentellen Resultaten inelastischer Neutronenstreuung [5] haben. Hierbei konnten wir charakteristische Eigenschaften von Ca_2RuO_4, wie das Maximum der Transversalmode, reproduzieren. Die dynamischen Eigenschaften sind sehr empfindlich gegenüber einer Änderung in Δ und λ und scheinen stark von der Lochdichte im xy Orbital n_{xy} abzuhängen. Wir haben festgestellt, dass n_{xy} für Ca_2RuO_4 einen nichtverschwindenden Beitrag hat. Dies ist ein klares Indiz, dass Spin-Bahn Kopplung eine relevante Rolle in Ca_2RuO_4 spielt. Wir schlussfolgern daher, dass der Grundzustand exzitonischer Natur ist. Die starke Abhängigkeit der dynamischen Eigenschaften von n_{xy}, macht unsere gute Übereinstimmung mit experimentellen Resultaten bemerkenswert.

Zuletzt haben wir das Verhalten des Spin-Bahn-Modells, im speziellen Ca_2RuO_4, für endliche Temperaturen untersucht. Monte-Carlo Simulationen liefern sowohl die spezifische Wärmekapazität $C(T)$ als auch die Suszeptibilität $\chi(T)$ welche Qualitativ mit experimentellen Messungen verglichen werden können. Mit diesen Simulationen war es uns möglich, die Néel Temperatur von Ca_2RuO_4 zu identifizieren, welche den Phasenübergang von einem antiferromagnetischen in einen paramagnetischen Mott Isolator markiert. Unsere numerischen Resultate haben eine gute qualitative Übereinstimmung mit dem Experiment gezeigt. Des Weiteren erscheint die Néel Temperatur sehr sensitiv gegenüber Änderungen in Δ und λ. Während T_N gleichmäßig mit steigendem λ ansteigt, sind die Änderungen durch ein variierendes Δ wesentlich abrupter und stark von der magnetischen Ordnung des Grundzustands abhängig. Die Orbitalordung zeigt keine signifikante Änderung bei T_N.

Im Prozess die Néel Temperatur möglichst genau zu bestimmen, haben wir die Effizienz der FOPT Methode für unser Modell untersucht. Es hat sich herausgestellt, dass unser System kein geeigneter Kandidat für FOPT ist, da es bereits relativ schnell mit PTMC konvergiert, während FOPT besonders für Probleme mit langen PTMC Konvergenzzeiten geeignet ist. Für Systeme, die unserem ähneln, empfehlen wir daher einen traditionellen PTMC Ansatz mit einer hohen Anzahl an verschiedenen Temperaturen.

Das effektive Spin-Bahn-Modell für d^4 Übergangsmetall basierte Mott Isolatoren, welches wir in dieser Thesis hergeleitet haben, ist ein guter Startpunkt für zukünftige Forschungen. Ein erster Ansatz wäre Monte-Carlo Resultate für Grundzustandseigenschaften auf größere Cluster zu erweitern, um somit die Effekte der Clustergröße auf Phasenübergänge besser abschätzen zu können. Des Weiteren wäre es interessant Licht-Materie Wechselwirkungen mithilfe des Floquet Formalismus zu untersuchen, wie wir es bereits für d^5 Materialien gemacht haben. Hierbei wäre vor allem das Triplon-Modell für dominante Spin-Bahn Kopplung von Interesse, um zu untersuchen, ob die Möglichkeit besteht Triplon Kondensation via Licht zu manipulieren. Zuletzt ist es möglich unser Modell auf ähnliche Materialien anzuwenden wie z.B. Vanadate [116]. Hier müsste man das Modell für drei Dimensionen anpassen, um den Einfluss von Δ und λ zu untersuchen.

Acknowledgements

Bibliography

[1] Jackeli, G. and Khaliullin, G. *Phys. Rev. Lett.* **102**, 017205 Jan (2009).

[2] Takagi, H., Takayama, T., Jackeli, G., Khaliullin, G., and Nagler, S. E. *Nature Reviews Physics* **1**, 264–280 Mar (2019).

[3] Winter, S. M., Tsirlin, A. A., Daghofer, M., van den Brink, J., Singh, Y., Gegenwart, P., and Valenti, R. *Journal of Physics: Condensed Matter* **29**(49), 493002 Nov (2017).

[4] Kitagawa, K., Takayama, T., Matsumoto, Y., Kato, A., Takano, R., Kishimoto, Y., Bette, S., Dinnebier, R., Jackeli, G., and Takagi, H. *Nature* **554**, 341–345 Feb (2018).

[5] Jain, A., Krautloher, M., Porras, J., Ryu, G. H., Chen, D. P., Abernathy, D. L., Park, J. T., Ivanov, A., Chaloupka, J., Khaliullin, G., Keimer, B., and Kim, B. J. *Nature Physics* **13**, 633 July (2017).

[6] Kitaev, A. *Annals of Physics* **321**(1), 2–111 Jan (2006).

[7] Singh, Y. and Gegenwart, P. *Phys. Rev. B* **82**, 064412 Aug (2010).

[8] Kobayashi, H., Tabuchi, M., Shikano, M., Kageyama, H., and Kanno, R. *J. Mater. Chem.* **13**, 957–962 Feb (2003).

[9] Ye, F., Chi, S., Cao, H., Chakoumakos, B. C., Fernandez-Baca, J. A., Custelcean, R., Qi, T. F., Korneta, O. B., and Cao, G. *Phys. Rev. B* **85**, 180403 May (2012).

[10] Choi, S. K., Coldea, R., Kolmogorov, A. N., Lancaster, T., Mazin, I. I., Blundell, S. J., Radaelli, P. G., Singh, Y., Gegenwart, P., Choi, K. R., Cheong, S.-W., Baker, P. J., Stock, C., and Taylor, J. *Phys. Rev. Lett.* **108**, 127204 Mar (2012).

[11] Liu, X., Berlijn, T., Yin, W.-G., Ku, W., Tsvelik, A., Kim, Y.-J., Gretarsson, H., Singh, Y., Gegenwart, P., and Hill, J. P. *Phys. Rev. B* **83**, 220403 Jun (2011).

[12] Williams, S. C., Johnson, R. D., Freund, F., Choi, S., Jesche, A., Kimchi, I., Manni, S., Bombardi, A., Manuel, P., Gegenwart, P., and Coldea, R. *Phys. Rev. B* **93**, 195158 May (2016).

[13] Plumb, K. W., Clancy, J. P., Sandilands, L. J., Shankar, V. V., Hu, Y. F., Burch, K. S., Kee, H.-Y., and Kim, Y.-J. *Phys. Rev. B* **90**, 041112 Jul (2014).

[14] Yadav, R., Bogdanov, N. A., Katukuri, V. M., Nishimoto, S., van den Brink, J., and Hozoi, L. *Scientific Reports* **6**, 37925 Nov (2016).

[15] Banerjee, A., Lampen-Kelley, P., Knolle, J., Balz, C., Aczel, A. A., Winn, B., Liu, Y., Pajerowski, D., Yan, J., Bridges, C. A., Savici, A. T., Chakoumakos, B. C., Lumsden, M. D., Tennant, D. A., Moessner, R., Mandrus, D. G., and Nagler, S. E. *npj Quantum Materials* **3**, 8 Feb (2018).

[16] Leahy, I. A., Pocs, C. A., Siegfried, P. E., Graf, D., Do, S.-H., Choi, K.-Y., Normand, B., and Lee, M. *Phys. Rev. Lett.* **118**, 187203 May (2017).

[17] Baek, S.-H., Do, S.-H., Choi, K.-Y., Kwon, Y. S., Wolter, A. U. B., Nishimoto, S., van den Brink, J., and Büchner, B. *Phys. Rev. Lett.* **119**, 037201 Jul (2017).

[18] Sears, J. A., Zhao, Y., Xu, Z., Lynn, J. W., and Kim, Y.-J. *Phys. Rev. B* **95**, 180411 May (2017).

[19] Zheng, J., Ran, K., Li, T., Wang, J., Wang, P., Liu, B., Liu, Z.-X., Normand, B., Wen, J., and Yu, W. *Phys. Rev. Lett.* **119**, 227208 Dec (2017).

[20] Hentrich, R., Wolter, A. U. B., Zotos, X., Brenig, W., Nowak, D., Isaeva, A., Doert, T., Banerjee, A., Lampen-Kelley, P., Mandrus, D. G., Nagler, S. E., Sears, J., Kim, Y.-J., Büchner, B., and Hess, C. *Phys. Rev. Lett.* **120**, 117204 Mar (2018).

[21] Cui, Y., Zheng, J., Ran, K., Wen, J., Liu, Z.-X., Liu, B., Guo, W., and Yu, W. *Phys. Rev. B* **96**, 205147 Nov (2017).

[22] Wang, Z., Guo, J., Tafti, F. F., Hegg, A., Sen, S., Sidorov, V. A., Wang, L., Cai, S., Yi, W., Zhou, Y., Wang, H., Zhang, S., Yang, K., Li, A., Li, X., Li, Y., Liu, J., Shi, Y., Ku, W., Wu, Q., Cava, R. J., and Sun, L. *Phys. Rev. B* **97**, 245149 Jun (2018).

[23] Kaib, D. A. S., Biswas, S., Riedl, K., Winter, S. M., and Valenti, R. *Phys. Rev. B* **103**, L140402 Apr (2021).

[24] Koitzsch, A., Habenicht, C., Müller, E., Knupfer, M., Büchner, B., Kretschmer, S., Richter, M., van den Brink, J., Börrnert, F., Nowak, D., Isaeva, A., and Doert, T. *Phys. Rev. Materials* **1**, 052001 Oct (2017).

[25] Baek, S.-H., Yeo, H. W., Do, S.-H., Choi, K.-Y., Janssen, L., Vojta, M., and Büchner, B. *Phys. Rev. B* **102**, 094407 Sep (2020).

[26] Bastien, G., Roslova, M., Haghighi, M. H., Mehlawat, K., Hunger, J., Isaeva, A., Doert, T., Vojta, M., Büchner, B., and Wolter, A. U. B. *Phys. Rev. B* **99**, 214410 Jun (2019).

[27] Kuwahara, T., Mori, T., and Saito, K. *Annals of Physics* **367**, 96–124 Apr (2016).

[28] Mori, T., Kuwahara, T., and Saito, K. *Phys. Rev. Lett.* **116**, 120401 Mar (2016).

[29] Abanin, D. A., De Roeck, W., and Huveneers, F. *Phys. Rev. Lett.* **115**, 256803 Dec (2015).

[30] Arakawa, N. and Yonemitsu, K. *Phys. Rev. B* **103**, L100408 Mar (2021).

[31] Kumar, U., Banerjee, S., and Lin, S.-Z. *Communications Physics* **5**, 157 Jun (2022).

[32] Sriram, A. and Claassen, M. *Phys. Rev. Research* **4**, L032036 Sep (2022).

[33] Winter, S. M., Li, Y., Jeschke, H. O., and Valenti, R. *Phys. Rev. B* **93**, 214431 Jun (2016).

[34] Rau, J. G., Lee, E. K.-H., and Kee, H.-Y. *Phys. Rev. Lett.* **112**, 077204 Feb (2014).

[35] Quito, V. L. and Flint, R. *Phys. Rev. Lett.* **126**, 177201 Apr (2021).

[36] Quito, V. L. and Flint, R. *Phys. Rev. B* **103**, 134435 Apr (2021).

[37] Trevisan, T. V., Arribi, P. V., Heinonen, O., Slager, R.-J., and Orth, P. P. *Phys. Rev. Lett.* **128**, 066602 Feb (2022).

[38] Nag, T., Slager, R.-J., Higuchi, T., and Oka, T. *Phys. Rev. B* **100**, 134301 Oct (2019).

[39] Khaliullin, G. *Phys. Rev. Lett.* **111**, 197201 Nov (2013).

[40] Kunkemöller, S., Khomskii, D., Steffens, P., Piovano, A., Nugroho, A. A., and Braden, M. *Phys. Rev. Lett.* **115**, 247201 Dec (2015).

[41] Zhang, G. and Pavarini, E. *Phys. Rev. B* **101**, 205128 May (2020).

[42] Cao, G., McCall, S., Shepard, M., Crow, J. E., and Guertin, R. P. *Phys. Rev. B* **56**, R2916–R2919 Aug (1997).

[43] Nakamura, F., Goko, T., Ito, M., Fujita, T., Nakatsuji, S., Fukazawa, H., Maeno, Y., Alireza, P., Forsythe, D., and Julian, S. R. *Phys. Rev. B* **65**, 220402 May (2002).

[44] Mott, N. *Metal-Insulator Transitions*. Taylor & Francis, London, Aug (1990).

[45] Imada, M., Fujimori, A., and Tokura, Y. *Rev. Mod. Phys.* **70**, 1039–1263 Oct (1998).

[46] Zegkinoglou, I., Strempfer, J., Nelson, C. S., Hill, J. P., Chakhalian, J., Bernhard, C., Lang, J. C., Srajer, G., Fukazawa, H., Nakatsuji, S., Maeno, Y., and Keimer, B. *Phys. Rev. Lett.* **95**, 136401 Sep (2005).

[47] Souliou, S.-M., Chaloupka, J., Khaliullin, G., Ryu, G., Jain, A., Kim, B. J., Le Tacon, M., and Keimer, B. *Phys. Rev. Lett.* **119**, 067201 Aug (2017).

[48] Mizokawa, T., Tjeng, L. H., Sawatzky, G. A., Ghiringhelli, G., Tjernberg, O., Brookes, N. B., Fukazawa, H., Nakatsuji, S., and Maeno, Y. *Phys. Rev. Lett.* **87**, 077202 Jul (2001).

[49] Vergara, I., Magnaterra, M., Warzanowski, P., Attig, J., Kunkemöller, S., Khomskii, D. I., Braden, M., Hermanns, M., and Grüninger, M. *Phys. Rev. B* **106**, 085103 Aug (2022).

[50] Braden, M., André, G., Nakatsuji, S., and Maeno, Y. *Phys. Rev. B* **58**, 847–861 Jul (1998).

[51] Hotta, T. and Dagotto, E. *Phys. Rev. Lett.* **88**, 017201 Dec (2001).

[52] Kugel, K. I. and Khomskii, D. I. *Soviet Physics Uspekhi* **25**(4), 231 Apr (1982).

[53] Slater, J. C. and Koster, G. F. *Phys. Rev.* **94**, 1498–1524 Jun (1954).

[54] Khaliullin, G. *Progress of Theoretical Physics Supplement* **160**, 155–202 Jun (2005).

[55] Kanamori, J. *Progress of Theoretical Physics* **30**(3), 275–289 Sep (1963).

[56] Georges, A., Medici, L. d., and Mravlje, J. *Annual Review of Condensed Matter Physics* **4**(1), 137–178 (2013).

[57] Khomskii, D. I. *Transition Metal Compounds.* Cambridge University Press, Nov (2014).

[58] Khomskii, D. I. and Streltsov, S. V. (2022).

[59] Landau, L. and Lifshitz, E. *Quantum Mechanics.* Pergamon Press, (1965).

[60] Abragam, A. and Bleaney, B. *Electron Paramagnetic Resonance of Transition Ions.* Clarendon Press, (1970).

[61] Alexander, C. S., Cao, G., Dobrosavljevic, V., McCall, S., Crow, J. E., Lochner, E., and Guertin, R. P. *Phys. Rev. B* **60**, R8422–R8425 Sep (1999).

[62] Gorelov, E., Karolak, M., Wehling, T. O., Lechermann, F., Lichtenstein, A. I., and Pavarini, E. *Phys. Rev. Lett.* **104**, 226401 Jun (2010).

[63] Feldmaier, T., Strobel, P., Schmid, M., Hansmann, P., and Daghofer, M. *Phys. Rev. Research* **2**, 033201 Aug (2020).

[64] Khaliullin, G. and Okamoto, S. *Phys. Rev. Lett.* **89**, 167201 Sep (2002).

[65] Oleś, A. M., Khaliullin, G., Horsch, P., and Feiner, L. F. *Phys. Rev. B* **72**, 214431 Dec (2005).

[66] Oleś, A. M., Feiner, L. F., and Zaanen, J. *Phys. Rev. B* **61**, 6257–6287 Mar (2000).

[67] Feiner, L. F. and Oleś, A. M. *Phys. Rev. B* **59**, 3295–3298 Feb (1999).

[68] Foyevtsova, K., Jeschke, H. O., Mazin, I. I., Khomskii, D. I., and Valenti, R. *Phys. Rev. B* **88**, 035107 Jul (2013).

[69] Kim, H.-S., V., V. S., Catuneanu, A., and Kee, H.-Y. *Phys. Rev. B* **91**, 241110 Jun (2015).

[70] Johnson, R. D., Williams, S. C., Haghighirad, A. A., Singleton, J., Zapf, V., Manuel, P., Mazin, I. I., Li, Y., Jeschke, H. O., Valenti, R., and Coldea, R. *Phys. Rev. B* **92**, 235119 Dec (2015).

[71] Akbari, A. and Khaliullin, G. *Phys. Rev. B* **90**, 035137 Jul (2014).

[72] Eckardt, A. and Anisimovas, E. *New Journal of Physics* **17**(9), 093039 Sep (2015).

[73] Sambe, H. *Phys. Rev. A* **7**, 2203–2213 Jun (1973).

[74] Koch, E. *Exact Diagonalization and Lanczos Method.* Autumn School on Correlated Electrons:Many-Body Methods for Real Materials, Sep (2019).

[75] Lanczos, C. *Journal of research of the National Bureau of Standards* **45**, 255–282 Oct (1950).

[76] Falcioni, M. and Deem, M. W. *The Journal of Chemical Physics* **110**(3), 1754–1766 Jan (1999).

[77] Strobel, P., Aust, F., and Daghofer, M. *Phys. Rev. B* **104**, 115148 Sep (2021).

[78] Stoudenmire, E. M., Trebst, S., and Balents, L. *Phys. Rev. B* **79**, 214436 Jun (2009).

[79] Remund, K., Pohle, R., Akagi, Y., Romhányi, J., and Shannon, N. *Phys. Rev. Res.* **4**, 033106 Aug (2022).

[80] Strobel, P. and Daghofer, M. *Phys. Rev. B* **105**, 085144 Feb (2022).

[81] Biffin, A., Johnson, R. D., Kimchi, I., Morris, R., Bombardi, A., Analytis, J. G., Vishwanath, A., and Coldea, R. *Phys. Rev. Lett.* **113**, 197201 Nov (2014).

[82] Biswas, S., Li, Y., Winter, S. M., Knolle, J., and Valenti, R. *Phys. Rev. Lett.* **123**, 237201 Dec (2019).

[83] Eckardt, A. *Rev. Mod. Phys.* **89**, 011004 Mar (2017).

[84] Mentink, J. H. *Journal of Physics: Condensed Matter* **29**(45), 453001 Oct (2017).

[85] Oka, T. and Kitamura, S. *Annual Review of Condensed Matter Physics* **10**(1), 387–408 Mar (2019).

[86] Liu, J., Hejazi, K., and Balents, L. *Phys. Rev. Lett.* **121**, 107201 Sep (2018).

[87] Mentink, J., Balzer, K., and Eckstein, M. *Nature Communications* **6**, 6708 Mar (2015).

[88] Bukov, M., Kolodrubetz, M., and Polkovnikov, A. *Phys. Rev. Lett.* **116**, 125301 Mar (2016).

[89] Claassen, M., Jiang, H.-C., Moritz, B., and Devereaux, T. P. *Nature Communications* **8** Oct (2017).

[90] Lucchini, M., Medeghini, F., Wu, Y., Vismarra, F., Borrego-Varillas, R., Crego, A., Frassetto, F., Poletto, L., Sato, S. A., Hübener, H., De Giovannini, U., Rubio, A., and Nisoli, M. *Nature Communications* **13**, 7103 Nov (2022).

[91] Peierls, R. *Zeitschrift für Physik* **80** Nov (1933).

[92] Feynman, R. P. *Ch. 21: The Schrödinger Equation in a Classical Context: A Seminar on Superconductivity.* The Feynman Lectures on Physics Vol. III.

[93] Hejazi, K., Liu, J., and Balents, L. *Phys. Rev. B* **99**, 205111 May (2019).

[94] Arakawa, N. and Yonemitsu, K. *Phys. Rev. B* **104**, 214413 Dec (2021).

[95] Mohan, P., Saxena, R., Kundu, A., and Rao, S. *Phys. Rev. B* **94**, 235419 Dec (2016).

[96] Khomskii, D. I. and Streltsov, S. V. (2022).

[97] Chaloupka, J., Jackeli, G., and Khaliullin, G. *Phys. Rev. Lett.* **105**, 027204 Jul (2010).

[98] Brinkman, W. F. and Rice, T. M. *Phys. Rev. B* **2**, 1324–1338 Sep (1970).

[99] Liu, H., Chaloupka, J., and Khaliullin, G. *Phys. Rev. Lett.* **125**, 047201 Jul (2020).

[100] Yamaji, Y., Nomura, Y., Kurita, M., Arita, R., and Imada, M. *Phys. Rev. Lett.* **113**, 107201 Sep (2014).

[101] Janssen, L., Andrade, E. C., and Vojta, M. *Phys. Rev. B* **96**, 064430 Aug (2017).

[102] Amano, T., Kawakami, Y., Itoh, H., Konno, K., Hasegawa, Y., Aoyama, T., Imai, Y., Ohgushi, K., Takeuchi, Y., Wakabayashi, Y., Goto, K., Nakamura, Y., Kishida, H., Yonemitsu, K., and Iwai, S. *Phys. Rev. Research* **4**, L032032 Aug (2022).

[103] Banerjee, S., Kumar, U., and Lin, S.-Z. *Phys. Rev. B* **105**, L180414 May (2022).

[104] Kim, H.-S. and Kee, H.-Y. *Phys. Rev. B* **93**, 155143 Apr (2016).

[105] Sinn, S., Kim, C. H., Kim, B. H., Lee, K. D., Won, C. J., Oh, J. S., Han, M., Chang, Y. J., Hur, N., Sato, H., Park, B.-G., Kim, C., Kim, H.-D., and Noh, T. W. *Scientific Reports* **6**, 39544 Dec (2016).

[106] Bertinshaw, J., Gurung, N., Jorba, P., Liu, H., Schmid, M., Mantadakis, D. T., Daghofer, M., Krautloher, M., Jain, A., Ryu, G. H., Fabelo, O., Hansmann, P., Khaliullin, G., Pfleiderer, C., Keimer, B., and Kim, B. J. *Phys. Rev. Lett.* **123**, 137204 Sep (2019).

[107] Gretarsson, H., Suzuki, H., Kim, H., Ueda, K., Krautloher, M., Kim, B. J., Yavaş, H., Khaliullin, G., and Keimer, B. *Phys. Rev. B* **100**, 045123 Jul (2019).

[108] Cuoco, M., Forte, F., and Noce, C. *Phys. Rev. B* **74**, 195124 Nov (2006).

[109] Katzgraber, H. G., Trebst, S., Huse, D. A., and Troyer, M. *Journal of Statistical Mechanics: Theory and Experiment* **2006**(03), P03018 Mar (2006).

[110] Kotze, J. *arXiv* , 0803.0217 (2008).

[111] Earl, D. J. and Deem, M. W. *Phys. Chem. Chem. Phys.* **7**, 3910–3916 (2005).

[112] Hukushima, K. and Nemoto, K. *Journal of the Physical Society of Japan* **65**(6), 1604–1608 (1996).

[113] Janssen, L., Andrade, E. C., and Vojta, M. *Phys. Rev. Lett.* **117**, 277202 Dec (2016).

[114] Rozada, I., Aramon, M., Machta, J., and Katzgraber, H. G. *Phys. Rev. E* **100**, 043311 Oct (2019).

[115] Weber, L., Boström, E. V., Claassen, M., Rubio, A., and Kennes, D. M. *arXiv* , 2302.08528 (2023).

[116] Khaliullin, G., Horsch, P., and Oleś, A. M. *Phys. Rev. Lett.* **86**, 3879–3882 Apr (2001).

[117] Kim, H.-S. *Applied Science and Convergence Technology* **30**, 191–194 Nov (2021).

[118] Imai, Y., Nawa, K., Shimizu, Y., Yamada, W., Fujihara, H., Aoyama, T., Takahashi, R., Okuyama, D., Ohashi, T., Hagihala, M., Torii, S., Morikawa, D., Terauchi, M., Kawamata, T., Kato, M., Gotou, H., Itoh, M., Sato, T. J., and Ohgushi, K. *Phys. Rev. B* **105**, L041112 Jan (2022).

[119] Nawa, K., Imai, Y., Yamaji, Y., Fujihara, H., Yamada, W., Takahashi, R., Hiraoka, T., Hagihala, M., Torii, S., Aoyama, T., Ohashi, T., Shimizu, Y., Gotou, H., Itoh, M., Ohgushi, K., and Sato, T. J. *Journal of the Physical Society of Japan* **90**(12), 123703 (2021).

[120] Ni, D., Gui, X., Powderly, K. M., and Cava, R. J. *Advanced Materials* **34**(7), 2106831 (2022).

[121] Kaib, David A. S. and Riedl, Kira and Razpopov, Aleksandar and Li, Ying and Backes, Steffen and Mazin, Igor I. and Valenti, Roser. *npj Quantum Materials* **7**, 75 Jul (2022).

[122] Gotfryd, D., Rusnačko, J., Wohlfeld, K., Jackeli, G., Chaloupka, J. c. v., and Oleś, A. M. *Phys. Rev. B* **95**, 024426 Jan (2017).

[123] Weinberg, P. and Bukov, M. *SciPost Phys.* **7**, 020 Aug (2019).

[124] Weinberg, P. and Bukov, M. *SciPost Phys.* **2**, 003 Feb (2017).

Statutory Declaration

I herewith declare that I have composed the present thesis myself and without use of any other than the cited sources and aids. Sentences or parts of sentences quoted literally are marked as such; other references with regard to the statement and scope are indicated by full details of the publications concerned. The thesis in the same or similar form has not been submitted to any examination body and has not been published. This thesis was not yet, even in part, used in another examination or as a course performance. Furthermore I declare that the submitted written (bound) copies of the present thesis and the version submitted on a data carrier are consistent with each other in contents.

_____   _____
Pascal Strobel   Date